Micromecanical model : correlation between hydraulic and acoustic parameters of cement-based materials

Sirine Maalej

N ° d'odre: 137

ECOLE CENTRALE DE LILLE

THESE

présentée en vue
d'obtenir le grade de

DOCTEUR

en
Spécialité: Génie Civil

par

Sirine MAALEJ

DOCTORAT DELIVRE PAR L'ECOLE CENTRALE DE LILLE

Titre de la thèse:

Micromechanical model: correlation between hydraulic and acoustic parameters of cement-based materials

Soutenue le 13 Décembre 2010 devant le jury d'examen

Président du jury	M. Denis DAMIDOT	Professeur, *Ecole des Mines de Douai, France*
Rapporteur	M. Mariusz KACZMAREK	Professeur, *IEMACS, Bydgoszcz, Pologne*
Rapporteur	M. Sami EL BORGI	Professeur, *Ecole Polytechnique de Tunisie, Tunisie*
Examinateur	M. Hichem SMAOUI	Professeur, *Ecole Nationale d'Ingénieurs de Tunis, Tunisie*
Examinateur	M. Issam DOGHRI	Professeur, *Université Catholique de Louvain, Belgique*
Directeur de thèse	M. Zoubeir LAFHAJ	Professeur, *Ecole Centrale de Lille, France*
Co-Directeur de thèse	M. Mounir BOUASSIDA	Professeur, *Ecole Nationale d'Ingénieurs de Tunis, Tunisie*

Thèse préparée dans le Laboratoire de Mécanique de Lille UMR CNRS 8107 EDSPI 072

To my first teachers: my parents

Acknowledgements

The research project reported in this thesis was a part of a cooperation between l'Ecole Cenrale de Lille, ECL France and l'Ecole Nationale d'Ingénieurs de Tunis, ENIT Tunisia. I would like to express my sincere gratitude to my supervisors Professor Zoubeir LAFHAJ and Professor Mounir BOUASSIDA, who gave me the chance to work within this collaboration on this interesting project.

I extend my warmest thanks to Mr. Zoubeir LAFHAJ, professor at the Ecole Centrale de Lille and Director of the International Relations for his great contribution to the successful completion of this work. His valuable guidance, inspiring discussions, great patience and confidence helped to complete the project in good conditions.

I cordially thank, Mr. Mounir BOUASSIDA, professor at the Ecole Nationale d'Ingénieur de Tunis for his participation, advice, encouragement and support throughout these years.

I would like to record my debt of gratitude to Mr. Nemkumar BANTHIA, Professor of Civil Engineering at the University of British Columbia, for inviting me to UBC as visiting student and for giving me the unforgettable oppotunity to work with his team.

I would also like to express my gratitude to Mr. Jean Yves Dauphin for his help and encouragements. I have a lot of respect for this great man for his scientific and human qualities.

A most special thank to Mr. Marc GOUEYGOU. The discussions I had with him were always very intersting and very fruitful.

I would like to thank Professors, Denis DAMIDOT, Mariusz KACZMAREK, Sami EL BORGI, Hichem SMAOUI and Issam DOGHRI for giving me the honor to accept being part of my thesis jury. Their careful reading of my thesis report and their comments were relevant and contributed to improve the report.

I would like to thank the whole team of the Unité de Recherche et d'Ingénierie Géothechnique at the ENIT for their cooperation and support. I take this opportunity to thank also all the staff of the Ecole Centrale de Lille where I enjoyed a pleasant working environment. My special thanks to the material group members at the University of British Columbia.

My very heartfelt thanks go to my friends who shared a lot of laughter, debates, ideas, cooking evenings and shopping, but who, above all, proved their support and understanding.

I owe much to my parents and grand parents for their long-distance encouragement and support. I am also grateful to my beloved sisters, Sonia and Maroua who looked out for me

always. Thanks for my family in law who believed in me.

Last, but surely not least, the great words I would like to give to my dear husband, Anouar, for his love, understanding and support in every aspect. Thanks my darling for giving me the freedom to undertake this challenge and continue the adventure.

Finally, I thank all High, Allah, for allowing me to go after this great work.

Summary

The objective of this work is the characterization of unsaturated cement paste porosity through the use of ultrasonics. The correlation between ultrasonic velocity and porosity in cement paste material is studied based on both micromechanical modelling and experiments.

Experimental measurements of ultrasonic longitudinal and transverse velocities as a function of water to cement ratio were performed on cement paste with and without air-entrained adjuvant. Different saturation states were considered within both materials. The longitudinal and transverse velocities showed a decrease when increasing the W/C ratios.

In the micromechanical modeling, the porous structure was modelled by spherical pores arbitrary embedded in a nonporous cementitious matrix. The effects of saturation were modeled by approximating the porous structure as a penny shaped ellipsoidal inclusions of aspect ratio varying with the W/C ratio. Several different micromechanical models for estimating the homogenized elastic moduli of cement paste and air-entrained cement paste were studied. The micromechanical modelling has shown that the longitudinal and transverse wave velocities of the dry cement paste are lower than those of the water saturated cement paste. This effect is equally prominent for all the cement paste W/C ratios (or porosities).

The model of Mori-Tanaka was found to give the best fit with the experimental results for the cement paste modeling. While, the self-consistent model gave the best estimate of the mechanical and ultrasonic air-entrained cement paste properties when compared to the laboratory experimental results. The measured velocities on the cement paste samples as a function of porosity and saturation were found by varying the inclusions aspect ratio.

The findings of this work should be most appropriate as a foundation for an inversion process and improved cementitious material porosity determination by nondestructive methods.

Keywords: Cement paste, Micromechanical modelling, Ultrasound, Porosity, Saturation.

Résumé

L'objectif de cette thèse est la caractérisation de la porosité de la pâte de ciment partiellement saturée par des ondes ultrasonores. Les corrélations entre les vitesses ultrasonores et la porosité ont été étudiées en se basant à la fois sur les résultats expérimentaux et la modélisation micromécanique.

Des mesures expérimentales de vitesses ultrasonores longitudinales et transversales en fonction du rapport eau/ciment ont été effectuées sur la pâte de ciment avec et sans entraîneur d'air. Différents états de saturation ont été considérés pour les deux matériaux. Les vitesses longitudinales et transversales ont montré une décroissance lors de l'augmentation du rapport E/C.

En modélisation micromécanique, les effets de saturation ont été modélisés en supposant que la structure poreuse est formée d'inclusions ellipsoïdales de facteur de forme variable selon le rapport E/C. Afin d'estimer les modules homogénéisés élastique de la pâte de ciment et de pâte de ciment à entraîneur d'air différents modèles micromécaniques ont été étudiés. Les résultats de la modélisation micromécanique ainsi que les résultats expérimentaux ont montré que les vitesses des ondes longitudinales et transversales de la pâte de ciment à l'état sec sont inférieures à ceux de l'état saturé. Cet effet est tout aussi important pour l'ensemble des rapports E/C (ou porosités).

Le modèle de Mori-Tanaka a donné la meilleure estimation des résultats expérimentaux mesurés sur la pâte de ciment. Alors que le modèle auto-cohérente a donné la meilleure estimation des propriétés mécaniques et ultrasonores de la pâte de ciment avec entraîneur d'air. Les vitesses mesurées sur les échantillons de pâte de ciment en fonction de la porosité et la saturation ont été retrouvées en faisant varier le facteur de forme des pores.

Les résultats de ce travail devraient être les plus appropriés en tant que fondement d'un processus d'inversion et l'amélioration de la détermination de la porosité de la pâte de ciment par les ultrasons en tant que méthodes non destructives.

Mots clés: Pâte de ciment, Modélisation micromécaniques, Ultrason, Porosité, Saturation. 2

Contents

Introduction **1**

I Linear homogenization of elastic composites 7

1 General considerations in linear homogenization **11**
1.1 Representative Volume Element (RVE) . . . 12
1.2 Average fields of composite medium . . . 13
1.2.1 The average strain . . . 13
1.2.2 The average stress . . . 15
1.3 Inclusions' geometry . . . 16
1.3.1 Inclusions' shape . . . 16
1.3.2 Inclusions' orientation . . . 17
1.4 Effective Elastic properties of composite . . . 19

2 Bounding homogenization methods **23**
2.1 Hill's bounds . . . 23
2.1.1 Energy approach . . . 24
2.1.2 Averaging fields approach . . . 26
2.2 Hashin & Shtrikman method . . . 29
2.2.1 Hashin & Shtrikman variational principle . . . 29
2.2.2 Hashin & Shtrikman bounds . . . 31

3 Eshelby equivalent inclusion principle **35**
3.1 Eshelby's problem . . . 35
3.2 Stressed inclusion problem : The equivalent inclusion . . . 37
3.3 Dilute inclusion model . . . 39

4 Micromechanical homogenization models **41**
4.1 Mori-Tanaka model . . . 41
4.1.1 Inverse Mori-Tanaka model . . . 42
4.1.2 Interpolative model . . . 44
4.2 Self-consistent model . . . 44
4.2.1 Resolution and iteration scheme . . . 46
4.2.2 generalized self consistent method . . . 46
4.3 Kuster-Toksöz approximation . . . 47
4.4 Double inclusion model . . . 50
4.5 Differential Method . . . 52
4.5.1 Zimmerman resolution . . . 52

4.5.2 Berge resolution 53

II Experiments: Materials, techniques and procedures 57

5 Materials 61
5.1 Cement-based mix compositions 62
5.1.1 Cement paste 62
5.1.2 Air entrained cement paste 62
5.2 Cement properties 64
5.2.1 Cement chemical composition 64
5.2.2 Cement hydration 65

6 Evaluation of the cement paste internal structure 73
6.1 Water imbibition porosimetry and density 73
6.1.1 Water imbibition porosimetry 74
6.1.2 Material density 76
6.2 Mercury Intrusion Porosimetry (MIP) 78
6.2.1 MIP principle 78
6.2.2 MIP measurements 80
6.3 X-ray Microtomography 83
6.3.1 Image acquisition 83
6.3.2 Image processing 84
6.3.3 Air entrained voids determination 87
6.4 Scanning Electron Microscope (SEM) 89
6.4.1 Principle of SEM and sample preparation 90
6.4.2 SEM image observations on cement paste 92

7 Static mechanical measurements on cement paste 95
7.1 Materials and equipment for the compression test 95
7.2 Static Elastic moduli 95

8 Ultrasonic Pulse Velocity Measurements on Cement-based Materials 99
8.1 Principle of ultrasonic pulse velocity techniques 100
8.1.1 Christoffel equation 100
8.1.2 Christoffel equation resolution 101
8.2 Ultrasonic experimental measurements 102
8.2.1 Ultrasonic set-up 102
8.2.2 Signal processing 103

III Application of micromechanical modeling to the cement paste material **109**

9 Identification of the cement-based materials matrix properties **113**
9.1 Cement paste matrix properties . . . 113
9.1.1 Linear regression on the experimental data . . . 114
9.1.2 Homogenization on the matrix solid phases . . . 116
9.2 Air-entrained cement paste matrix properties . . . 121

10 Cement paste modeling **123**
10.1 Dry cement paste modeling . . . 123
10.1.1 Dilute inclusion formulation . . . 124
10.1.2 Self-consistent formulation . . . 125
10.1.3 Mori-Tanaka and Kuste-Toksöz formulations for dry cement paste 126
10.2 Saturated cement paste modeling and Biot's theory . . . 129
10.3 Partially saturated cementitious material modeling . . . 133
10.3.1 Two-phase modeling of unsaturated material . . . 134
10.3.2 Three-phase modeling of unsaturated cement paste . . . 137

11 Air-entrained cement paste modeling **141**

IV Correlation between ultrasound velocities and the hydraulic properties of the cement paste materials **149**

12 Investigation of the frequency regime **153**

13 Cement paste **155**
13.1 Cement paste proposed modeling . . . 155
13.2 Ultrasonic measured results . . . 159
13.3 Correlations . . . 162

14 Air-entrained cement paste **167**
14.1 Ultrasonic measured results . . . 167
14.2 Correlations . . . 169

Conclusions **175**

Appendices **179**

A Elastic constants relations **181**

B Elastic constant tensor **183**

C Proof of the Hashin-Shtrikman statements **185**

D Expressions of the Eshelby's tensor **189**

D.1 Ellipsoidal inclusion 190

D.2 Spherical inclusion 190

D.3 Flat disk 191

D.4 Cylinder 191

E WU-Eshelby Tensor **193**

F Double inclusion sub-problems **197**

Bibliography **201**

List of Tables

4.1 Assumptions, limitations and scopes of the different models 55

5.1 Composition and properties of the cement paste samples in (kg/m^3) . . 63
5.2 Composition and properties of the air-entrained cement paste samples in (kg/m^3) 64
5.3 Chemical properties of Portland cement CPA CEM I 52.5 used in this study 65
5.4 Portland cement compounds weights as determined by Bogue calculation 65
5.5 Coefficients a_i, b_i and c_i 70

6.1 Density values of air, water and cement paste matrix 77
6.2 Pore size distribution of the benchmark 86

7.1 Static Young modulus and Poisson ratio of cement paste at different saturation states 97

8.1 Specifications of ultrasonic transducers 103

9.1 Cement paste elastic moduli at zero porosity by linear regression on experimental measurements 115
9.2 Intrinsic elastic properties of hydrated and unhydrated cement paste phases 118
9.3 Computed hydration degree of the cement paste samples 119
9.4 Cement paste matrix density obtained by homogenization on the solid phases 120
9.5 Ultrasonic and mechanical properties of cement paste without air-entrained 121

10.1 Homogenized bulk K_{hom} and shear G_{hom} moduli for two-phase Mori-Tanaka and Kuster-Toksöz micromechanical models 127
10.2 Water properties 132
10.3 Bulk and density values of air and water 135

11.1 Homogenized micromechanical bulk and shear moduli for dry two-phase material - spherical pores 142
11.2 Applicability of micromechanical models to the cement paste 147

13.1 Varied aspect ratio for different W/C ratio compositions 165

A.1 Elastic constants relations 182

E.1 The coefficients P_{ij} and Q_{ij} for spheoidal inclusions 194

List of Figures

1 Thesis structure flowchart 5

1.1 A Representative Volume Element (RVE) 12
1.2 RVE subjected to macroscopic displacement u_i 14
1.3 RVE subjected to macroscopic boundary tensile strain t_i 15
1.4 Ellipsoidal shape (a) Sphere $\alpha = 1$, (b) Penny $\alpha = 0.2 < 1$, (c) Needle $\alpha = 2 > 1$ 17
1.5 Coordinate system used for specifying a general state orientation of an ellipsoidal inclusion 18
1.6 Schematic representation of a RVE of composite material 19

2.1 Schematic representation of Voigt model 25
2.2 Schematic representation of Reuss model 26
2.3 Schematic representation of Hirsh model 29

3.1 Schematic illustration of homogenization according to Eshelby method . 36
3.2 Eshelby homogenization procedure for stressed inclusion 38
3.3 Schematic representation of the Dilute inclusion model 39

4.1 Schematic representation of homogenization according to Mori-Tanaka method 42
4.2 Schematic representation of Inverse Mori-Tanaka method 43
4.3 Schematic representation of Self-consistent method : Isolation of inclusion and homogenization of its surrounding 45
4.4 Schematic representation of Generalized Self-consistent model 47
4.5 Schematic representation of the Kuster-Toksöz scattering problem 47
4.6 Associated schematic representation of the Kuster-Toksöz model 49
4.7 Schematic representation of the double inclusion model 50

5.1 Evolution of hydration solid products and porosity in the cement paste [235] 66
5.2 Schematic representation of the cement paste hydration 67
5.3 The plate-like C-H morphology and fine bundles of Type I C-S-H, platy-Type II C-S-H, and ettringite needles [201]. 68
5.4 Model of hydrated Portland Cement by Feldman & Sedera (1968) [70] . 69
5.5 Entrapped and capillary pores observed on a cement paste sample . . . 70

6.1 Relative mass loss of the cement paste materials when drying for (a) different W/C ratios and (b) different air-entrained contents 74
6.2 Measured capillary porosity for (a) cement paste and (b) air-entrained cement paste 75

6.3 Comparasion between the measured and the Powers estimated capillary porosity . . . 76
6.4 Variation of cement paste density with porosity and saturation degree: lines refers to the computed densities and dots to the measured ones . . 78
6.5 Mercury intrusion results obtained on cement paste sample with W/C= 0.3 79
6.6 Pore size distribution of (a) cement paste with different W/C ratios and (b) air-entrained cement paste with different air-entrained adjuvant amount, according to MIP test . . . 81
6.7 Porosity determined by Water imbibition and MIP on cement paste and air-entrained cement paste samples . . . 82
6.8 Tomographic images of air-entrained cement paste sample. Left- A tomographic cross section. Right- A 3D-reconstruction. . . . 83
6.9 Image processing steps on an air-entrained cement paste cross section . 84
6.10 Diagram of the image processing steps used on X-ray microtomography obtained images . . . 85
6.11 benchmark sample for image processing validation . . . 86
6.12 Benchmark hole size distribution . . . 87
6.13 Macroscopic pores volume fraction vs. entrained air content . . . 88
6.14 Macroporosity distribution (a) and mean diameter (b) of the different air-entrained contents . . . 89
6.15 Micro-, macro-, and total porosity relative to the air-entrained content. . 90
6.16 Cement paste sample (a) cast into epoxy and (b) coated with gold. . . . 91
6.17 Cement paste sample with 0.4 W/C observed with SEM . . . 92

7.1 Affixed (L) longitudinal and (T) transverse strain gauges on a cylindrical sample . . . 96
7.2 Variation of the static Young modulus of the cement paste with (a) the W/C ratio and (b) the saturation degree . . . 98
7.3 Variation of the static Poisson modulus of the cement paste with (a) the W/C ratio and (b) the saturation degree . . . 98

8.1 Frequency ranges for various ultrasonic applications . . . 99
8.2 Photo of the ultrasonic measurement set up . . . 103
8.3 Scheme of the ultrasonic measurement system . . . 104

9.1 Increased degree of hydration of PC pastes with increasing W/C ratios [135] . . . 114
9.2 Variation of experimental dynamic elastic moduli vs porosity for dry and saturated states . . . 115
9.3 Variation of measured capillary porosity and determined hydrated and unhydrated volume fractions . . . 119
9.4 Variation of the Hill determined cement paste matrix elastic moduli as function of material porosity . . . 121

9.5 Photos of the air-entrained cement paste porous structure for different amount of air-entrained adjuvant (as percentage of the cement mass) . . 122

10.1 Modeling of dry cement paste 124
10.2 Comparison between the measured cement paste (a) bulk and (b) shear moduli and those determined by the dilute inclusion model using matrix elastic moduli obtained by (I) linear regression on experimental measurements (II) homogenization on matrix phases 125
10.3 Estimates of bulk and shear dry cement paste moduli based on self-consistent model vs. porosity for different pores aspect ratio 126
10.4 Homogenized (a) bulk and (b) shear moduli of dry cement paste according to M-T and K-T models for different aspect ratio of pores 128
10.5 Estimated dry cement paste bulk modulus according to M-T and K-T for spherical pores 129
10.6 Estimated dry cement paste shear modulus according to M-T and K-T for spherical pores 130
10.7 Modelling of saturated cement paste 130
10.8 Saturated cement paste bulk modulus determined by Biot theory and micromechanical models (a) Mori-Tanaka (b) Kuster-Toksöz. 134
10.9 Two phases modeling of partially saturated cement paste 135
10.10 Bulk modulus of an air-water suspension 136
10.11 The variation of longitudinal velocity in air-water mixture at 20 °C . . . 137
10.12 Three phases modeling of partially saturated cement paste 138

11.1 Schematic representation of air-entrained cement paste as two phase composite for micromechanical modeling 142
11.2 Air entrained cement paste bulk modulus versus macroporosity for (a) dry and (b) saturated states. 143
11.3 Air entrained cement paste shear modulus versus macroporosity for (a) dry and (b) saturated states. 144
11.4 Air entrained cement paste (a) bulk and (b) shear moduli versus macroporosity for dry and saturated states. 145

13.1 Comparison between the measured and the Mori-Tanaka estimates of the Cement paste (a) bulk and (b) shear modulus for spherical pores assumption. 156
13.2 Relative variation of the shear modulus vs. the saturation degree 157
13.3 Variation of saturated cement paste bulk modulus vs. pores' aspect ratio; comparison between experiments and Mori-Tanaka model 158
13.4 Measured cement paste longitudinal (a) and transverse (b) velocity vs. porosity for different saturation degrees 160
13.5 Measured cement paste longitudinal velocity vs. saturation for different W/C ratio 161

13.6 Measured cement paste transverse velocity vs. saturation for different W/C ratio 161

13.7 Comparison between measured ultrasonic velocities (dots) and Mori-Tanaka model (lines) estimates; W/C=0.3; $\alpha = 1$ 162

13.8 Comparison between measured ultrasonic longitudinal velocities (dots) and Mori-Tanaka model (lines) estimates vs. saturation degree 164

13.9 Comparison between the measured ultrasonic transverse velocities (dots) and the Mori-Tanaka model (lines) estimates when varying the saturation degree 164

13.10 Relative error between (a) longitudinal and (b) transverse Mori-Tanaka estimated velocity and measured velocity 166

14.1 ultrasonic wave velocities versus wavelength (λ) to macropore diameter ratio for the air-entrained cement paste. 167

14.2 Variation of (a) longitudinal and (b) transverse ultrasonic velocity vs. porosity for saturated and dry air-entrained cement paste. 168

14.3 Experimental and estimated velocities for saturated cement paste material vs porosity (a) Longitudinal (b) Transverse 169

14.4 Experimental and estimated velocities for dry cement paste material vs porosity (a) Longitudinal (b) Transverse 170

E.1 Exact and approximated isoytopic part of the Wu-Eshelby tensor for a porous two-phase composite. 195

E.2 Exact and approximated deviatoric part of the Wu-Eshelby tensor for a porous two-phase composite. 196

F.1 The average on $V' - V$ vanishes when V' and V are ellipsoids of the same shape 199

Nomenclature

Roman lower case letters

f_i	Volume fraction of the i^{th} phase	[−]
n_i	Outward normal	[−]
p	Porosity	[−]

Roman capital letters

$\mathbf{A}$	Strain concentration tensor	[−]
$\mathbf{B}$	Stress concentration tensor	[−]
$\mathbf{C}_0$	Matrix stiffness elastic constants tensor	$[MPa]$
$\mathbf{C}_{hom}$	Homogenized composite stiffness elastic constants tensor	$[MPa]$
$\mathbf{C}_i$	i^{th} inclusion stiffness elastic constants tensor	$[MPa]$
$\mathbf{S}_0$	Matrix compliance elastic constants tensor	$[1/MPa]$
$\mathbf{S}_{hom}$	Homogenized composite compliance elastic constants tensor	$[1/MPa]$
$\mathbf{S}_i$	i^{th} inclusion compliance elastic constants tensor	$[1/MPa]$
E	Young modulus	$[1/MPa]$
$\mathbf{I}$	Unit tensor	
K_0	Matrix bulk modulus	$[MPa]$
G_0	Matrix shear modulus	$[MPa]$
K_{hom}	Homogenized bulk modulus	$[MPa]$
G_{hom}	Homogenized shear modulus	$[MPa]$
K_i	Bulk modulus of the i^{th} phase	$[MPa]$
G_i	Shear modulus of the i^{th} phase	$[MPa]$
S	Surface separating the matrix and the inclusion	$[mm^2]$
$\mathbb{S}$	Eshelby tensor	[−]
S_r	Water material saturation	[−]
V	Volume of the RVE	$[mm^3]$
V_0	Volume of the matrix	$[mm^3]$
V_a	Volume of air in the porous structure	$[mm^3]$
V_i	Volume of the i^{th} inclusion	$[mm^3]$
V_w	Volume of water in the porous structure	$[mm^3]$
W	Total deformation energy	

Greek lower case letters

α	Aspect ratio	$[dB/(MHzcm)]$
α_a	Attenuation coefficient	$[-]$
δ_{ij}	Kronecker delta	$[-]$
$\bar{\boldsymbol{\varepsilon}}$	Macroscopic strain tensor	$[-]$
$\boldsymbol{\varepsilon}_0$	Matrix micro-strain tensor	$[-]$
$\boldsymbol{\varepsilon}_i$	i^{th} inclusion's micro-strain tensor	$[-]$
η	Fluid viscosity	$[Pa.s]$
θ	Water content	$[-]$
ν	Poisson ratio	$[kg/m^3]$
ρ	Composite density	$[kg/m^3]$
ρ_0	Matrix density	$[kg/m^3]$
ρ_f	Fluid density	$[kg/m^3]$
$\bar{\boldsymbol{\sigma}}$	Macroscopic stress tensor	$[MPa]$
$\boldsymbol{\sigma}_0$	Matrix micro-stress tensor	$[MPa]$
$\boldsymbol{\sigma}_i$	i^{th} inclusion's micro-stress tensor	$[MPa]$
ω	Angular frequency	$[rad/s]$

Symbols

$< >$	Orientation average

Abbreviations

RVE	Representative Volume Element
W/C	Water to cement ratio

Introduction

Context

The cement-based materials, such as cement paste, mortar and concrete, are the most worldwide used materials in constructions. In 2007, for instance, the Lafarge group, first cement producer in the world, has produced 136 millions of tons of cement.
Unfortunately, various factors affect the cement-based materials causing their degradation, namely aging, chemical and physical damages, freezing, fire, reinforcement corrosion [6, 39] etc. These factors are well identified and are described with some detail in different publications [2, 189].
The degrading aggressive factors penetrate generally into the material through connected pores [11, 168]. Thus, porosity is a key parameter in the degradation process. It quantifies the resistance of the material against penetrating agents and is widely recognized as indicator of cementitious material durability [12]. Consequently and in order to follow up and monitor the structure degradation, current on-site tests aim to determine the material hydraulic properties, in particular, porosity and permeability.

Testing and control of materials is even more important nowadays due to the progress in the developing technologies used in such tests and the nature of materials that should be tested without any disturbance or damage. Thus, new technologies that do not affect the material future usefulness have been developed for materials testing, control and evaluation [129, 210]. These techniques are called *non-destructive* techniques and include radiography, ultrasonic, radar, thermography etc. A summery of the basic principles of the nondestructive methods and practical information for their use are given in [150, 210].

In the inspection of metals, nondestructive testing is a common practice as for steel pipelines inspection. However, the nondestructive inspection of cement-based material is relatively new. Hence, the application of these methods to the control and assessment of aging structures is receiving a great attention in the last decades. In the U.S for instance, the nondestructive methods have been considered for biennial inspections of bridges [179]. In particular, the nondestructive method based on elastic wave: the ultrasound, are becoming the most investigated as they are particularly flexibility, characterized by a low cost, and are capable of yielding information about the microscopic material structure. Indeed, the ultrasonic non-destructive testing has been standardized by many organizations in different countries. A critical comparison of eight standards was presented by Komloš et al. [125].

Background

The most commonly measured ultrasonic parameters are ultrasonic pulse velocities (UPV) [100]. The latter are directly related to the elastic parameters of the porous material they propagate into it. As elastic moduli depend on porosity [85, 212], this induces a relationship between porosity and ultrasonic velocity. Empirical (or semi-empirical) expressions that relate the porosity to elastic moduli were developed [81]. The use of these expressions is limited in situ, as the assumptions considered in such models are simplistic. On the other hand, FEM numerical computations, which are considered to be accurate and very general, were successful in estimating the elastic moduli of composite materials [13, 172]. However, they are expensive in terms of user's time, CPU time, and machine memory usage. For these reasons, general mechanical models based on the homogenization approach, i.e. micromechanical models, were developed. The micromechanical models make it possible to determine the overall properties of a composite material when the mechanical properties of all the constituents are known. Although they generally give approximations of the unknown properties, these models are easy to use, very fast, and consume low machine memory. In addition, these models provide physical explanations to the observed macro-phenomena.

The most ancient composites were used in planes. Recently they have many applications in polymer, metal, rubber, concrete matrix composites, biomaterial (e.g. arterial walls), etc. A composite is a combination of two materials or more that are combined at a macroscopic level and are not soluble in each other. One component is called the matrix (the continuous component), the others are called inclusions. Thus a composite can be seen as a micro-heterogeneous material.
The analysis of such material is not a recent development. 150 years ago, research began on the estimation of the effective responses of a composite material under a variety of assumptions on the internal fields within the microstructure. Works dating back at least to Maxwell (1873) [152], he focused on determining overall macroscopic transport phenomena. Then Voigt (1889) focused on the effective mechanical properties with a later contribution by Reuss (1929).
Later, various methods where developed to resolve a composite homogenization problem. Two main procedures can be distinguished according to the effective environment for which the inclusions are subjected. The first, is the effective fields method (EFM) [151], which consists in placing the inclusions in mechanical fields with effective strain or stress. The second is the effective medium method (EMM), where the inclusions are placed in a medium where the elastic properties have already been homogenized. The most known EFM are the Dilute inclusion, the Mori-Tanaka [14, 157] and the Kuster-Toksöz [23, 130, 131]. The EMM concerns two principal methods called the self-consistent ([18], [19]) and differential methods([164]).

Application of the aforementioned methods to cementitious materials is still a chal-

lenging issue. Few works dealt with this subject. One can mention the study carried out by Hernández et al. [98] where cement paste with only two different porosities was considered. Hernández et al. applied [96] a two-phase micromechanical model based on the Mori-Tanaka theory in order to relate the porosity and ultrasonic properties of mortar. They formulated [99] and applied [97] later a three-phase micromechanical model for ultrasonic characterization of mortar. The authors found that mortar porosity can be estimated by non-destructive ultrasonic testing with a mean error of 10%. Yaman et al. [230, 231] described active and non-active porosity in concrete by investigating the correlations between ultrasonic measurements and the mechanical, semi-empirical and micromechanical models. Unlike the mechanical and semi-empirical models, the theoretical models give good estimates for the mechanical and acoustic parameters of concrete. Zimmerman [239] focused on describing cement paste using a single model: the Kuster-Toksöz model. He found a good compromise with experimental data when varying porosity for a particular form of pores: spheroidal pores with radius ratio (aspect ratio) equal to 0.31. Other studies were carried out to compare the theoretical predictions of different micromechanical models [18, 19, 121] without experimental validation.

A comprehensive experimental measurements were carried on our laboratory on the cement paste material. It included namely porosity and ultrasonic measurements on cement paste with different water to cement ratio. Aiming to enhance the understanding of this material's behavior, the present study was essential. Thus, this work intends to improve the effective cement paste elastic parameters predictions based on micromechanical modelling. Indeed, various micromechanical models were evaluated in this study. As on site cementitious structures can be either dry, partially or fully saturated by two or more different fluids, a special attention was dedicated to the effect of water saturation on the micromechanical modeling and ultrasonic testing of cement paste material. Indeed, rare works focused on the subject [21].

Theses Objectives

The objective of this thesis is to develop a correlation between the measured macroscopic ultrasonic properties and the micro-structural hydraulic characteristics of selected cement-based materials. This includes a comprehensive understanding of ultrasonic wave propagation characteristics in cement-based materials as well as a large interpretation and application of composite multi-scale theories relating the material micro-properties to its macro-properties.
The selected cementitious material was the cement paste with and without air-entrained adjuvant. Indeed, this material is a critical binding material in mortar and concrete. Thus its properties influence the structural integrity and durability of mortar and concrete structures. The investigation of the air-entrained cement paste aimed to study the effect of porosity variation when fixing the water to cement ratio.

The present study dealt with the following considerations:

- A single cement paste material was studied: the Portland cement paste;
- The water/cement ratio was varied experimentally from 0.3 to 0.7;
- Two types of adjuvant were included within the studied materials: the superplasticizer and the air-entrained;
- Moisture state was varied: dry, partially and fully saturation states were investigated;
- A single frequency of 500 *kHz* was fixed for the ultrasonic measurements;
- Selected multi-scale theories were developed; namely the most used micromechanical models: the Hashin-Shtrikman, the dilute inclusion model, the Mori-Tanaka model, the Kuster-Toksöz model and the self-consistent model.

Dissertation structure

The conducted research project is described in the **four parts** of this thesis. The flowchart of the structure is shown in Fig.1. In the first part (chs.2-3-4), the theoretical background of composite modeling is outlined. Comprehensive descriptions of existing research on the modeling of a multiphase composite were reviewed in details. The most used micromechanical models investigated in the homogenization of composite are described in chapter 4.
In the second part (chs.5-6-7-8) of this thesis, the experimental materials, techniques and procedures are presented in detail. The prepared cement paste samples mix properties are detailed. In chapter 6, the pore structure of cement paste was detected by water imbibition, mercury intrusion porosimetry (MIP), X-ray microtomography and scanning electron microscopy (SEM). Ultrasonic pulse velocity (UPV) measurements were performed on cement paste with and without air-entrained adjuvant as described in chapter 8.
In the third part (chs.9-10-11), the application of the existing micromechanical models to the cement paste materials were discussed. The cement paste phases properties needed for the modeling are determined. In chapters 10 and 11, the parameters influencing the homogenized macro-structural properties, such as pore fraction and shape, the saturation degree and matrix elastic properties, are varied. The simulated homogenized properties using different micromechanical models are compared. The applicability of each of them to the cement paste material is investigated.
In the last part (chs.12-13-14), the simulated elastic properties and ultrasonic velocities are compared to the experimental results. The theoretical and measured velocities behaviors of cement paste were examined under different porosities and saturation states.

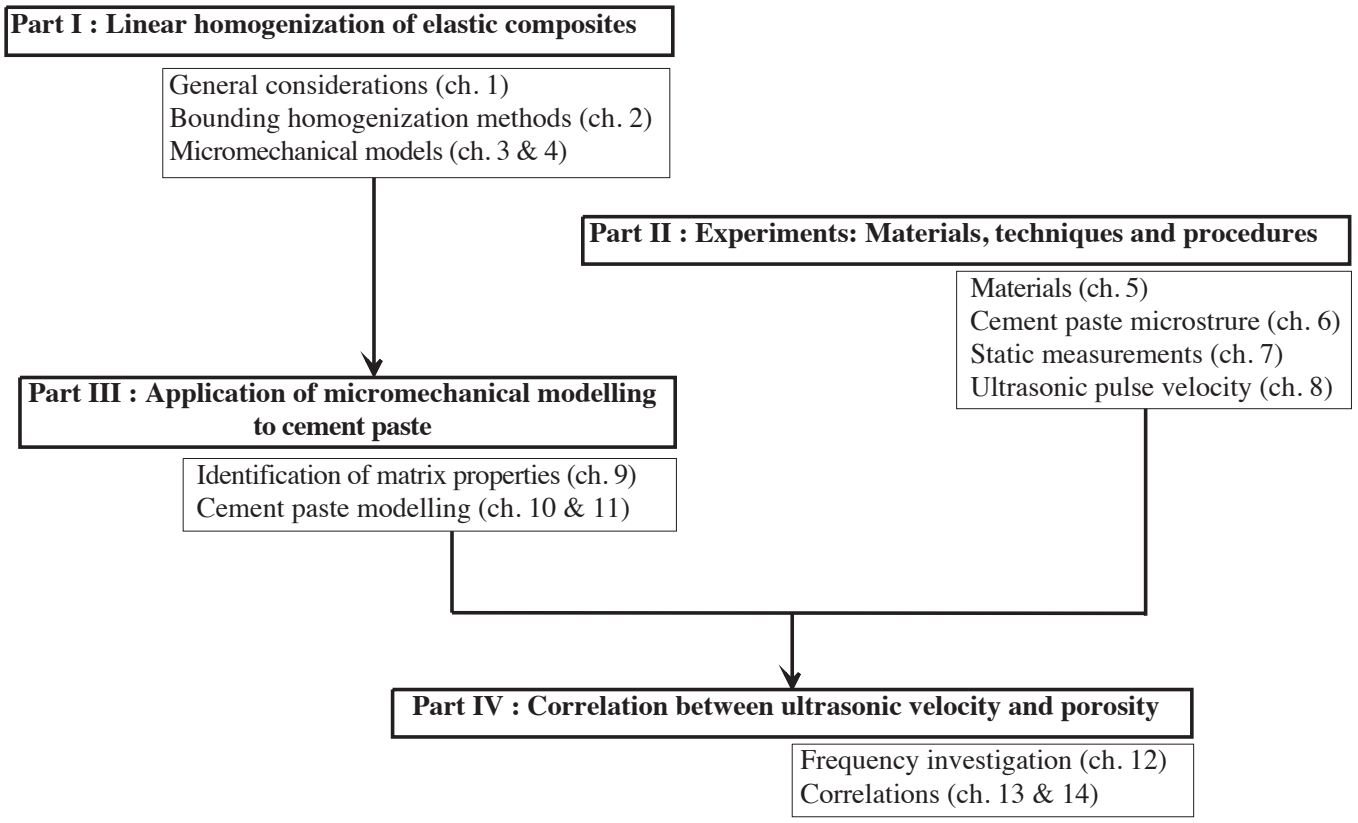

Figure 1: Thesis structure flowchart

Part I

Linear homogenization of elastic composites

1 General considerations in linear homogenization 11

2 Bounding homogenization methods 23

3 Eshelby equivalent inclusion principle 35

4 Micromechanical homogenization models 41

Introduction

The study of the behavior of composite materials can be carried out either on the macro or on the micro-scale. A better understanding of the mechanical, physical and chemical interactions within the material is achieved when focusing of the micro-scale. This latter can be reached through the scale-transition method that was developed since the fifties to overtake the limitations of the classical solid mechanics that was based on experiments. The principle of this method is the transition from microscopic to macroscopic scale using homogenization approaches.
Indeed, a homogenization approach is based on the relationships between microscopic and macroscopic material's properties. It characterizes the mechanical properties and the behavior of the material at the macroscopic scale from the description of its constituents at the microscopic scale [30, 159, 141].
Among the developed homogenization approaches, there is the cell and the subcell methods [1, 62] , the FE simulations based Unit Cell method [132, 144], the asymptotic expansion based displacement field method [114] and the mean-field based approach. In this chapter, the latter will be investigated and detailed. Such choice is argued by the fact that the mean-field based methods are the less expensive in terms of user's time, CPU time, and machine memory usage. In addition, they have proved good results in modeling the behavior of various materials, namely polymer composites . However, they were rarely applied to cementitious composite. Thus, this thesis aims to focus on the possible applications of the mean-fields based homogenization approach to cement-based materials, especially cement paste. A first attempt to apply these approaches to mortar was presented in [146] but is not presented in this work.

In this part, general considerations, assumptions and notations of elastic composites' homogenization are first introduced. The most two used bounding methods in homogenization are then presented. In the fourth chapter, the Eshelby inclusion's principle, that is considered to be in the basis of micromechanical modeling, is detailed. Later, different micromechanical methods are explained, such as, the Mori-Tanaka, the Kuster-Toksöz and the self-consistent.
It is necessary to note that in the following, we will proceed with basically mathematical description of the homogenization methods since the key of their development are essentially mathematical rather than physical.

Chapter 1

General considerations in linear homogenization

Homogenization of composite material allows the determination of material's macro-properties based on the micro-properties of its constituents. The link between micro-level and macro-level properties is established based on suitable micro-macro relationships, such as averaging procedures in the case of the mean-field homogenization approach. In this chapter, the general tools used in homogenization approaches, namely, the Representative Volume Element (RVE) and the average fields theory are presented. The chapter includes as well the inclusions' morphology description tools, such as the Orientation Distribution Function (ODF) and the coordinate system transformation tensors. Finally, the general expression that gives the homogenized elastic properties of a composite material is formulated.

Some useful mathematical relations that will be used in the following developments are presented here in. In the case of isotropic medium, the linear elastic behavior is defined by the stress $\boldsymbol{\sigma}$ and strain $\boldsymbol{\varepsilon}$ (noted also $\boldsymbol{e}$) fields as:

$$\varepsilon_{ij} = e_{ij} = \frac{1}{2}(u_{i,j} + u_{j,i}) \tag{1.1}$$

$$\sigma_{ij} = \lambda e_{mm}\delta_{ij} + 2\mu e_{ij} \tag{1.2}$$

Where:

- λ and μ are the Lamé constants, having direct relation to the most meaningful mechanical characteristics: the Young's modulus, E, the shear modulus G, and the Poisson's ratio, ν (see Appendix A);
- $u_{i,j}$ is the derivative of the displacement u_j with respect to x_j;
- a repeated suffix is a summation over the values 1, 2 and 3.

A second order tensor f_{ij} can be split into its symmetric and deviatoric parts such that:

$$f_{ij} = f^*_{ij} + \frac{1}{3} f \delta_{ij} \tag{1.3}$$

Where: $f = f_{mm}$ and $f^*_{ij} = f_{ij} - \frac{1}{3} f \delta_{ij}$
Using Eq.(1.2), the previous equation writes:

$$\sigma = 3Ke \quad , \quad \sigma^*_{ij} = 2\mu e^*_{ij} \tag{1.4}$$

Where K is the bulk modulus [1] ; $K = \lambda + \frac{2}{3}\mu$.

1.1 Representative Volume Element (RVE)

The concept of Representative Volume Element (RVE) was first introduced by Hill (1963 [103], 1967[107]) to relate the macro-properties of a composite material point to its micro-properties that correspond to those of its micro-constituents. If a composite material formed by a matrix and multiple inclusions is considered, then a RVE can be defined as shown on Fig.1.1.

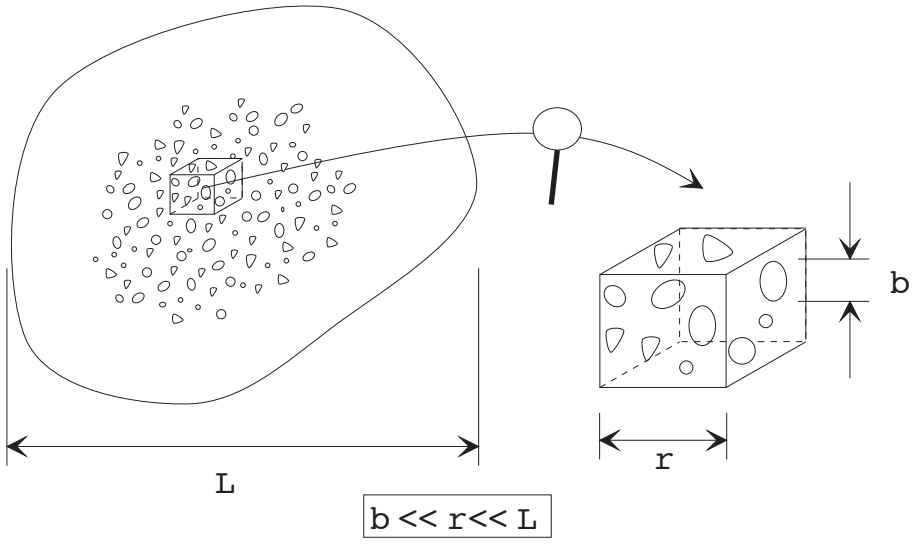

Figure 1.1: A Representative Volume Element (RVE)

The characteristic dimensions of the composite, the RVE and the inclusions are respectively L, r and b.
In essence, the characteristic dimension r of the RVE must be chosen in a manner to respect the following conditions [31]:

- $r << L$: so that the structure can be considered as continuous medium;
- $r >> b$: so that the RVE is sufficiently large to consider that the cell is statistically representative of the heterogeneous microstructure.

In addition, the chosen RVE must be subjected to the correct boundary conditions in order to represent the macromechanical problem.
In some special cases where the inclusions' distribution is periodic, the RVE is generally

[1] Bulk modulus (or modulus of volumetric elasticity) is defined as the ratio of hydrostatic pressure to the relative volume change and is given by : $K = V_0 \frac{\Delta P}{\Delta V}$.
Where : ΔP is the increase in pressure; ΔV is the decrease in volume and V_0 is the initial volume.

restrained to one cell, for instance, an hexagon for a honeycomb structured composite. If a RVE of a composite material is consider to be formed by $N+1$ phases: a matrix and N inclusions, then its volume and mass are given by the following summations:

$$V = V_0 + \sum_i V_i \tag{1.5}$$

$$M = M_0 + \sum_i M_i \tag{1.6}$$

Where:
(V_0, M_0) and (V_i, M_i) are, respectively, volumes and masses of the matrix and the i^{th} inclusion.
Then, assuming that all the phases are homogeneous, elastic and isotropic, the composite density (or unit mass) ρ is determined by:

$$\rho = \frac{M}{V} = \frac{\rho_0 V_0 + \sum_i (\rho_i V_i)}{V} = \rho_0 f_0 + \sum_i \rho_i f_i \tag{1.7}$$

where ρ_0 and ρ_i are respectively the matrix and the i^{th} inclusion density. $f_i = \dfrac{V_i}{V}$ is the volume fraction of the i^{th} phase and verify:

$$\sum_{i=0}^{N} f_i = 1 \qquad ; \qquad f_0 = 1 - \sum_i f_i \tag{1.8}$$

Because the RVE is, as presented, a heterogeneous material, the stress and strain fields inside it are expected to be non uniform. Consequently, averaging mechanical fields over the RVE is needed to express macro-properties in terms of the micro-properties.

1.2 Average fields of composite medium

The strain and stress fields in the RVE are not necessary uniform. Then average quantities have to be considered to describe the strain and stress fields at the micro-level.
In order the determine the average strain and stress over the RVE, two boundary condition configurations are considered in the following.

1.2.1 The average strain

Consider that the RVE is subjected to linear boundary displacements u_i corresponding to a macroscopic strain $\bar{\boldsymbol{\varepsilon}}$ (see Fig.1.2).

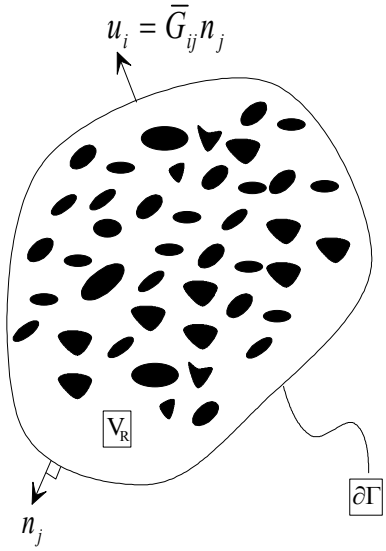

Figure 1.2: RVE subjected to macroscopic displacement u_i

Then, the micro-displacements are related to the macro-displacement gradient $\overline{\mathbf{G}}$ (not necessary symmetric but constant through the RVE) by the following relation:

$$u_i = \overline{G}_{ij} x_j \quad ; \quad \overline{G}_{ij} = \frac{\partial u_i}{\partial x_j} \tag{1.9}$$

Due to the small strain assumption, then:

$$\overline{\varepsilon_{ij}} = \frac{1}{2}(\overline{G}_{ij} + \overline{G}_{ji}) = \frac{1}{2}(\frac{\partial u_i}{\partial x_j} + \frac{\partial u_j}{\partial x_i}) \tag{1.10}$$

The average of the micro-strains over the RVE is then computed as follows,

$$\langle \varepsilon_{ij} \rangle_V = \frac{1}{V} \int_V \varepsilon_{ij} dV \tag{1.11}$$

$$\overset{Stokes}{=} \frac{1}{V} \frac{1}{2} \int_{\partial\Gamma} (u_i n_j + u_j n_i) d\Gamma \tag{1.12}$$

$$= \frac{1}{2V} \int_{\partial\Gamma} \underbrace{\overline{G}_{ik}}_{constant} n_k n_j + \underbrace{\overline{G}_{jk}}_{constant} n_k n_i d\Gamma \tag{1.13}$$

$$= \frac{1}{2V} (\overline{G}_{ik} \int_{\partial V} \underbrace{\frac{\partial n_k}{\partial n_j}}_{=\delta_{kj}} dV + \overline{G}_{jk} \int_{\partial V} \underbrace{\frac{\partial n_k}{\partial n_i}}_{=\delta_{ki}} dV) \tag{1.14}$$

$$= \bar{\varepsilon}_{ij} \tag{1.15}$$

It can be concluded that the average of the micro-strains over the RVE is equal to the macro-strain.

$$\langle \boldsymbol{\varepsilon} \rangle_V = \bar{\boldsymbol{\varepsilon}} \tag{1.16}$$

it should be noted that the presence of finite body forces does not affect this result [241].

1.2.2 The average stress

It it is assumed that the RVE be subjected to a uniform macro-stress $\bar{\sigma}$ corresponding to a uniform boundary tensile strain $t_i = \bar{\sigma}_{ij} n_j$ (see Fig.1.3) and that there is no body forces in the RVE (they are assumed to act at the macro level), then static equilibrium equations give:

$$div\boldsymbol{\sigma} = 0 \tag{1.17}$$

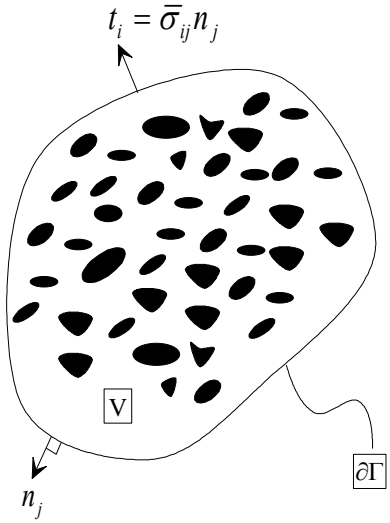

Figure 1.3: RVE subjected to macroscopic boundary tensile strain t_i

Considering the previous assumptions, the average stress over the RVE writes:

$$\langle \sigma_{ij} \rangle_V = \frac{1}{V} \int_V \sigma_{ij} dV \tag{1.18}$$

$$= \frac{1}{V} \int_V \left(\frac{\partial}{\partial n_k} (\sigma_{ik} n_j) - \underbrace{\frac{\partial \sigma_{ik}}{\partial n_k}}_{=0, Eq.1.17} n_j \right) dV \tag{1.19}$$

$$\overset{Stokes}{=} \frac{1}{V} \int_\Gamma \underbrace{\sigma_{ik}}_{=\bar{\sigma}_{ik}, \text{on the boundary surface}} n_k n_j d\Gamma \tag{1.20}$$

$$= \frac{1}{V} \bar{\sigma}_{ik} \int_\Gamma n_k n_j d\Gamma \tag{1.21}$$

$$= \bar{\sigma}_{ij} \tag{1.22}$$

Thereby, the average micro-stress σ over the volume of the RVE is equal to the macro-stress, such that:

$$\langle \sigma \rangle_V = \bar{\sigma} \tag{1.23}$$

It can be also observed that debonding (interface separation) does not affect this result [241].

1.3 Inclusions' geometry

Although in some homogenization approaches, no restrictions are imposed on the composite's phases, in general, the matrix is supposed to be continuous, while inclusions are modeled as ellipsoids or special cases of ellipsoids having specific orientations.

In this section, basic properties related to the inclusions geometry are introduced, mainly, the shape and the inclusions orientations' considerations in homogenization's modeling.

1.3.1 Inclusions' shape

The inclusions' shape modeling is an interesting issue in micromechanical models. First reflex assumed no condition on the inclusion shape such as the bounding methods of Hashin and Shtrikman [88, 93], and Walpole [216, 217]. Then, specific shapes were introduced in homogenization approaches. As the latter are almost based on analytical or FE computations, it was convenient to adopt symmetrical considerations when modeling inclusions' geometry. Thus, the most popular shapes in homogenization methods are ellipsoids [65], or special cases of ellipsoids such as spheres [36], elliptical cylinders [220], circular cylinders [26], penny or needle shaped ellipsoids, etc.
An ellipsoidal geometry is characterized by a revolution axis a_3 (taken here according to $X_3^{'}$). The axis according to $X_1^{'}$ and $X_2^{'}$ are permutable i.e. $a_1 = a_2$. The ratio between a_3 and a_1 is called the aspect ratio α. Accordingly, five different aspect ratios can be distinguished:

- $\alpha = 1$ spherical inclusion;
- $\alpha = \frac{a_3}{a_1} > 1$ prolate spheroid (needle shaped inclusion);
- $\alpha = \frac{a_3}{a_1} < 1$ oblate spheroid (penny shaped inclusion);
- $\alpha \simeq 0$ flat disk;
- $\alpha \simeq \infty$ cylinder.

The zero and infinite aspect ratios are generally used for modeling respectively cracks and fibers in composite materials. While the first ones concerns with other possible inclusion's shape modeling and are illustrated in Fig.1.4.

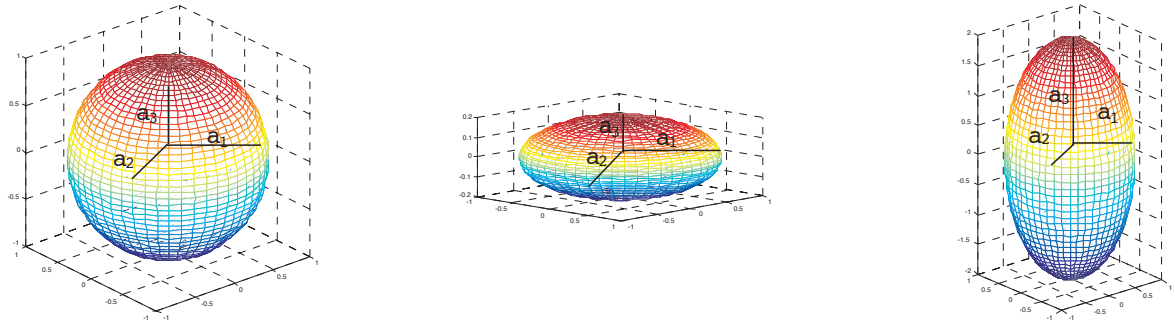

(a) (b) (c)

Figure 1.4: Ellipsoidal shape (a) Sphere $\alpha = 1$, (b) Penny $\alpha = 0.2 < 1$, (c) Needle $\alpha = 2 > 1$

1.3.2 Inclusions' orientation

In general, the orientation of an inclusion having a local coordinate system (X_1', X_2', X_3') is related to the global coordinate system (X_1, X_2, X_3) by the Euler angles (θ, ϕ, φ). If q_{ij} define the direction cosine between the i^{th} primed (local) axis and the j^{th} unprimed (global) axis, it can be expressed [116] as:

$$[q] = \begin{bmatrix} \sin\theta\cos\phi & \sin\theta\sin\phi & \cos\theta \\ -\cos\theta\cos\phi - \sin\phi\sin\varphi & -\cos\theta\sin\phi\cos\varphi + \cos\phi\sin\varphi & \sin\theta\cos\varphi \\ -\cos\theta\cos\phi\sin\varphi + \sin\phi\cos\varphi & -\cos\theta\sin\phi\sin\varphi - \cos\phi\cos\varphi & \sin\theta\sin\varphi \end{bmatrix} \tag{1.24}$$

If now, **A'** is a fourth rank tensor (relative to an ellipsoidal inclusion randomly oriented in the composite) expressed in the local coordinates system, then, the computation of **A** in the global coordinate system is given by:

$$A_{ijkl} = q_{pi}q_{rj}q_{sk}q_{tl}A'_{prst} \tag{1.25}$$

If the inclusion is of spheroïdal shape, then it can be presented in the global coordinate system by a unit vector p directed along its axis of revolution as showed in Fig.1.5.

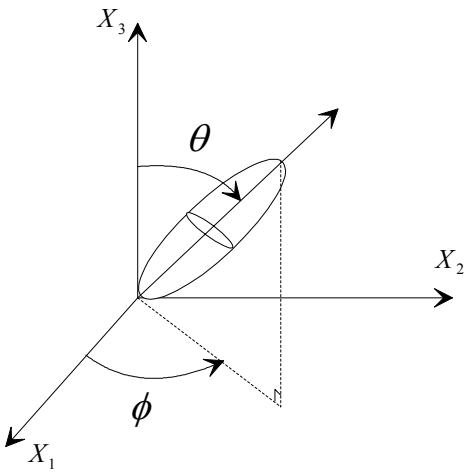

Figure 1.5: Coordinate system used for specifying a general state orientation of an ellipsoidal inclusion

The Orientation Distribution Function (ODF)

The properties and anisotropy of composite materials are influenced by the orientation distribution of the inclusions which is characterized by the Orientation Distribution Function (ODF) denoted by $\Gamma(\phi, \theta, \psi)$ [117]. The ODF informs about the density of probability for a particular orientation and must verify the following equation:

$$\frac{1}{8\pi^2}\int_{\theta=0}^{\pi}\int_{\phi=0}^{2\pi}\int_{\psi=0}^{2\pi}\Gamma(\phi,\theta,\psi)sin\theta d\phi d\theta d\psi = 1 \tag{1.26}$$

In the case of transversally isotropic material (X_3 is the axis of symmetry), $\Gamma(\phi, \theta, \psi)$ only depends on θ, then Eq.(1.26) writes:

$$\int_{\theta=0}^{\pi}\Gamma(\theta)sin\theta d\theta = 2 \tag{1.27}$$

In the particular case of isotropic inclusions distribution, the ODF is constant.
Furthermore, an ODF can be used to describe the inclusions alignment using two coefficients θ and d. Where d is a parameter that represents the degree of alignment:

$$d = 0 \Rightarrow \text{isotropic distribution of inclusions}$$

$$d \to \infty \Rightarrow \text{aligned distribution of inclusions}$$

For instance, Vu [214] has chosen the following ODF for the determination of effective properties of porous rocks:

$$\Gamma(\theta, d) = d\cosh(d\cos\theta)\sinh d \tag{1.28}$$

1.4 Effective Elastic properties of composite

In micromechanical formulations, the expressions of the effective elastic properties are generally obtained from the relationship between average stress and average strain in a chosen representative volume element (RVE). Consider a linearly elastic composite material with $N+1$ phases. One phase is the matrix; the others are the inclusions. The matrix is considered to be continuous with stiffness $\mathbf{C}_0$. Inclusions were supposed to have stiffness and volume fractions $\mathbf{C}_i$ and f_i. Let V be the volume of a representative volume element of the composite material (Fig.1.6). If V is subjected to a constant

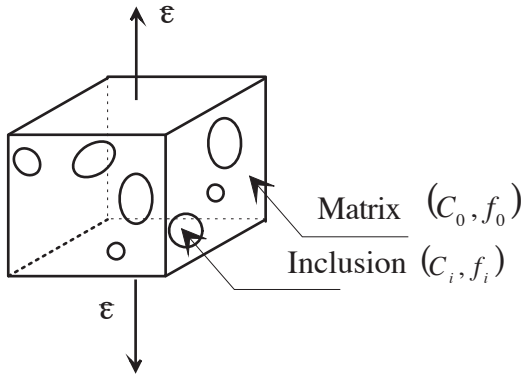

Figure 1.6: Schematic representation of a RVE of composite material

uniform overall strain field $\bar{\boldsymbol{\varepsilon}}$, then, the volume average of $\boldsymbol{\varepsilon}$ is defined by:

$$\langle \boldsymbol{\varepsilon} \rangle_V \overset{Eq.1.16}{=} \bar{\boldsymbol{\varepsilon}} = \frac{1}{V} \int \boldsymbol{\varepsilon} dV \tag{1.29}$$

The previous integral can be decomposed into the sum of integrals over the different volumes such that:

$$\bar{\boldsymbol{\varepsilon}} = \frac{1}{V} \int_{V_0} \boldsymbol{\varepsilon}_0 dV + \frac{1}{V} \sum \int_{V_i} \boldsymbol{\varepsilon}_i dV \tag{1.30}$$

From Eq.(1.29), one can deduce that the average strain in the matrix $\overline{\boldsymbol{\varepsilon}_0}$ is given by:

$$\overline{\boldsymbol{\varepsilon}_0} = \frac{1}{V_0} \int_{V_0} \boldsymbol{\varepsilon}_0 dV \tag{1.31}$$

Multiplying Eq.(1.31) by $f_0 = \frac{V_0}{V}$, the first integral of Eq.(1.30) is evaluated to:

$$\frac{1}{V} \int_{V_0} \boldsymbol{\varepsilon}_0 dV = f_0 \overline{\boldsymbol{\varepsilon}_0} \tag{1.32}$$

However, the second and third integrals should be computed over all possible orientations because the strain field in each inclusion depends on its orientation. This can

be solved by using the Orientation Distribution Function (ODF) $\Gamma(\phi, \theta, \psi)$. Thus, the volume integral over an inclusions yields:

$$\frac{1}{V}\int_{V_i} \boldsymbol{\varepsilon}_i dV = f_i \langle \boldsymbol{\varepsilon}_i \rangle \tag{1.33}$$

Where $\langle \boldsymbol{\varepsilon}_i \rangle$ is the orientation-dependent average strain in phase i and is defined by:

$$\langle \boldsymbol{\varepsilon}_i \rangle = \frac{\int_0^{\phi=2\pi}\int_0^{\theta=\pi}\int_0^{\psi=2\pi} \boldsymbol{\varepsilon}_i \Gamma(\phi,\theta,\psi) sin\theta d\phi d\theta d\psi}{\int_0^{\phi=2\pi}\int_0^{\theta=\pi}\int_0^{\psi=2\pi} \Gamma(\phi,\theta,\psi) sin\theta d\phi d\theta d\psi} \tag{1.34}$$

Then, the average strain in the composite given in Eq.(1.30) writes:

$$\bar{\boldsymbol{\varepsilon}} = f_0 \overline{\boldsymbol{\varepsilon}_0} + \sum f_i \langle \boldsymbol{\varepsilon}_i \rangle \tag{1.35}$$

Similarly, the average stress in the composite is:

$$\bar{\boldsymbol{\sigma}} = \langle \boldsymbol{\sigma} \rangle_V = f_0 \overline{\boldsymbol{\sigma}_0} + \sum f_i \langle \boldsymbol{\sigma}_i \rangle \tag{1.36}$$

If the matrix and inclusions are assumed to be linearly elastic, then the whole composite can be supposed to be linearly elastic. Therefore, the average stresses in the composite, the matrix and in the inclusions are related to the respective average strains by the Hooke's law:

$$\bar{\boldsymbol{\sigma}} = \mathbf{C}_{hom} \bar{\boldsymbol{\varepsilon}} \tag{1.37}$$

$$\bar{\boldsymbol{\varepsilon}} = \mathbf{S}_{hom} \bar{\boldsymbol{\sigma}} \tag{1.38}$$

$$\begin{aligned} \overline{\boldsymbol{\sigma}_0} &= \mathbf{C}_0 \overline{\boldsymbol{\varepsilon}_0} \\ \langle \boldsymbol{\sigma}_i \rangle &= \mathbf{C}_i \langle \boldsymbol{\varepsilon}_i \rangle \end{aligned} \tag{1.39}$$

$$\begin{aligned} \overline{\boldsymbol{\varepsilon}_0} &= \mathbf{S}_0 \overline{\boldsymbol{\sigma}_0} \\ \langle \boldsymbol{\varepsilon}_i \rangle &= \mathbf{S}_i \langle \boldsymbol{\sigma}_i \rangle \end{aligned} \tag{1.40}$$

Where ($\mathbf{C}_{hom}$, $\mathbf{S}_{hom}$), ($\mathbf{C}_0$, $\mathbf{S}_0$) and ($\mathbf{C}_i$, $\mathbf{S}_i$) are, respectively, the stiffness and the compliance tensors of the composite, the matrix and the inclusions . These latter verify the following condition:

$$C_{ijkl} S_{klmn} = \frac{1}{2}(\delta_{im}\delta_{jn} + \delta_{in}\delta_{jm}) \tag{1.41}$$

Substituting Eq.(1.39), resp. Eq.(1.40) into Eq.(1.36), resp. Eq.(1.35), yields to the following formulation of the macro-stress and macro-strain:

$$\bar{\boldsymbol{\sigma}} = f_0 \mathbf{C}_0 \overline{\boldsymbol{\varepsilon}_0} + \sum_i f_i \mathbf{C}_i \langle \boldsymbol{\varepsilon}_i \rangle \tag{1.42}$$

$$\bar{\boldsymbol{\varepsilon}} = f_0 \mathbf{S}_0 \overline{\boldsymbol{\sigma}_0} + \sum_i f_i \mathbf{S}_i \langle \boldsymbol{\sigma}_i \rangle \tag{1.43}$$

The average strain in the matrix and each phase i is related to the average strain in the overall composite as follows:

$$\begin{aligned} \overline{\boldsymbol{\varepsilon}_0} &= \bar{\mathbf{A}}_0 \bar{\boldsymbol{\varepsilon}} \\ \langle \boldsymbol{\varepsilon}_i \rangle &= \langle \bar{\mathbf{A}}_i \rangle \bar{\boldsymbol{\varepsilon}} \end{aligned} \tag{1.44}$$

Where the $\mathbf{A}_i$ are matrices dependent upon phases' concentrations and moduli. They are called strain concentration tensors and were introduced by Hill [103]. They were defined later as dependent also upon the geometry by Laws [139] and Jeong et al. [116]. Similarly, the stress fields in the matrix and each phase are related to the overall composite's stress by the stress concentration tensors $\mathbf{B}_i$:

$$\begin{aligned} \overline{\boldsymbol{\sigma}_0} &= \bar{\mathbf{B}}_0 \bar{\boldsymbol{\sigma}} \\ \langle \boldsymbol{\sigma}_i \rangle &= \langle \bar{\mathbf{B}}_i \rangle \bar{\boldsymbol{\sigma}} \end{aligned} \tag{1.45}$$

From Eq.(1.42) and using Eqs.(1.37)-(1.44), the homogenized stiffness tensor of the composite material is expressed:

$$\mathbf{C}_{hom} = f_0 \mathbf{C}_0 \bar{\mathbf{A}}_0 + \sum f_i \mathbf{C}_i \langle \bar{\mathbf{A}}_i \rangle \tag{1.46}$$

Substituting Eq.(1.44) into Eq.(1.35) gives:

$$f_0 \bar{\mathbf{A}}_0 + \sum f_i \langle \bar{\mathbf{A}}_i \rangle = \mathbf{I} \tag{1.47}$$

Where $\mathbf{I}$ is the fourth-rank unit tensor defined by:

$$I_{ijkl} = \frac{\delta_{ik}\delta_{jl} + \delta_{il}\delta_{jk}}{2} \tag{1.48}$$

with δ_{ik} being the Kronecker delta.
Determining $\bar{\mathbf{A}}_0$ from Eq.(1.47) and substituting it in Eq.(1.46) provides the effective stiffness tensor in the following form:

$$\mathbf{C}_{hom} = \mathbf{C}_0 + \sum_i f_i (\mathbf{C}_i - \mathbf{C}_0) \langle \bar{\mathbf{A}}_i \rangle \tag{1.49}$$

Following similar calculation as detailed above for $\mathbf{C}_{hom}$, the compliance composite homogenized tensor can be drawn:

$$\mathbf{S}_{hom} = \mathbf{S}_0 + \sum_i f_i (\mathbf{S}_i - \mathbf{S}_0) \langle \bar{\mathbf{B}}_i \rangle \tag{1.50}$$

This procedure enables the evaluation of the overall elastic properties $\mathbf{C}_{hom}$ with the help of orientation-dependent average strain concentration tensor $\langle \bar{\mathbf{A}}_i \rangle$. This tensor was evaluated in numerous of studies using for example Mori-Tanaka's average field theory [157] and Eshelby's equivalent inclusion principle [65] which are described in the next sections.

Chapter 2

Bounding homogenization methods

Although homogenization approaches aim to provide estimates of a composite's elastic properties values, some methods can only give bounds for these properties. Among the various used bounds in composites' elastic moduli assessment, there is the Hill's bounds and the Hashin-Shtrikman bounds. Concerning the first bounds, they correspond to two separate models called Voigt and Reuss models. The latter provide low and upper bounds for the elastic overall properties, when applied to characterize a composite material. The second bounds are known to be rigorous bounds and are obtained using appropriate variational principles. Both bounds are detailed in this chapter.

2.1 Hill's bounds

Hill's upper and lower bounds correspond to Voigt and Reuss estimates of elastic properties of composite material. Indeed, many homogenization approaches can be used to express the Voigt (1889) and Reuss (1929) models. Here in, two approaches are detailed. The first approach, was carried out by Hill [103] and computes, using two different methods, the total deformation energy stored in a material subjected to stress loading. The second approach uses the average stresses and strains to establish the Voigt and Reuss models. A generalization of the Voigt and Reuss models to N components' composites was introduced by Watt et al. [215].
V denotes the volume of a composite material with an overall elastic moduli $\mathbf{C}_{hom}$. Consider that the composite is formed by N phases with elastic moduli and volume $\mathbf{C}_i$ and V_i, respectively, where i refers to the phase i. The volume fraction of phase i is defined by:

$$f_i = \frac{V_i}{V} \tag{2.1}$$

2.1.1 Energy approach

if the material is assumed to be subjected to an uniaxial and uniform compressive stress $\bar{\sigma}$ counted positevely, then the total deformation energy W is given by [196]:

$$W = \frac{1}{2}\int_V \bar{\sigma}\bar{\varepsilon}dV \tag{2.2}$$

$$= \frac{1}{2}\bar{\sigma}\bar{\varepsilon}V \tag{2.3}$$

$$= \frac{1}{2}\bar{\sigma}^2\mathbf{C}_{hom}^{-1}V \tag{2.4}$$

$$= \frac{1}{2}\bar{\varepsilon}^2\mathbf{C}_{hom}V \tag{2.5}$$

Where $\bar{\varepsilon}$ is the average deformation given by:

$$\bar{\varepsilon} = \frac{dV}{V} = \bar{\sigma}\mathbf{C}_{hom}^{-1} \tag{2.6}$$

Consider now that the material is heterogeneous with N phases and that it is subjected to uniform stress $\bar{\sigma}$. Two configurations can be considered: composite's phases are arranged in series (the Reuss model) or in parallel (Voigt model) with respect to the loading axis.

2.1.1.1 Voigt model

In this case, it is assumed that the arrangement of phases is parallel to the loading axis (see Fig.2.1). Thus, the strain field in each phase $\boldsymbol{\varepsilon}_i$ is uniform and equal to the average strain $\bar{\varepsilon}$. So, the stress field in each phase can be written in the form:

$$\boldsymbol{\sigma}_i = \mathbf{C}_i\bar{\boldsymbol{\varepsilon}} \tag{2.7}$$

where $\mathbf{C}_i$ is the stiffness tensor of phase i.
The total deformation energy is:

$$W = \sum_{i=1}^{N} W_i = \sum_{i=1}^{N} \frac{\bar{\varepsilon}^2\mathbf{C}_i V_i}{2} \tag{2.8}$$

Where: V_i is the volume of the i^{th} phase.
The identification of Eq.(2.5) and Eq.(2.8) implies that the homogenized elastic modulus

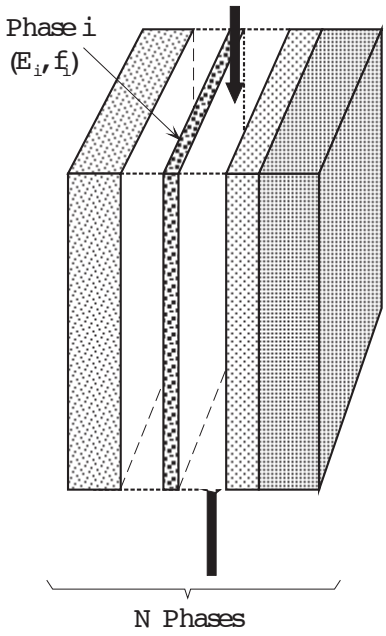

Figure 2.1: Schematic representation of Voigt model

writes:

$$\frac{1}{2}\bar{\boldsymbol{\varepsilon}}^2\mathbf{C}_{hom}V = \sum_{i=1}^{N}\frac{\bar{\boldsymbol{\varepsilon}}^2\mathbf{C}_i V_i}{2} \tag{2.9}$$

$$\mathbf{C}_{hom} = \sum_{i=1}^{N}\mathbf{C}_i \underbrace{\frac{V_i}{V}}_{=f_i} \tag{2.10}$$

$$\mathbf{C}_{hom}^{Voigt} = \sum_{i=1}^{N} f_i\mathbf{C}_i \tag{2.11}$$

Where $\mathbf{C}_{hom}^{Voigt}$ denotes the composite elastic tensor determined by using Voigt model.

2.1.1.2 Reuss model

Reuss model considers uniform stress field $\bar{\sigma}$ applied in perpendicular to the arrangement of phases (Fig.2.2). The total energy is written as:

$$W = \sum_{i=1}^{N} W_i = \sum_{i=1}^{N}\frac{\bar{\boldsymbol{\sigma}}^2 V_i}{2}\mathbf{C}_i^{-1} \tag{2.12}$$

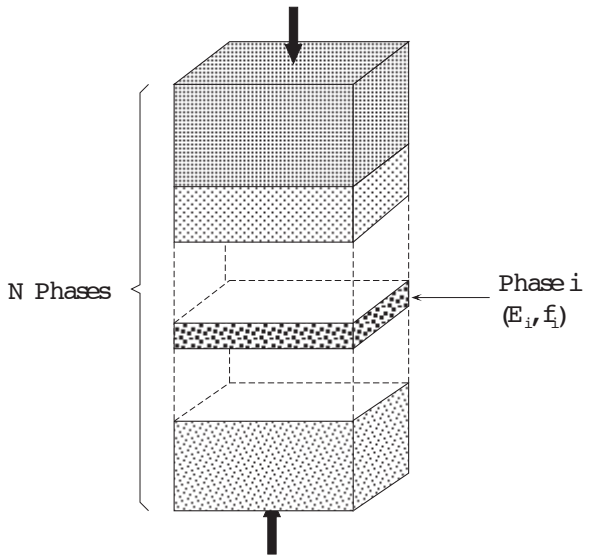

Figure 2.2: Schematic representation of Reuss model

As the composite is assumed to be a homogeneous material and the stress field is the same in the N phases, Eqs.(2.4)-(2.12) lead to :

$$\frac{\bar{\sigma}^2 V}{2}\mathbf{C}_{hom}^{-1} = \sum_{i=1}^{N}\frac{\bar{\sigma}^2 V_i}{2}\mathbf{C}_i^{-1} \tag{2.13}$$

$$\mathbf{C}_{hom}^{-1} = \sum_{i=1}^{N}\mathbf{C}_i^{-1}\underbrace{\frac{V_i}{V}}_{=f_i} \tag{2.14}$$

$$(\mathbf{C}_{hom}^{Reuss})^{-1} = \sum_{i=1}^{N} f_i\mathbf{C}_i^{-1} \tag{2.15}$$

2.1.2 Averaging fields approach

The approach that uses average stress and strain to determine the Voigt and Reuss homognized characteristics is detailed here after.
The Voigt model considers that the strain is uniform in the composite. Thus, the average strain is the same for all the phases:

$$\langle\boldsymbol{\varepsilon}_i\rangle = \bar{\boldsymbol{\varepsilon}} \tag{2.16}$$

Then, Eq.(1.44) implies that for each phase:

$$\langle\mathbf{A}_i\rangle = \mathbf{I} \tag{2.17}$$

While, The Reuss model assumes that the stress is uniform in the composite and Eq.(1.45) gives:

$$\langle \mathbf{B}_i \rangle = \mathbf{I} \tag{2.18}$$

According to Eqs.(1.49)-(1.50), the elastic moduli estimated by Voigt and Reuss, are respectively:

$$\mathbf{C}_{hom}^{Voigt} = \sum_i f_i \mathbf{C}_i \tag{2.19}$$

$$(\mathbf{C}_{hom}^{Reuss})^{-1} = \sum_i f_i \mathbf{C}_i^{-1} \tag{2.20}$$

These tensors are isotropic since $\mathbf{C}_i$ are so. If the overall properties of the composite are isotropic then only two constants have to be determined, namely the bulk and shear moduli, K and G (see Appendix B). Then, these moduli can be expressed from Eq.(2.19) for the Voigt (K_V, G_V) and Reuss (K_R, G_R) assumptions as follows:

$$K_V^* = \sum_i f_i K_i \quad ; \quad G_V^* = \sum_i f_i G_i \tag{2.21}$$

$$\frac{1}{K_R^*} = \sum_i \frac{f_i}{K_i} \quad ; \quad \frac{1}{G_R^*} = \sum_i \frac{f_i}{G_i} \tag{2.22}$$

To the author knowledge, there is no specific composite materials that have effective moduli equal to those predicted by Voigt or Reuss models. However, there are some that have identical response when subjected to particular solicitations. According to Bornert [30], a laminate multi-layer with isotropic phases subjected to a simple shear (parallel to the plan of layers), has the same response as described by Reuss. A one-direction composite formed by isotropic phases having identical Poisson ratios has the same response as described by Voigt when it is solicited along its axis. But the latter are not isotropic and then can not be described by Voigt or Reuss tensors.
Voigt and Reuss moduli form, respectively, upper and lower bounds for the overall elastic modulus given elastic properties and volume fractions of phases [102]. These bounds are called Hill's bounds and are considered to be the simplest ones. They are found to be accurate enough for polycrystals and agree fairly well with experiment, but they have many limitations. The major one is that the range between upper and lower bounds may grow largely for composites whose constituent phases have very different properties: the difference is by more than a factor of two according to Hill [103]. However, it is important to point out that Hill's bounds are achieved for some geometrical structures of composites such as simple laminate or fiber media [38].
Hill suggested an approximation of the elastic moduli of a composite given by either the arithmetic $(M^{Voigt}+M^{Reuss})/2$ or geometric $(M^{Voigt}M^{Reuss})^{1/2}$ average. M^{Voigt} and M^{Reuss} are the overall moduli (either bulk, shear or Young moduli) determined using Voigt

and Reuss models, respectively. The arithmetic average is also known as the Voigt-Reuss-Hill (VRH) average or the Hill's estimation.
Shukla and Padial [197] proposed a harmonic mean of Voigt and Reuss models for the determination of elastic moduli:

$$M_{hom} = 2\frac{M^{Voigt}M^{Reuss}}{M^{Voigt} + M^{Reuss}} \tag{2.23}$$

Arithmetic, harmonic, and geometric averages were compared by Böhlke and Bertram [29] showing that for cubic crystal aggregates all of these averages depend on the same irreducible fourth-order tensor, which represents the pure anisotropic portion of the effective elasticity tensor.

Hirsh Model

Another expression for the elastic modulus was introduced by Hirsh in 1962. Hirsh considered a composite material formed by two different phases (referred by 1 and 2) in series and in parallel arrangements, that his model is a linear combination of the series and parallel models such that:

$$\frac{1}{E} = \frac{f_{1s}}{E_1} + \frac{f_{2s}}{E_2} + \frac{(f_{1p} + f_{2p})^2}{f_{1p}E_1 + f_{2p}E_2} \tag{2.24}$$

Where f_{1s} and f_{2s} are the volume fractions of phases 1 and 2, respectively, in series arrangement, and f_{1p}, f_{1p} are the volume fractions of phases 1 and 2, respectively, in parallel arrangement.
From the Hirsh model, Christensen et al. [47] have derived expression of the mechanical stiffness of the Hot Mix Asphalt (HMA). Assuming that the relative proportions of phase 1 and phase 2 are the same in the series and parallel portion of the Hirsh model, Christensen presents the effective Young modulus such that the elastic composite modulus is:

$$\frac{1}{E} = x\frac{1}{\sum_i E_i f_i} + (1-x)\sum_i \frac{f_i}{E_i} \tag{2.25}$$

Where x is a parameter that determine the stress transfer between inclusions and the matrix. It is also defined as the ratio of all phases in parallel arrangement to the total volume. An example of the Hirsch model for a mix of two phases: Ph_1 and Ph_2 is presented in Fig.2.3 where two phases (Ph_1 and Ph_1) were considered.
Modified Hirsh models were also developed by Christensen et al. [47] for estimating the complex modulus and phase angle of asphalt concrete in shear and compression. A simplified Hirsh model that involves the contact volume that represents the proportion of parallel to total phase volume was proposed for modeling the reclaimed asphalt pavement [240]).

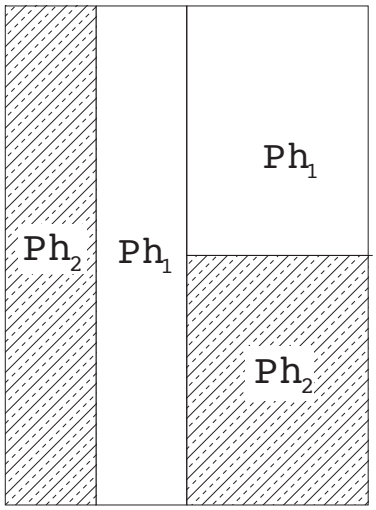

Figure 2.3: Schematic representation of Hirsh model

2.2 Hashin & Shtrikman method

The method is due to Hashin [88] and was formulated by Hashin and Shtrikman. They proposed [93] more rigorous bounds (than those given by Reuss and Voigt) for the effective shear and bulk moduli (as a function of elastic moduli and volume fractions of the constituents) of a multiphase composite. Their bounds are obtained using variational principles in elasticity.
The considered composite is modeled as a mixture of different isotropic and homogeneous phases and then will be regarded as quasi-isotropic and quasi-homogeneous with arbitrary phase geometry and orientation distribution.

2.2.1 Hashin & Shtrikman variational principle

The authors consider, first, stress and strain fields $\overset{\circ}{\sigma}_{ij}$ and $\overset{\circ}{\varepsilon}_{ij}$ in a deformed elastic body of volume V and surface S. The body is characterized by the Lamé constant λ_0, the shear moduli G_0 and the elastic constants tensor $\overset{\circ}{C}_{ijkl}$ that are taken to be constant throughout the body. The case of no body forces was considered here. Then, a boundary value problem of this body writes [141]:

$$\overset{\circ}{\sigma}_{ij,j} = 0 \tag{2.26}$$

$$\overset{\circ}{\sigma}_{ij} = \overset{\circ}{C}_{ijkl}\overset{\circ}{\varepsilon}_{kl} = L_0(\overset{\circ}{\varepsilon}_{ij}) \tag{2.27}$$

$$U_0 = \frac{1}{2}\overset{\circ}{C}_{ijkl}\overset{\circ}{\varepsilon}_{ij}\overset{\circ}{\varepsilon}_{kl} \tag{2.28}$$

$$\overset{\circ}{u}_i = \bar{u}_i; \forall x \in S \tag{2.29}$$

where U_0 is the potential energy density and u_i is the surface displacement.
The operator L_0 is in accordance with the Hashin-Shtrikman notation [93]. The range

of subscripts is $1, 2, 3$ and a repeated subscript denotes a summation.
Part or whole of the body is changed to material of different moduli. Thus, new body is obtained with new stress and strain fields σ_{ij} and ε_{ij} and with new elastic constants tensor C_{ijkl}. A new boundary value problem is obtained:

$$\begin{aligned} \sigma_{ij,j} &= 0 && (2.30)\\ \sigma_{ij} &= C_{ijkl}\varepsilon_{kl} = L(\varepsilon_{ij}) && (2.31)\\ U &= \frac{1}{2}C_{ijkl}\varepsilon_{ij}\varepsilon_{kl} && (2.32)\\ u_i &= \bar{u}_i; \forall x \in S && (2.33) \end{aligned}$$

The authors define also the following displacement and strain fields to relate the two previous problems.

$$u_i^{'} = u_i - \overset{\circ}{u_i} \tag{2.34}$$

$$\varepsilon_{ij}^{'} = \varepsilon_{ij} - \overset{\circ}{\varepsilon_{ij}} \tag{2.35}$$

where $\overset{\circ}{u_i}$ and u_i are displacements in the original and new bodies, respectively; $u_i^{'}$ is the disturbance displacement.
Hashin and Shtrikman introduced [91] the volume integral:

$$\Pi = \Pi_0 - \frac{1}{2}\int_V p_{ij}H(p_{ij}) - p_{ij}\varepsilon_{ij}^{'} - 2p_{ij}\overset{\circ}{\varepsilon_{ij}}dV \tag{2.36}$$

with

$$p_{ij}H(p_{ij}) = -\frac{\lambda - \lambda_0}{6(G - G_0)(K - K_0)}p_{kk}^2 + \frac{1}{2(G - G_0)}p_{ij}p_{ij} \tag{2.37}$$

where the stress polarization tensor [1] p_{ij} is defined by:

$$\begin{aligned} \sigma_{ij} &= p_{ij} + \overset{\circ}{C}_{ijkl}\varepsilon_{ij} && (2.38)\\ &= p_{ij} + \overset{\circ}{C}_{ijkl}(\overset{\circ}{\varepsilon_{ij}} + \varepsilon_{ij}^{'}) && (2.39)\\ &= p_{ij} + \overset{\circ}{\sigma_{ij}} + \overset{\circ}{C}_{ijkl}\varepsilon_{ij}^{'} && (2.40) \end{aligned}$$

and the operator H is given by:

$$H = (L - L_0)^{-1}$$

Since the boundary conditions in the two problems impose:

$$\sigma_{ij,j} = 0 \qquad ; \qquad \overset{\circ}{\sigma_{ij,j}} = 0 \tag{2.41}$$

Then, the stress polarization tensor has to verify:

$$p_{ij,j} + (\overset{\circ}{C}_{ijkl}\varepsilon_{kl}^{'})_{,j} = 0 \tag{2.42}$$

[1] The polarization tensor of transversally isotropic material containing an ellipsoidal inclusion was studied by Klcker et al. [123]

That is called "subsidiary condition" in the Hashin and Shtrikman variational principles formulation.
According to the previously defined problems, Hashin and Shtrikman established [93] the following variational statements:

1. The functional Π is stationary, i.e. $\delta\Pi = 0$, if the subsidiary condition (Eq.2.42) is satisfied;

2. $$\begin{aligned} \delta^2\Pi > 0, \quad \text{if} \quad \Delta\mathbf{C} < 0 \quad \Rightarrow \quad \Pi \quad \text{is an } \textit{Absolute Minimum} \\ \delta^2\Pi < 0, \quad \text{if} \quad \Delta\mathbf{C} > 0 \quad \Rightarrow \quad \Pi \quad \text{is an } \textit{Absolute Maximum} \end{aligned}$$

Details of these two statements are given in Appendix C.

2.2.2 Hashin & Shtrikman bounds

The variational formulation detailed above is applied in this section to a composite consisting of N different phases. The composite is regarded as quasi-homogeneous and quasi-isotropic with elastic moduli K_{hom} and G_{hom} and is subjected to the following displacement:

$$u_i^\circ(S) = \varepsilon_{ij}^\circ x_j \tag{2.43}$$

where ε_{ij}° is constant and x_j are Cartesian coordinates. The quasi-homogeneous assumption is interpreted by considering a Representative Volume Element. Hashin and Shtrikman considered a reference cube of unit volume as an RVE. They evaluated then the expression in Eq.(2.36) for the reference cube by choosing the following polarization tensor:

$$p_{ij} = p_{ij}^i, \quad \text{in} \quad V_i \quad \forall \quad \text{phase} \quad i \tag{2.44}$$

where p_{ij}^i is shown [93] to be constant throughout the volume of each phase V_i.
As the reference cube is of unit volume, then $V = 1$ and Eq.(2.1) implies:

$$f_i = V_i \tag{2.45}$$

Splitting all tensors into isotropic and deviatoric parts such that:

$$p_{ij} = p\delta_{ij} + f_{ij} \tag{2.46}$$

$$\varepsilon_{ij}^\circ = \varepsilon^\circ \delta_{ij} + e_{ij}^\circ \tag{2.47}$$

with the properties:

$$tr(f_{ij}) = 0 \quad ; \quad tr(e_{ij}) = 0$$

Eq.(2.36) gives:

$$\Pi = \Pi_0 + \frac{1}{2}(3\bar{\bar{p}}\varepsilon^\circ + \bar{\bar{f}}_{ij}e_{ij}^\circ) \tag{2.48}$$

with

$$\bar{\bar{p}} = \overset{\circ}{\varepsilon} \frac{3A}{1 + \alpha_0 A} \tag{2.49}$$

$$\bar{\bar{f}}_{ij} = \overset{\circ}{e}_{ij} \frac{B}{1 + \beta_0 B} \tag{2.50}$$

Where

$$A = \sum_{i=1}^{i=N} \frac{f_i}{\frac{1}{K_i - K_0} - \alpha_0}$$

$$B = \sum_{i=1}^{i=N} \frac{f_i}{\frac{1}{2(G_i - G_0)} - \beta_0}$$

And

$$\alpha_0 = -\frac{3}{3K_0 + 4G_0} \tag{2.51}$$

$$\beta_0 = -\frac{3(K_0 + 2G_0)}{5G_0(3K_0 + 4G_0)} \tag{2.52}$$

The maximum and minimum conditions given by the second Hashin statement imply:

$$\Delta \mathbf{C} > 0 \quad , \quad \Delta \mathbf{C} < 0$$

Where $\mathbf{C}$ is the matrix expressed in Eq.(B.2). For a mixture whose overall properties are isotropic, this matrix depend on only two elastic constants, namely the bulk and shear moduli K_{hom} and G_{hom}.
Then, Π is an absolute maximum when for *every* K_i and G_i, the moduli K_0 and G_0 satisfy:

$$K_i < K_0 \quad , \quad G_i < G_0 \tag{2.53}$$

Analogously, Π is an absolute minimum when for *every* K_i and G_i, the moduli K_0 and G_0 satisfy:

$$K_i > K_0 \quad , \quad G_i > G_0 \tag{2.54}$$

Since only two elastic constants have to be determined, it is not necessary to impose a perfectly general overall strain. It is enough to consider just two independent strains, chosen at will.
To determine, first, the bounds for the effective bulk modulus, Hashin and Shtrikman considered the mean strain applied to the composite is in the form:

$$\overset{\circ}{\varepsilon}_{ij} = \overset{\circ}{\varepsilon} \delta_{ij} \tag{2.55}$$

Substituting Eq.(2.55) into Eq.(2.48) and considering that Π is an absolute minimum then an absolute maximum leads to the following inequalities:

$$\Pi_{hom} > \Pi \quad \Rightarrow \quad K_{hom} > K_0 + \frac{A}{1 + \alpha_0 A} \tag{2.56}$$

$$\Pi_{hom} < \Pi \quad \Rightarrow \quad K_{hom} < K_0 + \frac{A}{1 + \alpha_0 A} \tag{2.57}$$

The first inequality Eq.(2.56) (respectively the second inequality Eq.2.57) applies for the condition of Eq.(2.54) (respectively the condition Eq.2.53).
Similarly, if the strain is chosen to be deviatoric form such as:

$$\overset{\circ}{\varepsilon}_{ij} = \overset{\circ}{e}_{ij} \quad , \quad e_{kk} = 0 \tag{2.58}$$

$$\Pi_{hom} > \Pi \quad \Rightarrow \quad G_{hom} > G_0 + \frac{1}{2}\frac{B}{1 + \beta_0 B} \tag{2.59}$$

$$\Pi_{hom} < \Pi \quad \Rightarrow \quad G_{hom} < G_0 + \frac{1}{2}\frac{B}{1 + \beta_0 B} \tag{2.60}$$

The first inequality Eq.(2.59) (respectively the second inequality Eq.2.60) applies for the condition of Eq.(2.54) (respectively the condition Eq.2.53).
Thus, Bounds for the bulk and shear of the composite are determined by considering the lowest and highest modulus in the composite components.
If K_1 and G_1 are the smallest shear and bulk moduli of the composite components and K_n and G_n the largest ones, then the bounds' expressions are derived such that:

- ***Bulk modulus***
  The effective bulk modulus K_{hom} is comprised between the lower and upper bounds K^1_{hom} and K^2_{hom} :

  $$K^1_{hom} < K_{hom} < K^2_{hom} \tag{2.61}$$

  With

  $$K^1_{hom} = K_1 + \frac{A_1}{1 + \alpha_1 A_1} \quad ; \quad K^2_{hom} = K_n + \frac{A_n}{1 + \alpha_n A_n}$$

  Where

  $$\alpha_1 = -\frac{3}{3K_1 + 4G_1}; \alpha_n = -\frac{3}{3K_n + 4G_n}; A_1 = \sum_{i=2}^{r=N} \frac{f_i}{\frac{1}{K_i - K_1} - \alpha_1}; A_n = \sum_{i=1}^{r=N-1} \frac{f_i}{\frac{1}{K_i - K_n} - \alpha_n}$$

- ***Shear modulus***
  The effective shear modulus is comprised between the lower and upper bounds G^*_1 and G^*_2 :

  $$G^*_1 < G^* < G^*_2 \tag{2.62}$$

  With:

  $$G^*_1 = G_1 + \frac{1}{2}\frac{B_1}{1 + \beta_1 B_1} \quad ; \quad G^*_2 = G_n + \frac{1}{2}\frac{B_n}{1 + \beta_n B_n}$$

  Where:

  $$\beta_1 = -\frac{3(K_1 + 2G_1)}{5G_1(3K_1 + 4G_1)} \quad ; \quad \beta_n = -\frac{3(K_n + 2G_n)}{5G_n(3K_n + 4G_n)} \quad ;$$

$$B_1 = \sum_{r=2}^{r=n} \frac{f_r}{\frac{1}{2(G_r - G_1)} - \beta_1} \qquad ; \qquad B_n = \sum_{r=1}^{r=n-1} \frac{f_r}{\frac{1}{2(G_r - G_n)} - \beta_n}$$

The Hashin-Shtrikman bounding method presented above provides upper and lower bounds on effective moduli of a composite material given its micro-structural properties. They are applicable to composite materials with inclusion volume fraction ranging from zero to 1. They are valid for a material composed of N elastic, homogeneous and isotropic phases with volume fractions f_i.

It is interesting to note that the ratio between the different phases' moduli has to be not too large. Moreover, the Hashin and Shtrikman bounds have practical signification only if the ratio between phases' elastic moduli is less than 10 [61]. Otherwise, when considering porous phase, the error becomes too large. For example, in the case of porous media, the lower bound is very close to zero.

The Hashin and Shtrikman bounds were also applied to estimate the elastic properties of periodic microstructures [124]. Hashin and Shtrikman developed more general bounds for the overall moduli of anisotropic and non-homogeneous materials [92]. In later developments, Hashin [89] and Hill [104] gave bounds for elastic constants when the material is macroscopically transversely isotropic and translation invariant in the axial direction.

Many works were carried out to take into account the nonlinearity of composites. Among them, Ponte Castañeda [41] proposed variational method for bounding the effective properties of nonlinear composites with isotropic phases.

Bounding procedure was also proposed by Hsieh and Tuan [111] to predict the upper and lower bounds for the Poisson ratio of two-phase composites. Only the elastic modulus and Poisson ratio of each component were needed in order to carry out the prediction.

Chapter 3

Eshelby equivalent inclusion principle

The solution of the Eshelby inclusion's problem, is in the basis of almost all the micromechanical models developed for estimating heterogeneous materials' properties. The Eshleby problem deals with the effect of *a stress free-strain* of an ellipsoidal inclusion embedded in an infinite medium.

3.1 Eshelby's problem

Consider an infinite domain ω formed by a matrix material ω_0 in which is embedded a spheroidal inclusion ω_1 made by the same material as the matrix. As showed in Fig.3.1, stress and strain fields are initially zero in the two media. In the following, subscripts 0 and 1 refer, respectively, to the matrix and the inclusion.

Assume that the inclusion undergoes a uniform transformation strain $\mathbf{e}^T$ in the absence of the matrix. $\mathbf{e}^T$ is called " stress-free strain " since no stress is associated to the strain $\mathbf{e}^T$. The Eshelby work [65] aimed to find the constrained strain $\mathbf{e}^C$ in the inclusion when it transforms while it is inside the matrix. $\mathbf{e}^C$ is also the strain set up in the matrix. This was carried up through a set of imaginary cutting, straining and welding operations as is detailed in this section.

The steps considered by Eshelby are:

1. Remove the inclusion from the matrix and allow it to undergo the stress-free strain $\mathbf{e}^T$ without changing its elastic constants ($\mathbf{C}_0$ is the stiffness tensor and λ_0 and μ_0 are the lamé constants). See step 1 in Fig.3.1. According to the Hooke's law, the stress derived from $\mathbf{e}^T$ is:

$$\boldsymbol{\sigma}^T = \mathbf{C}_0 \mathbf{e}^T \tag{3.1}$$

   At this stage, the stress in the inclusion and matrix are zero.

2. To the inclusion removed from the matrix, a surface traction $-\sigma_{ij}^T n_j$ is applied.The inclusion is, then, brought to its initial form and size, see step 2 in Fig.3.1. Now, the inclusion is putted back in the matrix and re-welded across S (the surface separating matrix and inclusion, with outward normal n_i). Thus, the surface forces formed a layer of body force spread over S.

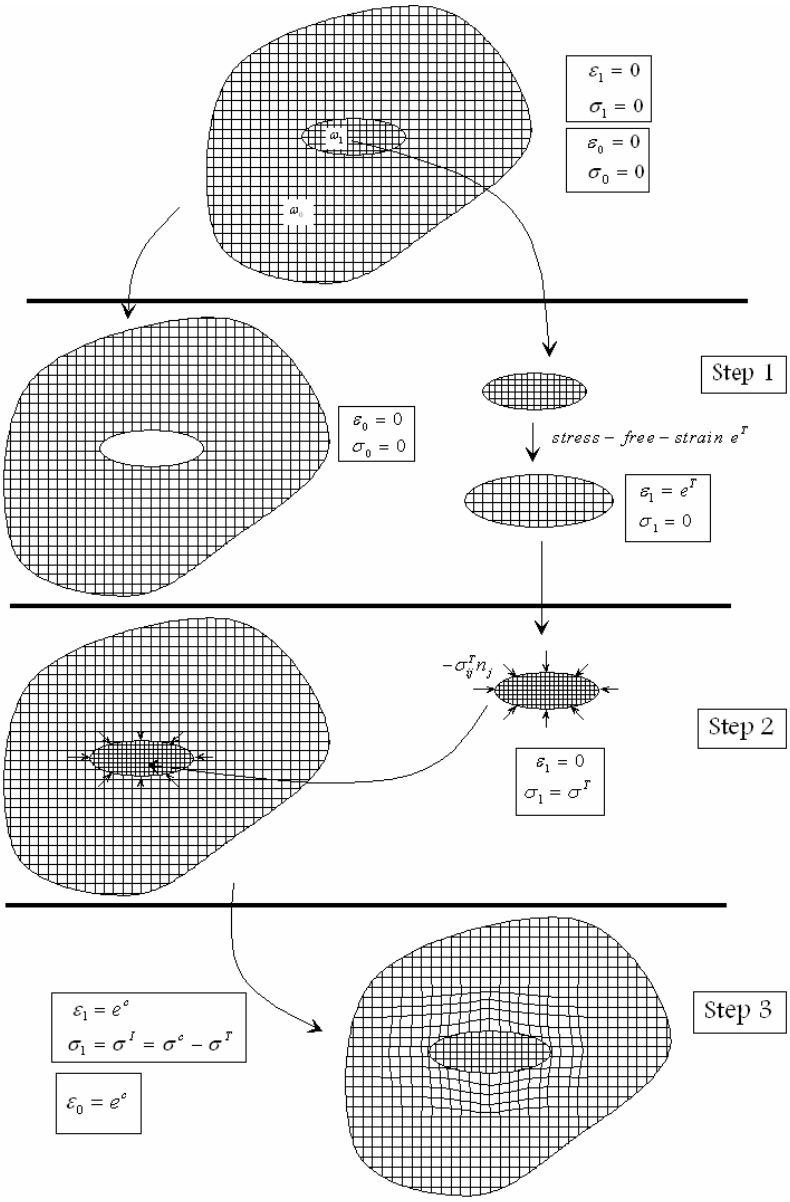

Figure 3.1: Schematic illustration of homogenization according to Eshelby method

3. In order to eliminate these forces, further distribution $+\sigma_{ij}^T n_j$ is applied over S. This make the body free of external forces but self-stress (because of the inclusion's transformation). See step 3 in Fig.3.1.

The strain $\mathbf{e}^C$ in the matrix (or in the inclusion), is determined in terms of the displacement impressed on the material in step 3. The correspondent stress is found using Hooke's law:

$$\boldsymbol{\sigma}^C = \mathbf{C}_0 \mathbf{e}^C \tag{3.2}$$

The inclusion had a stress $-\boldsymbol{\sigma}^T$ before step 3 so the remaining stress is the following

sum:

$$\sigma^I = \sigma^C - \sigma^T = \mathbf{C}_0(\mathbf{e}^C - \mathbf{e}^T) \tag{3.3}$$

The constrained strain $\mathbf{e}^C$ can then be written in terms of the stress free transformation strain $\mathbf{e}^T$ and a tensor, called the Eshelby tensor $\mathbb{S}$, dependent on the inclusion geometry and the Poisson's ratio of the medium [65]:

$$\mathbf{e}^C = \mathbb{S}\mathbf{e}^T \tag{3.4}$$

Where $\mathbb{S}$ is the Eshelby's tensor and has the following properties:

- $\mathbb{S}$ has the minor symmetry:
$$\mathbb{S}_{ijkl} = \mathbb{S}_{jikl} = \mathbb{S}_{ijlk}$$
- For the particular case of isotropic matrix and spheroidal inclusions, $\mathbb{S}$ is completely analytically defined ([65],[66]) in function of the inclusions' geometry (aspect ratio) and the mechanical properties of the matrix (Poisson ratio) as given in Appendix D;
- Other Eshelby tensors were developed for particular cases. Faivre [67] extended the Eshelby method for anisotropic crystals. Sevostianov et al. [192] have derived the Eshelby tensor for composites containing transversely isotropic phases.

Substituting Eq.(3.4) into Eq.(3.2), the total stress in the matrix is:

$$\sigma^C = \mathbf{C}_0\mathbb{S}\mathbf{e}^T \tag{3.5}$$

3.2 Stressed inclusion problem : The equivalent inclusion

As yet no external stress has been applied, in this section an imposed uniform strain $\mathbf{e}^A$ is superposed to $\mathbf{e}^C$ (see Fig.3.2). The deformation of the inclusion is then :

$$\mathbf{e} = \mathbf{e}^C + \mathbf{e}^A \tag{3.6}$$

However, the strain in the inclusion is:

$$\varepsilon_1 = \mathbf{e}^C + \mathbf{e}^A - \mathbf{e}^T \tag{3.7}$$

Then, the uniform stress in the inclusion is obtained by applying Hooke's law not to $(\mathbf{e}^C + \mathbf{e}^A)$ but to $(\mathbf{e}^C + \mathbf{e}^A - \mathbf{e}^T)$. Then, the stress is:

$$\sigma = \mathbf{C}_0(\mathbf{e}^C + \mathbf{e}^A - \mathbf{e}^T) \tag{3.8}$$

In the following, an ellipsoid is assumed having the same shape and size of the untransformed inclusion but made of a different isotropic material with elastic stiffness

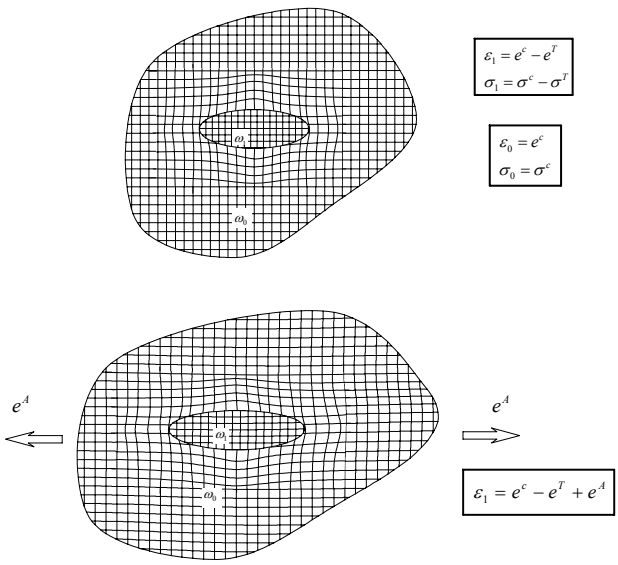

Figure 3.2: Eshelby homogenization procedure for stressed inclusion

tensor $\mathbf{C}_1$ and lamé constants λ_1, μ_1.
Subject this ellipsoid to the strain given in Eq.(3.6) until it develops the stress presented in Eq.(3.8) so it can replace the inclusion. Eshelby called the presented imaginary transformation inclusion "*equivalent inclusion*".
The correct stress is developed by choosing suitable $\mathbf{C}_1$ that satisfy:

$$\mathbf{C}_1(\mathbf{e}^C + \mathbf{e}^A) = \mathbf{C}_0(\mathbf{e}^C + \mathbf{e}^A - \mathbf{e}^T) \tag{3.9}$$

In one hand, the total strain inside the inhomogeneity $\mathbf{e} = \mathbf{e}^C + \mathbf{e}^A$ is expressed as following:

$$\mathbf{e} = \mathbf{C}_0(\mathbf{C}_0 - \mathbf{C}_1)^{-1}\mathbf{e}^T \tag{3.10}$$

In the other hand, Eq.(3.9) have to be solved for $\mathbf{e}^T$ in terms of $\mathbf{e}^A$, $\mathbf{C}_0$, $\mathbf{C}_1$ and $\mathbb{S}$ after eliminating $\mathbf{e}^C$ using Eq.(3.10).
Thus, The strain in the single inclusion $\mathbf{e}$ is linked to the far-field strain $\mathbf{e}^A$ by:

$$\mathbf{e} = (\mathbf{I_4} + \mathbb{S} : (\mathbf{C_0}^{-1} : \mathbf{C_1} - \mathbf{I_4}))^{-1}\mathbf{e}^A \tag{3.11}$$

Accordingly, the strain concentration factor is:

$$\bar{\mathbf{A}}_1^{Eshelby} = (\mathbf{I_4} + \mathbb{S} : (\mathbf{C_0}^{-1} : \mathbf{C_1} - \mathbf{I_4}))^{-1} \tag{3.12}$$

3.3 Dilute inclusion model

A dilute inclusion homogenization model is based on the Eshelby solution. Consider a medium in which a low fraction of inclusions is embedded as represented in Fig.3.3. The inclusions are of different forms and orientations. We assume that all phases are isotropic, homogeneous and elastic.

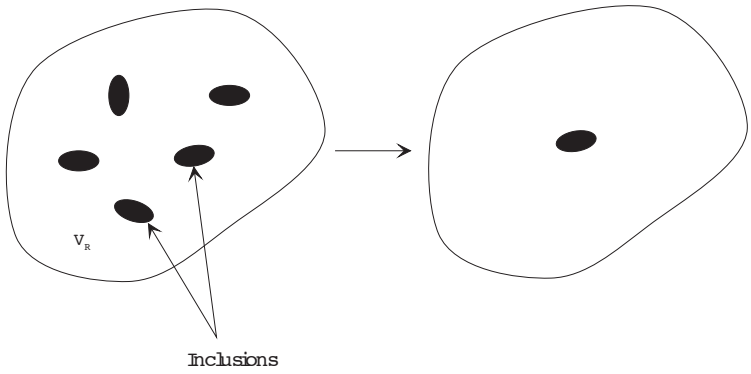

Figure 3.3: Schematic representation of the Dilute inclusion model

The dilute inclusion model assumes very low concentrations of inclusions. The latter are sufficiently distant and the interaction between them is neglected. Thus, each inclusion can be considered as isolated in an infinite matrix and subjected to a macroscopic stress at infinity: the Eshelby model (Fig.3.3). So, the Eshelby solution can be applied to estimate the strain concentration tensor as given in Eq.3.12.

$$\bar{\mathbf{A}}_1^{Eshelby} = (\mathbf{I}_4 + \mathbb{S} : (\mathbf{C}_0^{-1} : \mathbf{C}_1 - \mathbf{I}_4))^{-1} \tag{3.13}$$

Dilute inclusion model is, then, valid only for low inclusions' concentration because it neglects the interaction between them. It provides good estimates if the inclusion's concentration doesn't exceed 10%. This method was also used to predict mechanical properties of short fiber composite by Withers et al. [226]. They have investigated this model to show that the relaxation phenomena play an important role in the development of internal stress and to understand the energetics and resultant stress redistribution between phases.

Wu-Eshelby tensor

Following the Wu notation [228], the Wu-Eshelby tensor was defined to relate the average strain in the host material $\langle \boldsymbol{\varepsilon}_i \rangle$ to the average strain in the inclusion $\langle \boldsymbol{\varepsilon}_j \rangle$:

$$\langle \boldsymbol{\varepsilon}_j \rangle = \langle \mathbf{T}^{ij} \rangle \langle \boldsymbol{\varepsilon}_i \rangle \tag{3.14}$$

Where the the Wu-Eshelby tensor is given by:

$$\mathbf{T}^{ij} = (\mathbf{I}_4 + \mathbb{S}^i : (\mathbf{C}_i^{-1} : \mathbf{C}_j - \mathbf{I}_4))^{-1} \tag{3.15}$$

Remark that $\mathbf{T}^{ii} = \mathbf{I}$.
It is interesting to note that, for the particular case of isotropic and homogenious material, a simplified expression of the isotropic P_{ij} and deviatoric Q_{ij} parts of the Wu-Eshelby tensor can be deduced. The exact expressions as well as possible approximations are detailed in Appendix E.

Chapter 4

Micromechanical homogenization models

4.1 Mori-Tanaka model

The non-interaction assumption considered in Eshelby model is not representative of real composite. Thus, involving slight modifications in the dilute model was carried out by Mori T. and Tanaka K. [157]. They have calculated the average internal stress in a matrix containing inclusions with transformation strain. They used similar development as that of the dilute inclusion model presented in chapter 3. Rather, the Mori-Tanaka Method involved more complex manipulations of the stress and strain fields variables with particular concepts of eigenstrain and backstress.
Benveniste [14] provided a simplified derivation of the Mori-Tanaka method. The details on the method given here will closely follow the development of Benveniste but expressed in a different notation to be in accordance with the previous sections.
The authors consider a specimen V with N inclusions uniformly distributed in it. Then, they assumed that the average of inclusions' strains can be approached to that of a single inclusion of the same forme, having the same elastic properties and isolated in an infinite medium but submitted at infinity to the average matrix strain $\langle \boldsymbol{\varepsilon}_0 \rangle$ as illustrated in Fig.4.1.

Applying the Eshelby solution (3.11) to such scheme allows the determination of the average strain $\langle \boldsymbol{\varepsilon}_1 \rangle$ in the inclusion in terms of the matrix average strain such that:

$$\langle \boldsymbol{\varepsilon}_1 \rangle = (I_4 + \mathbb{S} : (\mathbf{C}_0^{-1} : \mathbf{C}_1 - \mathbf{I}_4))^{-1} \langle \boldsymbol{\varepsilon}_0 \rangle \tag{4.1}$$

The latter can also be written in the form:

$$\langle \boldsymbol{\varepsilon}_1 \rangle = \mathbf{T}^{01} \langle \boldsymbol{\varepsilon}_0 \rangle \tag{4.2}$$

It can be noted that the matrix strain is $\langle \boldsymbol{\varepsilon}_0 \rangle$.
Using Eq.(4.2), formulation of Eq.(1.35) for a two-phase composite with a single inclusion, that corresponds to the considered scheme, of Fig.4.1, writes:

$$\bar{\boldsymbol{\varepsilon}} = f_0 \langle \boldsymbol{\varepsilon}_0 \rangle + f_1 \langle \boldsymbol{\varepsilon}_1 \rangle \tag{4.3}$$

$$= f_0 \left(\mathbf{T}^{01} \right)^{-1} \langle \boldsymbol{\varepsilon}_1 \rangle + f_1 \langle \boldsymbol{\varepsilon}_1 \rangle \tag{4.4}$$

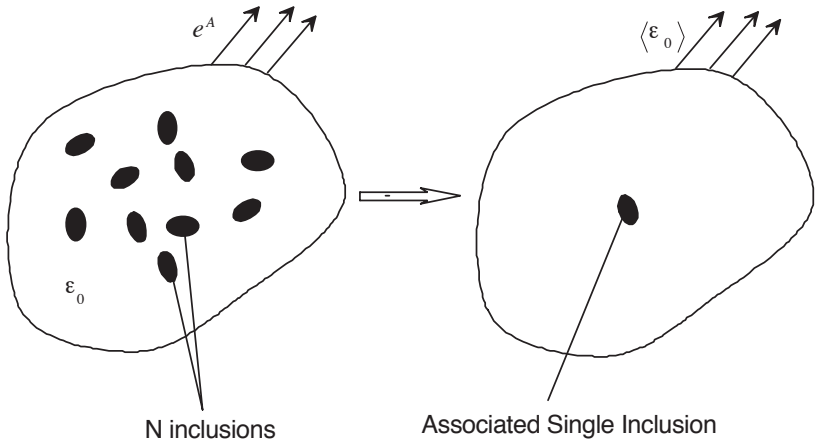

Figure 4.1: Schematic representation of homogenization according to Mori-Tanaka method

For the previous equation follows an expression of the average strain in the inclusion in function of the macrostrain $\bar{\boldsymbol{\varepsilon}}$ as:

$$\langle \boldsymbol{\varepsilon}_1 \rangle = \left[f_0 \left(\mathbf{T}^{01} \right)^{-1} + f_1 \mathbf{I} \right]^{-1} \bar{\boldsymbol{\varepsilon}} \tag{4.5}$$

According to Eq.(1.44) the strain concentration tensors related to the Mori-Tanaka model **A** when two-phases composite is considered is:

$$\bar{\mathbf{A}}_1^{M-T} = \left[f_0 \left(\mathbf{T}^{01} \right)^{-1} + f_1 \mathbf{I} \right]^{-1} \tag{4.6}$$

$$\bar{\mathbf{A}}_0^{M-T} = \left(\mathbf{T}^{01} \right)^{-1} \bar{\mathbf{A}}_1^{M-T} \tag{4.7}$$

It have to be noted that the previous expressions are valid only in the case of two-phases composite and that different formulation have to be carried out if multi-phases composite has to be modelled.
Then, the elastic tensor of a composite material is estimated according to the Mori-Tanaka method by:

$$\mathbf{C}_{hom} = \mathbf{C}_0 + f_1 (\mathbf{C}_1 - \mathbf{C}_0) \langle \bar{A}_1^{M-T} \rangle \tag{4.8}$$

The Mori-Tanaka model gives good estimates for the effective properties for composite with low to moderate volume fraction. If aligned inclusions are concidered, the model is realiable up to 30 % [71]. For high volume fractions, the inclusions acts as the matrix and vise versa as presented in the following.

4.1.1 Inverse Mori-Tanaka model

The inverse Mori-Tanaka method is used for the case of high inclusions concentration. In such situation, the composite is represented as if inclusions of the matrix material

are embedded into a matrix of inclusions' material (Fig.4.2). Thus, the properties of both phases are switched and an inverse scheme is obtained.

Identifation of such problem with the Mori-Tanaka formulation leads to writting the

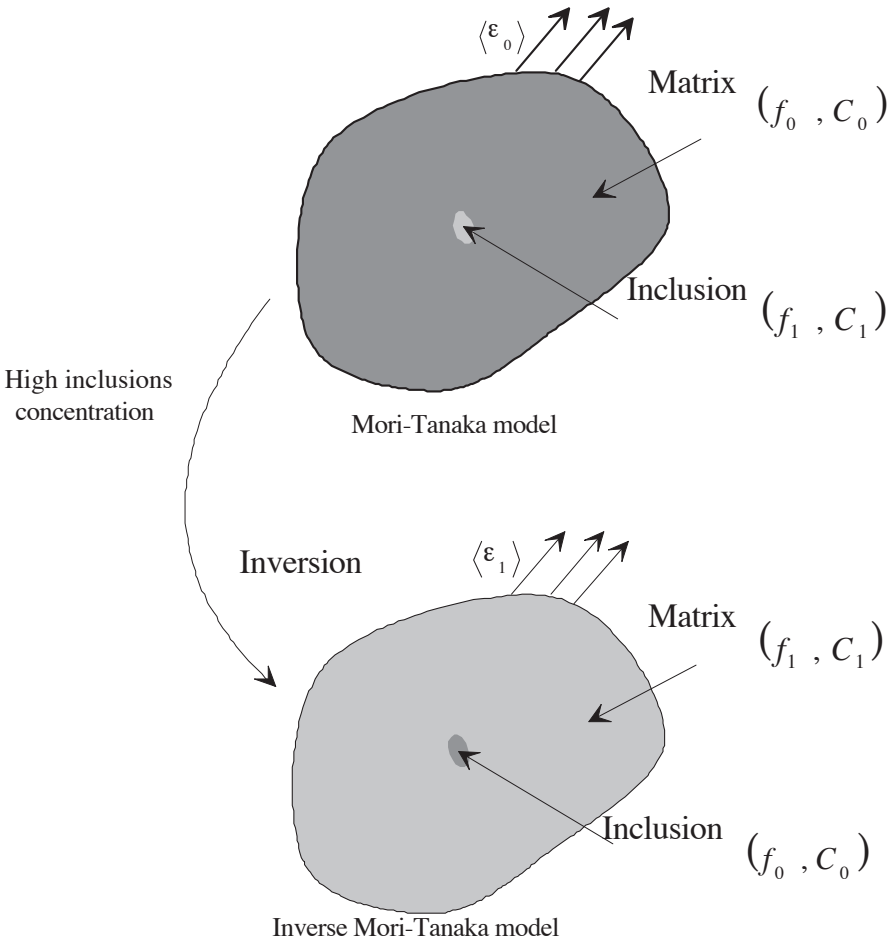

Figure 4.2: Schematic representation of Inverse Mori-Tanaka method

Eq.(4.2) as following:

$$\langle \boldsymbol{\varepsilon}_0 \rangle = \mathbf{T}^{10} \langle \boldsymbol{\varepsilon}_1 \rangle \tag{4.9}$$

Then, a similar developpment as the one given for Mori-Tanaka leads to the strain concentration tensor of the "Inverse" Mori-Tanaka model:

$$\bar{\mathbf{A}}_1^{I-M-T} = \left[f_0 \mathbf{T}^{10} + f_1 \mathbf{I} \right]^{-1} \tag{4.10}$$

4.1.2 Interpolative model

The interpolative model is based on the double-inclusion model [162] that is detailed later. It was introduced by Lielens [142] to predict effective properties of composite material with intermediate concentration of inclusion. Lielens suggests:

- For low concentrations, the effective stiffness of the composite can be predicted by Mori-Tanaka model;
- For high concentrations, the inclusion phase is taken as the continuous ohase. Thus, the effective stiffness;
- For inermediate concentrations, Lielens proposed the use of a mixing rule as following:

$$\mathbf{C}_{hom} = \left[(1 - \xi(f_1))\left(\mathbf{C}_{hom}^{I-M-T}\right)^{-1} + \xi(f_1)\left(\mathbf{C}_{hom}^{M-T}\right)^{-1}\right]^{-1} \tag{4.11}$$

  where $\mathbf{C}_{hom}^{M-T}$ and $\mathbf{C}_{hom}^{I-M-T}$ refer to the homogenized elastic tensor according to the Mori-Tanaka and the inverse Mori-Tanaka models. $\xi(f_1)$ is a smooth interpolation function which was proposed by Lielens [171]. It is expressed by:

$$\xi(f_1) = \frac{1}{2} f_1(1 + f_1) \tag{4.12}$$

4.2 Self-consistent model

The Self-consistent model was introduced first by Hershey [101] for crystalline aggregates. The model was then reformulated by Hill [106] for material with ellipsoidal inclusions. The self-consistent method is an approach that incorporates the interaction between inclusions by assuming that the matrix is made of the effective medium. Indeed, the material is formed of inclusions or inhomogeneities placed side by side to each other. In this case, it is supposed that each inclusion is surrounded by all the other phases and so by the average homogenized field.
In order to develop the details of the self-consistent formulation, a homogeneous medium in which inclusions are embedded has to be considered as in Fig.4.3. The inclusions are randomly distributed into the matrix. ($\mathbf{C}_0$, $\mathbf{C}_1$) and (f_0,f_1) denote the elastic constants tensors and the volume fractions of the matrix and inclusions respectively. The displacement at infinity is assumed to correspond to an overall stain $\overline{\varepsilon}$. Denote the elastic tensor of the surrounding homogenized material by $\mathbf{C}^{hom}$. Thus, the obtained configuration can be identified to a single inclusion problem. The latter is solved using Eshelby isolated inclusion problem presented in chapter 3. The strain in the isolated inclusion according to Eq.(3.14) is then:

$$\langle \boldsymbol{\varepsilon}_1 \rangle = \mathbf{T}^{hom1} \langle \overline{\boldsymbol{\varepsilon}} \rangle \tag{4.13}$$

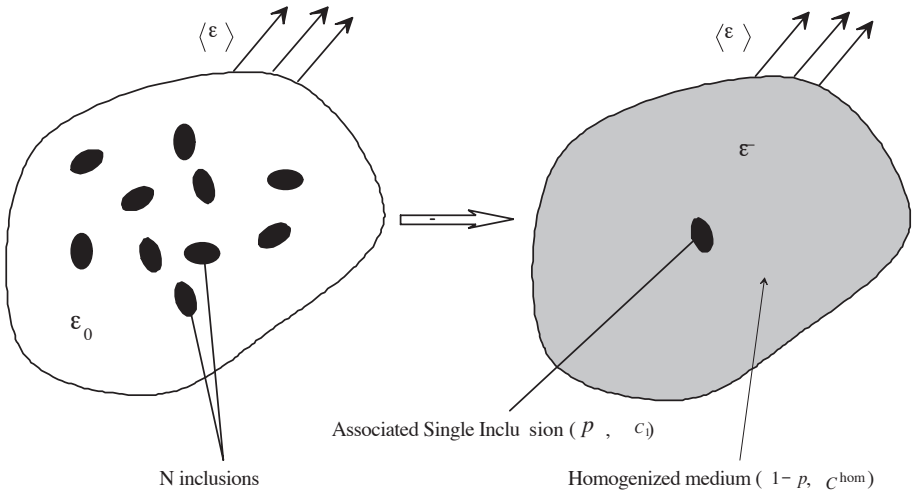

Figure 4.3: Schematic representation of Self-consistent method : Isolation of inclusion and homogenization of its surrounding

Consequently, the strain concentration tensor corresponding to the self-consistent model $\mathbf{A}^{S-C}$ is:

$$\bar{\mathbf{A}}_1^{S-C} = \mathbf{T}^{hom1} \tag{4.14}$$

$$\mathbf{C}^{hom} = \mathbf{C}_0 + (\mathbf{C}_i - \mathbf{C}_0) : \sum_i f_i \bar{\mathbf{A}}_1^{S-C} \tag{4.15}$$

$\mathbf{C}^{hom}$ would be determined by solving iteratively the previous expressions .The explicit formulas for upper Hashin-Shtrikman bounds can be used as values of the first iteration.
For the case where the inclusions are of different materials, Budiansky presents [36] a heuristic analysis for the determination of the elastic moduli of such a composite material. The different constituents are supposed to be isotropic and elastic. The results are intended to apply to heterogeneous materials composed of spherical grains of each of the phases (N phases, the 1^{st} phase is the matrix).

The given implicit formulas for effective shear and bulk moduli are, then presented as follows:

$$K^{hom} = K_0 + (K_i - K_0) \sum_i f_i (A_i^{S-C})^{iso} \tag{4.16}$$

$$G^{hom} = G_0 + (G_i - G_0) \sum_i f_i (A_i^{S-C})^{dev} \tag{4.17}$$

The previously presented micromechanical models (such as the dilute inclusion model and the Mori-Tanaka model) are suitable for a structure formed by a continuous matrix containing heterogeneities. However, the self-consistent scheme can be applied in the case where no continuous phase is considered within the composite.

4.2.1 Resolution and iteration scheme

The implicitit formulas for the sef-consistet model expressed above must be solved simultaniously. Different possible solutions and approximations were presented in the litterature. These solutions were performed either by static [36, 228] or dynamic [18, 19] methods.
As the present research is closly related to wave propagation, the dynamic solution method of the self consistent formulation is considered. The latter was introduced by Berryman [19] who proposed an iteration scheme for estimating effective macroscopic elastic constants for inhomogeneous materials with spherical inclusions from the self consistent formulation. His method is based on elastic-wave scattering theory. Thus, the implicit formulas for effective moduli written in the form useful for iteration scheme are given by:

$$K_{n+1} = \frac{\sum_{i=1}^{N} f_i K_i P_n^i}{\sum_{i=1}^{N} f_i P_n^i} \tag{4.18}$$

$$G_{n+1} = \frac{\sum_{i=1}^{N} f_i G_i Q_n^i}{\sum_{i=1}^{N} f_i Q_n^i} \tag{4.19}$$

Where:
$P_n^i = \frac{K_n + \frac{4}{3}G_n}{K_i + \frac{4}{3}G_n}$; $Q_n^i = \frac{G_n + F_n}{G_i + F_n}$; $F_n = \frac{G_n}{6}\frac{9K_n + 8G_n}{K_n + 2G_n}$.
According to Zohdi and Wriggers [241], the self-consistent method predicts negative effective bulk and shear moduli for voids volume fraction above 50%. For rigid inclusions, this method produces infinite effective bulk modulus for any volume fraction and infinite effective shear modulus above 40 % Then, the self consistent method can be used safely for low volume fractions.
The self-consistent procedure has been also established for the case of elastoplastic materials (see [105, 224, 143]).

4.2.2 generalized self consistent method

The generalized self consistent method was formalized by Christensen and Lo and considers a spherical inclusion embedded in a concentric spherical annulus made of the matrix material, which is embedded in an infinite medium assumed to have the effective properties (that are unknown). The problem is illustrated in Fig.4.4. The solution for the effective bulk modulus of such problem is given by:

$$K^{hom} = K_0 + \frac{f_1(K_1 - K_0)}{1 + (1 - f_1)\frac{K_1 - K_0}{K_0 + \frac{4}{3}G_0}} \tag{4.20}$$

It should be noted that the previous solution correspends to that given by Hashin (upper bound of Eq.2.61) and that the model does not yield a solution for the effective shear modulus, except for the case of dilute inclusion [46].

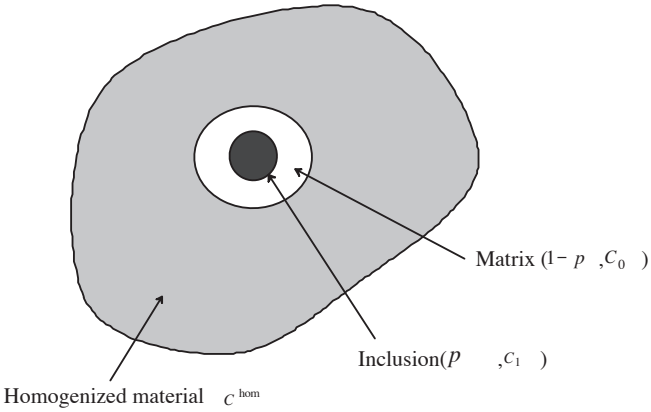

Figure 4.4: Schematic representation of Generalized Self-consistent model

4.3 Kuster-Toksöz approximation

Kuster and Toksöz derived [130] a multi-phase model for porous media by considering a process of wave propagation in an inhomogeneous elastic material and equating the displacements fields, expanded in series, for waves scattered by an "effective" composite medium and waves scattered by individual inclusions.
Consider N inclusions randomly embedded in a volume V_0 in an infinite medium, as shown in Fig.(4.5). V_0 is taken spherical so that the scattered waves do not depend on the orientation of this latter with respect to the incident wave. u° denotes an elastic

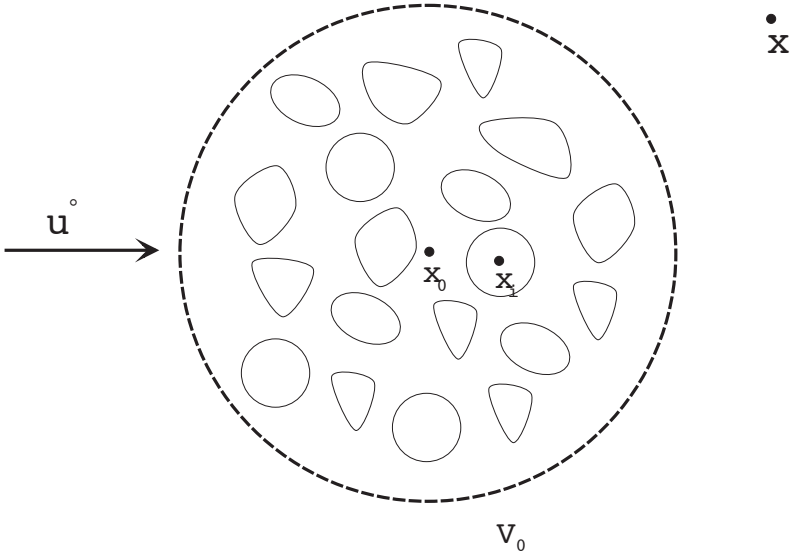

Figure 4.5: Schematic representation of the Kuster-Toksöz scattering problem

incident wave from infinity. The observed displacement $u(x)$ at point x (outside the

volume V_0) is:

$$u(x) = u^{\circ}(x) + \sum_{1}^{N} u^{i}(x, x_i) \tag{4.21}$$

Where $u^i(x, x_i)$ is the displacement observed at x due to the wave scattered by the i^{th} inclusion located at x_i.
Assume now that the medium V_0 is homogeneous with effective moduli K^* and G^*. If this medium is subjected to the same incident wave u°, then the displacement field at x writes:

$$u(x) = u^{\circ}(x) + u^{*}(x, x_0) \tag{4.22}$$

Where $u^*(x, x_0)$ is the displacement observed at point x and scattering by the effective volume centered at x_0. Equating Eq.(4.21) and Eq.(4.22), the equation defining the effective volume is obtained:

$$u^{*}(x, x_0) = \sum_{1}^{N} u^{i}(x, x_i) \tag{4.23}$$

Kuster and Toksöz expressed the radial and transverse displacements u and v corresponding to each wave in an infinite series of spherical Bessel functions and Legendre polynomials. The coefficients of these series expansions provide a relationship between the elastic elastic moduli of the effective medium and those of the matrix and inclusions. The detailed developpements of these expansions are not given in this report, reader can refer to the Kuster and Toksöz article [130]. Instead, a simplified formulation of the Kuster-Toksöz is presented based on an identified scheme associated to the problem. This scheme reflects the Kuster-Toksöz assumptions and allows the application of the Eshelby solution to conduct the same homogenized result given by the authers.
Consider a matrix with moduli K_0 and G_0 and N inclusions. To take into account the interaction between the inclusions, the concidered scheme suppose that the each inclusion is embedded into the homogenized material that is seen as a second inclusions embedded into the matrix material as ilustrated in Fig.4.6. Both of the inclusions see the average matrix strain as the far field. Applying the Eshelby solution (Eq.3.14) to this problem situation leads to the following equation:

$$\langle \bar{\boldsymbol{\varepsilon}} \rangle = \mathbf{T}^{0hom} \langle \boldsymbol{\varepsilon}_0 \rangle \tag{4.24}$$

$$\langle \boldsymbol{\varepsilon}_1 \rangle = \mathbf{T}^{01} \langle \boldsymbol{\varepsilon}_0 \rangle \tag{4.25}$$

Combining the previous equations and identification to Eq.(1.44) give the strain concentration tensor expression according to the Kuster-Toksöz model in the form:

$$\mathbf{A}_1^{\bar{K}-T} = \mathbf{T}^{01} \left(\mathbf{T}^{0hom} \right)^{-1} \tag{4.26}$$

Note that the Kuster and Toksöz (1974) made the assumption that the tensor $\mathbf{T}^{0hom}$ is always the tensor for spherical inclusions. Accordingly, a generalization of effective bulk

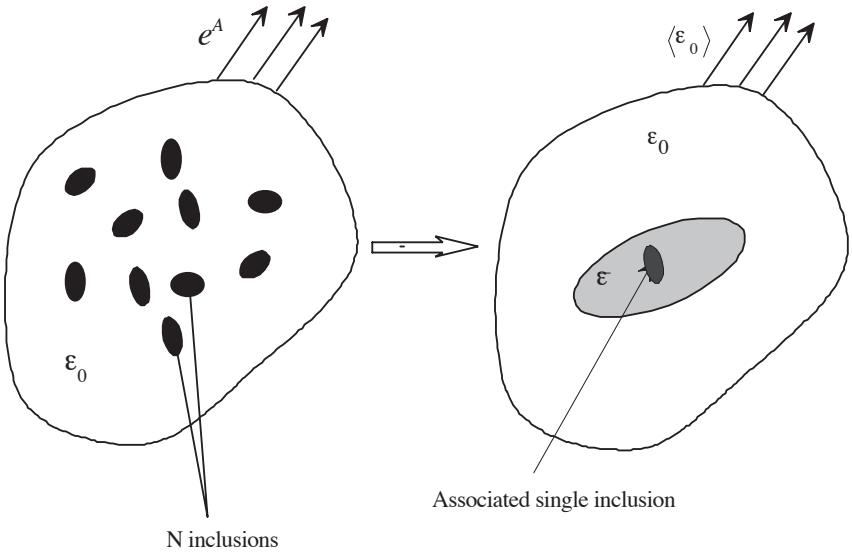

Figure 4.6: Associated schematic representation of the Kuster-Toksöz model

and shear moduli of an isotropic and homogenious composite medium, are formulated [23] as given by the following expressions:

$$(K^* - K_0)\frac{K_0 + \frac{4}{3}G_0}{K^* + \frac{4}{3}G_0} = \sum_{i=1}^{N} f_i(K_i - K_0)\alpha^{0i} \tag{4.27}$$

$$(G^* - G_0)\frac{G_0 + \zeta_0}{G^* + \zeta_0} = \sum_{i=1}^{N} f_i(G_i - G_0)\beta^{0i} \tag{4.28}$$

Where:
f_i is the volume fraction of the phase i;
α^{0i} and β^{0i} are given in the Table E.

Kuster and Toksöz consider their approach to be a "low concentration approximation" based on a "noninteraction" assumption. This assumption is kept valid when assuming that the aspect ratio of spheroidal inclusions doesn't exceed the corresponding volume fraction. Otherwise, inclusions are, at least partially, overlapping [130]. Zimmerman et al. showed in [239] through validations of experimental results, that the Kuster-Toksöz model provided a very good estimation of the elastic moduli of a composite as the concentration of sand in mortar and the porosity of the cement paste are allowed to vary.

4.4 Double inclusion model

The double inclusion model was first introduced by Nemat-Nasser and Hori in 1993 [108, 162]. The model takes into account the different interactions in a composite material: the interaction between the inclusion and the matrix and the interaction In the case of two-phase composite, the double inclusion model considers an inclusion surrounded by a coating (second inclusion) made of the matrix material. Both are embedded in a reference medium.
The first inclusion V_1 is ellipsoïdal of stiffness $\mathbf{C}_1$ and is embedded into a second inclusion V_0 of similar shape and of stiffness $\mathbf{C}_0$. Both are contained in an infinitely large medium V with stiffness $\mathbf{C}_V$ as shown in Fig. 4.7.
The model assumes the following conditions:

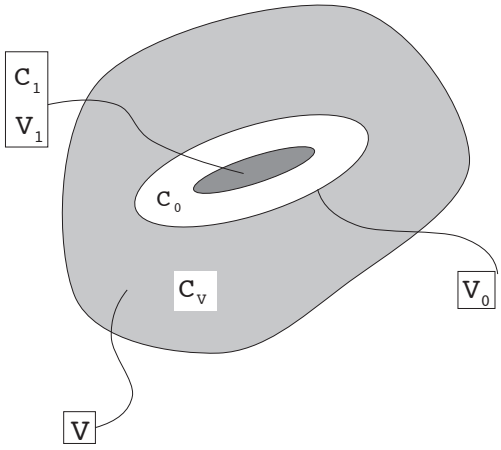

Figure 4.7: Schematic representation of the double inclusion model

- V_0 is large enough to contain the inclusion V_1;
- The volume fraction $\dfrac{V_1}{V_0 - V_1}$ must be equal to the volume fraction of inclusions $f_1 = \dfrac{V_1}{V_0}$;
- The geometry of V_0 must be similar to that of the composites inclusions. If for example, the inclusions are spheroïds, then, V_0 and V_1 must be coaxial.

The material is subjected to a uniform strain ε^{∞} at infinity. The objective is to determine the overall elastic tensor of the homogenized medium $\mathbf{C}_{hom}$ through computing the developed strains and stresses in V_1 and $V_0 - V_1$. In order to achieve this purpose, two sub-problems were considered in a manner that when superposed they lead to the original problem. For each problem, the strain and stress fields were expressed, based on the Eshelby isolated inclusion solution, for the considered sub-problem and

the corresponding homogenized medium as detailed in Appendix F.
Eq.F.36 defines the strain concentration tensor for a two-phase composite formulated by the double inclusion model as:

$$\bar{\mathbf{A}}^{DI} = \left[f_1 \mathbf{I} + f_0 (\mathbf{T}^{V1})^{-1} \mathbf{T}^{V0} \right]^{-1} \tag{4.29}$$

As one can notice, in the Double Inclusion strain concentration tensor (Eq.4.29), $\mathbf{C}_V$ was left unknown. Depending on the material that one can affect to $\mathbf{C}_V$, different expressions are obtained:

- The surrounding material V has the same properties as of the matrix V_0 i.e. $\mathbf{C}_V = \mathbf{C}_0$. Then, Eq.(4.29) writes:

$$\bar{\mathbf{A}}^{DI} = \left[f_1 \mathbf{I} + f_0 (\mathbf{T}^{01})^{-1} \right]^{-1} \tag{4.30}$$

  The latter is identical to the strain concentration tensor that was determined according to Mori-Tanaka model (Eq.4.6).

- The surrounding material V has the same properties as of the inclusion V_1 i.e. $\mathbf{C}_V = \mathbf{C}_1$. Then, Eq.(4.29) writes:

$$\bar{\mathbf{A}}^{DI} = \left[f_1 \mathbf{I} + f_0 \mathbf{T}^{10} \right]^{-1} \tag{4.31}$$

  This corresponds to the strain concentration tensor of what we introduced as "Inverse Mori-Tanaka" (Eq.4.10).

- The surrounding material V has the same properties as of the composite i.e. $\mathbf{C}_V = \mathbf{C}_{hom}$. Then, Eq.(4.29) writes:

$$\bar{\mathbf{A}}^{DI} = \left[f_1 \mathbf{I} + f_0 (\mathbf{T}^{hom1})^{-1} \mathbf{T}^{hom0} \right]^{-1} \tag{4.32}$$

  This expression can be considered as a developed form of the self consistent model.

The single and double inclusion models have, according to literature [99], limited success in the porosity characterization. In few cases, the models show that the composite modulus is equal to the matrix one which is not true. However, the model can be applied to model composites with coated inclusion or to model the Interface Transition Zone.

Yang and Huang formulated models for single inclusion [232] and double inclusion [233]. These models aims to improve the isolated inclusion problem, when considering a slightly more complex geometry. They, were applied to predict the elastic moduli of two-phase and three-phase materials and using experimental results, the elastic moduli of inclusions can be determined [232].
In the following, single and double inclusion models are presented.

4.5 Differential Method

Zimmerman proposed in [238] a differential method that considers a gradual increase of a small concentration of inclusions to an initially homogeneous matrix material (host material, [90, 164, 165]). The method assumes that the inclusions are spherical and both components are isotropic. Then, the shear and bulk moduli are given by the following differential equations:

$$\frac{1}{K}\frac{dK}{d\Gamma} = F_K = \frac{(3K+4G)(K_2-K)}{(3K_2+4G)K} \tag{4.33}$$

$$\frac{1}{G}\frac{dG}{d\Gamma} = F_G = \frac{(15K+20G)(G_2-G)}{(6K+12G)G_2+(9K+8G)G} \tag{4.34}$$

The initial conditions are: $K = K_1$ and $G = G_1$. The inclusions' fraction is related to Γ by the relation: $f_1 = 1 - exp(-\Gamma)$.
Different resolutions of the differential equation were proposed. Next, two resolution methods will be presented.

4.5.1 Zimmerman resolution

Zimmerman presented in [238] numerical resolution for the case of rigid inclusions and spherical pores.

4.5.1.1 Rigid inclusions

In the case of rigid inclusions, the elastic moduli K_1 and G_1 approach infinity, then the differential equations write:

$$\frac{1}{K}\frac{dK}{d\Gamma} = F_K = 1 + \frac{4G}{3K} = \frac{3(1-\nu)}{1+\nu} \tag{4.35}$$

$$\frac{1}{G}\frac{dG}{d\Gamma} = F_G = \frac{15K+20G}{6K+12G} = \frac{15(1-\nu)}{2(4-5\nu)} \tag{4.36}$$

The resolution of the previous equations (Eqs.4.35-4.36) gives [238]:

$$\frac{G}{G_0} = \frac{1}{(1-f_1)^2}\left[\frac{3(1-\nu_0)}{4(1-2\nu_0)-(1-5\nu_0)(\frac{G}{G_0})^{-0.6}}\right]^{1/3} \tag{4.37}$$

$$\frac{K}{G} = \frac{4}{3} - \frac{2(1-5\nu_0)}{3(1-2\nu_0)}\left(\frac{G}{G_0}\right)^{-3/5} \tag{4.38}$$

4.5.1.2 Spherical dry inclusions

In the case of vacuous pores, the elastic moduli of the inclusion phase vanish ($K_1 = 0, G_1 = 0$) and the differential equations take the form:

$$\frac{1}{K}\frac{dK}{d\Gamma} = F_K = -\left(1 + \frac{3K}{4G}\right) \tag{4.39}$$

$$\frac{1}{G}\frac{dG}{d\Gamma} = F_G = -\frac{15K + 20G}{9K + 8G} \tag{4.40}$$

Zimmerman gives the solution of these differential equations in the form:

$$\frac{G}{K} = \frac{3}{4} + \frac{3(1 - 5\nu_0)}{4(1 + \nu_0)}\left(\frac{G}{G_0}\right)^{3/5} \tag{4.41}$$

$$\frac{G}{G_0} = (1 - f_1)^2\left[\frac{2(1 + \nu_0) + (1 - 5\nu_0)(\frac{G}{G_0})^{3/5}}{3(1 - \nu_0)}\right]^{1/3} \tag{4.42}$$

Where : $\nu_0 = \frac{3K_0 - 2G_0}{3K_0 + 2G_0}$.

4.5.2 Berge resolution

Berge et al. proposed an iterative method [15] to the resolution of the differential equations. The resolution is valid for the case of spherical pores and is given by:

$$K - K_0 = -\sum_{m=1}^{M} \frac{m}{M} K_{m-1} \frac{K_{m-1} + \frac{4}{3}G_{m-1}}{\frac{4}{3}G_{m-1}} f \tag{4.43}$$

$$G - G_0 = -\sum_{m=1}^{M} \frac{m}{5M} G_{m-1} \frac{G_{m-1} + \frac{G_{m-1}}{6}\frac{9K_{m-1} + 8G_{m-1}}{K_{m-1} + 2G_{m-1}}}{\frac{G_{m-1}}{6}\frac{9K_{m-1} + 8G_{m-1}}{K_{m-1} + 2G_{m-1}}} f \tag{4.44}$$

Where: M is the total number of iterations.

Conclusion

This part is intended to introduce the specifics of the micromechanical modeling, notations and assumptions. The most commonly used micromechanical models, which can be applied to N-phase composite materials, were introduced, detailed and commented. For each model, the assumptions were clearly noted. The possible applications of each presented micromechanical model was noted as well as references of researches conducted on the application of the model to a specified composite material as summirized in Table 4.1.

It was noted at this stage that limited researches dealt with the application of microme-

Table 4.1: Assumptions, limitations and scopes of the different models

Model	Assumptions and limitations	Examples of scopes
Dilute inclusion	• No interaction between inclusions • Very low inclusion concentration	Mechanical properties determination of short fiber composite
Mori-Tanaka	• Low to moderate inclusion concentration • Direct implementation	Relate porosity to ultrasonic properties of mortar
Kuster-Toksöz	• Not realizable for all microstructures • Violate some of the rigorous bounds • Direct implementation	Cement paste description with penny pores
Self-consistent	• Matrix phase can be non-continuous • Iterative resolution	Geophysical and rock mechanics studies (cracks asect ratio distribution and porosity)

chanical models on cement-based materials. Aiming to enhance the micromechanical modelling of the cement paste material, that is considered to be the binding material of cement-based materials, the present study was developed. Thus, this work intends to improve the effective cement paste elastic parameters predictions based on micromechanical modelling.
Accordingly, the following part will be devoted to the understanding of the cement paste material's microstructure, in order to define the possible applications of micromechanical formulations at different porosities and saturation states.

Part II

Experiments: Materials, techniques and procedures

5 Materials 61

6 Evaluation of the cement paste internal structure 73

7 Static mechanical measurements on cement paste 95

8 Ultrasonic Pulse Velocity Measurements on Cement-based Materials 99

Introduction

The material considered within the frame of this work is cement paste with and without air-entrained adjuvant. In fact, cement paste represents the matrix phase of mortar and concrete that are two of the most widely used building materials. Thus, to understand the behavior of such complex cement-based composite material, it is essential to investigation their matrix: the cement paste.
The main objective of this study is to find a correlation between ultrasonic and hydraulic properties of the cement paste. Therefore, the experimental efforts focused basically on ultrasonic measurement and internal cement paste microstructre investigation, as the latter influences the hydraulic properties.
In this part, the microstructure investigation of the cement paste was carried on to determine the required inputs for the micromechanical modeling. In particular, porosity that is considered as a principal hydraulic property, was measured using different techniques and equipments, namely water imbibition, mercury intrusion and image processing. In addition, scanning electron microscopy was used to visualize the internal microstructure of the cement paste material. Later, the static tests as well as the dynamic ultrasonic device and measurements were presented. All these techniques allowed the observation and quantification of the cement paste microstructure in order to perform its control but also to verify the assumptions considered within this research.

Chapter 5

Materials

Cementitious materials form the most used construction material in the world as it is characterized by its relatively low cost and considerable mechanical properties. In order to evaluate this material with the previously presented micromechanical models, two materials were made in the laboratory: cement paste and air entrained cement paste. The samples compositions and preparation are presented in this chapter.
A cement paste material is formed by different constituents. Here after its principal constituents are described.

The Portland cement: The Portland cement is the resulting product of a thermal treatment at 1450 $^{\circ}C$ of a mix of clay (20 to 30 $\%$) and limestone [204]. Indeed, after the calcination of the obtained mix, it is ground to get the Clinker to which is added a small quantity of gypsum (3 to 5 $\%$) and possibly other constituents like limestone fillers, silicate fume, slag furnace or fly ash depending on the desired cement. As for the gypsum, it delays the hydration of the cement to ensure a better workability.

Water: The water proportion used for the preparation of the cementitious material is of great importance. It influences, for instance, the material porosity, mechanical properties and durability. Mixing the cement to the water leads to an extremely complex reactions. The latter are presented in the following section.

Adjuvants: Adjuvants are added to the cement-based material in a very small quantities, generally less that $10kg/m^3$ [178]. In this study, two types of adjuvants were used in the preparation of the materials: the superplasticizer and the air-entrained adjuvants. The first allows the redaction of water proportion when conserving the material workability and fluidity [186]. Indeed, superplasticizers are capable of reducing the water requirements by about 30$\%$. The second involves adsorption at the air-water and solid-water interfaces. Indeed the air-entrained surfactant ions are adsorbed on the cement particles making them hydrophobic. Thus, the bubbles generated when mixing adhere to cement. This process stabilizes bubbles, preventing their coalescence.

In the present work, all the materials were made up of cement CPA CEM I 52.5. To study the effect of porosity variation on the prediction of elastic and/or ultrasonic velocities, different water/cement ratios were considered within each material.

On site cementitious structures can be either dry, partially or fully saturated by two or more different fluids. The saturation condition affects the elastic properties and the velocities of ultrasonic waves propagating into the material. In order to qualify and quantify this dependence, a variation of the saturation degree was realized on each of the studied material.
The fluid (here water) saturation is defined as the fraction of liquid-filled void space V_w by the total pore volume V_{pore}. It is commonly expressed in percentage:

$$S_r = 100\frac{V_w}{V_{pore}}\% = 100\frac{V_w}{Vp}\% \tag{5.1}$$

where V is the total material volume and $p = \frac{V_{pore}}{V}$ is the porosity. Thus, the water saturation ranges between $0 < S_r < 100$.
It should be noted that the saturation degree differs from the water content (or the moisture content). The latter refers to the quantity of water contained in a material and is expressed as follows:

$$\theta = \frac{V_w}{V_T} \tag{5.2}$$

Where V_w is the volume of water and V_T is the total volume.

5.1 Cement-based mix compositions

5.1.1 Cement paste

As a first stage study, the considered material was the cement paste. The latter is an existing, but simplified cement-based material, that consists of Portland cement and water. The interest to the cement paste material is argued by the fact that this material consists the binding matrix of all the other cement-based materials (mortar, concrete...). Thus, monitoring the elastic properties homogenization and the wave propagation would be a key for the understanding and control of both issues in mortar and concrete.
In the present work, the cement paste samples were made with different water/cement (W/C) ratios, namely 0.3, 0.4, 0.5, 0.6 and 0.7. Super-plasticizer adjuvant (structuro311 [205]) was used in a proportion of 1 % of the cement weight. This adjuvant provides a high workability of the cement paste material. Indeed, the super-plasticizer adjuvants correspond generally to different polymers or different conformations of these polymers. The specimens were cast in a rectangular slabs of dimensions $(100 * 50 * 10)\ cm^3$. Table 5.1.1 gives the proportions of the seven compositions of the samples.

5.1.2 Air entrained cement paste

Aiming to perform the study carried on the cement paste material, air-entrained cement paste specimens were made with varied air-entrained adjuvant. Thus porosity were

Table 5.1: Composition and properties of the cement paste samples in (kg/m^3)

Samples	W/C	Cement	Water	Super-plasticizer
CP030	0.30	400	120	4
CP040	0.40	400	160	4
CP050	0.50	400	200	4
CP060	0.60	400	240	4
CP070	0.70	400	280	4

varied for a fixed W/C ratio in order to decouple both effects on the studied ultrasonic and hydraulic properties.
Entrained air bubbles with a diameter of 50 to 200 μm , can be introduced in cement paste by adding small amounts of air-entraining adjuvant. They contribute in protecting the material from damage due to frost action characterized by the expansion of freezing water [59, 126]. Indeed, during the freezing process, the expansion of water, which is being converted from liquid to solid, creates a pressure on the remaining liquid. Entrained air bubbles provide space for the water to flow into. This decreases the water pressure and prevents degradation [182].
The use of air-entrained admixture introduce a modification in the air-void system of the material. Powers [176] reported that the voids present when an entraining agent is not added to a concrete material are also present when the agent is used. Accordingly, the air-entraining admixture increases the air voids having a smaller size (than those present in the sample without air-entrained: the entrapped voids) and stabilizes them during the mixing. The air-void system obtained with an air-entrained admixture is then a "composite" of the entrained voids resulting from handling and placing and entrapped voids formed during mixing [110].
In the present study, the air entrained cement paste was prepared with a fixed water, according to cement, ratio W/C= 0.4. In order to keep water content constant and vary porosity, different amounts of air-entrained (AE) adjuvant FOSROC Resi Air 200 were used. Super-plasticizer adjuvant (structuro311) was used in a proportion of 1% of the cement weight. Table 5.1.2 gives the proportions of the seven compositions of the samples. The samples were cast in two shapes designed for different investigations. All the mix were prepared in both slabs of dimension 30 cm ∗30 cm ∗5 cm and cylindrical specimens of 11cm diameter and 22cm of high. The water imbibition measurements were performed on both shapes. However, the MIP and the X-ray microtomography were carried out on samples casted into the slabs.

The molds of the different materials were watertight and protected from hydraulic exchanges with the surrounding environment during 48 hours. After that, the slabs were removed from the molds and stored in a lime water solution for 28 days at a constant temperature of 21 ± 1C°.

Table 5.2: Composition and properties of the air-entrained cement paste samples in (kg/m^3)

Samples	Cement	Water	Super-plasticizer	Air-entrained
ACPC	400	160	4	0
ACP12	400	160	4	0.48
ACP25	400	160	4	1
ACP50	400	160	4	2
ACP15	400	160	4	6
ACP45	400	160	4	18
ACP60	400	160	4	24

The influence of water on ultrasound results were studied by considering two saturation states, dry and fully saturated with water. The samples were first saturated and stored in a lime solution. The dried samples were obtained by submitting the saturated ones to moderate oven-drying at a temperature of $60 \pm 2C°$. Such temperature is suitable to prevent micro-cracks. The oven-drying was selected for this experiments as it is suggested to be the more rigorous procedure for complete removal of water. It is considered as the best way of assessing the total pore space present in the structure [158].

The drying was stopped when the weight of the sample remained constant, i.e. when the variation between two successive weightings was less than 0.05%.

5.2 Cement properties

5.2.1 Cement chemical composition

Portland cement CPA CEM I 52.5 was used for the preparation of the previously detailed compositions. This type is known to be among the most used in civil engineering in France. Chemical composition of CPA CEM I 52.5 Portland cement used for this study is given in Table 5.2.1.

In an ordinary Portland cement, it is generally assumed that four components are the major constituents. The latter are pure minerals with the following compositions:

- Alite: C_3S, or tricalcium silicate; [1];
- Belite: C_2S, or dicalcium silicate;
- Aluminate phase: C_3A, or tricalcium aluminate;
- Ferrite phase: C_4AF, or tetracalcium aluminoferrite.

[1]Notation: $C = CaO$; $S = SiO_2$; $A = Al_2O_3$

Table 5.3: Chemical properties of Portland cement CPA CEM I 52.5 used in this study

Chemical product	Content (%)
CaO	52.46
SiO_2	23.40
Al_2O_3	3.3
$(Fe)_2O_3$	3.36
$(Na)_2O$	0.17
K_2O	0.44
MgO	2.05
MnO	0.03

The initial percentage of weight for each of these compound can be calculated based on the Bogue calculation [204]. The latter assumes that (1) the Fe_2O_3 occurs as C_4AF and (2) the remaining $A1_2O_3$ occurs as C_3A. Then, the compound masses are:

$$C_3S = 4.0710CaO - 7.6024SiO_2 - 6.7187Al_2O_3 - 1.4297Fe_2O_3 \quad (5.3)$$

$$C_2S = -3.0710CaO + 8.6024SiO_2 + 5.0683Al_2O_3 + 1.0785Fe_2O_3 \quad (5.4)$$

$$C_3A = 2.6504Al_2O_3 - 1.6920Fe_2O_3 \quad (5.5)$$

$$C_4AF = 3.0432Fe_2O_3 \quad (5.6)$$

According to Bogue formula given above and knowing the chemical composition of the used Portland cement (Table 5.2.1), the initial percentage of weight W_i of each compound was computed and listed in Table 5.2.1. A summery of the aforementioned

Table 5.4: Portland cement compounds weights as determined by Bogue calculation

Reacting compound	Weight (W %)
C_3S	4.62
C_2S	63.61
C_3A	3.06
C_4AF	10.22

compounds weights for different types of cement Portland is given in [76]. Such calculation is useful for an estimation of the considered cement hydration as will be detailed next.

5.2.2 Cement hydration

The hydration is the chemical reaction between the clinker phases and the water. It results in the cement paste that is formed essentially by a solid phase and a porous

structure. The different products of the solid phase as well as the porous structure are detailed in following. The formation of these latter in function of the hydration time are given in Fig.5.1. The figure plots the formation of three main products during hydration: calcium silicate hydrates (C-S-H), calcium hydroxide (C-H) and ettringite (or trisulfate; AFt) in addition to other minor products. In fact, after the dormant stage, C_3S, that is the most active phase during the first stage of hydration reacts and leads to the formation of the outer $C-S-H$ (long fibers). After several days, a second type of C-S-H can be observed (short fibers).

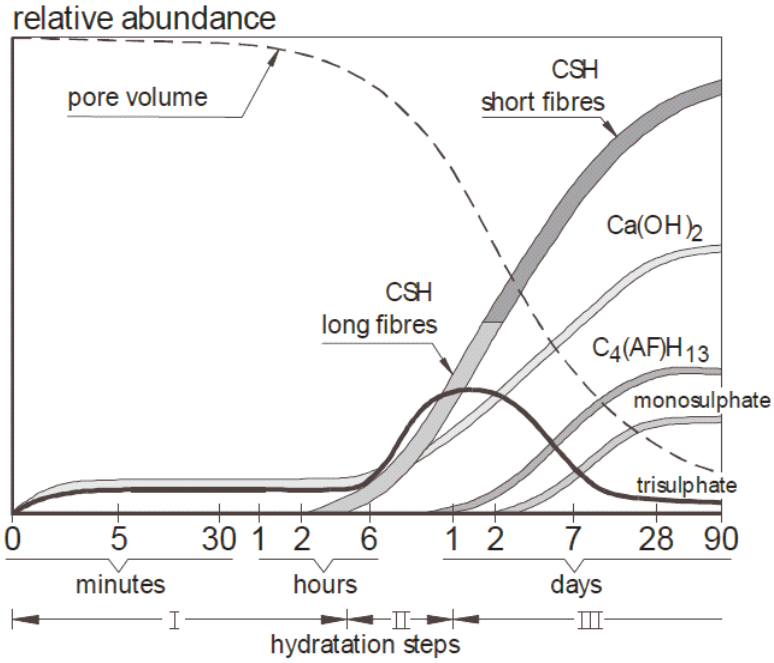

Figure 5.1: Evolution of hydration solid products and porosity in the cement paste [235]

5.2.2.1 Solid hydration products

The solid phase contains five different chemical phases with a domination of two of them: The Calcium-Silicate-Hydrates (C-S-H) and the Calcium Hydroxide (C-H). These two products constitute about 85 % of the cement paste volume. They are resulting from the hydration of the aluminates ($C_3A \equiv 3CaO.Al_2O_3$) and silicates ($C_3S \equiv 3CaO.SiO_2$ and $C_2S \equiv 2CaO.SiO_2$) present in the clinker.

- The Calcium-Silicate-Hydrates (C-S-H) forms in the cement paste in different morphological forms [57, 209] (see Fig.5.3), volume fractions [206] and elastic properties [52]. The two dominant forms of C-S-H are characterized by two different densities; a high-density (HD) C-S-H and a low-density (LD) C-S-H

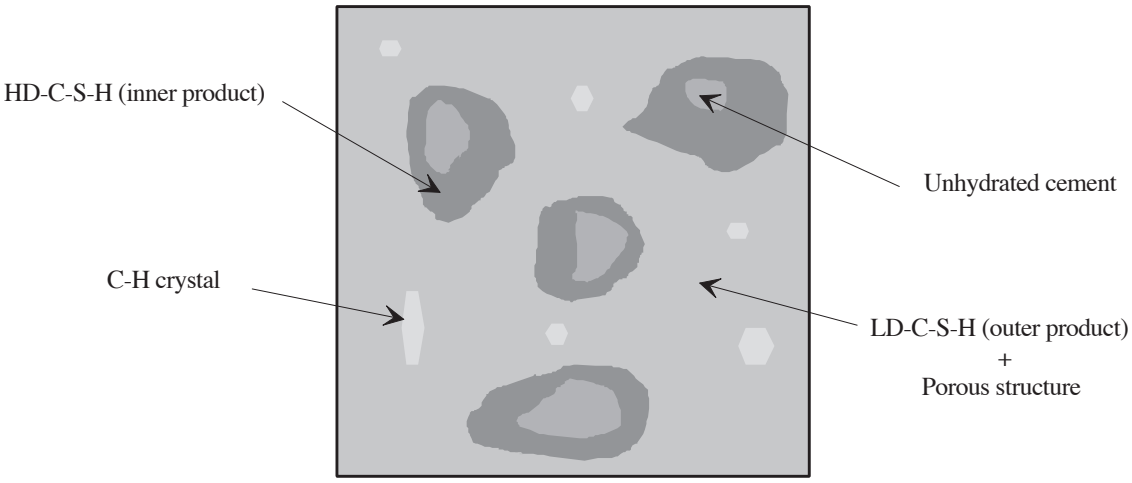

Figure 5.2: Schematic representation of the cement paste hydration

[115] or called also inner (or TypeII) and outer (or TypeI) products, respectively. These two C-S-H forms are resulting from two different processes of hydration of the clinker [17]. Indeed, at the early stages of hydration, C-S-H products are formed at the surface of the cement grains. These latter lead to the outer products. Then, as hydration progress, a growing layer of C-S-H covers the cement grains and new C-S-H products are formed in the space between the existing C-S-H layer and the cement grains. The new C-S-H products, called inner products, have a higher density than the outer products. According to this hydration process, (LD) C-S-H has more porosity than the (HD) C-S-H.

- The Calcium Hydroxide ($Ca(OH)_2$ noted C-H), or Portlandite, are crystals that present about 10 to 20 % of the hydration products. This product is distinguished in the cement paste microstructure by its clear hexagonal prism geometry as can be seen on Fig.5.3.

- The Calcium Sulfates, Aluminates, Ferrites and ettringite (tri-sulfate) are three minor products of the clinker hydration. They present approximately 15 to 20 % of the non-porous volume of the cement paste.

It has to be noted that it is not obvious that all the clinker phases react with the water and that some cement grains remain unhydrated. The amount of the unhydrated product depends on the cement particle size, the duration of hydration but mainly the water content in the mix. It has been shown experimentally in the literature [163] that the minimum amount of water required completely hydration corresponds to W/C= 0.42.
More details on the different phases of the cement hydration can be found in [51]

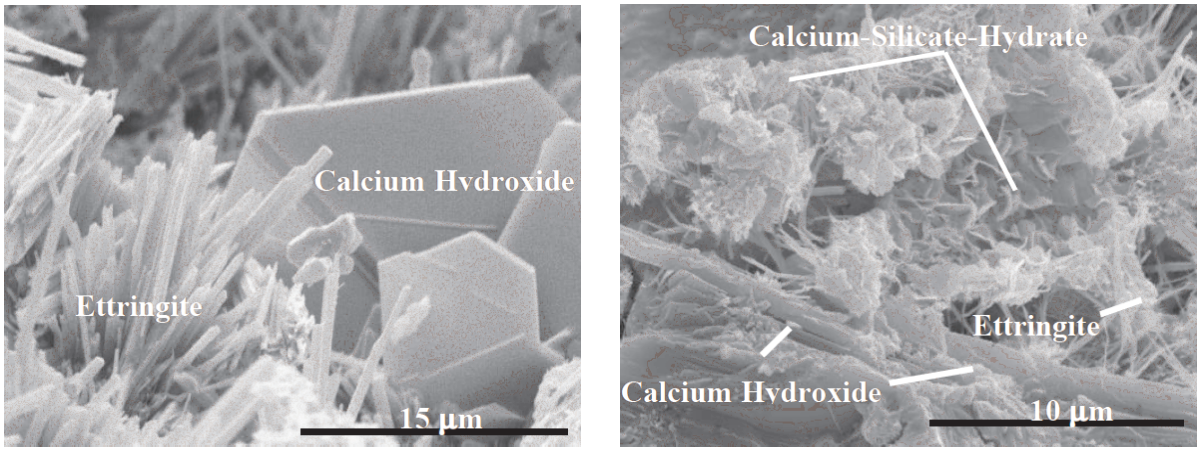

Figure 5.3: The plate-like C-H morphology and fine bundles of Type I C-S-H, platy-Type II C-S-H, and ettringite needles [201].

5.2.2.2 Porous structure of hydrated cement

In addition to the solid products mentioned above, the hydrated cement paste contains a porous structure. The latter is formed of many types of pores that affect the properties of the cement paste. Five principal pores can be distinguished: interlayer space in C-S-H, capillary voids, entrained air voids, entrapped air voids, and fractures [153].

- Interlayer space in C-S-H: called also "gel porosity", it results from the chemical formation of the C-S-H and have a volume fraction of 28% in the hydrated solid paste according to Powers model. The C-S-H interlayer space is of $1.8nm$. Thus, this porosity shouldn't affect the properties of the cement paste as such pores are of small dimension to contribute to the transfer of degrading agents.

- Capillary voids : are the areas that was not filled with any of the hydration products. In contrast to the gel pores, these pores are large enough to ensure aggressive agents transfer inside the cement paste. The diameter of the capillary pores varies from low (10 to $100nm$) to high (3 to 5) water/cement ratio. Note that these pores have no regular shape due to the process of their formation.
  An attempt to represent diagrammatically the interlayer and the capillary porosity was made by Feldman and Sereda [70] in Fig.5.4. The layers of C-S-H appear to be irregular and the inter particle bonding was represented as a solid-to-solid contact.

- Entrained air voids: are of 50 to 200 of diameter and can be introduced in cement paste by adding small amounts of air-entraining adjuvant. They contribute to protect the material from damage due to frost action characterized by the expansion of freezing water [59, 126].

- Entrapped air voids: are the larger pores of the cement paste porous structure. They can reach few mm of size. They are resulting from the entrapped air when

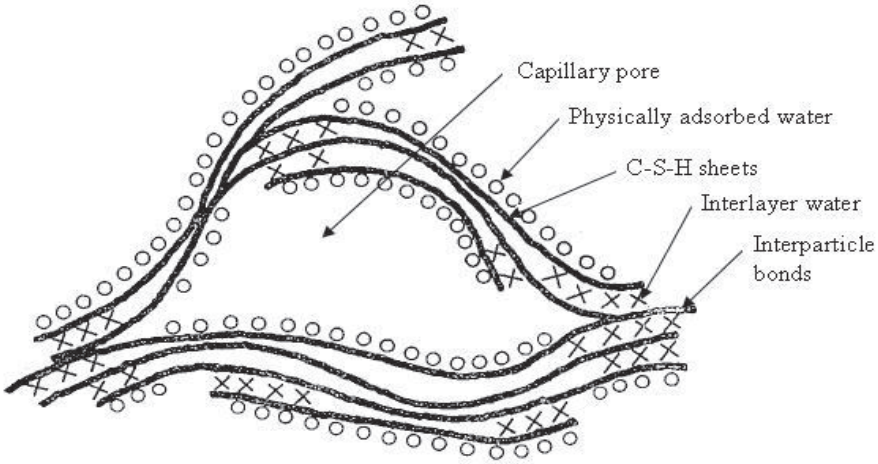

Figure 5.4: Model of hydrated Portland Cement by Feldman & Sedera (1968) [70]

mixing. Thus, properly mixing and vibrating the cement-water mix can reduce them. Example of entrapped air-void observed by SEM technique on a cement paste sample is shown in Fig.5.5.

5.2.2.3 Hydration degree and products volume fractions

The hydration degree of a cement paste material is related to the hydration degrees of all the compound present in the Portland cement by a weighted average [229]:

$$\alpha = \alpha_{C_3S} W_{C_3S} + \alpha_{C_2S} W_{C_2S} + \alpha_{C_3A} W_{C_3A} + \alpha_{C_4AF} W_{C_4AF} \tag{5.7}$$

Where W_i are the initial percentage of compounds weight, that have been computed and listed in Table 5.2.1 and α_i the hydration degree of each compound. The latter are assumed to be given by approximations based on Avrami equations of the form:

$$\alpha_i = 1 - exp(-a_i(t - b_i)^{c_i}) \tag{5.8}$$

Where t is time in day and a_i, b_i and c_i are constants empirically determined by Taylor and are given in Table 5.2.2.3 [50, 229]. In this study, the experimental measurements were carried out starting from 120 days of hydration. Accordingly, the hydration degree was found to be $\alpha = 0.5548$. It should be noted that such hydration degree is unexpected and means that the hydration reaction was not completed at this date. This could be due to the chemical composition of the used Portland cement that influences the kinetics of hydration.
The Powers hydration model provides the volume fractions of unhydrated cement particles f_{unhyd}, hydrated products (cement gel) f_{hyd}, capillary pores $f_{cap} = 1 - f_{unhyd} - f_{hyd}$, non-evaporable water f_{wat} and the total porosity of the paste f_p in function of the water

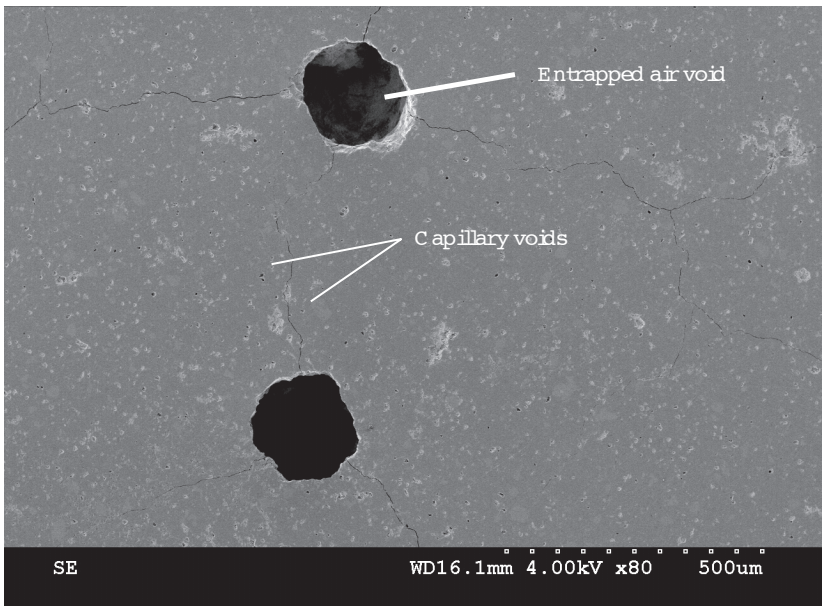

Figure 5.5: Entrapped and capillary pores observed on a cement paste sample

Table 5.5: Coefficients a_i, b_i and c_i

Compound	a_i	b_i	c_i
C_3S	0.25	0.9	0.7
C_2S	0.46	0	0.12
C_3A	0.28	0.9	0.77
C_4AF	0.26	0.9	0.55

to cement ratio W/C and the degree of hydration α as given by the following equations [87, 190].

$$f_{unhyd} = \frac{0.32(1-\alpha)}{w/c + 0.32} \tag{5.9}$$

$$f_{hyd} = \frac{0.68\alpha}{w/c + 0.32} \tag{5.10}$$

$$f_{cap} = \frac{w/c - 0.36\alpha}{w/c + 0.32} \tag{5.11}$$

$$f_{wat} = \frac{w/c - 0.4175\alpha}{w/c + 0.32} \tag{5.12}$$

$$f_{p} = \frac{w/c - 0.17\alpha}{w/c + 0.32} \tag{5.13}$$

The model is widely cited and many work have been carried on cement paste hydration and proved that it can be considered as a rigorous model [163, 204]. An analysis presented by Brouwers [33, 34] clarifies the Powers model, experiments and applications. The degree of hydration reaches a maximum value α^{max} when water is available from external sources. This maximum corresponds to the depletion of the unhydrated cement or the water in the capillary pores. α^{max} can be determined from Eq.(5.11) so that:

$$\alpha^{max} = \begin{cases} 1 & \text{for} \quad w/c > 0.36 \\ \frac{w/c}{0.36} & \text{for} \quad w/c < 0.36 \end{cases} \tag{5.14}$$

However, the total hydration can not be reached in general. Indeed, beyond a critical hydration degree the kinetics of the hydration reactions are stopped because the dissolved ions can not diffuse through the layers of hydrates surrounding the clinker [16].

In this chapter, the cement paste compositions were presented. Five cement paste compositions with varied water to cement ratio and seven air-entrained cement paste mix with different amounts of air-entrained adjuvant were prepared for the study. The used Portland cement chemical properties were mentioned. The mechanism of cement hydration was briefly described as well. The microstructure of a hydrating cement paste states various solid products and a porous structure. The volume fraction and the hydration degree of a cement paste were defined and computed.

Chapter 6

Evaluation of the cement paste internal structure

The motivation for this microstructural study is to gather details on the cement-based material morphology in order to approve the micromechanical modeling assumptions that were considered in the homogenization schemes. Indeed, different parameters affect the cement paste microstructure and the major one is the W/C ratio. Indeed, the variation of the W/C ratio induces changes in both the solid matrix and the capillary voids [184].
Hence, microscopic observations and quantification are essential for the examination of cementitious materials. Various techniques have been investigated in order to examine the cementitious microstructural details at the micrometer scale. Among these techniques, we used in this study the Optical Microscope, the Scanning Electron Microscope (SEM), the X-ray microtomography and the Mercury Intrusion Porosimetry (MIP) on both cement paste and air-entrained cement paste.
The cement paste samples were cast in a single mold shape (slabs). However, the air-entrained cement paste mix were prepared in two different shape molds: slabs of dimension 30cm $\times$ 30cm $\times$ 5cm and cylinders of 11 cm diameter and 22 cm of high. Thus, it is important to note which test was done on which mold shape. Indeed, the water imbibition measurements were performed on both shapes. Thus, presenting two water porosity results on the same compositions will not be contradictory, as a scale factor would influence such measurement. However, the MIP and the X-ray microtomography were carried out on samples casted into the slabs.

6.1 Water imbibition porosimetry and density

The degradation of cementitious structures is mainly caused by penetration of aggressive agents, present in the surrounding water for instance, through capillary porosity. Thus, capillary imbibition is an important transport phenomenon that affects the cement-based material. Hence, the determination of the capillary porosity by water imbibition is necessary for the present study.

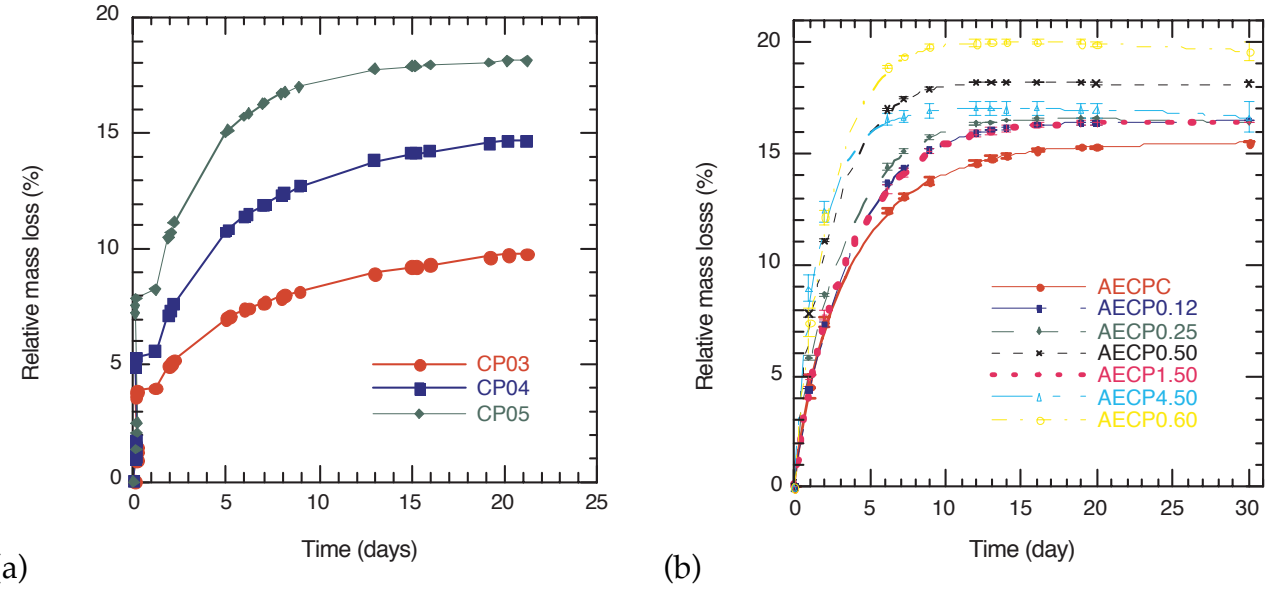

Figure 6.1: Relative mass loss of the cement paste materials when drying for (a) different W/C ratios and (b) different air-entrained contents

6.1.1 Water imbibition porosimetry

Water imbibition porosity was measured by the gravity method [3], using vacuum saturation. This method consists in saturating the cement paste sample with distilled water under vacuum. The vacuum was created in a dissicator using a vacuum pump so that water can displace air and fill the interstices. Once fully saturated, it was weighted with centigram precision and its volume V determined by hydrostatic weighing. These measurements were used in order to obtain good precision over the mass and volume of the sample. Then, the sample is submitted to moderate oven-drying at a temperature of $60 \pm 2°C$. Such temperature is suitable to prevent micro-cracks. The drying is stopped when the weight of the sample remains constant, which is achieved when the variation between two successive weightings does not exceed 0.05%. Figure 6.1(a) shows the mass loss in function of time for three cement paste compositions with different W/C ratios: 0.3, 0.4 and 0.5. It is noted that the mass loss kinetic depends on the W/C ratio. For example, for a period of seven days of drying in an oven at a temperature of $60°C$, there was a mass loss of 7.69%, 11.87% and 16.24% for cement paste samples with W/C equal to 0.3, 0.4 and 0.5, respectively. This kinetic is argued by the fact that the more the material is porous with an opened porosity, the more the drying is efficient and rapid. Figure 6.1(b) shows the mass loss in function of time for all the air-entrained cement paste compositions with different air-entrained adjuvant. It is remarked that, the relative mass curve for the control air-entrained cement paste sample (without air-entrained add) is the same as for the cement paste with W/C= 0.4 plotted in Fig.6.1(a). That confirms the reproducibility of the mass loss measurements on a same cement

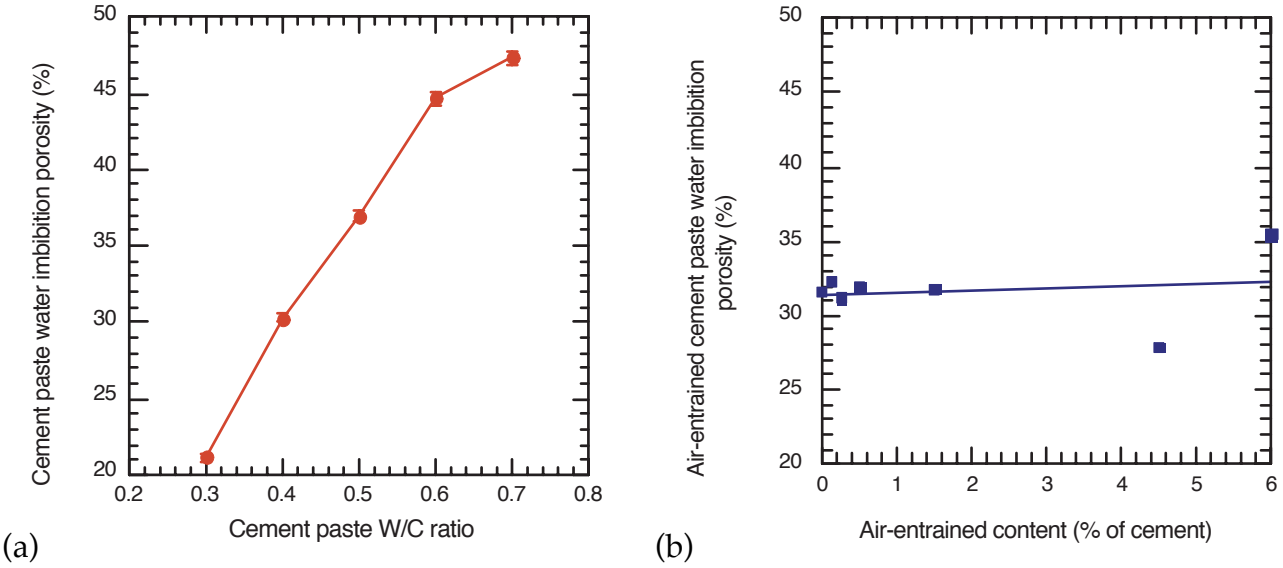

Figure 6.2: Measured capillary porosity for (a) cement paste and (b) air-entrained cement paste

paste composition (with the same W/C ratio). Different mass loss kinetics are observed when varying the air-entrained added amount. However, no clear trend can be found in function of the air-entrained adjuvant. Although, one can assume that the mass loss kinetic is higher for increasing amount of air-entrained adjuvant, if some compositions are excluded (AECP0.50 and AECP1.50).
The mass of dried sample is obtained after 25 days of drying. Porosity p is then determined using the following formula:

$$p = \frac{M_{sat} - M_{dry}}{\rho_w V} \tag{6.1}$$

where ρ_w is the unit mass of water, V is the sample volume; M_{dry} and M_{sat} respectively denote, the weight of the dried and fully saturated sample. The measured water porosity of cement paste is plotted in function of the W/C ratio on Fig.6.2(a) and of the air-entrained cement paste in function of the air-entrained content on Fig.6.2(b). As expected, porosity increases with the W/C ratio. Porosity values range from 21.13% for the lowest W/C ratio to 47.34% for the highest one. The determined range of porosity presented in Fig.6.2(a) is coherent with the commonly obtained porosities on the cement paste material [73, 74, 79, 127]. For instance, Krus et al. reported [127] that water saturation porosity varies from 36% to 50% when Portland cement pastes with W/C equal to 0.35 and 0.6 were considered. Similarly, [74] found, using the same experimental water porosity determination procedure, that capillary cement paste porosity presents the same trend with comparable values with those determined in this study.
Further comparison has been plotted on Fig.6.3 between this measured capillary poros-

ity and the capillary porosity estimated by Powers theory (Eq.5.11) when assuming that the hydration degree is computed according to Eq.(5.7). It is clear that the Powers model

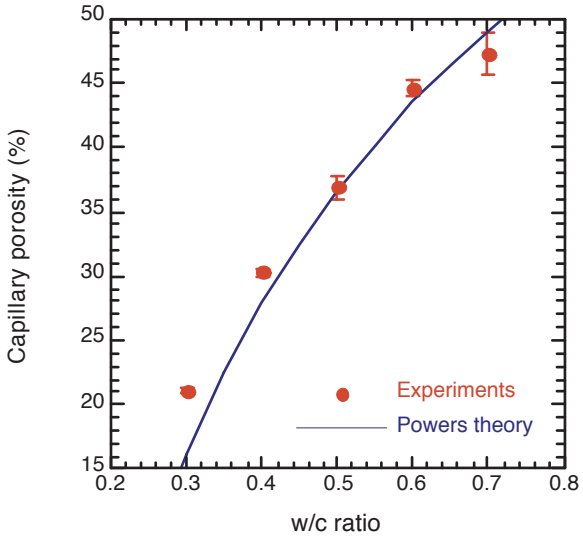

Figure 6.3: Comparasion between the measured and the Powers estimated capillary porosity

based on an estimate of the hydration degree provides a good estimate of the capillary porosity when varying the water to cement ratio. The observed scattering especially for W/C= 0.3 is due especially to the estimation of the hydration degree as no sufficient water is available for such composition to allow the maximum possible hydration (W/C=0.3 0.36; Eq.5.14). In the next part an inverse computation will be applied in order to determine the hydration degree of each mix based on the measured capillary porosity and Powers theory.

6.1.2 Material density

The density of the cement paste material depends on both the porosity and the water saturation degree. In this study the cement paste density was determined using experimental measurements and theoretical formulations.
The densities of the five cement paste compositions were measured and estimated for different saturation states.
The materials densities were also computed using Eq.(1.7) for a two phases partially water saturated cement paste. Let V_w and V_a be the total volume of water and air present in the porous structure, respectively. Thus Eq.(1.7) writes:

$$\rho = \frac{M}{V} = \frac{\rho_0 V_0 + (\rho_w V_w + \rho_a V_a)}{V} = \rho_0 f_0 + \rho_w \frac{V_w}{V} + \rho_a \frac{V_a}{V} \tag{6.2}$$

Knowing that:

- $S_r = \frac{V_w}{Vp}$ (Eq.5.1) $\rightarrow \frac{V_w}{V} = pS_r$
- $\frac{V_w + V_a}{V} = p \rightarrow \frac{V_a}{V} = (1-p)S_r$
- $f_0 = 1 - p$

The homogenized density of a partially saturated material is deduced from Eq.(6.2) as:

$$\rho = (1-p)\rho_0 + pS_r\rho_w + (1-p)S_r\rho_a \tag{6.3}$$

In the previous equation the water and air densities were considered to be well known in the literature [231]. However, the cement paste matrix density is a intrinsic property of the studied cement paste. It was determined on a dry cement paste sample using a volumenometer [68]. The material was pounded and crushed until the material grains dimensions became less than $0.2mm$. This aimed to eliminate the pores and voids present in the material. Then, the sample was put in a recipient containing an inert liquid (spirit of turpentine) to determine its absolute volumetric mass. Table 6.1 summarizes the different values of the densities that were considered within this study.

Figure 6.4 shows both the measured and computed densities in function of cement

Table 6.1: Density values of air, water and cement paste matrix

	Air	Water	cement paste matrix
Density (kg/m^3 at 20 °C)	1.204	1000	2579

paste porosities for different saturation states. It is noted that the measured and computed densities have almost the same linear trend with comparable values.
On the one hand, the density of the cement paste samples decreases with porosity. For the dry cement samples for instance, the experimental density decreases by 34% when the W/C ratio is increased from 0.3 to 0.7. While it decreases by 18% if the material is saturated with water. This noticed difference in the decrease slope of density vs. porosity when varying the saturation state is mechanically stated in Eq.(6.3). The latter can be written in the following form:

$$\rho = \rho_0 + S_r\rho_a - p(\rho_0 - S_r(\rho_w - \rho_a)) \tag{6.4}$$

As the water density is higher than air density, then Eq.(6.4) proves that if the saturation degree is increased, the slope of the overall density vs. porosity decreases.
On the other hand, the cement paste density increases with the saturation degree. As higher is the porosity as larger is the increase of density with the saturation degree. Indeed, the density increases by 10% for W/C=0.3 and 36% for W/C= 0.7 from dry to saturated state. Such trend is logical if assuming Eq.(6.4) and knowing that the density of water is higher than the density of air (see Table 6.1).

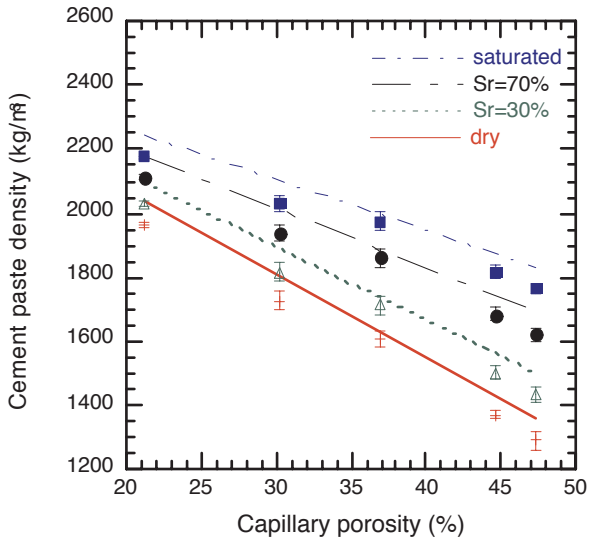

Figure 6.4: Variation of cement paste density with porosity and saturation degree: lines refers to the computed densities and dots to the measured ones

6.2 Mercury Intrusion Porosimetry (MIP)

The early use of Mercury Intrusion Porosimetry (MIP) method for cementitious materials was reported by Winslow and Diamond (in 1970). Since then, the method has been widely used to study the pore structure of cement-based materials as it is a simple and fast test and investigate a large range of porosity ($200\mu m$ to $2nm$).

6.2.1 MIP principle

The mercury intrusion principle is based on the fact that mercury does not wet most substances. Then it will penetrate pores only by pressure application. This technique was used for the porosity and pore diameter distribution determination of the studied cementitious materials. Measurements were conducted at the Ecole des Mines de Douai, Civil Engineering Department. The equipment used was an *Autopore IV 9500* . The test involves putting a cementitious material sample previously dried and degassed under vacuum in the presence of mercury. An incrementally rising mercury pressure was applied. Thus the liquid gradually penetrates the material. For each applied pressure corresponds a mercury intruded volume into the sample, V_V. The latter is determined by measuring the electrical capacitance in the stem of the penetrometer. Once the maximum average pressure of mercury is reached (about 200 MPa), the extrusion of mercury is processed. Thus, data of intruded and extruded volume of mercury versus applied pressure were obtained and the pressures were converted to pore diameter D. Indeed, the pore diameter D was determined by assimilating pores

to cylindrical capillaries [56]. Then, according to Washburn-Laplace equation [222], the diameter was given by Eq.(6.5).

$$D = \frac{-4\gamma cos\theta}{P} \tag{6.5}$$

Where $\gamma(N/m)$ is the surface tension and is equal to 485 dynes/cm (1 dyne= $10^{-5}N$), $\theta(°)$ is the contact angle, which value is 130° and $P(Pa)$ is the applied pressure. The cumulative intrusion volume can, then, be plotted versus the computed pore diameter (see Fig.6.5).

The porosity p is defined as the total volume occupied by pores (total cumulative

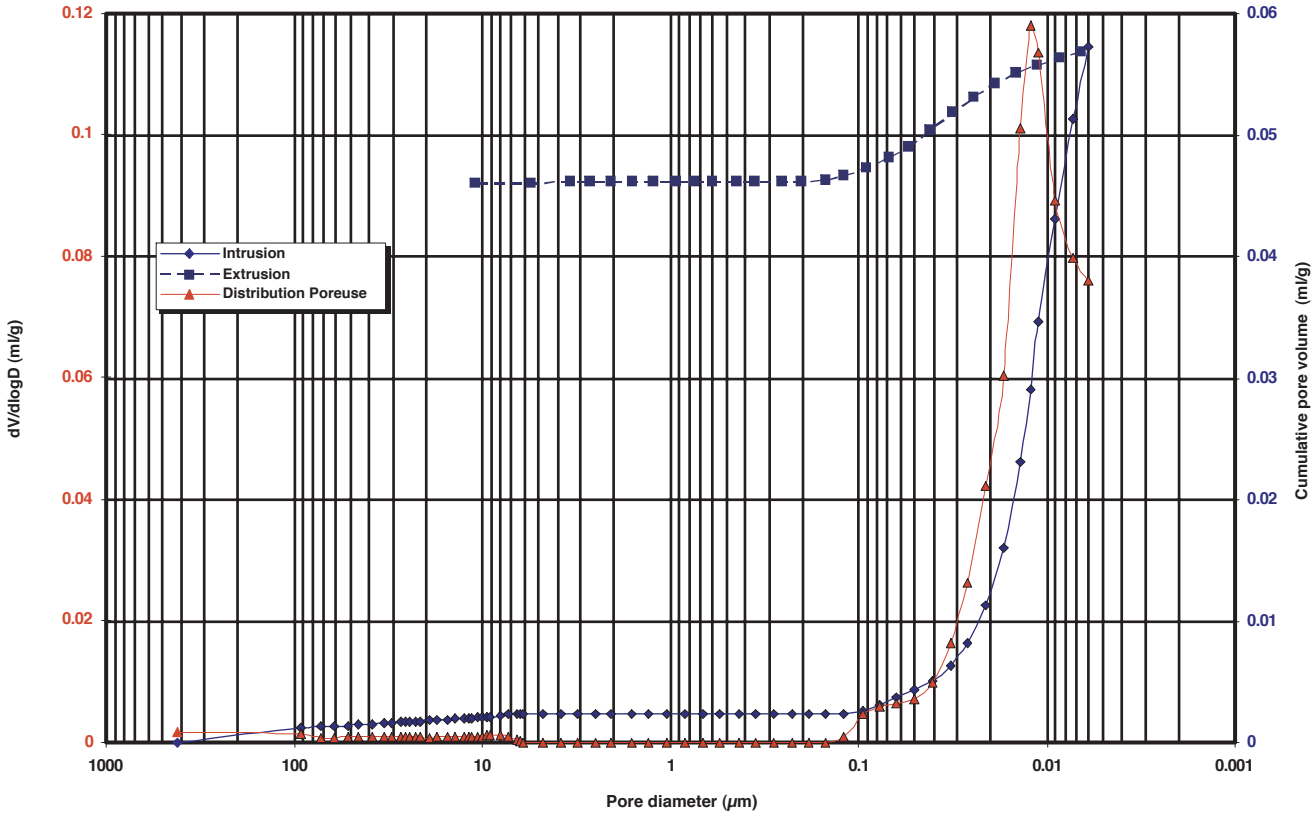

Figure 6.5: Mercury intrusion results obtained on cement paste sample with W/C= 0.3

volume plotted in Fig.6.5) per unit volume of material.The particle (or Skeletal) density, $\rho_{particle}$, is computed after the volume of all pores larger than those measured at maximum intrusion pressure have been excluded from the volume presumed occupied by the material.

The bulk density, ρ_{bulk}, is defined as the unit weight, M_{dry}, per unit volume of the dry material, V_T, after the volume of the largest open pores has been subtracted. In the

present study, the typical value for the largest pore included in the bulk density was approximated to be larger than 430 μm (which corresponds to an intrusion pressure of about 0.1 psi). The bulk density is given by the ratio:

$$\rho_{bulk} = \frac{M_{dry}}{V_T} \tag{6.6}$$

Porosity can also be calculated from bulk density and particle density using:

$$p(\%) = (1 - \frac{\rho_{bulk}}{\rho_{particle}}) * 100 \tag{6.7}$$

Where $\rho_{particle}$ and ρ_{bulk} are the particle and bulk densities, respectively.

6.2.2 MIP measurements

MIP measurements were conducted on both cement paste and air-entrained cement paste samples. The pore size distributions as well as porosity were determined. Figure 6.6(a) shows the pore size distribution obtained by MIP on the cement paste samples for different W/C ratios. Figure 6.6(b) shows the pore size distribution obtained by MIP the air-entrained cement paste samples when varying the air-entrained adjuvant amount. The pore distribution is clearly unimodal for all the cement paste compositions as the shape of the curves is characterized by the single dominant pore radius (critical pore radius). Hence, except for the W/C= 0.3 composition, all the cement paste samples present a dominant pore radius between 0.0625 and 0.0771μm. The cement paste with W/C= 0.3 presented a five time smaller critical radius with 0.0122μm. This may be related to the hydration phenomena that is not completed for cement paste material with W/C under 0.38 according to Powers. Noting such small range of pore diameters determined for the cement paste samples, this kind of porosity (capillary porosity) will also be called by *microporosity* in the following.
Concerning the air-entrained cement paste MIP measurements, Fig.6.6(b) shows a single dominant pore radius for all the composition with a value of 0.077μm which is the same for the control (air-entrained free) sample. This is meaningful, as the amount of air voids created by the air-entrained adjuvant is much small that capillary porosity. In addition, air voids are not connected to each other, and thus will be considered as having small pore radius because of the ink-bottle effect. This remark will be detailed and argued later.
An single different plot is shown on Fig.6.6(b) for the special case of air-entrained cement paste with air-entrained adjuvant amount of 4.5% of the cement mass. In fact, the pore size distribution for this composition is not unimodal and presents considerable percentages of pores with diameter larger than 0.077μm and reaching 100μm. This uncommon distribution may be caused by the difficulty in preparing the air-entrained samples.

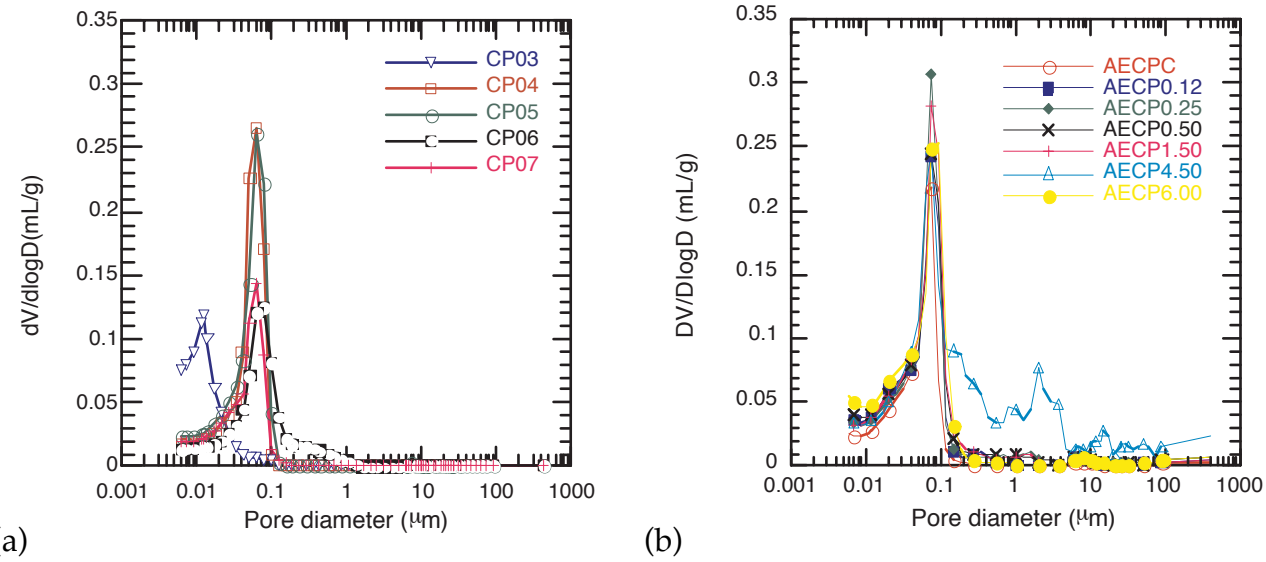

Figure 6.6: Pore size distribution of (a) cement paste with different W/C ratios and (b) air-entrained cement paste with different air-entrained adjuvant amount, according to MIP test

The mercury porosity results on cement-paste and air-entrained cement paste were plotted on Fig. 6.7. On the same figure, porosities obtained through the gravity method were plotted in order to compare both methods.
For the case of cement paste, an increase of pore volume with the W/C ratio was observed. Indeed, MIP indicates a porosity of 12%, 18% and 32% for pastes with W/C 0.3, 0.5 and 0.7, respectively. Such trend was also observed by Cook and Hover [53] on cement paste samples with the same W/C ratios as considered in this study. However, for the mercury porosity determined on the air-entrained cement paste samples, the increase in function of the air-entrained amount was less significant. In fact, the increase of porosity with respect to the control sample was less than 7.5% of porosity for all composition and 17% of porosity for the AECP4.50 sample. The results of mercury porosimetry plotted on Fig.6.7 shows an underestimation of pore volume for both materials. Mercury measured porosity are much lower than those determined by the conventional method (water imbibition). For example, this decrease ranges between 32 to 50% for plain cement paste. This variation is due to several factors. First, the cylindrical pore distribution model which is based on Washburn's theory does not describe precisely the pore structure of cement paste [56]. Second, the size and shape differences between the samples used for the water imbibition method and the MIP can cause a scale effect [128]. Indeed, the first are generally cylindrical samples of a few hundred of grams while the second are usually fragments of a few grams. Third, it should be emphasized that mercury porosimetry is a qualitative method. It cannot be considered to be reliable for porosity quantification as the range of pore accesses

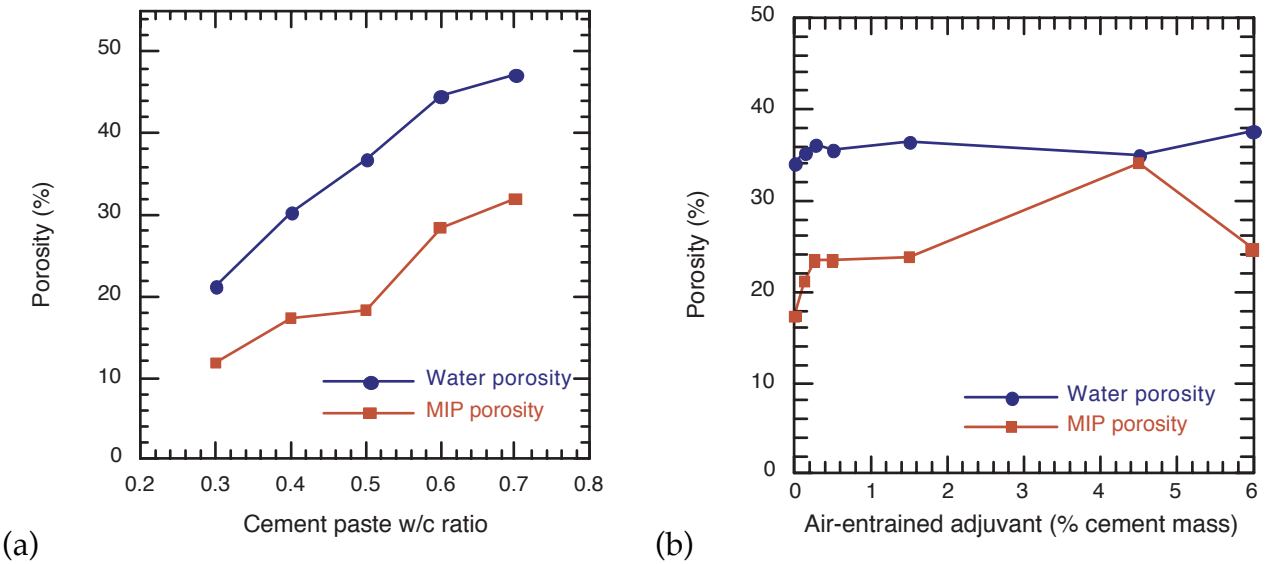

Figure 6.7: Porosity determined by Water imbibition and MIP on cement paste and air-entrained cement paste samples

is limited to approximately 375 mm to around 3 nm (depending on the equipment). Thus, all porosities below and above these values are not considered. Consequently, the mercury porosimetry gives an underestimated value of total porosity for cement-based materials compared with water porosity. It is known that water can access too smaller pores, up to 0.5 *nm* [74].

To conclude, MIP is widely used for porosity determination because it is considered as a fast technique. However, it presents a number of problem when applied to a complex pore structure which is the case of cementitious materials [69]. Indeed, it cannot give an accurate measurement of the pore distribution. This is due to the misinterpretation of the volume of large pores that are accessible by narrow throats and so under hight pressure. This phenomena is called the *ink-bottle* [181]. This leads to an overestimation of the fine pore volume and an underestimation of the large pore volume. Besides, the pore-size distributions is influenced by both the selection of contact angle [195] and the sample size effects [94]. In addition, the method of the sample drying influences theses distributions [54]. Other drawbacks of this technique are the fact that pores are assumed to have pores cylindrical geometry and that it is basically a destructive method.

6.3 X-ray Microtomography

The X-ray microtomography is a non-destructive technique that allows observing the internal structure of a material. In the last decade, significant studies [137, 138, 193, 199] have been made in the development of X-ray microtomography to non-destructive assessment of cracks and damage in cementitious materials. Recently, this technique was investigated in the characterization of pores structure, distribution and quantification.

6.3.1 Image acquisition

X-ray microtomography method is a three-dimensional imaging method that uses multiple radiographic images to reconstruct a 3-D representation of the material. Indeed, the considered specimens were cylindrical and were rotating around their axis. The X-rays illuminate the specimen in a perpendicular orientation. Thus, multiple radiographic discrete images were obtained at different angles. The number of these images depends on both the equipment and the chosen resolution. Figure 6.8 shows an example of tomographic image of an air-entrained cement paste sample and its 3-D reconstruction. On the figure, there are voids created by the air entrained adjuvant are clearly visible. The voids appear to be perfect spheres, randomly distributed in the matrix and having different size. In this study, the X-ray microtomography experiments have been carried out at the LAMIH (Laboratoire d'Automatique, de Mecanique et informativeness industrielles et Humaines de valenciennes). There a Skyscan1172 X-Ray microtomograph, having a resolution of $7\mu m$, was used to investigate the microstructure of air-entrained cylindrical samples with a $14mm$ of diameter and $50mm$ of high.
For each sample about 500 transverse image were taken within $1cm$ of thickness.

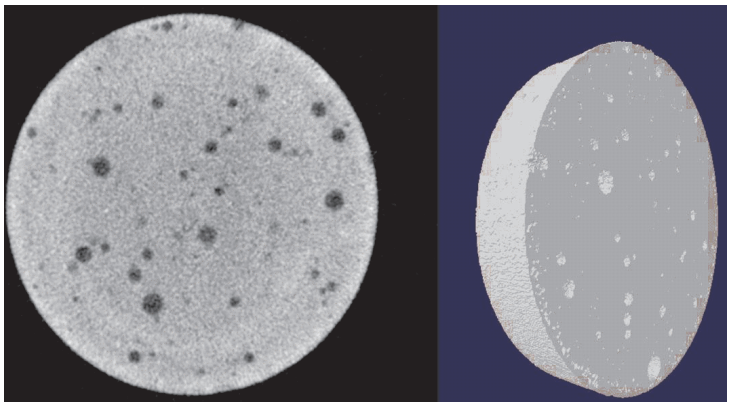

Figure 6.8: Tomographic images of air-entrained cement paste sample. Left- A tomographic cross section. Right- A 3D-reconstruction.

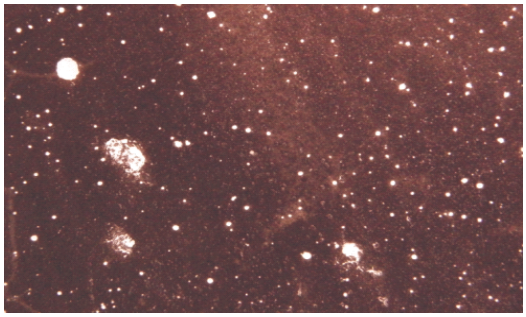

(a)

(b)

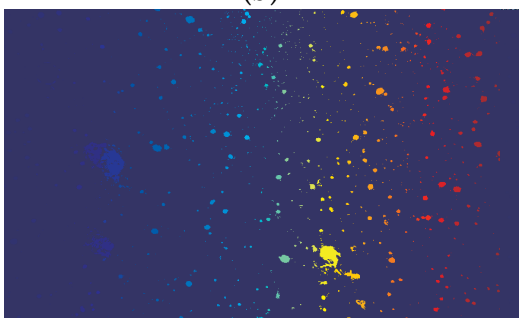

(c)

Figure 6.9: Image processing steps on an air-entrained cement paste cross section

Analysis of the obtained images aim to the determination of the volume fraction as well as the distribution of the air entrained pores.

6.3.2 Image processing

The images obtained from the tomographic scan and the digital camera, were grayscale surfaces (Fig.6.9(a)) where each pixel's intensity corresponds to the material density. In order to obtain an accurate quantification of the macroporosity, the analysis was carried on many images, taken from the clearest and the most representative image section, for statistical confidence.

The different steps that were developed on computational software for the image processing are presented on the diagram of Fig.6.10. First, the grayscale images are binarized, based on choice of a color threshold, to end up with a black and white

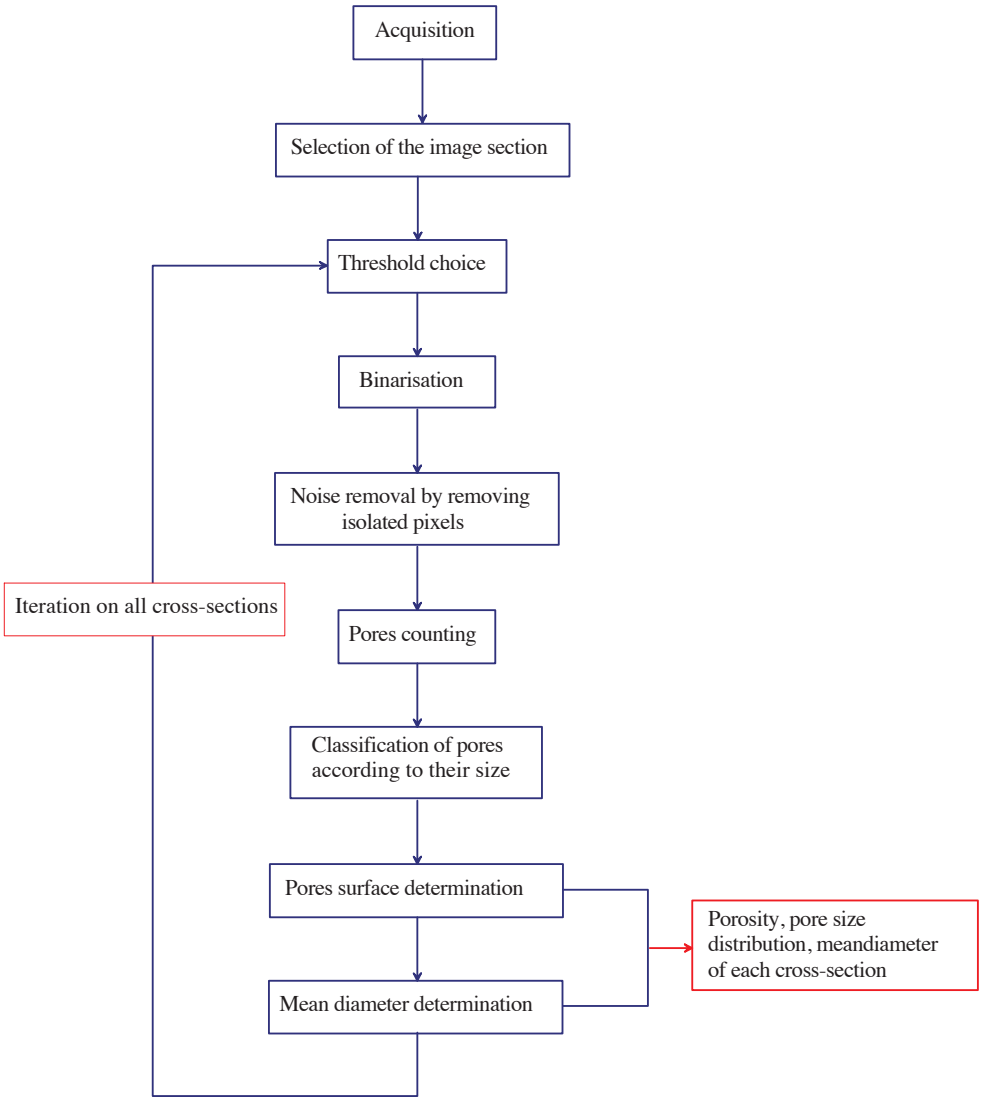

Figure 6.10: Diagram of the image processing steps used on X-ray microtomography obtained images

image as illustrated in Fig.6.9(b). On these images, the black continuous zone refers to the matrix (the cement paste with micropores), while the white zones represent the macropores created by the air-entrained adjuvant. It should be noted that the choice of the pore threshold is crucial for the image binarisation. The grayscale threshold choice was left to the operator judgment. More pursued studies have focused on performing the threshold choice. Wong et al. [227] determined the threshold from the inflection point of the cumulative brightness histogram of the analyzed image. Then, the obtained black-white images were subjected to a second image-processing program in order to distinguish the different pore size categories. This was achieved by attributing to each pore size category a different color as show on Fig.6.9(c). Thus the pore size distribution, the number and the mean-diameter of pores were obtained for each sample cross-section. The macroporosity was determined when considering the ratio between the sum of the macropores-areas A_{MP} and the total area A_T using Eq.(6.8):

$$A = \frac{A_{MP}}{A_T} \tag{6.8}$$

Validation of the image processing method

In order to validate the previously presented image processing method, a benchmark sample was specially made. The latter is a black Bakelite surface on which holes with different well-known diameters were created (Fig.6.11). The holes are distributed

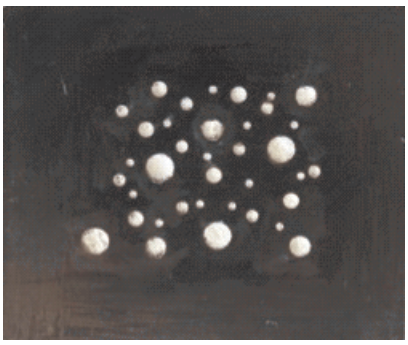

Figure 6.11: benchmark sample for image processing validation

as indicated in Table 6.2.

The total surface of the benchmark was found to be equal to $4556.81 mm^2$. Accordingly

Table 6.2: Pore size distribution of the benchmark

Hole diameter (mm)	7	5	4	3	2	Total
Number of holes	4	4	6	9	14	37
Hole surface (mm^2)	153.93	78.53	75.39	63.61	43.98	415.47

the benchmark porosity is:

$$p = \frac{415.47}{4556.81} \times 100 = 9.11\% \tag{6.9}$$

On the other hand, the image processing method was applied to the benchmark high resolution photograph. Figure 6.12 shows the obtained hole distribution on the benchmark. It is noted that all the created holes were detected. However, for a given the determined diameter is often not of exact dimension of the created one. Aiming to com-

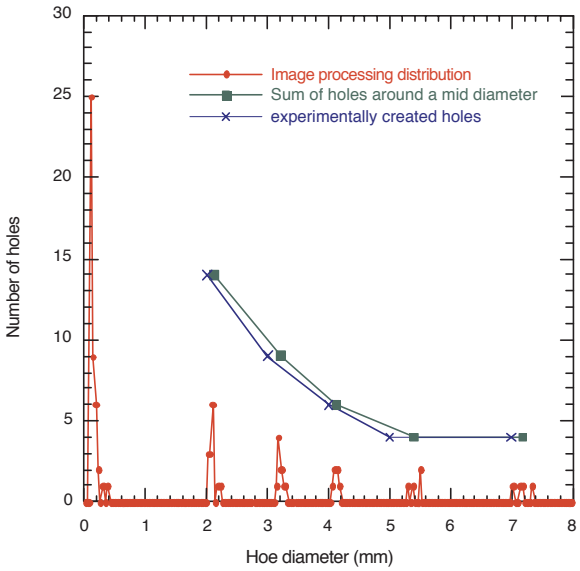

Figure 6.12: Benchmark hole size distribution

pare the obtained result with those created experimentally, the computed holes with close diameter were summed and plotted with respect to a mid-diameter. First, note that the obtained hole distribution presented in Fig.6.12 is coherent with the data given in Table 6.2. Secondly, the image processing program detected more than forty holes with a diameter around $0.120mm$ that were not created on the benchmark. The small diameter of these thought holes; argue the assumption that they correspond to noise. Finally, it was remarked that the computed diameter of holes, and consequently the determined porosity (p= 9.99%), is higher than the created ones. This over-estimation is caused basically by the perforation quality that produces holes slightly larger than the used driller.

6.3.3 Air entrained voids determination

The image processing technique, which investigated on the pore structure of the cement paste, concerns especially with the macropores created by the air-entrained adjuvant.

It was supposed that the saturation state has no effect on the size and distribution of the macropores. For each composition, the pore size distribution curve was determined. Indeed, for each pore size, the number of pores per cm^2 was computed and the mean diameter was determined using the previously detailed image processing numerical program.
Figure 6.13 shows the variation of macroporosity according to increasing amount of air-entrained in the cement paste. The macroporosity is generally increasing with the entrained air content except for two compositions. This is caused, basically, by the mixing and placement methods of the cement paste with the entrained air. This trend was also observed by Powers, for different W/C ratios [176]. Actually, the setting of the air-entrained adjuvant is considerably complicated and can result on such non-expected porosity. Figure 6.13 shows that the increase in terms of macro-pores is important when adding small amounts of air-entrained admixture (less that 2%). For air-entrained add over 2% of the cement mass, the macroporosity increase is generally less significant. Beyond 5% of air-entrained, there was no further increase in the volume of air voids, which reached a threshold of 23%.
Figure 6.14(a) shows the macropores distribution for the different studied air-entrained

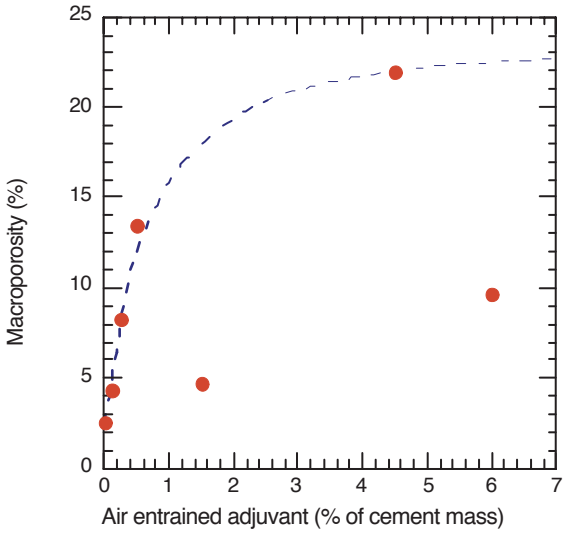

Figure 6.13: Macroscopic pores volume fraction vs. entrained air content

cement paste samples based on image processing technique. It was noted that the pores size ranged from $20\mu m$ to $1000\mu m$. It can be remarked that the different compositions present almost the same trend with respect to the pore diameter. Aiming to investigate the influence of the air-entrained adjuvant on the porous structure of the cement paste, a mean diameter for the macropores was determined based on the obtained distribution of all the compositions. Figure 6.14(b) shows the evolution of macropores mean diameter with respect to the macroposity. Accordingly, the majority of macropores

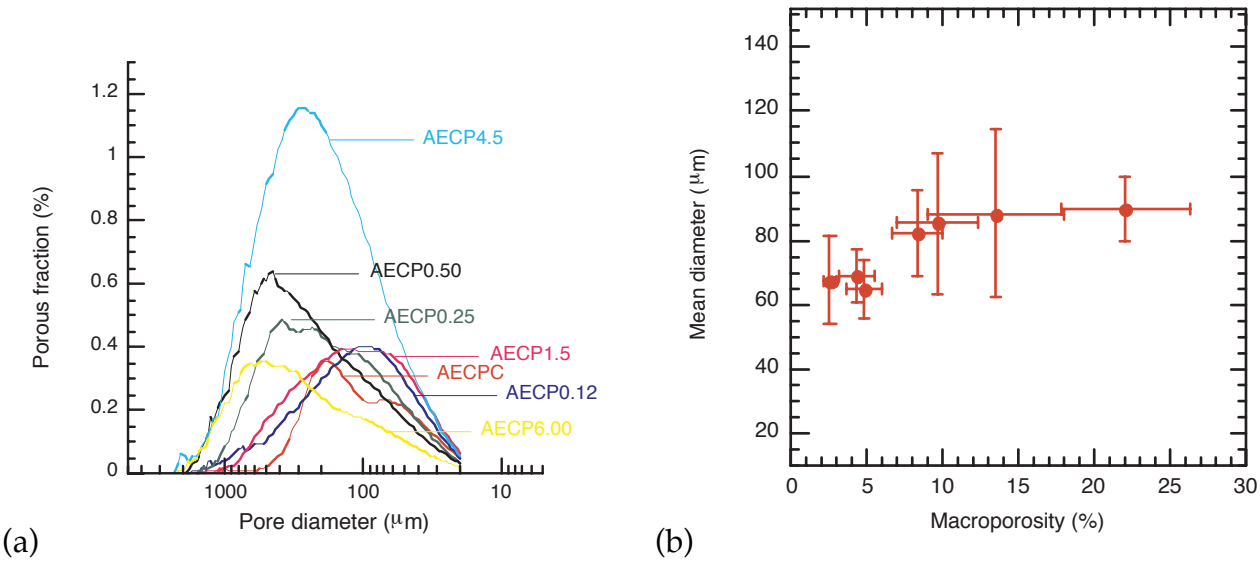

Figure 6.14: Macroporosity distribution (a) and mean diameter (b) of the different air-entrained contents

present in the samples have a diameter between $20\mu m$ and $100\mu m$. A slight increase in the pore mean diameter was observed when increasing the amount of air-entrained adjuvant. As an example the pore mean diameter increased by 22 μm when macroporosity increases from 2.52% to 22%. This states that the air-entrained adjuvant creates macropores with comparable diameter regardless of the used amount.

Figure 6.15 shows the variation of macro, micro and total porosity according to increasing amount of air-entrained in the cement paste. The volumetric fraction of macropores in the cement paste was obtained using image processing techniques. The microporosity was determined based on water porosity. The total porosity was assumed to be equal to the sum of the micro and macro porosities. It is noted that the macroporosity is generally increasing with the entrained air content except for two compositions. However, the microporosity is almost constant with an average value of 31.93%. This was expected, as the W/C ratio was kept constant for all samples. Thus, the air-entrained admixture didn't affect the microporous connected structure (especially, the volume fraction of micropores) of the cement paste. Consequently, the total porosity follows the macroposity trend. It increases with the air-entrained increasing amount.

6.4 Scanning Electron Microscope (SEM)

In this section, the microstructure of the prepared cement paste samples were investigated using Scanning Electron Microscopy (SEM) including the Backscattered Scanning Electron (BSE) imaging and the Xray microanalysis. The measurements were carried

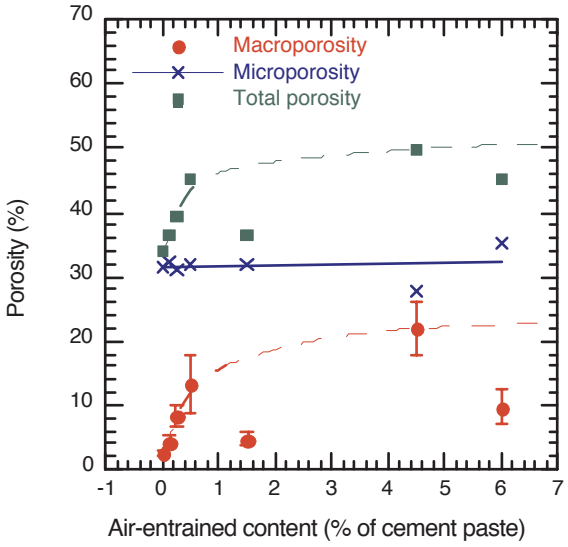

Figure 6.15: Micro-, macro-, and total porosity relative to the air-entrained content.

on at the Ecole Centrale de Lille. In order to take advantage from these measurements, the cement paste sample has to be well prepared, especially; a flat observation surface is required. Thus, various steps of sample preparation were performed. After cutting and grinding the considered samples were impregnated with epoxy. Then, their surfaces were polished. Polishing is a common operation for observations on cementitious material. This operation removes the imperfections of the sample surface caused by damage created by the sawing and grinding operations. A $3\mu m$ diamond suspension on a lap wheel covered with a polishing cloth, was used at this stage for both microscope and SEM observations. The details on such procedure are resumed in [200] and [122]. In order to observe samples with the SEM test, they were coated with gold in order to provide a conductive surface and to prevent charging.
A single composition of dry cement paste with W/C= 0.3 will be presented here after.

6.4.1 Principle of SEM and sample preparation

The observations were achieved using a Scanning Electron Microscope (SEM) equipped with two detectors. The first detects the Secondary Electrons (SE) and gives image where the topological contrasts of the scanned surface are emphasized. The resulting image appears as having a three-dimension aspect with edges brighter than flat surfaces. The second detector is designed for the backscattered electrons (BSE) to allow differentiating the particle chemical compositions based on their atomic number. Indeed, as the particle atomic number is higher as it is brighter. Note that the sample in the SEM is under low vacuum condition to improve the observation quality.
A special preparation is necessary for cementitious specimen scanning electron mi-

(a) (b)

Figure 6.16: Cement paste sample (a) cast into epoxy and (b) coated with gold.

croscope observations. In fact, if the material surface is not properly prepared, then severe artifacts can result and the microstructure will be misinterpreted [201]. Thus, the preparation of flat-polished cement paste surface was a hard task. Various operation modes were applied to cement paste samples with different procedures and equipments aiming to obtain a satisfactory flat surface.

6.4.2 SEM image observations on cement paste

The images were obtained on the cement paste sample using both the SE and the BSE detectors. Low acceleration voltages were chosen $\langle 15kV$. The contrast, brightness, magnification and focus depth were adjusted to give the best images of the observed surface. Different phases were observed on a dry cement phase sample of W/C= 0.4. On Fig.6.17 one can distinguish in particular:

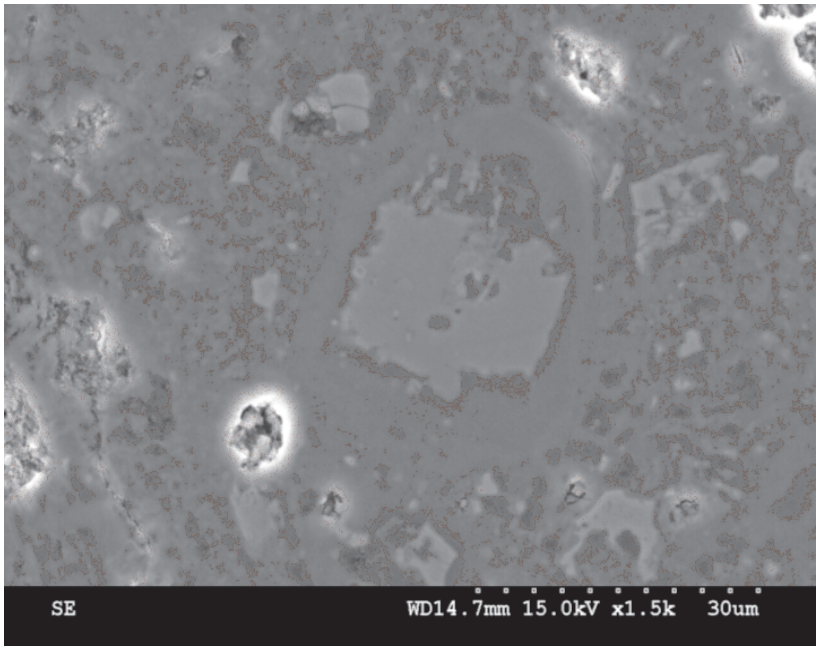

Figure 6.17: Cement paste sample with 0.4 W/C observed with SEM

- white areas: represent the anhydrous grains;
- gray areas around white ones: High density hydrates;
- gray and black mixed areas: Low density hydrates, which seem to be more porous than high density hydrates (black areas being pores);
- light gray areas: Portlandite crystals;

- black areas: pores

In this section, different techniques were introduced and applied to the cement paste with and without air-entrained adjuvant. Water imbibition method was applied to both cement paste and air-entrained cement paste to measure their capillary porosity and density. The air-entrained cement paste capillary porosity was found to be independent from the air-entrained amount. Mercury intrusion porosimetry was used to determine the pore volume and pore size distribution. The MIP underestimated the capillary porosity. X-ray microtomography was utilized to determine the macropores fraction, size and distribution in the air-entrained cement paste material and scanning electron microscopy was employed to examine the different phases of a hydrating cement paste.

Chapter 7

Static mechanical measurements on cement paste

The Young modulus, the Poisson ratio and the compressive strength are the principal three characteristics of structural materials. Their determination can be achieved in the static or dynamic regime. In this study we are basically interested in the wave propagation in cementitious material to determine the elastic properties of the cementitious material. However, it would be interested to compare the dynamic values to the static experiments conducted for the determination of the material elastic properties, basically, the compression test.
Thus, in this section, the experiments as well as the preliminary results of a static compression tests carried on the studied materials are presented.

7.1 Materials and equipment for the compression test

The compression test is performed in order to determine the behavior of materials under crushing loads. The specimen is compressed and deformation at various loads is recorded. The, stress and strain are measured and plotted as a stress-strain diagram which is used to determine the elastic moduli and the compressive strength.
In order to perform this test, cylindrical samples for each of the studied cement paste and air-entrained materials where considered. To each specimen, four strain gages where affixed: two in one side of the lateral cylinder surface and the two other diametrically opposed to them. In each side, one gage is affixed in lateral direction, the other in longitudinal direction (Fig.7.1) . The compression testing machine used in the tests is with a capacity of 20 kN on which a digital strength sensor was fitted. This sensor can measure the stress and deduce the compression strength.

7.2 Static Elastic moduli

The elastic moduli that are commonly measured on a material are the Young modulus and the Poisson ratio using a compression test as will be detailed in the following.
The value of the Young modulus is a material property useful for calculating the compliance of a structural material that follows Hooke's law when subjected to uniaxial loading. The Young modulus is defined as the velocity of strain with respect to the

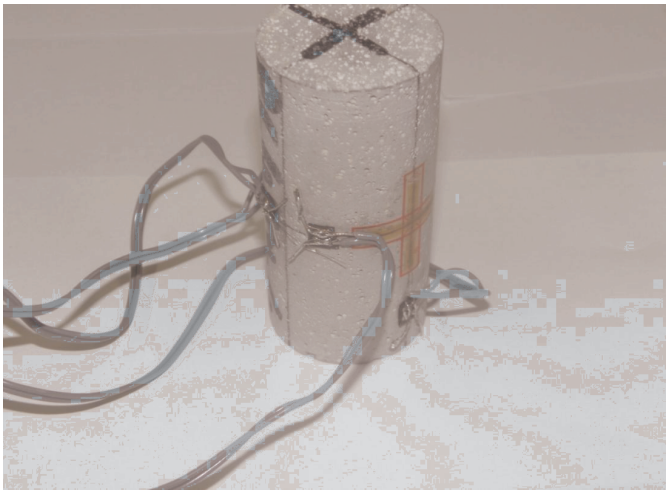

Figure 7.1: Affixed (L) longitudinal and (T) transverse strain gauges on a cylindrical sample

applied stress. This corresponds to the straight portion of a stress-strain curve. Commonly, two Young moduli are defined: the tangent and the secant moduli. The tangent Young modulus is the slope of the compression stress-strain curve at any specified stress or strain. The secant Young modulus is equal to the ratio of the stress with respect to the strain in any point. These two modulus are equal in the linear behavior limit of the material.
In this study, only the linear part of the stress-strain experimental curve was considered in the determination of the static Young modulus. Thus, the tangent and secant Young modulus will not be differentiated [211].
The Poisson ratio is the ratio of transverse strain to longitudinal strain. The transverse, respectively longitudinal, strain is perpendicular, respectively parallel, to the direction of the load. The theoretical Poisson's ratio of a stable, isotropic and linear elastic material is between -1 and 0.5 due to the requirement that the elastic modulus, the shear modulus and bulk modulus have positive values [78].

The compression test was performed on three W/C compositions of the cement paste : 0.3, 0.4 and 0.5. For each composition four saturation states were investigated: dry, 30%, 70% and fully saturated. Table 7.1 gives the measured Young modulus and Poisson ratio of the cement paste tested specimens.

The variation of the obtained static moduli in function of the W/C ratio and the saturation degree was plotted in Fig.7.2-7.3. As seen on Fig.7.2(a), an increase of W/C ratio produces a decrease of the Young modulus for the different saturation states. Indeed, the W/C ratio increment produces changes in the material microstructure, in particular, it increases the porosity. This justifies the decrease observed in the Young modulus. Figure 7.2(b) shows the variation of the cement paste static modulus

Table 7.1: Static Young modulus and Poisson ratio of cement paste at different saturation states

		CP03	CP04	CP05
Dry	$E(MPa)$	29718	20802	13257
	ν	0.21	0.21	0.22
Sr=30%	$E(MPa)$	20951	15013	9187
	ν	0.20	0.25	0.22
Sr=70%	$E(MPa)$	21438	16840	11267
	ν	0.28	0.38	0.33
Saturated	$E(MPa)$	29177	18302	14826
	ν	0.25	0.26	0.28

when varying the saturation degree. It is noted that Young's modulus decreases when saturating the material until 30% of saturation then increases to the fully saturation state. Actually, water in saturated and partially saturated pores limits the deformation and enlarges the stiffness of cement paste. The static Poisson ratio behavior is almost constant when varying the W/C ratio for the dry and saturated states. As a function of saturation state, the Poisson ratio presents generally an increase. In fact, the water present in pores limits the cement paste deforming into pores causing such increase. Ito et al. [112] found that in sandstone the Poisson's ratio undergoes a marked increase upon the transition from the steam saturated to water-saturated state.
A comprehensive presentation and interpretation of the previously introduced static measurements are detailed within the work of Soltani [198].

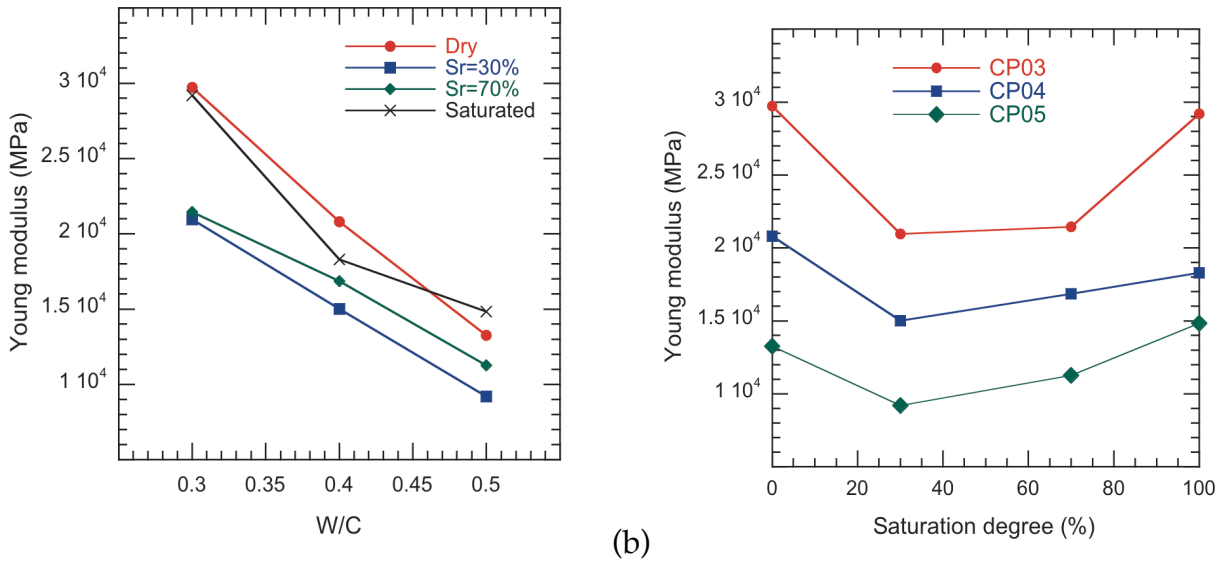

Figure 7.2: Variation of the static Young modulus of the cement paste with (a) the W/C ratio and (b) the saturation degree

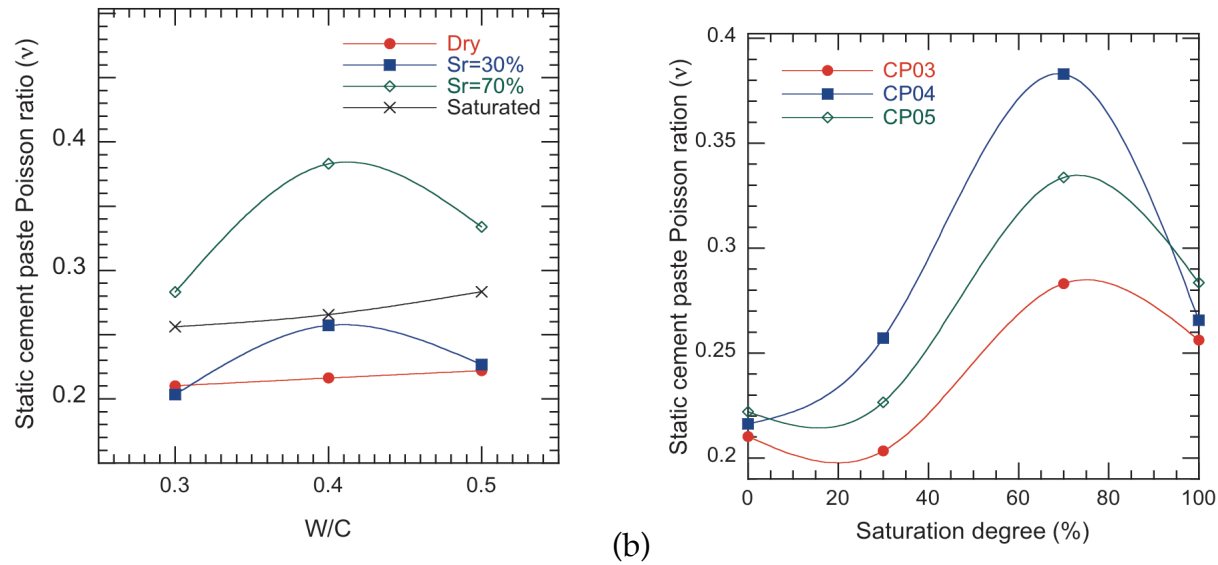

Figure 7.3: Variation of the static Poisson modulus of the cement paste with (a) the W/C ratio and (b) the saturation degree

Chapter 8

Ultrasonic Pulse Velocity Measurements on Cement-based Materials

The non-destructive methods used for cementitious materials evaluation consist generally of techniques that indicate indirectly the materials properties. Ultrasound is one of the non-destructive on-site tests methods that have been developed recently. This technique presents numerous advantages. Indeed, it is ease to implement, it offers the possibility of material investigation on a single side i.e. there is no need to access the opposite structure side and it can control different material depth depending on the selected frequency. In addition, the ultrasonic technique is suitable for material characterization thanks to relationships that relate the ultrasonic propagating wave to the material properties.
The ultrasonic wave corresponds to frequencies above 20 kHz [45] to a range around 1 GHz. Above the latter, the regime is called hypersonic. Figure 8.1 shows the typical ranges of frequency for the most interesting fields of waves application. The Surface acoustic waves (SAW) are high-frequency versions of the surface waves discovered by Lord Rayleigh in seismology.
The first experimental application on sound velocities goes back to 1827, when Col-

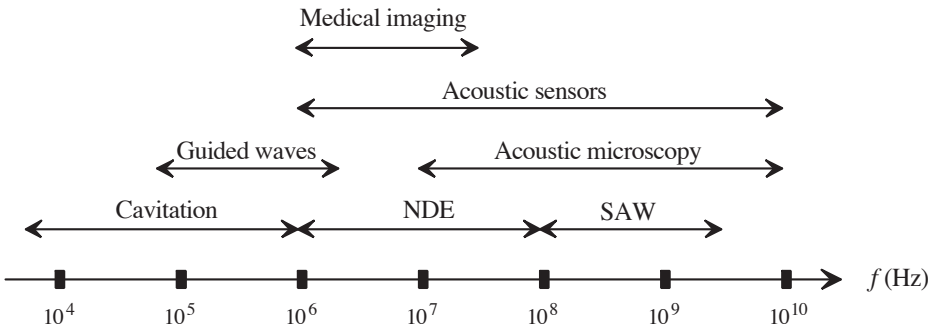

Figure 8.1: Frequency ranges for various ultrasonic applications

ladom and Sturm found the ultrasonic velocity of the water in Lake Geneva [175]. Later, in the last century, sound velocity was adopted as a standard method for determining the adiabatic compressibility of materials as well as the ratio of specific heats

[236]. Nowadays, the ultrasonic velocity measurements are implemented in various industrial precesses [45, 177] such as in level and concentration devices, or also for flow measurement in fluids [194]. In the medical field [180], ultrasound techniques are implemented in many medical apparatuses [174], for instance in the blood flow [72]. In biology studies, the ultrasonic evaluation are investigated for measuring the internal changes during fruit ripening [154].
Since the mid 1940's, ultrasound have been carried for nondestructive Evaluation (NDE) and Testing (NDT) of cement based-materials but they have achieved a limited success. Recently, some experimental studies [173, 136] have been carried out in order to understand the propagation of ultrasonic waves in cement-based materials. Such studies focused understanding the effect of the microstructure on the mechanical properties and developing a non-destructive technique for in situ assessment of material degradation.

8.1 Principle of ultrasonic pulse velocity techniques

The commonly measured ultrasonic parameters are the pulse velocity. Ultrasonic attenuation (UA) is less frequently used for cementitious material characterization. It is difficult to measure due to scattering phenomena created by the material heterogeneity [82, 134, 207]. The pulse velocities used for materials control and characterization can be classified under two general groups: body (or bulk) waves and surface (or guided) waves. The first propagate through the material's body, while the second propagate on the surface. The body waves are of two types: longitudinal and shear waves. It is known that the longitudinal wave propagates at a faster speed than the shear wave. Thus, longitudinal waves are also called primary waves or P-waves and the shear waves are called secondary waves or S-waves.
In the case of longitudinal wave, the material particles vibrate in a parallel direction to the wave propagation. While, for transverse wave, the particles vibrate at a perpendicularly to the wave propagation.
In this section, the propagation of elastic wave in homogeneous elastic material, governed by Christoffel equation, is presented. Then, the solution for the case of isotropic material is detailed.

8.1.1 Christoffel equation

The fundamental dynamic principal for a linear elastic medium subjected to ultrasonic wave propagation leads to:

$$\rho \frac{\partial u_i}{\partial t^2} = \frac{\partial \sigma_{ij}}{\partial x_j} \tag{8.1}$$

where $\boldsymbol{\sigma}$ is the strain tensor, ρ is the material density and $\boldsymbol{u}$ is the displacement.
The solution of Eq.(8.1) is a plane wave, with an angular frequency ω and is written as:

$$\mathbf{u}(\mathbf{r}, t) = A\mathbf{P}e^{j(\omega t - \mathbf{kr})} \tag{8.2}$$

where A is the initial wave amplitude, $\mathbf{P}$ is the polarization unit vector [109] and $\mathbf{k}$ is the wave vector; $\mathbf{k} = \frac{\omega}{V}\mathbf{n}$ where $\mathbf{n}$ is a unit vector normal to the wave and V is the phase velocity.
The attenuation can be considered in the imaginary part of the wave vector such that:

$$\mathbf{k}^* = \left(\frac{\omega}{V} - j\alpha_a\right)\mathbf{n} \tag{8.3}$$

α_a is the attenuation coefficient ($\alpha_a > 0$).
Substituting Eq.(8.2) into Eq.(8.1) gives the Christoffel equation [9]:

$$\Gamma_{il}u_l - \rho V^2 u_i = 0 \tag{8.4}$$

where $\Gamma_{il} = C_{ijkl}n_j n_k$ is the Christoffel matrix. It is a second-order symmetric tensor as the elastic tensor C is symmetric (expressed in Appendix B).

8.1.2 Christoffel equation resolution

Eq.(8.4) can be identified to an "eigenequation", with eigenvalues $(\rho V^2)_m$ and eigenvectors u_m, $m = 1, 2, 3$. These later can be determined by solving the dispersion relation:

$$det(\boldsymbol{\Gamma} - \rho V^2 \mathbf{I}_3) = 0 \tag{8.5}$$

The three solutions obtained from the previous equation when considering $m = 1, 2, 3$ correspond to the three body waves propagating in an unbounded homogeneous medium [40] : the longitudinal, the horizontally transverse and the vertically transverse wave.
In the case of isotropic medium, the wave solutions are the same for the all directions of propagation and an explicit form of the Christoffel matrix can be given:

$$\boldsymbol{\Gamma} = \begin{bmatrix} c_{11} & 0 & 0 \\ 0 & c_{44} & 0 \\ 0 & 0 & c_{44} \end{bmatrix} \tag{8.6}$$

Thus, resolution of Eq.(8.5) gives one longitudinal and one transverse velocity:

$$V_L = \sqrt{\frac{c_{11}}{\rho}} = \sqrt{\frac{\lambda + 2\mu}{\rho}} = \sqrt{\frac{K + \frac{4}{3}G}{\rho}} \tag{8.7}$$

$$V_T = \sqrt{\frac{c_{44}}{\rho}} = \sqrt{\frac{\mu}{\rho}} = \sqrt{\frac{G}{\rho}} \tag{8.8}$$

where λ and μ are the Lamé constants, K and $G = \mu$ are the bulk and shear moduli of the considered medium.
The previous equations (Eqs.8.7-8.8) express the relation between the velocities of waves (compressive wave V_L and shear wave V_T) and the dynamic modulus of elasticity (K and G).
In the special case of anisotropic material, the phase and the group velocities have to be distinguished. These two velocities don't coincide as the material anisotropy deviates part of the incident energy. The phase velocity corresponds to the wavefront velocity and its vector is perpendicular to the wavefront. However, the group velocity corresponds to the energy propagation velocity in the energy flow direction. The previously defined velocities are related by:

$$V_{phase} = V_{group} cos\alpha \tag{8.9}$$

where α is the angle between the two velocities vectors. It should be noted that the group velocity is the one measured by observations of arrival times. Thus in the following the term ultrasonic velocity will refer to the group ultrasonic velocity.

8.2 Ultrasonic experimental measurements

8.2.1 Ultrasonic set-up

Broadband ultrasound spectroscopy [63] was used to obtain ultrasonic parameters of the materials (longitudinal V_L and transverse V_T velocities). Here, this technique is applied in pulsed mode, using a specially designed conventional through-transmission set up (Fig.8.2) with a pair of compression (Panametrics V191) and shear (Panametrics V151) wave contact transducers. Both the emitter and the receiver use the piezoelectric principle. Indeed, most of the piezoelectric materials contain polarized ferroelectric ceramics that are commonly made of lead, zirconium and titanium. Characteristics of the used pair of compression (Panametrics V191) and shear wave contact transducers are given in Table 8.1. A scheme of the ultrasonic measurement set up is shown on Fig.8.3. A pulser is placed upstream the transmitter and generates a high energy. The receiver is mounted on the other side of the sample (through-transmission mode). The region between the transducers and the sample is filled with a coupling agent. It is either a silicone gel (Sofranel D couplant) for longitudinal waves or a highly viscous liquid (Sofranel SWC couplant) for transverse waves. A digital oscilloscope is used to digitize the amplified signal. Its vertical axis represents voltage and the horizontal axis represents time. The received analog signal is converted into a digital signal that is then read by the acquisition system of the computer. The initially emitted ultrasonic pulse is wideband, with a central frequency of 500 kHz. To such frequency corresponds

a wavelength λ that is much greater than pores diameter D ($\lambda \times 10^3 D$) [8]. Thus, the effect of dispersion in the cement paste was neglected and the measured data were the phase velocity.
Details of the ultrasonic propagation measurements can be found in many articles, see for example [63], [155] and [185].

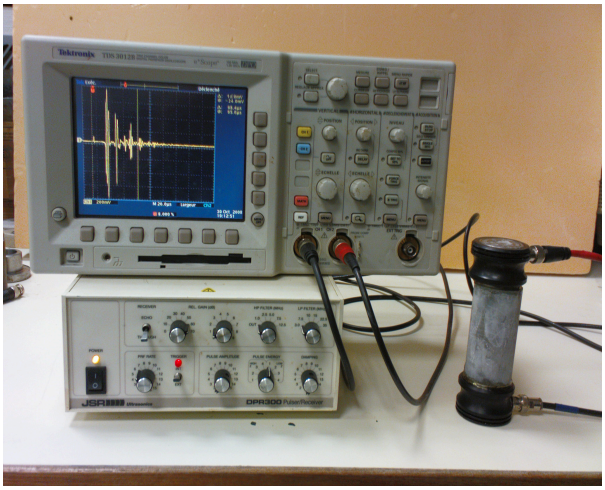

Figure 8.2: Photo of the ultrasonic measurement set up

Table 8.1: Specifications of ultrasonic transducers

Wave type	Transducer type	Nominal peak	Diameter	Coupling
Longitudinal	Panametrics V191	500 kHz	28.5 mm	Panametrics gel D
Transversal	Panametrics V151 (T&R)	500 kHz	28.5 mm	Panametrics viscous gel SWC

8.2.2 Signal processing

The signal processing technique is based on analyzing the signal on the frequency domain. An appropriate window is applied to a desired portion of the displayed signal. It

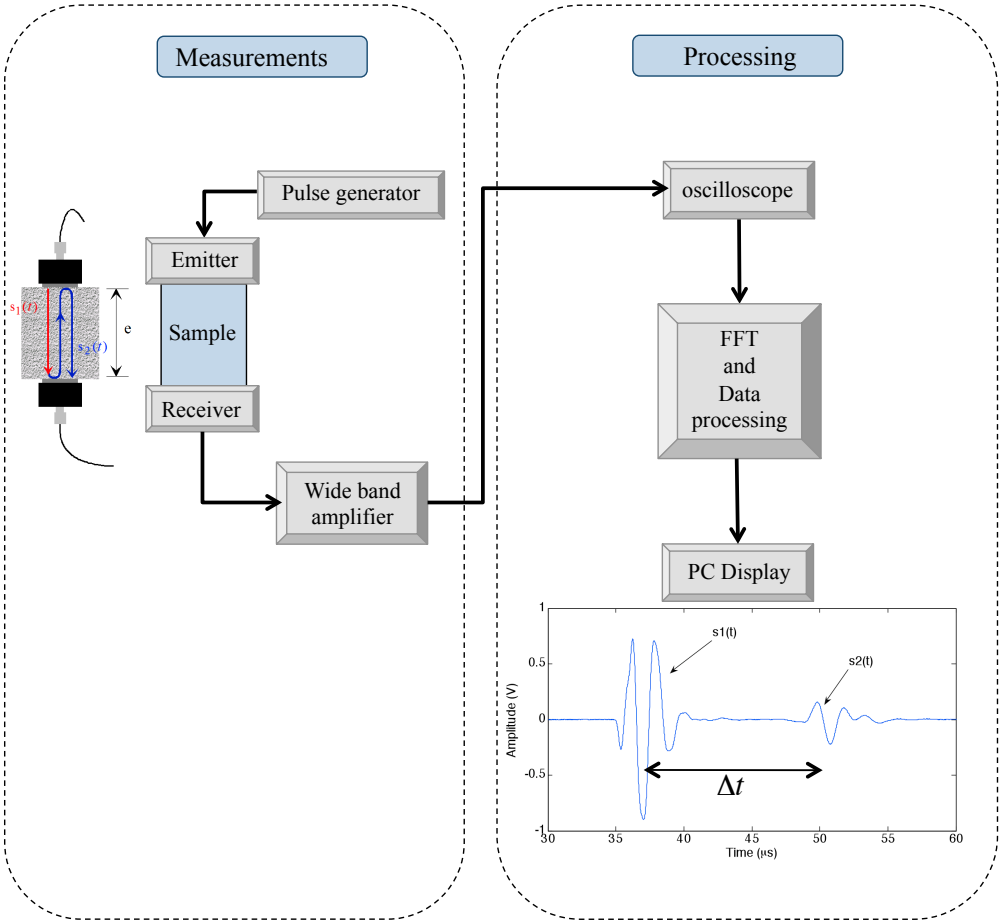

Figure 8.3: Scheme of the ultrasonic measurement system

should be noted that the digital sampling theory requires that a signal must be sampled at a minimum rate of twice of its highest frequency [167].

The pulse velocity is obtained from the cross-correlation function between the first and the second transmitted signals ($s_1(t)$, $s_2(t)$) as:

$$V_{L,T} = \frac{2e}{\Delta t} \tag{8.10}$$

where e is the thickness of the sample and Δt is the time delay between signals $s_1(t)$ and $s_2(t)$ (Fig. 8.3). Signal $s_1(t)$ corresponds to the first received signal; signal $s_2(t)$ to the second one. The time references for estimating Δt were the positive-slope zero-crossings for both signals $s_1(t)$ and $s_2(t)$ (for more details see [133]).

Conclusion

This part included a special attention to various experimental techniques that were necessary to the micromechanical modeling of the studied materials. They were also essential to validate the proposed correlation between the hydraulic and the ultrasonic properties of the considered materials.
In this part, different experimental techniques and procedures were presented and detailed. The preliminary results obtained on each conducted measurements were included and commented. The studied material was cement paste with and without air-entrained adjuvant.
The internal cement paste microstructre was investigated. Indeed, porosity was obtained by different experimental methods depending on the material porous structure and studied material. First, the porosity based on the gravity method, using vacuum saturation, was determined on both cement paste and air-entrained cement paste. Such porosity was called capillary porosity and was denoted as *micro*-porosity. Second, the Mercury Intrusion Porosimetry was carried out on both materials in order to be compared to the other porosity determination methods but in particular to construct an idea on the pore size distribution of the material. Finally, the image processing techniques were used for the estimation of the air voids volume fraction and distribution created in the material by adding air-entrained cement paste. These voids were referred to as a *macro*-porosity as they present a larger size than the capillary porosity.
The Scanning Electron Microscopy was also used within this experimental part in order to construct a comprehensive understanding of the microstructure of the cement paste material. It was observed that the hydrated cement paste present different solid phases with a porous structure. Unfortunately, no quantitative study was realized on these observations.
The water content variation in the porous volume was considered. Four degree of saturation were studied: 0% (or dry), 30%, 70% and 100% (or fully saturated). The variation of the saturation degree was achieved by adjusting the drying time of the fully saturated material.
Ultrasonic longitudinal and transverse velocities were measured using a couple of transducers with large band width and a central frequency of 500 kHz. The experimental obtained results show a decrease of velocity when the porosity increases and an increase of velocity when saturation degree increases.
Thus, this part is in the basis of the following considerations and assumptions for the micromechanical modeling of the cement paste material. Indeed, in the following part, micromechanical modeling will be applied to the studied materials in order to understand these different trends and to explain them through mechanical development. Later, on the one hand the experimental correlation between the ultrasonic velocities and the porosity will be presented. On the other hand, a micromechanical correlation between the same properties will be proposed and validated by the experimental

founds.

Part III

Application of micromechanical modeling to the cement paste material

9 Identification of the cement-based materials matrix properties 113

10 Cement paste modeling 123

11 Air-entrained cement paste modeling 141

Introduction

A cementitious material (cement paste, mortar or concrete) is a heterogeneous material. Thus it can be considered as a composite material. This part deals with the application of the homogenization methods descried in the first part to cementitious materials. The aim of such application is the prediction of the overall properties of a cementitious material when knowing the characteristics of each of its constituents. A particular attention is paid to the modeling and simulation of cement paste and air-entrained cement paste.
Few researchers have investigated on the modelling of the behavior of a cement-based material. In the field of micromechanics, the modeling of mortar was investigated mainly by Hernández et al. [99]. The authors considered that the mortar is a material composed of a matrix of cement paste, fine aggregates (sand) and pores. Li et al. [140] improved the Christensen and Los [46] three-phase sphere model for two-phase composites to a four-phase sphere model to estimate the overall mechanical properties of concrete. The Concrete material was modeled as a three-phase composite consisting in a continuous phase (cement paste), a dispersed phase (aggregates), and an inter-phase representing the Interface Transition Zone (ITZ) between cement paste and aggregates. Grimaldi and Luciano [84] modeled the tensile stiffness and strength of Fiber-Reinforced Concrete by considering that the concrete matrix is a non-tensile material having a rigid plastic bonding between matrix and fibers.
According to Mehta and Monteiro [153], the cement-based materials structure can be considered as a hierarchy of different levels, where each of them has a characteristic length scale .
Under the lights of the experimental study presented in the previous chapter, a proposed modeling of each of the cement-based material is presented here after. It should be noted that in this study, only cement paste is investigated. Once, (a) the different microstructural constituents (or phases) are identified, (b) their intrinsic constants, their volume fractions and their morphological shape and distribution determined; as well as the interaction considerations between the phases characteristics, a homogenization method can be appropriately applied.

As presented in the micromechanical formulations, the mechanical characteristics of a composite material depend on its microstructure morphology. Thus, before applying such methods to cementitious composites, it is necessary to define its microstructure. However, the morphology of the cementitious materials is very complicated. Then, simplified assumptions on the microstructure morphology will be considered in the cement-based material modeling developed in this part.
For cementitious materials, phases are considered to be isotropic and inclusions are arbitrary distributed. Thus, the composite is considered to be isotropic and the stiffness tensor C_{hom} only depends on two independent moduli K_{hom} and G_{hom}. The following

relations can be drawn from Eq.(1.49):

$$K_{hom} = K_0 + \sum_i (K_i - K_0) A_i^{iso} f_i \tag{8.11}$$

$$G_{hom} = G_0 + \sum_i (G_i - G_0) A_i^{dev} f_i \tag{8.12}$$

where (K_0 , K_i) and (G_0 , G_i) are the bulk and shear moduli of the matrix and inclusions, respectively. A_i^{iso} and A_i^{dev} are the isotropic and deviatoric parts of A_i given by:

$$A_i = A_i^{iso}\mathbf{J} + A_i^{dev}\mathbf{K} \tag{8.13}$$

with $J = \frac{1}{3}\mathbf{1} \otimes \mathbf{1}$ and $K = I - J$. $\mathbf{1}$ and $\mathbf{I}$ are respectively the second and fourth-rank symmetric unit tensors

Chapter 9

Identification of the cement-based materials matrix properties

In order to evaluate the homogenized cementitious material properties using micromechanical models, elastic moduli as well as density of the material (cement paste and air-entrained cement paste) with diminishing pores volume fraction (matrix) were needed. These properties will be called the matrix properties in the following sections. These properties are influenced by many factors such as the Portland cement type and chemical composition, the hydration degree, the material preparation and the degradation factors. In this study, we used the same Portland cement for all the mix and assumed that the samples preparation was performed in comparable conditions and procedures. Thus, two factors were kept as influencing the matrix elastic properties, which are the hydration degree and the degradation caused by the drying. It was assumed that these two factors affect independently the cement matrix of the cement paste samples.
During experiments, cement paste samples were prepared with different W/C ratios that results in different hydration degree as was experimentally proven in numerous studies. Figure .9.1 shows an example of determined hydration degrees for cement paste materials when varying the W/C. Accordingly, the elastic matrix properties are influenced by the W/C ratio. On the other hand, the samples were studied at different hydration degrees that were obtained by drying the material which created cracks inside the matrix. Thus, the elastic properties of the matrix should be varied with the saturation degree: as the saturation decreases as the elastic properties of the matrix decrease.
Taking into account the previously enumerated factors, we propose here in that the elastic properties of the cement paste matrix are function of both W/C ratio and saturation. Thus, one can write:

$$(K_0, G_0) = f(W/C, S_r) \tag{9.1}$$

In the following, an expression of function f will be proposed based on experimental obtained results and previous works available in the literature.

9.1 Cement paste matrix properties

Among the indirect methods that can be used for the estimation of the matrix elastic properties of the prepared cement paste materials, two are detailed and applied in

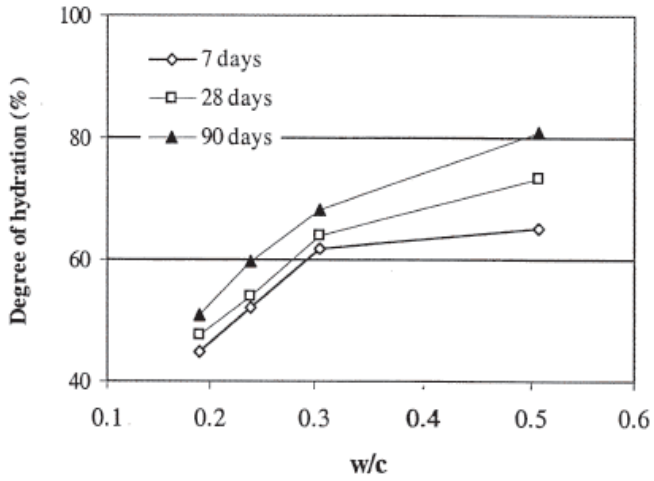

Figure 9.1: Increased degree of hydration of PC pastes with increasing W/C ratios [135]

this study. The two methods are based on the experimental obtained results. Indeed, the first considers a linear regression on the experimental data to estimate the matrix elastic properties. The second uses the experimental measured imbibition porosity to perform a homogenization on the material matrix phases in order to determine its elastic properties.

9.1.1 Linear regression on the experimental data

The cement paste matrix elastic properties can be determined by a linear regression (Fig.9.2) of the experimental data describing relationships between both dry and fully saturated bulk and shear moduli, and porosity. These data were obtained from ultrasonic measurements using an inversion of Eqs.(8.7)-(8.8). Figure 9.2 shows a general decrease in the elastic moduli of the cement paste with increasing porosity for both saturation states. It can be noted that the saturated samples have higher bulk and shear moduli than the dry ones. Indeed, the presence of water inside the pores of the saturated material provides additional stiffness, as water has higher stiffness than air. The scatter between the elastic moduli measured on dry and saturated cement paste samples is almost independent from the porosity. The values of bulk and shear moduli for the cement paste at zero porosity resulting from the linear regression in Fig.9.2 are given in Table 9.1.

It was expected that the elastic moduli of the cement paste at zero porosity are independent from the saturation degree, as they are intrinsic properties of the material. The observed relative variation of the bulk and shear moduli between saturated and dry states are respectively 11.07% and 1.24%. In fact, such variation was already observed on mortar samples [230]. Cracks created into the non-porous matrix when drying the

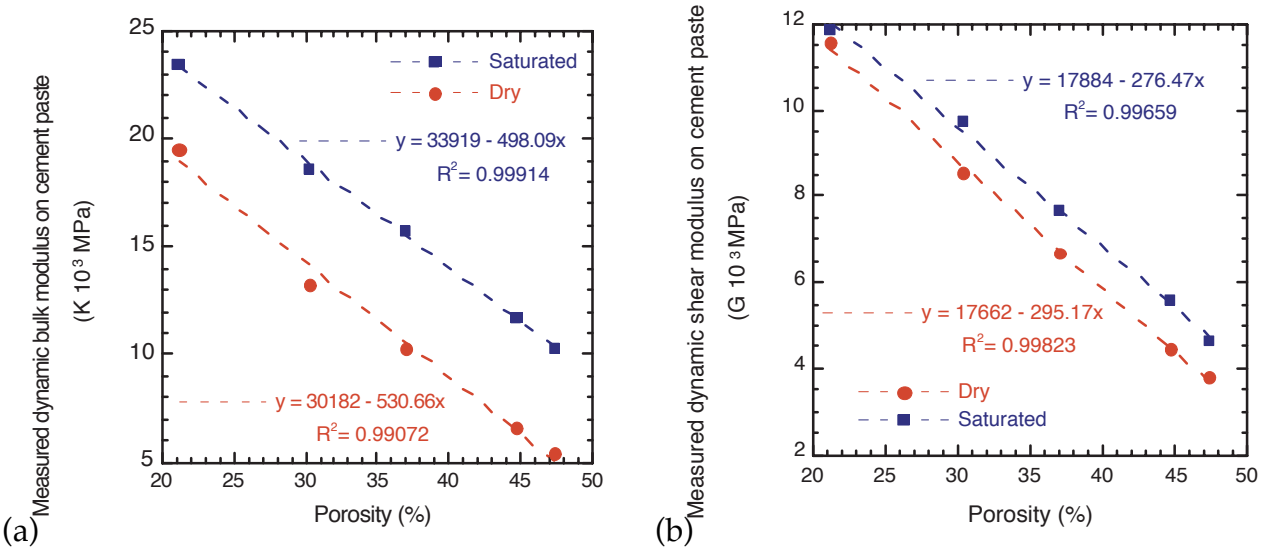

Figure 9.2: Variation of experimental dynamic elastic moduli vs porosity for dry and saturated states

Table 9.1: Cement paste elastic moduli at zero porosity by linear regression on experimental measurements

	Bulk modulus (*MPa*)	Shear modulus (*MPa*)
Saturated	33919	17884
Dry	30182	17662

sample can cause this difference in the elastic properties. It should be noted that such development was applied to correlate the ultrasonic velocity to the porosity of cement paste when considering three W/C ratios [148]. The obtained results were acceptable but needed improve to end up with better correlations.
Thus, modeling the cement paste with a fixed elastic matrix properties for all the saturation states will be not sensible. In order to take into account such variation, a linear variation of the matrix elastic properties in function of the saturation was suggested. The linear choice may seem simplistic. But, this is argued by the fact that the present study is a first attempt of cement paste modeling and that no possible measurements of such properties were available. According to the previously mentioned assumption, the elastic properties of the matrix (K_0 and G_0) will be assumed to be given in a linear function of the saturation degree S_r by:

$$K_0(S_r) = K_0^{dry} + (K_0^{saturated} - K_0^{dry})S_r \tag{9.2}$$

$$G_0(S_r) = G_0^{dry} + (G_0^{saturated} - G_0^{dry})S_r \tag{9.3}$$

Where K_0^{dry}, $K_0^{saturated}$, G_0^{dry} and $G_0^{saturated}$ are the experimentally determined values listed in Table 9.1 and $S_r \in [0,1]$. A general linear numerical expression of the previous equations writes:

$$K_0(S_r) = a_K + b_K S_r \tag{9.4}$$

$$G_0(S_r) = a_G + b_G S_r \tag{9.5}$$

Eqs.(9.4)-(9.5) present expressions for the matrix elastic properties in function of the saturation state. However, the effect of the W/C ratio is not considered in such expression and a further development needs to be performed. In fact, it is noted on Fig.9.2 that the variation of the elastic moduli from dry to saturated state is almost independent from the considered porosity that refers to the W/C ratio. Thus, one can suppose that the effect of the saturation and the initially used W/C ratio are decoupled. Then, the effect of the W/C ratio should be included in the expression of a_K and a_G, while b_K and b_G remain those determined based on the above linearization (Table 9.1) i.e. $b_K = 33919 - 30182 \simeq 4000MPa$ and $b_G = 17884 - 17662 \simeq 200MPa$. Hence, the matrix elastic properties write:

$$K_0(S_r, W/C) = a_K(W/C) + b_K S_r \tag{9.6}$$

$$G_0(S_r, W/C) = a_G(W/C) + b_G S_r \tag{9.7}$$

The following section will be devoted for the determination of $a_K(W/C)$ and $a_G(W/C)$.

9.1.2 Homogenization on the matrix solid phases

The elastic properties of the cement paste at zero porosity can be determined when homogenizing the different phases of this solid phase of the cement paste. Indeed, as it was detailed in section 5.2.2, the hydration of cement paste results in different

products. The major hydration products are the High and Low Densities Calcium-Silicate-Hydrates (C-S-H), the Calcium Hydroxide (C-H), the Calcium Sulfates, the aluminates and Ferrite. In addition, part of the Portland clinker will remain as an unhydrated product (called the Portland cement grains or Clinker grains).
Thus, if the different elastic properties of these phases are known, a possible homogenization can be carried out in order to end up with the elastic properties of the cement paste at zero porosities. Here in, the cement paste matrix will be homogenized based on three assumptions: (1) all the hydrated products will be considered to form one phase and represented by the elastic properties of the low density C-S-H [95], (2) the clinker elastic properties will be assumed as the average of its four phases (C_3S, C_2S, C_3A, and C_4AF), (3) the gel pores will be supposed to be part of the cement matrix with elastic properties included within the hydrated phase elastic properties (low C-S-H). In more elaborated studies, the hydrated product can be determined from homogenization on the low and high density C-S-H phases [17, 52, 80, 190, 206].
Thus, in this study the solid phase of the cement paste (the matrix) will be considered as a two phases material: one phase is the hydrated product, the second is the unhydrated product. Indeed, in such case, where a porous material is consisting of two or more solids, i.e. micro-heterogeneous, the elastic bulk and shear modulus of the solid phase are determined as a Hill average (Eq.2.25) of the various solid phase constituents moduli [24]. This average is given by:

$$\frac{1}{K_0^{Hill}} = \frac{x}{K_0^V} + \frac{1-x}{K_0^R} \tag{9.8}$$

$$\frac{1}{G_0^{Hill}} = \frac{x}{G_0^V} + \frac{1-x}{G_0^R} \tag{9.9}$$

Where (K_0^R, G_0^R) and (K_0^V, G_0^V) are the matrix bulk and shear moduli determined based on both the Reuss and Voigt averaging approaches (section 2.1.1.2 & 2.1.1.1) and x is a parameter ranging from 0 to 1 . Accordingly;

$$\frac{1}{K_0^R} = \frac{f_{hyd}/f_{solid}}{K_{hyd}} + \frac{f_{unhyd}/f_{solid}}{K_{unhyd}} \quad ; \quad K_0^V = \frac{f_{hyd}}{f_{solid}}K_{hyd} + \frac{f_{unhyd}}{f_{solid}}K_{unhyd} \tag{9.10}$$

$$\frac{1}{G_0^R} = \frac{f_{hyd}/f_{solid}}{G_{hyd}} + \frac{f_{unhyd}/f_{solid}}{G_{unhyd}} \quad ; \quad G_0^V = \frac{f_{hyd}}{f_{solid}}G_{hyd} + \frac{f_{unhyd}}{f_{solid}}G_{unhyd} \tag{9.11}$$

(K_{hyd}, G_{hyd}) and (K_{unhyd}, G_{unhyd}) are the bulk and shear moduli of the hydrated and unhydrated products, respectively. f_{hyd} and f_{unhyd} are the volume fractions of the hydrated and unhydrated products. $f_{solid} = f_{hyd} + f_{unhyd}$ is the volume fraction of the solid phase. In the following each of these parameters is defined and determined.
First, the weighting parameter x was chosen to be equal to 0.5 as no information on the phases arrangement is available. Second the elastic moduli of the hydrated and unhydrated matrix phases were assumed to have the indentation measured value as

Table 9.2: Intrinsic elastic properties of hydrated and unhydrated cement paste phases

Phase		Young modulus (GPa)	Poisson ratio	Bulk modulus (GPa)	Shear modulus (GPa)	density [170] (kg/m^3)
Unhydrated	C_3S [52] C_2S [52] C_3A [52] C_4AF [212]	140	0.3	116.7	53.8	3150
Hydrated	[52]	21.7 ± 2.2	0.24	13.91 ± 1.41	8.75 ± 0.88	2073

published in the literature and summarized in Table 9.1.2.

Finally, the volume fraction f_{hyd} and f_{unhyd} of the hydrated and unhydrated products were assumed as defined by Powers theory. The expressions for these fractions were detailed in section 5.2.2 and are given by Eqs. (9.12)-(9.13).

$$f_{unhyd} = \frac{0.32(1-\alpha)}{W/C + 0.32} \tag{9.12}$$

$$f_{hyd} = \frac{0.68\alpha}{W/C + 0.32} \tag{9.13}$$

It is noted that the volume fractions of the hydrated and unhydrated products are function of the W/C ratio and the hydration degree α. As the hydration degree was not measured experimentally on the cement paste studied samples, it was determined based on the experimental water imbibition porosimetry results carried out on the cement paste samples (section 6.1). This measured porosity corresponds to the volume fraction of capillary pores expressed in Eq.(5.11).
The hydration degree α was then computed as:

$$\alpha = \frac{(1 - f_{cap})\frac{w}{c} - 0.32 f_{cap}}{0.36} \tag{9.14}$$

The computed hydration degree for the five W/C samples as well as the bulk and shear moduli of the cement paste matrix (Eqs.9.10-9.11) are presented in Table 9.3. These computed hydration degrees are almost in accordance with the measurements carried out by Cook & Hover [53]. The authors obtained at 28 days of curing, a hydration degree of 0.48 and 0.66 for W/C equal to 0.3 and 0.5, respectively. It was expected that the hydration degree reaches 1 for mix with W/C > 0.38 and thus no unhydrate products remain in the matrix as assumed by Constantinides and Ulm [52]. This discordance is possibly due to the chemical composition of the used Portland cement and the samples preparation. In addition, It was found that the hydration degree almost increases with increasing W/C ratios, as it is remarked in Table 9.3.
Based on this table, the hydrated and unhydrated products volumes fraction where

Table 9.3: Computed hydration degree of the cement paste samples

W/C	0.3	0.4	0.5	0.6	0.7
f_{cap}=$p(\%)$	21.13	30.28	36.93	44.68	47.34
Hydration degree α	0.4694	0.5055	0.5477	0.5248	0.6031

determined. Their variations in function of the cement paste water to cement ratios are plotted in Fig.9.3.

Later, the cement paste matrix elastic moduli were determined according to the Hill

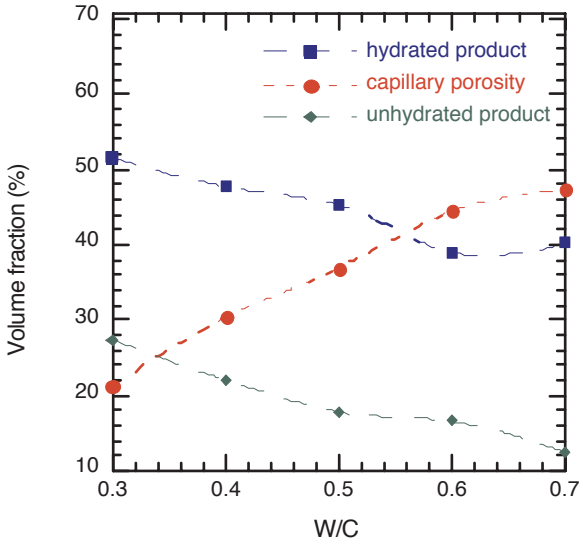

Figure 9.3: Variation of measured capillary porosity and determined hydrated and unhydrated volume fractions

averaging model. A similar development have been adopted by Xi and Jennings [229] to determine the elastic properties of the cement paste matrix. But, the authors considered that the unreacted grains, C-H crystals and C-S-H solids form the solid matrix phase. Then, based on Christensen model (4.2.2) they end up to the Bulk homogenized moduli of the matrix. This model was not considered in the present development as it gives estimates for the shear modulus only in case of dilute inclusion. The obtained bulk values by Xi and Jennings [229] were 25.5, 26.2 and 24.2 *GPa* when the W/C is fixed to 0.3, 0.4 and 0.5, respectively. These values are slightly lower but remain coherent with those obtained on the cement paste studied here in. Indeed, the obtained bulk and shear moduli were plotted as function of the capillary porosity in Fig.9.4. It is noted that the matrix elastic properties are not constant when the W/C ratio is varying (and so the porosity). Then, aiming to propose a general correlation between the porosity and the elastic bulk and shear moduli of the cement paste matrix, a linear fit of these latter

was plotted in Fig.9.4. The latter shows the decrease of cement matrix elastic moduli with the W/C ratio which refers to the hydration degree.
As already mentioned, the bulk and shear moduli are averages of the elastic moduli of the two solid constituents of cement (hydrated and unhydrated products). This is due to the fact that the elastic modulus of anhydrous grains is significantly larger than that of hydrate (see Table 9.1.2). Indeed, during hydration, anhydrous grains react with water and form hydrates. Therefore, the decrease in the matrix modulus is due to the decrease in the quantity of anhydrous grains during the hydration.

The obtained linear equations for the matrix bulk and shear moduli are given by Eqs.(9.15)-(9.16).

$$K_0 = 32282 - 173.49p \tag{9.15}$$

$$G_0 = 18409 - 93.844p \tag{9.16}$$

Where K_0 and G_0 are in MPa and porosity ranging between 0 and 100. For both equations, the coefficient of determination R^2 is higher than 0.92 especially when excluding the W/C=0.6 composition. Thus, the linear regression on the experimental determined matrix elastic moduli with respect to porosity can be assumed as quite good.
Combining Eqs.(9.15)-(9.16) with Eqs.(9.6)-(9.7) leads to saturation and W/C ratio dependent general expressions of the bulk and shear moduli of the cement paste matrix. These expressions are given by:

$$K_0 = 32282 - 173.49p + 4000S_r \tag{9.17}$$

$$G_0 = 18409 - 93.844p + 200S_r \tag{9.18}$$

The dependence of the elastic moduli on the W/C ratio is implicitly expressed by the a dependence of the same moduli on the porosity. In fact, porosity and the W/C are strongly dependent one on the other as has been mentioned in section 6.

The matrix density can also be determined according to the aforementioned homogenization of the material solid phases. It is given by the following expression:

$$\rho_{hom} = \frac{f_{unhyd}}{f_{solid}}\rho_{unhyd} + \frac{f_{hyd}}{f_{solid}}\rho_{hyd} \tag{9.19}$$

The matrix densities determined according to Eq.(9.19) are listed in Table 9.4. It should

Table 9.4: Cement paste matrix density obtained by homogenization on the solid phases

W/C	0.3	0.4	0.5	0.6	0.7
density (kg/m^3)	2446.9	2412.5	2374.4	2394.8	2327.6

be noted that the matrix density is decreasing with the W/C ratio as the volume fraction of the unhydrated product, that has the higher density of both matrix phases, is decreasing. However its variation is not significant and all values can be considered to be consistent with the experimentally determined density ($\rho_0 = 2579kg/m^3$).

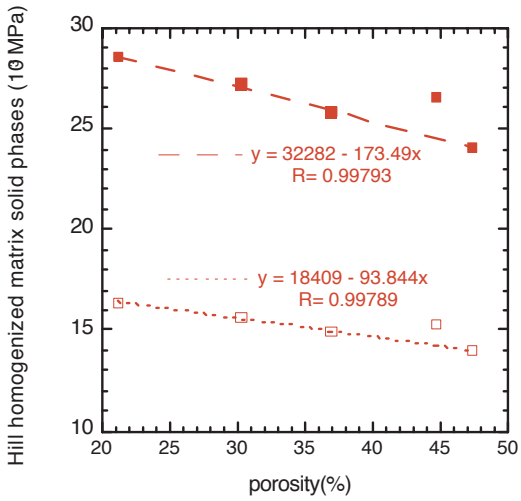

Figure 9.4: Variation of the Hill determined cement paste matrix elastic moduli as function of material porosity

9.2 Air-entrained cement paste matrix properties

Aiming to perform the cement paste modeling and porous structure investigation, seven air-entrained cement paste mixture were prepared at the ECLille laboratory. The particularity of the porous structure of the air-entrained cement paste is that the created pores are of relatively big size and are perfectly spherical shaped. On Fig.9.5, all the compositions are presented with the corresponding added air-entrained adjuvant. Based on these samples observations, the air-entrained cement paste material can be considered as a two-phase composite. One phase is the matrix: cement paste with no air-entrained admixture; the second is the inclusions, i.e. pores that are created by air-entrained adjuvant. Thus, a reference cement paste sample with no air-entrained admixture was considered. Its mechanical properties were taken as the matrix properties of the air-entrained cement paste composites. Accordingly, the elastic moduli of the air-entrained matrix were obtained from ultrasonic measurements on the reference sample. The values of bulk and shear moduli obtained for the cement paste at zero macroporosity are given in Table 9.5.

Table 9.5: Ultrasonic and mechanical properties of cement paste without air-entrained

Reference sample	V_L (m/s)	V_T (m/s)	K_0 (MPa)	G_0 (MPa)	ρ_0 (kg/m^3)
Dry	3801.30	2310.94	12978	9456.3	1770.7
Saturated	4037.06	2304.13	18836	10847.0	2043.1

The mechanical properties of this reference sample were noted using 0 as subscript.

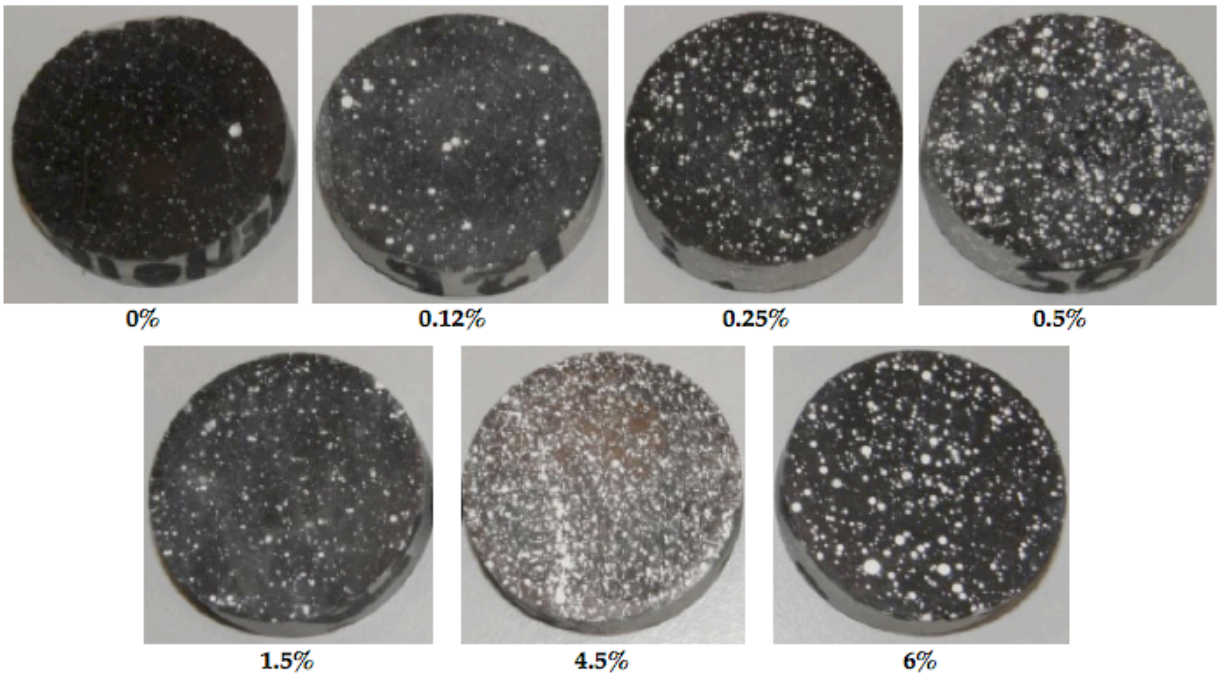

Figure 9.5: Photos of the air-entrained cement paste porous structure for different amount of air-entrained adjuvant (as percentage of the cement mass)

As expected, the longitudinal velocity as well as the bulk modulus increased considerably from dry to saturated state. However the transverse velocity and the shear modulus were almost independent of the saturation degree as water and air have both null shear moduli. The density ρ_0 was determined experimentally.

Chapter 10

Cement paste modeling

In a cement paste material, the anhydrous and hydrated phases look as a continuous phase. Thus the cement paste material can be considered as a multi-phase composite. One phase is the matrix: cement paste with zero pores; the others are inclusions, i.e. pores. The matrix is considered to be continuous with stiffness C_0. As no restriction on the cement paste pores was considered in this study, inclusions were supposed to be spherical, arbitrary distributed in the matrix. The pores volume fraction corresponds to material porosity p. This porosity only counts for the interconnected pores. Isolated pores must affect the elastic properties of the composite, but to simplify, this porosity is generally not considered [20]. This assumption corresponds to the porosity methods commonly used (e.g. mercury intrusion). The matrix volume fraction is $(1 - p)$. In the following subscripts, 0 and 1 respectively refer to the matrix and pores.

10.1 Dry cement paste modeling

If the cement paste is considered to be dry, then pores are modeled as ellipsoids having the same elastic properties as for air (Fig.10.1) i.e. $K_1 = 0$ and $G_1 = 0$. In addition, the volume fraction of inclusions is identified to the volume fraction of pores i.e. to porosity p. The porosity here, in the case of cement paste, refers to the microporosity.

$$f_1 = \frac{V_{pore}}{V_{total}} = p \tag{10.1}$$

However the continuous matrix phase properties have to be determined in function of the used cement paste, the hydration degree and many other properties that are often hard to control experimentally. In order to decide on the values of the cement-paste matrix elastic properties, it is convenient to conduct a study on the effect of these properties on the estimation of the overall elastic properties of the cement paste at different porosities. This study is presented here after for each of the Dilute inclusion, the Mori-Tanaka, the Kuster-Toksöz and the self-consistent formulation.
Formulation of the dry cement paste corresponds to expressing Eqs.(8.11)-(8.13) for the case of a two-phase material with null inclusions shear and bulk moduli which implies:

$$K_{hom} = K_0 - K_0 A_1^{iso} p \tag{10.2}$$

$$G_{hom} = G_0 - G_0 A_1^{dev} p \tag{10.3}$$

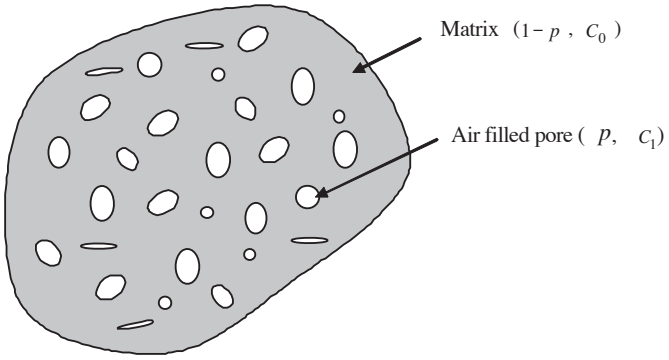

Figure 10.1: Modeling of dry cement paste

10.1.1 Dilute inclusion formulation

The dilute inclusion formulation of the dry cement paste is obtained when expressing the coefficients of the strain concentration tensor (A_1^{iso} and A_1^{dev}) in Eqs.(10.2)-(10.3) for the case of null inclusions shear and bulk moduli based on Eq.(3.13). Thus, for low porosities, the bulk and shear moduli according to the dilute inclusion model write:

$$K_{hom} = K_0(1 - pP_{01}) \tag{10.4}$$

$$G_{hom} = G_0(1 - pQ_{01}) \tag{10.5}$$

Where P_{01} and Q_{01} are given in Appendix E and are computed for null inclusion bulk and shear moduli.
Figure 10.2 shows the variation of the estimated bulk and shear moduli of a dry cement paste material based on the dilute inclusion model and considering spherical inclusions. The elastic properties of pores were assumed to be those of air (null bulk and shear moduli), while the elastic properties of the matrix were first taken as found by linear regression on the experimental ultrasonic measurements (Table 9.1). Then, determination of the same properties was done when considering that the elastic properties of the matrix vary in function of the W/C ratio, that corresponds to varying the porosity for micromechanical modeling (Eq.9.15). Both estimates (using different input for the matrix phase) were plotted in function of porosity ranging from 0 to 100% in Fig.10.2. On the same figure are plotted the bulk and shear moduli measured on the cement paste material using the previously mentioned ultrasonic set up and method. This aimed to compare the micromechanical estimates to the experimental measurements. Both the bulk and shear moduli determined according to the dilute inclusion model show a decrease when increasing the porosity. Such trend was expected from the bulk and shear expressions presented in Eqs.(10.2)-(10.3).
Bulk and shear moduli estimated by the dilute inclusion model when considering a fixed matrix elastic properties for all the W/C almost do not fit the measured data, except for very low porosities. The estimations of these properties when varying the

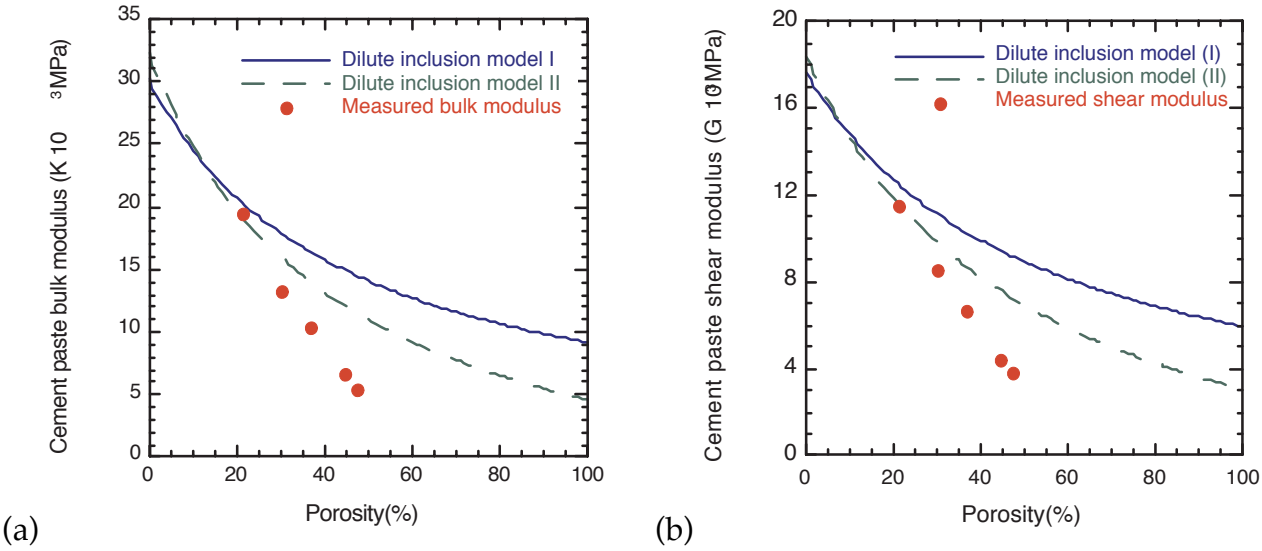

Figure 10.2: Comparison between the measured cement paste (a) bulk and (b) shear moduli and those determined by the dilute inclusion model using matrix elastic moduli obtained by (I) linear regression on experimental measurements (II) homogenization on matrix phases

matrix elastic properties present a better fit with the experimental data but still for low porosities: less than 20%.
In general, the dilute inclusion model overestimates the material elastic moduli, especially for samples with high porosities. Such result was predicted as this model assumes very low concentrations of inclusions and thus, low porosity. Thus in the following this model will not be considered further for the determination of homogenized properties of the cement paste material.

10.1.2 Self-consistent formulation

The elastic homogeneous elastic moduli of the dry cement paste according to the self-consistent method were determined using the iterative scheme detailed in section 4.2.1. If the particular case of spherical pores is assumed, non linear Eqs.(4.16)-(4.17) can be solved numerically. From Eq.(4.16), one find:

$$K^{hom} = \frac{4(1-p)K_0 G^{hom}}{3pK_0 + 4G^{hom}} \tag{10.6}$$

Substituting Eq.(10.6) into Eq.(4.17), a quadratic equation for G^{hom} is found:

$$8(G^{hom})^2 + \left[3K_0(3-p) - 4G_0(2-5p)\right] G^{hom} + 9K_0G_0(2p-1) = 0 \tag{10.7}$$

Resolution of this equation system yields the homogenized estimates of dry cement paste bulk and shear moduli according to the self-consistent method. Figure 10.3

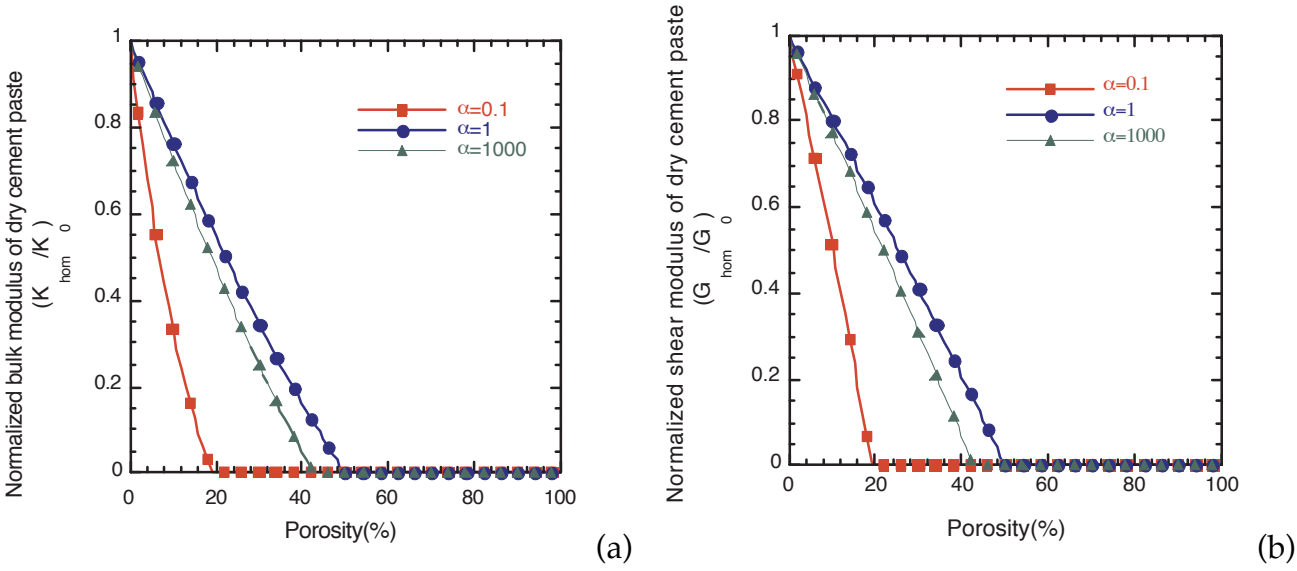

Figure 10.3: Estimates of bulk and shear dry cement paste moduli based on self-consistent model vs. porosity for different pores aspect ratio

shows the variation of the bulk and shear moduli when varying the porosity and the aspect ratio of pores. The matrix elastic properties were fixed to $K_0 = 30000MPa$ and $G_0 = 16000MPa$. Pores were assumed to be spherical; penny ($\alpha = 0.1$) or needle ($\alpha = 1000$) shaped having null elastic properties. It can be noted that the self-consistent method produces negative effective bulk and shear responses for porosity over 50% when pores are considered to be spherical. The same trend was noted when varying the pores aspect ratio, with a negative moduli for porosity above 20% and 43% for penny and needle shapes, respectively. This result can be explained by the fact that the self-consistent model assumes implicitly a perfect phases disorder, while for a high porosity, connected pores can be present in the medium. Even if rigid inclusions were considered, the self-consistent model produces infinite effective bulk responses for any volume fraction and infinite effective shear responses for inclusion volume fraction above 40%. Accordingly, the self-consistent method can be used safely only for low volume fractions (up to 40%). As the considered cement paste present relatively high porosity (between 20 and 50 %), it is expected that the self-consistent method will not give a satisfactory estimate of the overall elastic moduli of the material.

10.1.3 Mori-Tanaka and Kuste-Toksöz formulations for dry cement paste

In this section, both the Mori-Tanaka and Kuste-Toksöz models are presented. Their estimations for the homogenized bulk and shear moduli of the dry cement paste are

computed and compared based on two-phase formulation. First, expressions of bulk and shear moduli as given by the two models for a two phase material are summarized in Table 10.1.3. Then, simplifications on these expressions for the case of dry material are given successively.

Table 10.1: Homogenized bulk K_{hom} and shear G_{hom} moduli for two-phase Mori-Tanaka and Kuster-Toksöz micromechanical models

Model	Homogenized bulk and shear moduli
Mori-Tanaka	$K_{hom} = K_0 + \dfrac{(K_1 - K_0)P_{01}p}{(1-p) + P_{01}p}$ $G_{hom} = G_0 + \dfrac{(G_1 - G_0)Q_{01}p}{(1-p) + Q_{01}p}$
Kuste-Toksöz	$K_{hom} = \dfrac{K_0(K_0 + \frac{4}{3}G_0) + \frac{4}{3}G_0(K_1 - K_0)P_{01}p}{K_0 + \frac{4}{3}G_0 - (K_1 - K_0)P_{01}p}$ $G_{hom} = \dfrac{G_0(G_0 + \zeta_0) + (G_1 - G_0)\zeta_0 Q_{01}p}{G_0 + \zeta_0 - (G_1 - G_0)Q_{01}p}$
$\zeta_0 = \dfrac{G_0}{6}\dfrac{9K_0 + 8G_0}{K_0 + 2G_0}$	
P_{01} and Q_{01} are given in Appendix E	

- Mori-Tanaka model
  According to the Mori-Tanaka model, the strain concentration is given by Eq.(4.6). Computation of the isotropic and deviatoric parts of the latter and replacing them into Eqs.(10.2)-(10.5) for the case of dry material (null elastic moduli of pores) writes:

$$K_{hom} = K_0 - \frac{K_0 P_{01} p}{(1-p) + P_{01}p} \tag{10.8}$$

$$G_{hom} = G_0 - \frac{G_0 Q_{01} p}{(1-p) + Q_{01}p} \tag{10.9}$$

- Kuster-Toksöz model
  This model is widely used in geophysics field but remains less known in the mechanics field and even less in civil engineering applications. Its formulation for the particular case of dry cement paste when it is considered as two-phases composite implies the following bulk and shear homogenized moduli.

$$K_{hom} = \frac{K_0(K_0 + \frac{4}{3}G_0) - \frac{4}{3}G_0 K_0 P_{01} p}{K_0 + \frac{4}{3}G_0 + K_0 P_{01} p} \tag{10.10}$$

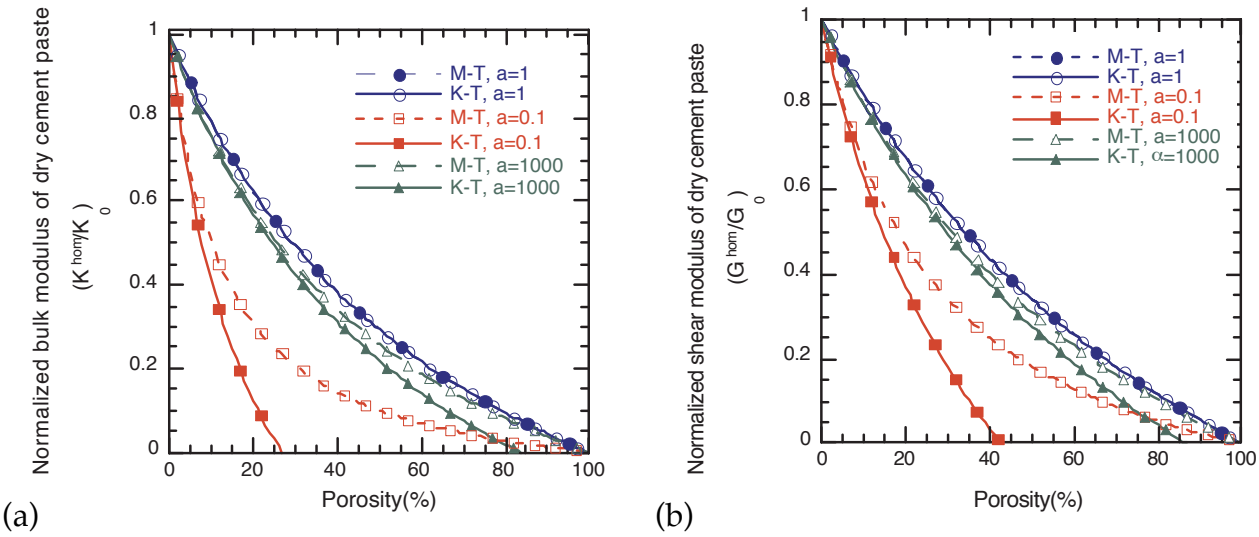

Figure 10.4: Homogenized (a) bulk and (b) shear moduli of dry cement paste according to M-T and K-T models for different aspect ratio of pores

$$G_{hom} = \frac{G_0(G_0 + \zeta_0) - G_0\zeta_0 Q_{01} p}{G_0 + \zeta_0 + G_0 Q_{01} p} \tag{10.11}$$

Aiming to compare the Kuster-Toksöz (K-T) and the Mori-Tanaka (M-T) models estimates, homogenized elastic moduli of dry cement paste were determined. Figure 10.4 shows the variations of bulk and shear homogenized moduli in function of porosity. Pores were assumed to be spheroidal with different shapes: penny (with an aspect ratio $\alpha = 0.1$), needle ($\alpha = 1000$) and spherical ($\alpha = 1$). The dotted lines represent the Mori-Tanaka model, while the solid lines refer to the Kuster-Toksoz model. Both bulk and shear moduli decrease when increasing porosity. As expected, the Kuster-Toksöz and the Mori-Tanaka estimates coincide for spherical pores. It is noted that the aspect ratio of pores influences the elastic moduli; the penny shaped pores affect the overall moduli more than the needle shaped pores. For a fixed porosity, the penny shaped pores induce a lower homogenized moduli that the spherical and needle pores. The Kuster-Toksöz model predicts a vanishing bulk modulus at a porosity near 84% if needle pores are assumed, and near 27% if penny pores are considered. The shear modulus determined by the same model for dry cement paste vanishes near 87% for needle shaped pores and near 43% for penny ones. However, the M-T model never allows the bulk nor the shear modulus to vanish except at 100% of porosity that was expected. According to these observations, the Mori-Tanaka model will be preferable to be applied to the cement paste material if penny shaped pores need to be considered. The influence of the matrix elastic properties (bulk and shear) on the estimated homogenized moduli, based on the Mori-Tanaka and Kuster-Toksöz two-phase models for dry cement paste, is plotted in Figs.10.5-10.6 and analyzed below. The aspect ratio

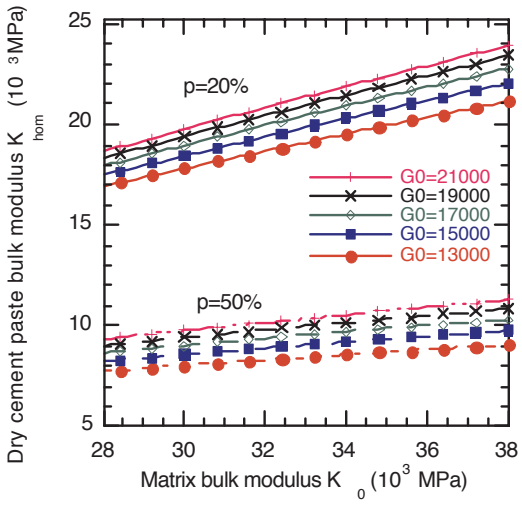

Figure 10.5: Estimated dry cement paste bulk modulus according to M-T and K-T for spherical pores

of pores was assumed to be spherical and then the two models coincide. The bulk and shear moduli of the matrix were varied, between (28 and 38 GPa) and (13 and 21 GPa), respectively. The porosity was fixed to the measured two extreme values, namely 20 and 50 %.

From Fig.10.5, it can be noted that the variation of the matrix shear modulus (G_0) has less influence on the estimated homogenized bulk modulus (K_{hom}) in comparison with the matrix bulk one (K_0). Indeed, an increase of K_0 of 10 GPa produces an average (for different matrix shear modulus) increase of 21% and 16% in the homogenized bulk modulus, when porosity is 20% and 50% respectively. However, the homogenized shear modulus is almost independent from the variation of the matrix bulk modulus. It is rather influenced by the matrix shear modulus variation. Thus, the identification of the matrix elastic moduli for application of the two micromechanical models must be treated with care.

10.2 Saturated cement paste modeling and Biot's theory

If the cement paste material is considered to be fully saturated with water, then it can be seen as a composite formed of a solid phase and a fluid phase (Fig.10.7). The solid phase is the non-porous structure and the fluid phase is the water filled porous structure. In such situation, specific phenomena appear within the material and their effect is detailed in this section. Indeed, when a pore is saturated by water, the latter exhibits capillary action against the force of gravity. Moreover, the fluid is in movement with respect to the solid in the particular case of dynamic solicitation. Aiming to determine

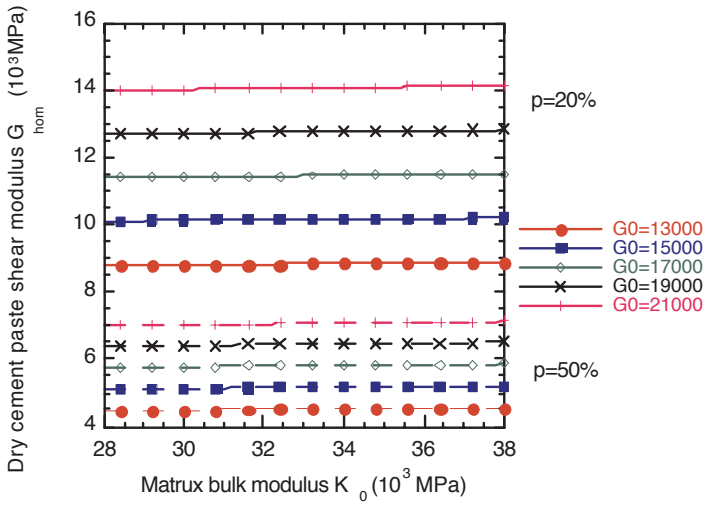

Figure 10.6: Estimated dry cement paste shear modulus according to M-T and K-T for spherical pores

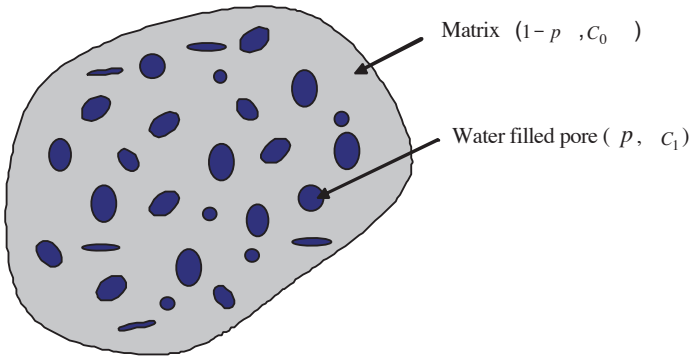

Figure 10.7: Modelling of saturated cement paste

the homogenized properties of the saturated cement paste material when investigating on such phenomena, the thermo-poro-elasticity of the material at the macro scale is studied through Biot developments [25], in addition to the micromechanical modeling. In this section, both methods are detailed for the determination of the elastic properties of the saturated cement paste.

The motivation for presenting the Biot theory is that the studied material was subjected to ultrasonic wave propagation (at a known frequency) that means a dynamic solicitation. Thus, the behavior of the saturated cement paste should be investigated in the dynamic case. In fact, the elastic properties of a material saturated by a compressible fluid were assumed to be described at a static assumption (low frequency) by Gassmann's equations [75]. Later, the dynamic behavior of such material was described by Biot's equations of poroelasticity [28].

Consider a fluid saturated medium with porosity p and denote the bulk and shear moduli of the dry porous frame, the matrix and pores respectively, by (K_{dry}, G_{dry}), (K_0, G_0) and (K_f, G_f). If an acoustic pulse is propagating through this medium, then average values of displacement of both the frame and the pores fluid [48, 21] can be defined. Let $\mathbf{u}$ be the average displacement vector in the solid frame (matrix) and $\mathbf{u}_f$ that of the pore's fluid. Then the average displacement of the fluid with respect to the solid frame is given by [28]:

$$\mathbf{w} = p(\mathbf{u}_f - \mathbf{u}) \tag{10.12}$$

The frame and fluid dilatations were defined as:

$$e = \nabla\mathbf{u} \tag{10.13}$$
$$e_f = \nabla\mathbf{u}_f \tag{10.14}$$

Thus, the relative fluid dilatation was defined [28] by:

$$\zeta = -\nabla\mathbf{w} = p(e - e_f) \tag{10.15}$$

If the medium is considered to be isotropic, then, the Fourier transformations of Biot's equations for poroelasticity with time dependence of the form $e^{i\omega t}$ write [28, 60]:

$$\mu\nabla^2\mathbf{u} + (H - \mu)\nabla e - C\nabla\zeta + \omega^2(\rho\mathbf{u} + \rho_f\mathbf{w}) = 0 \tag{10.16}$$
$$C\nabla e - M\nabla\zeta + \omega^2(\rho_f\mathbf{u} + q\mathbf{w}) = 0 \tag{10.17}$$

Where μ is the lame constant for the dry state and ρ is the overall composite density:

$$\rho = p\rho_f + (1 - p)\rho_0 \tag{10.18}$$

q is given by the following expression

$$q = \rho_f\left[\frac{\chi}{p} + \frac{i\Upsilon(\xi)\eta}{\kappa\omega}\right] \tag{10.19}$$

The parameter χ represents the tortuosity. If the low frequency case is assumed (frequency lower than the Biot's characteristic frequency), then the first term into brackets of Eq.(10.19) can be neglected . The permeability of the porous frame is denoted by κ. η is the kinematic viscosity of pores' fluid and $\Upsilon(\xi)$ is the dynamic viscosity factor [27]. The coefficients H, C and M are given by:

$$H = K_{dry} + \frac{4}{3}\mu + \sigma C \tag{10.20}$$

$$C = \sigma M \tag{10.21}$$

$$M = \left[\frac{\sigma - p}{K_0} + \frac{p}{K_f}\right]^{-1} \tag{10.22}$$

where

$$\sigma = 1 - \frac{K_{dry}}{K_0} \tag{10.23}$$

According to Eq.(10.20), Biot theory predicts the fluid-saturated bulk modulus K_{sat} as:

$$K_{sat} = K_{dry} + \sigma C \tag{10.24}$$

Concerning the shear modulus of the saturated medium, it was considered [75] to be the same as for the dry state:

$$G_{sat} = G_{dry} = \mu \tag{10.25}$$

For the micromechanical modeling of the saturated cement paste, the material is assumed to be composed of two phases where pores can be modeled as ellipsoids having the same elastic properties as of water. The latter are summarized in Table 10.2.

Consequently, the expressions of the homogenized bulk and shear moduli of a saturated cement paste are given by Eqs.(8.11)-(8.13) for the case of two-phase material, as follows:

Table 10.2: Water properties

Bulk (MPa)	Shear (MPa)	density (kg/m^3)
2200	0	1000

$$K_{hom} = K_0 + (K_1 - K_0)A_i^{iso}p \tag{10.26}$$

$$G_{hom} = G_0 - G_0 A_i^{dev}p \tag{10.27}$$

where K_0 and G_0 denotes the bulk and shear moduli of the saturated cement paste matrix. K_1 denotes the bulk modulus of pores i.e. water and p the porosity. In Eq.(10.27), the shear modulus of the porous phase was set to zero as suggested in Table 10.2.

If the elastic properties of the matrix are supposed to be independent from the saturation state, comparing the homogenized expression of the shear modulus for the case of dry (Eq.10.3) and saturated (Eq.10.27) cement paste implies that one should expect the same shear modulus for dry and saturated cement paste. Accordingly, it can be concluded that the shear modulus of the cement paste predicted by micromechanical models is not affected by the presence of the fluid in pores. Such conclusion is in agreement with the Biot theory that assumes, based on Gassmann's equations, that the shear modulus is not affected by the saturation state. This was proved to be a result of Gassman equation rather than an assumption by Berryman (reader can refer to [22]). A generalization of the Gassmann's equations given by Ciz and Shapiro [49] aimed to express the shear modulus of saturated porous material as dependent on frequency and viscosity. Their model shows a difference from the Gassmann's equation only for the case of pores filled with height viscous fluid (higher than 1000 kg/ms). Thus, for porous material saturated by water, the independence of shear modulus from the saturation degree statement was maintained if the independence of the matrix elastic

moduli from the saturation degree remains maintained.
The saturated cement paste samples considered in this study present the same range of porosity as the dry ones investigated above. Hence, the previously developed parametric studies and conclusions will be considered to remain verified. In particular, the fact that both the dilute inclusion and the self-consistent model can not be implemented for the determination of the homogenized properties of the studied saturated samples as their porosity exceed the range of low porosities (for which the mentioned models are applicable and give acceptable results). Thus, only the Mori-Tanaka and the Kuster-Toksöz models will be kept as potentially applicable for saturated cement paste modeling.
The bulk modulus of the saturated cement paste suggested by both Biot theory (Eq.10.24) and micromechanical modeling (Eq.10.26) are compared in the following. The elastic properties of the matrix were fixed to K_0 = 30000 MPa and G_0 = 16000 MPa and those of water were assumed to be given in Table 10.2. Both the Mori-Tanaka and the Kuster-Toksöz models were selected for the comparison. Saturated pores were considered to be spheroidal with varyed shapes: penny (with an aspect ratio α = 0.1), needle (α = 1000) and spherical (α = 1). For each model and pore shape, the homogenized bulk modulus was determined for dry cement paste. The obtained value was then considered for the determination of the Biot saturated bulk modulus estimate (Eq.10.24). The micromechanical saturated cement paste bulk modulus was computed according to models expression given in Table 10.1.3.

Figures 10.8(a) and 10.8(a) show the comparison between the Biot theory and the micromechanical modeling for the determination of a saturated cement paste bulk modulus. Both the Mori-Tanaka and the Kuster-Toksöz micromechanical models were plotted for different aspect ratios of pores. It can be noted that the Biot theory coincide with the micromechanical computation for both models and for the three pores shapes. Thus, the two approaches give the same result when estimating the elastic properties of a saturated material. Indeed, it is possible to find, using this micromechanical approach, the Biot homogeneous behavior as developed in the case of thermodynamics at the macroscale. The development of such proof was detailed in existing works, interested readers can refer to [10].
To conclude, the previously detailed Biot model sought to improve the cement paste mechanical modelling at saturated state. It was find that the latter coincide with the micromechanical modelling. Indeed, this theory would be more interesting if high frequency range is investigated. Thus, in the following, the unsaturated cement paste will be modelled based on micromechnical models.

10.3 Partially saturated cementitious material modeling

Many cementitious structures such as dams and bridges are often located in the water. However, they may not be fully saturated and remain unsaturated even if stored in water for a long time [44, 169]. Thus, it is interesting to study the partially saturated state

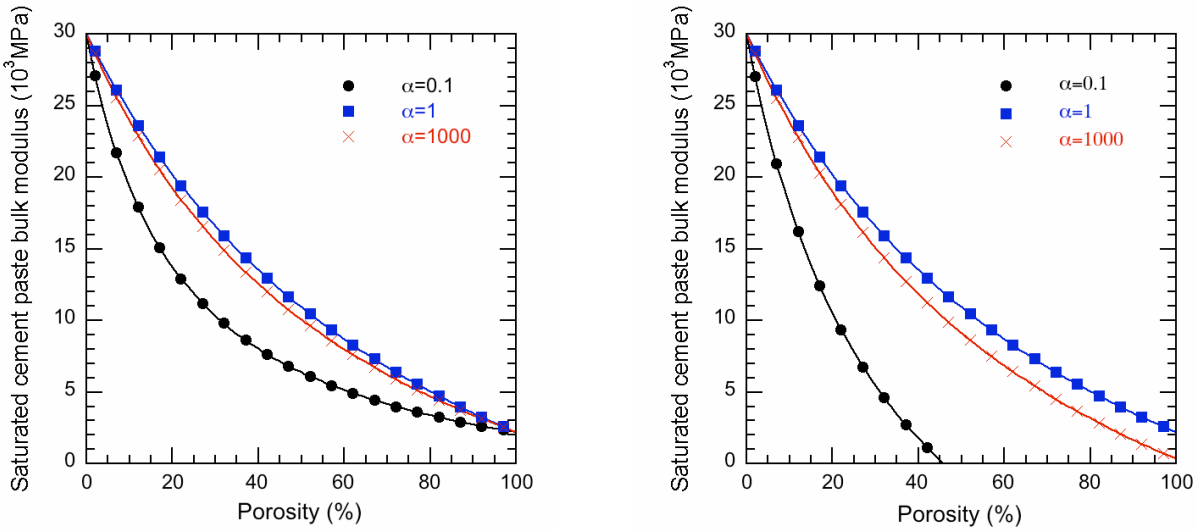

Figure 10.8: Saturated cement paste bulk modulus determined by Biot theory and micromechanical models (a) Mori-Tanaka (b) Kuster-Toksöz for different aspect ratios of pores. Lines refer to the micromechanical models and dots to the Biot formulation; $K_0 = 30000MPa$ and $G_0 = 16000MPa$.

of cementitious materials in order to understand their macro and micro behaviors. In the literature, few works have quantitatively dealt with the unsaturated cement-based material state. Indeed, few recent research investigated in the possibilities of a micromechanical modeling of a partially saturated composite [43, 221]. Accordingly, the objective of this section is to propose a micromechanical modeling of a partially saturated cement paste in order to predict its elastic moduli.
The behavior of a partially saturated cement paste can be seen as that of a two or three phase material. The first is when considering that a matrix and a porous structure constitute the material. Air and water are mixed inside the porous structure. The second is when air and water occupies two separate porous volumes in the partially saturated material in addition to the matrix phase.

10.3.1 Two-phase modeling of unsaturated material

When assuming that air and water are mixed into the pore volumes Fig.10.9, the unsaturated cement paste material can be considered as a two phase composite. One phase is the continuous matrix, the second is unsaturated pores. Thus, the elastic moduli of pores are those of an air-water mix obtained by a homogenization of the air and water phases. Such homogenization was obtained by applying the Reuss model in order to estimate the elastic moduli of the fluid mix (water and air) in pores.

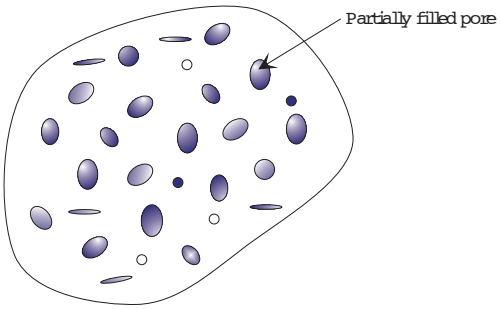

Figure 10.9: Two phases modeling of partially saturated cement paste

Let K_f denotes the bulk modulus of the fluid suspension in the partially saturated pores, then:

$$\frac{1}{K_f} = \frac{S_r}{K_w} + \frac{1 - S_r}{K_a} \tag{10.28}$$

where K_w and K_a are the bulk moduli of water and air, respectively.
Eq.(10.28) is known as Wood's formula and is an exact result of the homogenization of a suspension [191].
Obviously, the shear modulus of the suspension is null as the shear moduli of both water and air are null. While the air and water bulk modulus and density values are given in Table 10.3.

Table 10.3: Bulk and density values of air and water

	Bulk (MPa)	Density (kg/m^3 at 20 °C)
Air	0.145	1.204
Water	2200	1000

Figure 10.10 shows the evolution of a Reuss homogenization (Eq.10.28) of an air-water suspension for increased water saturation S_r in the air-pore. It is remarked that the pore homogenized bulk modulus is constant for all the saturation degree that are lower than 98% and is almost equal to the air bulk modulus (less that $1MPa$). An abrupt increase of the bulk modulus is observed when approaching the total water saturation to meet the water bulk modulus of $2200MPa$ at $S_r = 100\%$. This behavior can be understood from equation 10.28. Since the bulk modulus of air is about two thousands orders of magnitude less than that of water, any amount of air significantly different from zero will cause the right hand side of Eq.(10.28) to be strongly influenced by the air term.
As we are dealing with the ultrasonic propagation in partially saturated cementitious material, it is interesting to investigate the variation of the velocity when propagating through the air-fluid suspension. If we consider that the pores' size are small compared

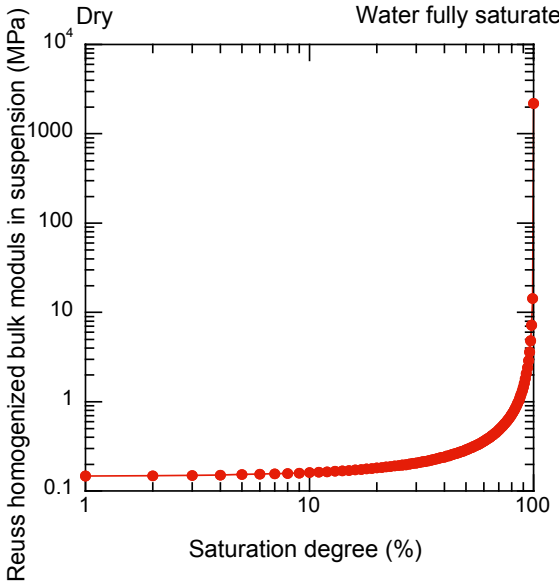

Figure 10.10: Bulk modulus of an air-water suspension

with the wavelength, then the ultrasonic longitudinal (sound) velocity in the fluid mixture is given exactly by the following Wood's relation:

$$V_L = \sqrt{\frac{K_f}{\rho_f}} \tag{10.29}$$

where K_f is given in Eq.(10.28) and ρ_f is the average density as defined in between the air and water densities ρ_a and ρ_w, respectively.

$$\rho_f = S_r\rho_w + (1 - S_r)\rho_a \tag{10.30}$$

Figure 10.11 plots the variation of the sound velocity in an air-water mix according to Wood's formulation. For clarity reasons, in the x-axis are plotted the air saturation degrees $(100 - S_r(\%))$ instead of the water saturation $S_r(\%)$. The features of Fig.10.11 are of great importance to the understanding of the behavior of sound velocity in pores when varying the saturation degree of a cement-based material. The figure highlights the suspended air bubbles impact on the acoustic propagation in water. First, it is noted that a very small amount of air in the mix can have a strong effect on the reduction of the velocity. Indeed, 9 ppm (part per million) of air in a fully saturated pore changes the velocity by 91.8%. Second, the velocity reaches a minimum of $23.81m/s$ at 50% of saturation. This minimum can be determined analytically in function of the air and

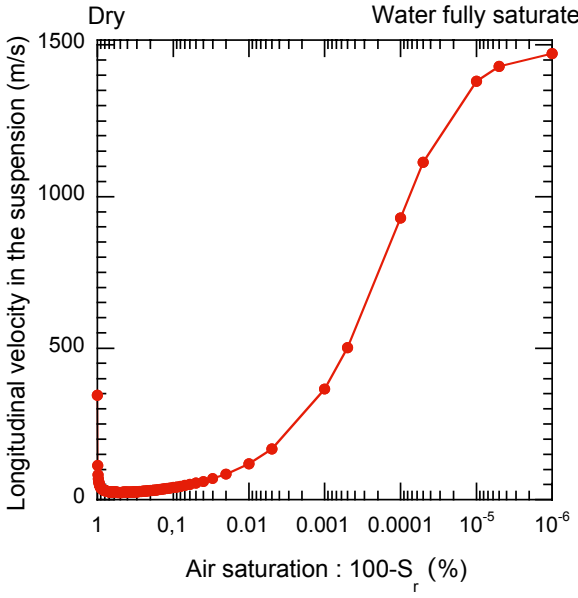

Figure 10.11: The variation of longitudinal velocity in air-water mixture at 20 °C

water bulk moduli and density by deriving Eq.(10.29), to obtain the water saturation degree corresponding to a minimum velocity:

$$Sr_{min} = \left[1 - \left(\frac{-(\frac{\rho_w}{K_a} + \frac{\rho_a}{K_w} - 2\frac{\rho_w}{K_w})}{2(\frac{1}{K_a} - \frac{1}{K_w}) * (\rho_a - \rho_w)}\right)\right] * 100 \tag{10.31}$$

Remark that this minimum is smaller than both the air ($344 m/s$) and water ($1483.2 m/s$) pure velocities. It was expected that the velocity will present a permanent increase when moving from air to water fully saturation according to the increase of the bulk modulus, plotted in Fig.10.10. The contradiction commented previously is argued by the effect of density variations on velocity.

10.3.2 Three-phase modeling of unsaturated cement paste

The partially saturated cement paste can be considered as a three phase composite with a non-porous cement paste matrix and inclusions being fully saturated or dry pores [145]. Example of such modeling is when a saturated air-entrained cement paste is considered. The water is occupying the micropores and cracks while the air is filling the macropores. In this case, the saturated and dry pores are considered to have the elastic moduli of water and air, respectively.

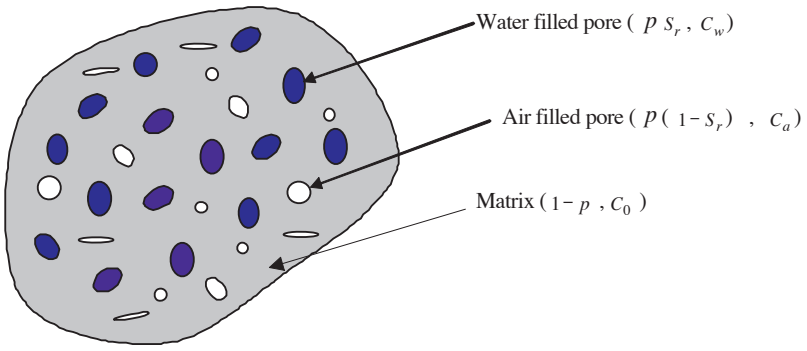

Figure 10.12: Three phases modeling of partially saturated cement paste

The volume fraction of each pore category is defined as follows:

$$f_{water}\frac{V_{water}}{V} = S_r p \tag{10.32}$$

$$f_{air}\frac{V_{air}}{V} = (1 - S_r)p \tag{10.33}$$

Then Eq.(1.49) writes:

$$C_{hom} = C_0 + (C_w - C_0)A_w S_r p + (C_a - C_0)A_0(1 - S_r)p \tag{10.34}$$

In Eq.(10.34) the subscripts w and a refer respectively to saturated and dry pores. The strain concentration tensors A_w and A_0 are determined by existing micromechanical models. Here, Mori-Tanaka and Kuster-Toksöz strain tensor expressions are detailed. The Hashin model is not presented since it coincides with the two previously mentioned ones when spherical inclusions are considered.

10.3.2.1 Mori-Tanaka formulation for three phases composite

Mori and Tanaka introduced a model based on Eshelby's single inclusion solution. The average strain in each inclusion was approached by considering that the latter was subjected to the average matrix strain ε^0 at infinity. Applying the Eshelby solution to this problem can be written in the following form:

$$\langle \boldsymbol{\varepsilon}^w \rangle = \mathbf{T}^{0w}\langle \boldsymbol{\varepsilon}^0 \rangle \tag{10.35}$$

$$\langle \boldsymbol{\varepsilon}^a \rangle = \mathbf{T}^{0a}\langle \boldsymbol{\varepsilon}^0 \rangle \tag{10.36}$$

where $\mathbf{T}^{ij}$ is the Wu-Eshelby defined in Eq.(3.15).
Considering Eqs.(10.35)-(10.36) and using Eq.(1.35), the strain concentration factor gives:

$$\mathbf{A}_w^{MT} = \mathbf{T}^{0w}\left[(1-p)\mathbf{I} + S_r p\mathbf{T}^{0w} + (1 - S_r)p\mathbf{T}^{0a}\right]^{-1} \tag{10.37}$$

$$\mathbf{A}_a^{MT} = \mathbf{T}^{0a}\left[(1-p)\mathbf{I} + (1 - S_r)p\mathbf{T}^{0a} + S_r p\mathbf{T}^{0w}\right]^{-1} \tag{10.38}$$

10.3.2.2 Kuster-Toksöz formulation for three phases composite

The Kuster-Toksöz model supposes that the composite material is embedded in the matrix, and that the inclusion is embedded in the matrix and is subjected to the average matrix strain ε^0 at infinity. Once the inclusion interactions are considered as formulated by Benveniste, the Kuster-Toksöz strain concentration tensor gives:

$$\mathbf{A}_w^{KT} = \mathbf{T}^{0w}\left(\mathbf{T}^{0*}\right)^{-1} \tag{10.39}$$

$$\mathbf{A}_a^{KT} = \mathbf{T}^{0a}\left(\mathbf{T}^{0*}\right)^{-1} \tag{10.40}$$

where star superscript refers to the homogenized properties and $\mathbf{T}^{0*}$ is the tensor for spherical inclusion.

The aforementioned developments of Mori-Tanaka and Kuster-Toksöz formulations for three phase unsaturated material were applied to the cement paste material. The obtained variations of bulk and shear moduli were not satisfactory. Actually, both moduli presented a continuously decrease versus porosity. No abrupt increase was observed when approaching the full saturation state. Thus, three phase modeling of partially saturated cement paste was excluded.
However, modeling a partially saturated material as a three phase material could be applied for the case of saturated air-entrained cement paste. The capillary pores would be assumed to be filled with water, while the entrained and entrapped voids remain empty i.e. air filled.

Chapter 11

Air-entrained cement paste modeling

The modeling of the air-entrained cement paste was based on the direct, optical and scanning electron microscopes (SEM) observations that were presented in section 6. Indeed, based on Fig.9.5, the entrained air hardened cement paste was modeled as a two-phase composite (Fig.11.1). One phase is the matrix: cement paste with no air-entrained admixture; the second is the inclusions, i.e. pores that are created by air-entrained adjuvant. These pores were considered to be of spherical shape in the micromechanical modeling as it was clearly visible on the prepared samples. Then, the inclusions were supposed to be spherical, arbitrary distributed in the matrix and having the same material with stiffness C_1. These inclusions were considered to be filled with air for the modeling of both dry and saturated air-entrained cement paste. Indeed, even if the sample is water saturated, the chemical properties of the air-entrained material implies that air bubbles are kept dry. So, the inclusion elastic properties were assumed to be those of air in the air-entrained micromechanical modeling. The inclusions' volume fraction corresponds to air-entrained porosity p. This porosity only counts for the pores created by adding the air-entrained adjuvant, the macropores p_{macro}. It was assumed that the air-entraining adjuvant only introduces large air voids (macropores), and does not affect the microporous characteristics of the structure [42]. Interconnected porosity was considered to be included in the matrix material. The matrix volume fraction is $1 - p$. In the following subscripts, 0 and 1 respectively refer to the matrix and pores. C_{hom} refers to the homogenized stiffness tensor determined for the overall air-entrained cement past. Taking into account the above assumption for the micromechanical modeling of the air-entrained cement paste, the bulk and shear homogenized moduli were determined according to dilute inclusion, Mori-Tanaka, Kuster-Toksöz and self-consistent models. As pores are spherical, then the Mori-Tanaka and the Kuster-Toksöz estimates coincide. Only the Mori-Tanaka model will be kept in the following as representative for both models. Table 11.1 summarizes the expressions of the air-entrained cement paste bulk and shear moduli with details presented in [149]. p represents the macroporosity, K_0 and G_0 are the saturation-dependant bulk and shear moduli of the air-entrained cement paste matrix. These parameters are given in Table 9.5. The density of the air-entrained samples were determined based on both capillary and image processing computed porosities. The difference between the two densities is due to the fact that microporosity was assumed not affected by the air-entrained add. Figure 11.2 and 11.3 show the behavior of bulk and shear homogenized moduli versus macroporosity for dry and saturated air-entrained cement paste according to three micromechanical models: Dilute inclusion, Mori-Tanaka and self-consistent. Dots on

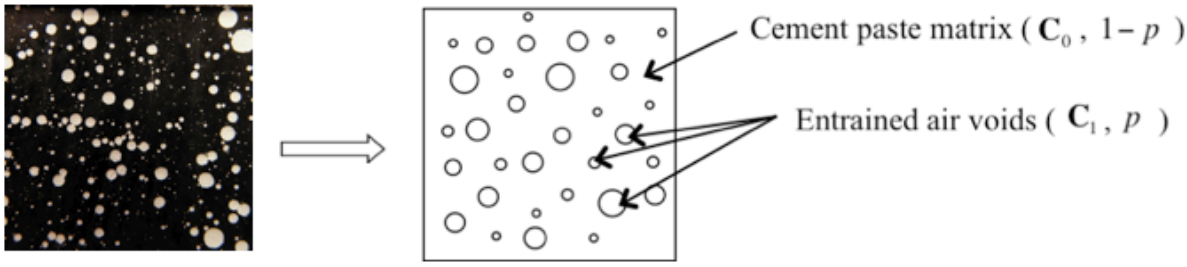

Figure 11.1: Schematic representation of air-entrained cement paste as two phase composite for micromechanical modeling

Table 11.1: Homogenized micromechanical bulk and shear moduli for dry two-phase material - spherical pores

Model	Homogenized bulk and shear moduli
Eshelby	$K_{hom} = K_0\left(1 + \frac{3K_0 + 4G_0}{4G_0}p\right)$ $G_{hom} = G_0\left(1 + \frac{5(3K_0 + 4G_0)}{9K_0 + 8G_0}p\right)$
Mori-Tanaka	$K_{hom} = K_0\frac{1-p}{1 + \frac{3K_0}{4G_0}p}$ $G_{hom} = G_0\frac{1-p}{1 + \frac{6(K_0 + 2G_0)}{9K_0 + 8G_0}p}$
Self-consistent	$K_{hom} = \frac{1-p}{K_{hom}} + \frac{p}{K_{hom} - K_0} = \frac{3}{3K_{hom} + 4G_{hom}}$ $G_{hom} = \frac{1-p}{G_{hom}} + \frac{p}{G_{hom} - G_0} = \frac{6(K_{hom} + 2G_{hom})}{5G_{hom}(3K_{hom} + 4G_{hom})}$

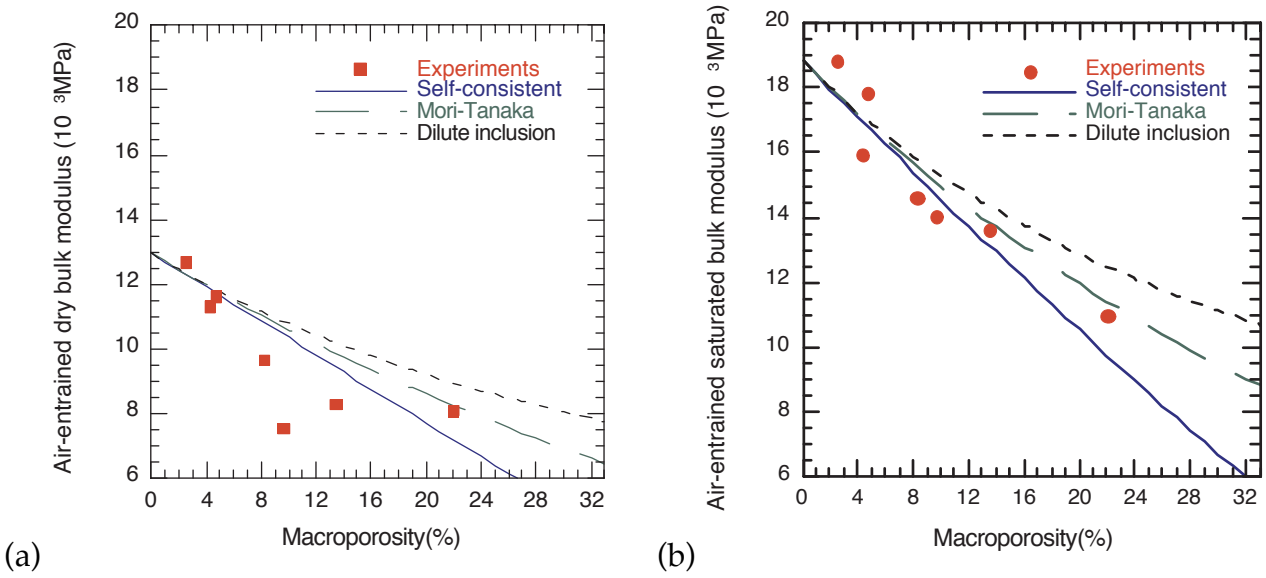

Figure 11.2: Air entrained cement paste bulk modulus versus macroporosity for (a) dry and (b) saturated states.

these figures (Fig.11.2-11.3) refer to the experimentally determined bulk and shear moduli based on the measured longitudinal and transverse velocities.

It should be noted that, as expected, all the micromechanical models present a decrease in both bulk and shear moduli when increasing the macroporosity. The same trend is observed for the dynamic measured bulk and shear properties. In addition, the micromechanical models present close estimates of the elastic moduli between each other. This is due to the considered relatively low inclusion concentration. Indeed, the macroporosity of the tested air-entrained cement paste samples was lower than 25%.
The bulk modulus of saturated air-entrained cement paste plotted in Fig.11.2 was amply higher than the dry one for all the macroporous fractions. This was noted for the micromechanical models as well as the experimental results. However, the gap between dry and saturated shear moduli (Fig.11.3) is much lower.
In fact, the difference between estimated saturated and dry elastic moduli is due to the difference between the matrix elastic properties that were assumed as given in Table 9.5. The bulk modulus of the air-entrained matrix presented a decrease of 31.1% from saturated to dry state. While the decrease on the shear moduli was by 12.8%. The elastic properties of the inclusions (the macropores) were assumed to be the same for the dry and saturated modelling. Thus, the effect of saturation was taken into account in the modelling of the air-entrained matrix. The latter contains the microporosity that is strongly influenced by the saturation state.

Although the Mori-Tanaka and the self-consistent models look to reproduce well the bulk homogenized modulus when compared to the experiment results, comparison

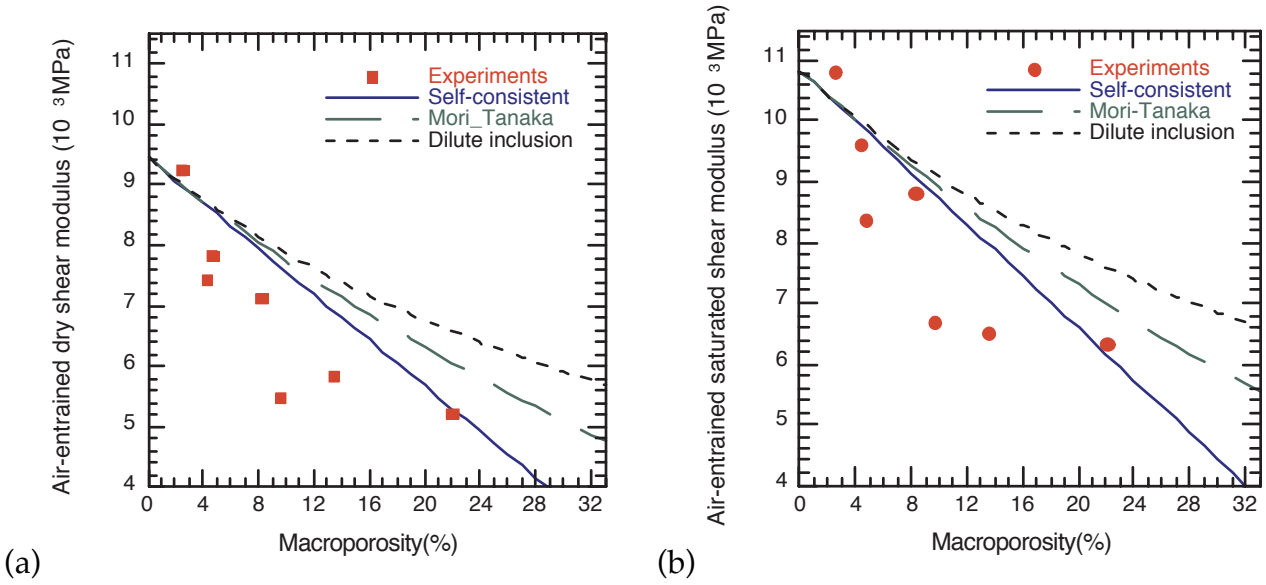

Figure 11.3: Air entrained cement paste shear modulus versus macroporosity for (a) dry and (b) saturated states.

with the experimental shear modulus suggest that the self-consistent model is more appropriate to model the air-entrained material. In order to present clearly the comparison between the self-consistent model and the experimentally measured bulk and shear moduli, the latter were plotted separately on Fig.11.4 for the two extreme saturation states: dry and fully saturated with water. Figure 11.4(a) argues a good fit between the measured and the micromechanical bulk modulus. The dry and saturated states are clearly differentiated. However, the shear modus plotted on Fig.11.4(b) are almost overlapped. This is due to the null shear properties of both air and water. Thus, the shear modulus was expected to be independent from the saturation state. Only the effect of cracks, created when drying the sample, that is supposed to influence the shear modulus.

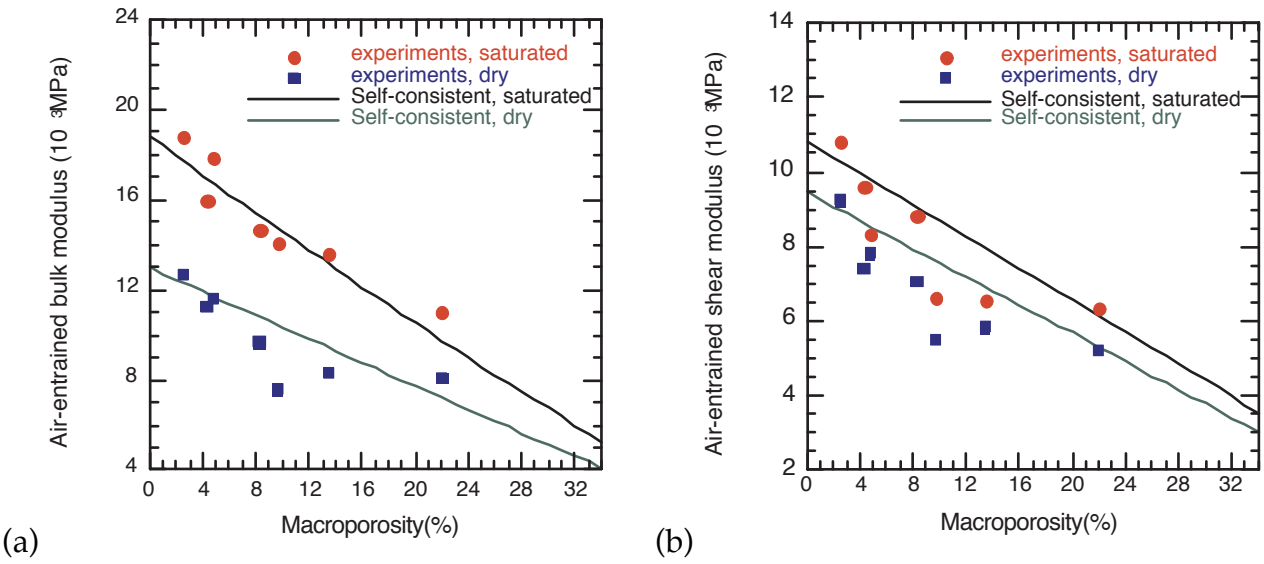

Figure 11.4: Air entrained cement paste (a) bulk and (b) shear moduli versus macroporosity for dry and saturated states.

Conclusion

To conclude, It has to be noted that in this part different micromechanical models were applied for the cement paste and air-entrained cement paste modeling at different saturation states.
The dry cement paste material was seen as a two-phase composite with air-filled inclusions. Different micromechanical models were applied for this composite in order to determine its elastic properties. The major observations are summarized in Table 11.2. It was found that the Mori-Tanaka model would be the most convenient to

Table 11.2: Applicability of micromechanical models to the cement paste

Model	Aspect ratio	Porosity	Observations
Dilute Inclusion	All the range of aspect ratios	$p > 20\%$	overestimated moduli
Self-consistent	$\alpha < 1$ $\alpha = 1$ $\alpha > 1$	$p > 20\%$ $p > 50\%$ $p > 43\%$	Negative moduli
Mori-Tanaka	$\alpha < 1$ $\alpha = 1$ $\alpha > 1$	All ranges	Acceptable estimation
Kuster-Toksöz	$\alpha < 1$	$p > 27\%$ $p > 43\%$	Null bulk modulus Null shear modulus
	$\alpha = 1$	All ranges	Coincide with the M-T model
	$\alpha > 1$	$p > 27\%$ $p > 87\%$	Null bulk modulus Null shear modulus

estimate the dry cement paste elastic moduli. In addition, it was remarked that both matrix elastic properties and the pore shape are key parameters for determining the homogenized stiffness. Indeed, the stiffer material estimate is given by the spheroidal pores.
As for the saturated cement paste modeling, pores were assumed to be water-filled and the material to be a two-phase composite. Both the micromechanical modeling and the Biot theory were investigated. It was shown that both theories gave the same estimated macro-elastic moduli of saturated cement paste material.
The partially saturated cement paste was modeled as a two-phase composite with pores being filled with an air-water mix. The behavior of this mix was studied by determining its homogenized elastic moduli and the ultrasonic velocity if an ultrasonic wave is propagating through it.
The micromechanical modeling was also applied to the air-entrained cement paste material. The latter was assumed to be a two phases porous structure. The properties of the non-porous phase, i.e. the matrix, were considered to be known. Indeed the

matrix of the air-entrained cement paste was assumed to correspond to a cement paste material with the same W/C ratio. The porous phase is formed by the macropores created by the air-entrained adjuvant. The macropores were supposed to be air-filled for both dry and saturated material saturation states.

Part IV

Correlation between ultrasound velocities and the hydraulic properties of the cement paste materials

12 Investigation of the frequency regime 153

13 Cement paste 155

14 Air-entrained cement paste 167

Introduction

Many investigators [113, 136, 7] have recently performed experimental and theoretical studies on the ultrasonic wave propagation in cement-based materials. Such researches aim to enhance the understanding of the effect of the cement-based materials' microstructure on their mechanical and ultrasonic properties. Furthermore, they intend to initiate the development of a non-destructive tool for the in situ assessment of cementitious structure degradation,

The objective of this study is twofold: the study of ultrasonic wave propagation in hardened cement paste and air-entrained cement paste at different saturation states followed by an investigation on the possibility of characterizing the material's hydraulic properties, in particular the porosity by means of ultrasonic measurements.

Using the experimental ultrasonic results carried out in our laboratory and the knowledge built on the application of micromechanical models to the cement paste material, it is possible to correlate both methods to characterize the relationship between the ultrasonic velocities and the porosity. The ultrasonic measurements concern both the transverse and longitudinal velocities.

In previous researches, two general approaches can be distinguished for modeling the velocity behavior of saturated media. The one focused on the only effect of saturation, with the pioneer works of Gassmann [22, 24]. The second was concerned with frequency effect in addition to expand the Gassmann works [26, 27, 35, 77].

Chapter 12

Investigation of the frequency regime

The objective of this work is to investigate the ultrasonic measurements as a nondestructive method for controlling the cementitious material. For this aim, an ultrasonic set-up (presented in section 8.2.1), was designed especially for the study. The latter has a wide band initially emitted ultrasonic pulse, with a central frequency of 500 kHz.
The acoustic waves are affected by several parameters such as the saturation degree and the frequency. The latter is one of the most important factors. Thus, the choice of the used frequency in an ultrasonic measurement is a key parameter. Consequently, the understanding of the frequency effect on the ultrasonic wave propagation in the studied cement-based material is essential for a reliable interpretation of the measured data.
The dependence of an ultrasonic wave velocity on its frequency was quantified by Biot who initiated the theory of elastic wave propagation in fluid-saturated porous media [26, 27]. Biot derived equations of motion for elastic waves from a variational principle based on the general form of the strain energy functional for an isotropic fluid-saturated medium. He found three types of waves: two compressional waves with different speeds (fast and slow waves) and a shear wave.
Indeed, these equations are derived from the equations system given in Eqs.(10.16)-(10.17). The latter can be decoupled into Helmholtz equations for three modes of propagation: the fast and slow compressional waves (+, -) and the shear wave (s). The wavenumbers of the propagating waves are given in [21, 118, 119]. For homogeneous viscoelastic waves, the phase velocity is given by the angular frequency divided by the real part of the complex wavenumber. At high frequencies both waves are propagatory but at low frequencies the slow wave is the solution of a diffusion equation. The critical frequency separating the low and high frequency regimes is called the Biot's characteristic frequency and expressed by:

$$f_c = \frac{\eta p}{2\pi\kappa\rho_f} \tag{12.1}$$

where η is the viscosity of the pore fluid, ρ_f is the density of the fluid; and p is the porosity.
If the employed frequency is lower than the critical frequency (i.e., $f/f_c < 0.15$ [187]), the fluid flow in the pore spaces is assumed to follow Poiseuille's law, and thus the frequency range is called *low frequency*. If the frequency, is greater or comparable to the critical frequency (i.e., $f/f_c > 0.15$), the Poiseuille's law can no more be assumed for the pores flow, and thus the frequency range is called *high frequency*.

Generally the water permeability of a cement paste material of a low W/C is within the interval of $[10^{-17}, 10^{-22}]$ [86, 237]. The air and water viscosity are respectively around 1.78 10^{-5} and 10^{-3} Pa.s depending on the temperature. Computation of the characteristic frequency when assuming the above parameters' values ends up with a characteristic frequency raging between:

$$\frac{1.5p10^{12}}{2\pi} \leq f_c(Hz) \leq \frac{1.5p10^{17}}{2\pi} \qquad \text{for dry cement paste}$$

$$\frac{p10^{11}}{2\pi} \leq f_c(Hz) \leq \frac{p10^{16}}{2\pi} \qquad \text{for water saturated cement paste}$$

Thus, one can consider that a frequency of $500kHz$ is within the low frequency range. Then, the effect of high order multiple scattering in the studied cement paste can be neglected. Indeed, in this frequency range, the viscous and thermal effects are predominant on the effects of multiple scattering. The propagation and absorption are so well described by the theory of homogenization [37].

Chapter 13

Cement paste

The purpose of this work is to specify the cement paste micromechanical model that describe the best the measured ultrasonic velocity. Once the fit is argued and proven, the model will enhance the understanding of the cement paste microstructure. Moreover, it will settle a mechanically assesed correlation between the ultrasonic velocity that can be measured at the macro-scale (in situ) and the porosity, which indicates the material degradation.

13.1 Cement paste proposed modeling

The cement paste was modeled as a two phase material for all the saturation states. The mechanical properties of both phases were determined in the previous chapters. One phase is the matrix that is characterized by two elastic properties: the bulk and shear moduli. The latter are dependent on the saturation state and the W/C ratio. The dependence on the W/C was replaced by a dependence on the porosity for the micromechanical modeling. Indeed, porosity is chosen as a parameter because it represents the indicator of durability. The second phase is the porous structure with properties dependent on the saturation state. When dry, respectively saturated, cement paste is considered, then pores properties correspond to the elastic properties of air, water respectively. In the case of partial saturation state is considered, then pores were assumed to contain a suspension of air and water and the modeling was carried out as detailed in section 10.3.
A parametric study was conducted in the previous chapter on the cement paste micromechanical modeling. It was found that only the Mori-Tanaka and the Kuster-Toksöz can be reliable in modeling the cement paste. However, it was then noted that the Kuster-Toksöz may estimate vanishing homogenized moduli for penny shaped inclusions. In conclusion, the Mori-Tanaka model appears to be the best-suited micromechanical model for the cement paste homogenization problem. Further, it is a simple explicit scheme and this makes it attractive to use.
In the following, only the Mori-Tanaka will be kept for the modeling of the cement paste. The model will be investigated for the estimation of the elastic properties of the cement paste material knowing the elastic properties of the matrix and pores and the volume fraction of each phase. The unknown parameter is the aspect ratio of the pores. Although, a comprehensive study on the cement paste microstructure was performed in section 6 using various methods, the pores exact form is still undetermined.

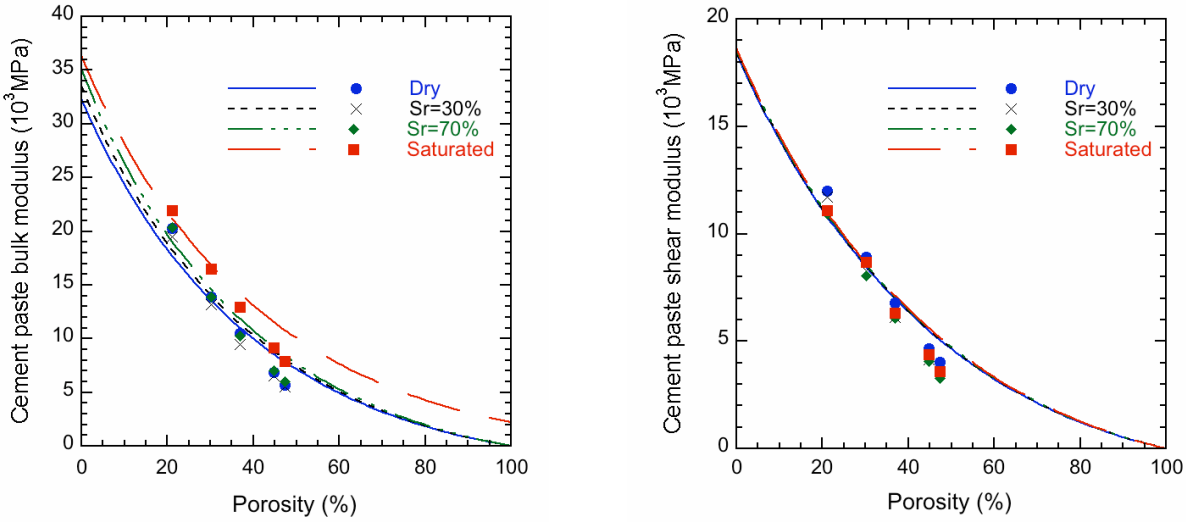

(a) (b)

Figure 13.1: Comparison between the measured and the Mori-Tanaka estimates of the Cement paste (a) bulk and (b) shear modulus for spherical pores assumption.

In this section, the bulk and shear moduli of the cement paste are determined by the Mori-Tanaka micromechanical model when varying the porosity and the saturation state. The obtained values are then compared to the bulk and shear moduli measured with the ultrasonic device. Indeed, the measured characteristics are the velocities, but using an inversion of both Eqs.(8.7)-(8.8), the dynamic bulk and shear moduli were obtained. The cement paste density was assumed to be given by Eq.(6.3).

Figures 13.1(a) and 13.1(b) show a comparison between the micromechanical and experimental evolution of the overall cement paste elastic moduli with porosity for the four considered saturation states: dry, 30%, 70% and fully saturated. Pores were assumed to be spherical. As expected, both the micromechanical and experimental elastic properties decrease when porosity increases.

Figure 13.1(a) shows that the measured and theoretical dynamic bulk modulus varies significantly between the dry and the fully saturated states. The measured dynamic bulk modulus of the saturated cement paste is clearly higher than the other states. For instance, the measured bulk modulus increases by 13.3% to 36.82% between the dry and the saturated 0.3 and 0.5 W/C samples. The Mori Tanaka model also predicts this trend. The bulk moduli of the dry and partially saturated cement paste are closer.

However, the dynamic shear modulus (Fig.13.1(b)) presents a little increase between the dry, partially and saturated states for both measured and theoretical values. These results were predicted by the theoretical Mori-Tanaka micromechanical formulation and approved by the ultrasonic measurements. On the one hand, the pores' shear modulus was considered to be null for all the saturation cases. So, the shear modulus was expected to be independent from the pores saturation state. Only the matrix shear

modulus changes with saturation affect the computed shear modulus, , which is not significant. On the other hand, the dynamic shear variation in function of the saturation degree is small and is under 20% for all the considered W/C ratio (Fig.13.2).
The Mori-Tanaka model present a general acceptable agreement with the experimental

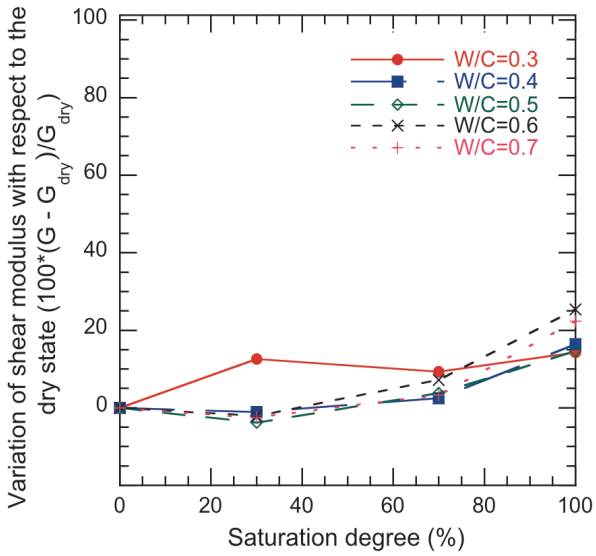

Figure 13.2: Relative variation of the shear modulus vs. the saturation degree

determined bulk and shear moduli. However, it is believed that taking into account an ellipsoidal shape of pores with a variable aspect ratio will improve the fit between the measured and the predicted moduli. Indeed, the effects of saturation and hydration on the cement paste microstructure is well known in cement paste [160, 231].
The porous structure of the cement paste depends on the W/C ratio used for the material preparation. Thus, it is expected that the pores' aspect ratio vary when varying the W/C ratio i.e. when porosity changes. Indeed, as the material is porous as pores are interconnected creating longer pores with smaller aspect ratio. In order to confirm this assumption on an example, the bulk modulus of a saturated cement paste was computed for penny shaped pores with different aspect ratio ranging from 0.1 to 1. Figure 13.3 plots the obtained values in function of the material porosity. It is noted that the pores aspect ratio influences the micromechanical bulk modulus as was highlighted in a previous section on dry cement paste (section 10.1.3). A better fit between the estimated Mori-Tanaka moduli and the measured values is obtained when decreasing the pores aspect ratio as porosity increases.
In addition, the saturation state influences the porous structure form and shape. Hence, the pore system of cement paste changes when drying the material [208]. The dry cement paste is known to be more interconnected structure (mainly presented more cracks), creating longer pore and thus smaller aspect ratio, than under saturated con-

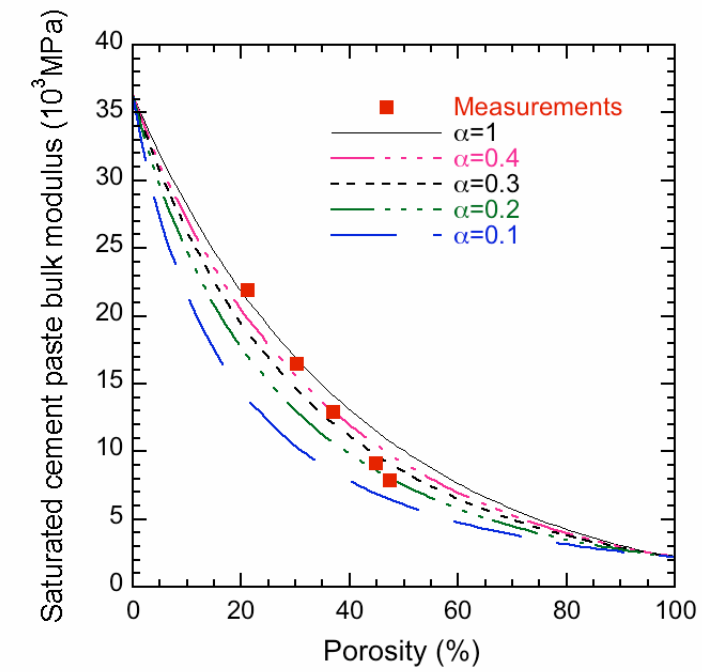

Figure 13.3: Variation of saturated cement paste bulk modulus vs. pores' aspect ratio; comparison between experiments and Mori-Tanaka model

ditions. Such behavior was noted by Yaman et al. [231] on concrete material. This phenomenon should be incorporated in the micromechanical modeling by considering that pores' aspect ratio varies with the saturation degree.

In the following, the investigated correlation between the ultrasonic velocities and the porosity. The next section will present first the measured ultrasonic velocities on the cement paste prepared materials. Later, comparison between these measurement and the estimations of the ultrasonic velocities based on the Mori-Tanaka model are presented.

13.2 Ultrasonic measured results

In this section, the longitudinal and transverse ultrasonic velocity measurements obtained on cement paste samples having different porosities at various saturation states are presented. Figure 13.4 shows the experimental data describing relationships between both longitudinal and transverse velocities, and porosity. The obtained longitudinal velocities are in accordance with recent study [234] investigating a laser based ultrasonic technique on the same material: the cement paste at dry and saturated states. Figures 13.5-13.6 show the same experimental results but when varying the saturation degree. It can be noted that velocity is affected by both porosity and water saturation. For a given value of water content, a significant decrease of velocity with increasing porosity is observed for longitudinal and transverse waves. As an example, the reduction of longitudinal velocity, for the fully saturated material, is about 13.23% when porosity increases from 19.65% to 37.9%.
Comparing the dry, partially and fully saturated longitudinal velocities for a given porosity, it can be observed that the velocity of the saturated material is higher than that of the dry material. This trend was expected as the longitudinal ultrasonic velocity is proportional to the elastic constants (Eqs.8.7-8.8), which were shown to be higher in saturated samples than in dry ones (Fig.9.2). The difference between the saturated and dry longitudinal velocities varies from 1.55% to 5.11% when porosity increases by 18.25%. The increase of ultrasonic longitudinal velocity with saturation degree has already been shown by Rollet et al. [183] and Ohdaira & Masuzawa [166]. As expected, longitudinal wave velocity values are about two times higher than shear wave velocity values.
The behavior of shear wave velocity regarding porosity is similar to that of longitudinal ultrasonic velocity. However, the comparison between dry and saturated states on the transverse velocities provides an opposite observation. Generally, it is noted that transverse velocity in a saturated sample is inferior to the one in a dry sample. This trend can be justified by the shear velocity expression given in Eqs.(8.7)-(8.8). As water and air have null shear moduli, the cement paste shear modulus is the same for the two saturation degrees. Then, transverse velocity is inversely proportional to the material density. Knowing that the water density is considerably higher than the air density,

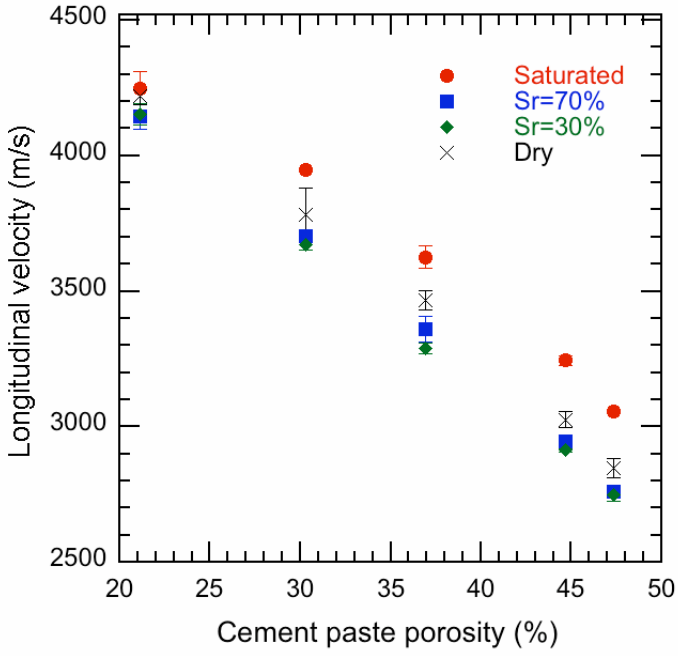

(a)

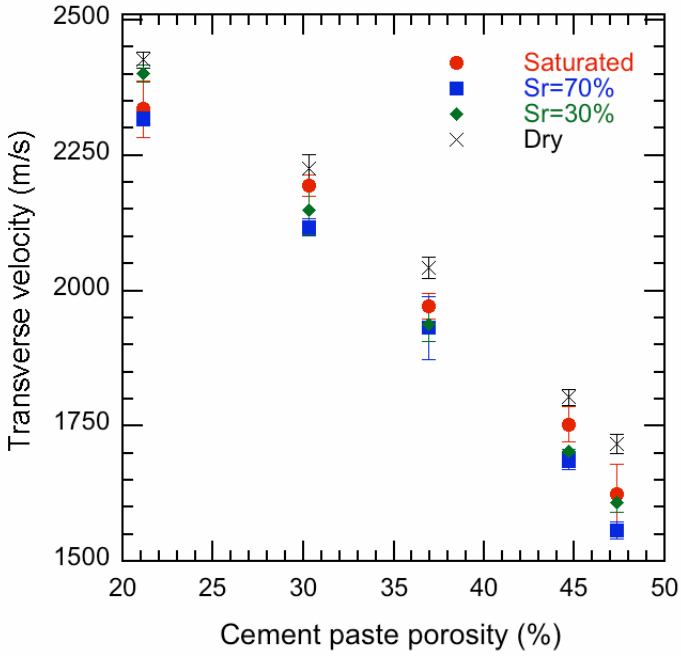

(b)

Figure 13.4: Measured cement paste longitudinal (a) and transverse (b) velocity vs. porosity for different saturation degrees

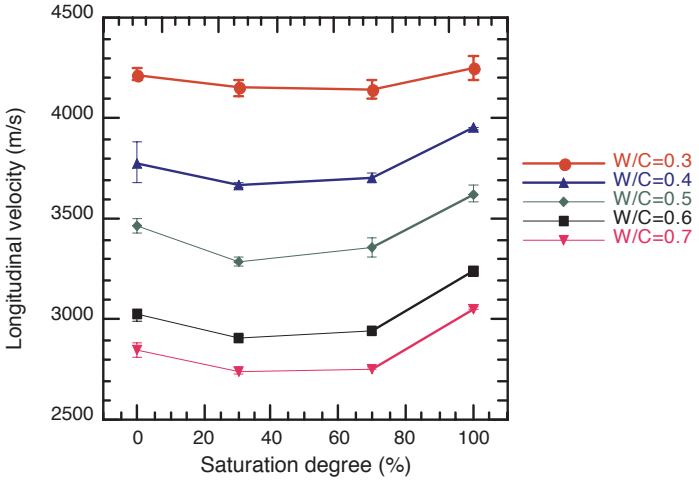

Figure 13.5: Measured cement paste longitudinal velocity vs. saturation for different W/C ratio

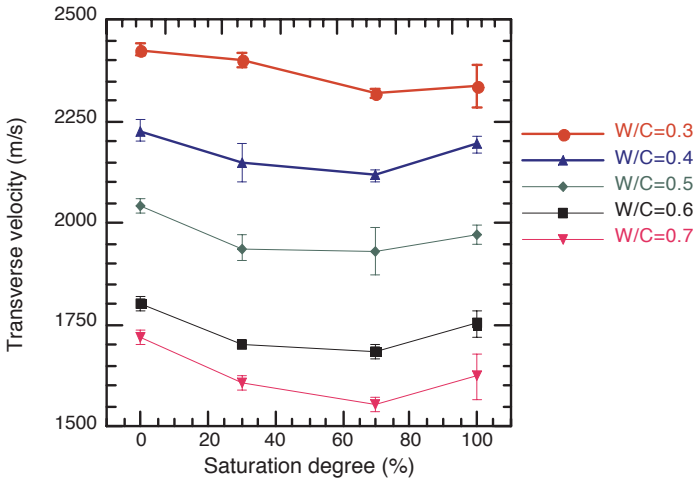

Figure 13.6: Measured cement paste transverse velocity vs. saturation for different W/C ratio

the transverse velocity value in the saturated material is expected to be inferior to the transverse velocity value in the dry material for a high range of porosity.
The partially saturated longitudinal and transverse velocities are lower than both dry and saturated states ones. Indeed, longitudinal and transverse velocities decrease as the degree of saturation increases until reaching a minimum at a partially saturated state and then increases at fully saturation (to a maximum value for longitudinal velocity). Such trend has often been observed for ultrasonic velocity measurements on various porous materials [58, 225]. For instance, Elliot and Wiley [64] noted similar variation for longitudinal velocity measured on Ottawa sand having a porosity of approximately 30%. Arguments and explanation on the partially saturation velocity observations will be detailed further when modeling the partial saturated cement paste in the next sections.

13.3 Correlations

Figure 13.7 shows a comparison between the experimental and computed longitudinal and transverse velocities when varying the saturation state and fixing the W/C to 0.3. It is noted that the general trend of the Mori-Tanaka estimated velocities follows the

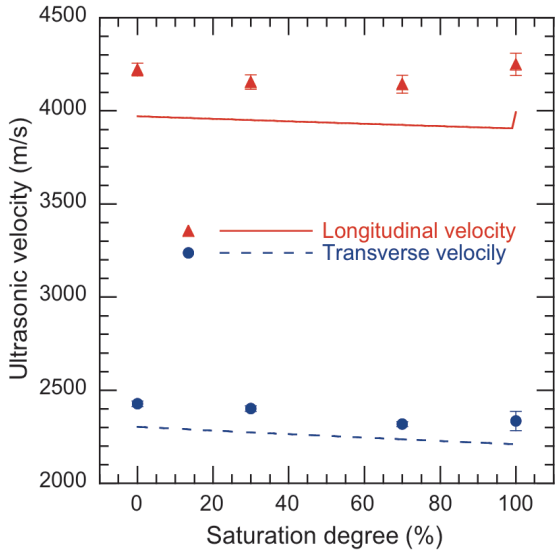

Figure 13.7: Comparison between measured ultrasonic velocities (dots) and Mori-Tanaka model (lines) estimates; W/C=0.3; $\alpha = 1$

measurements. However the model generally underestimates the measured velocities. The aspect ratio of pores was set in Fig.13.7 to 1 (spherical pores). Its variation to penny or needle shaped pores will induce lower estimate of the velocity. Indeed, it was

shown in Figs.13.3-10.4 that a penny or needle shaped pores cause the elastic moduli computed according to the Mori-Tanaka model to decrease. Moreover, experimental [4] and numerical [5] investigations on the influence of inclusion shape on the longitudinal wave velocity of mortar show that the velocity decreases when decreasing the aspect ratio of inclusion.
Thus, the parameters that should be investigated further to obtain a better description of the experimental measurement are the elastic moduli of the matrix phase. The latter were determined based on a homogenization of the matrix solid phases assuming that all the hydrated phases, including the high density C-S-H and the C-H crystals, form one phase represented by the low density C-S-H. Knowing that the high density C-S-H ($K = 18.84GPa$; $G = 11.85GPa$) and the C-H (33.99 < K (GPa) < 42.11 ; 15.23 < G (GPa) < 16.68 [156]) phases have stiffer elastic moduli than that of the low density C-S-H (Table 9.1.2), it was expected that the determined matrix moduli underestimate the actual values. In order to overcome this non-considered stiffness, an increase of the bulk and shear moduli was proposed. Simultaneously, the pores aspect ratio was varied for each W/C ratio composition.
As no similar development exist in the literature, a linear variation of the cement paste matrix elastic properties is proposed in this work. Eqs.(9.17)-(9.18) present a suggestion of the matrix bulk and shear dependence on the hydration degree and the saturation state.

$$K_0 = 40000 - 170p + 4000S_r \tag{13.1}$$

$$G_0 = 20000 - 90p + 200S_r \tag{13.2}$$

The fixed matrix elastic moduli are comparable to the direct measurements performed by Grasley et al. [83] on cement paste with varying the W/C ratio as reported in [213]. Figures 13.8 and 13.9 show the superposition of the experimental and mircomechanical longitudinal and transverse velocities in function of the saturation degree for the five cement paste compositions. Dots refer to the velocities that were directly measured on the cement paste samples as detailed previously. Vertical error bars correspond to the standard deviation of velocity estimated from three measurements. Lines represent the Mori-Tanaka model estimates of the longitudinal and transverse velocities. The latter were computed based on the determination of a homogenized bulk and shear moduli when considering that the cement paste is a two-phase material. The matrix was supposed to be continuous with elastic properties following Eqs.(13.1)-(13.2). Pores were assumed to be spheroidal and with aspect ratio lower than 1, i.e. penny shaped pores. Their elastic properties were supposed to vary when varying the saturation degree as suggested in Eq.(10.28).
The aspect ratio of pores was varied for each W/C ratio, the Mori-Tanaka estimated velocity was then compared to the experimental measurements. Based on a minimum distance between the measurements and the theoretical velocities that was detailed in previous work [147], the best fit was obtained for the pores' aspect ratio summarized in Table 13.1.

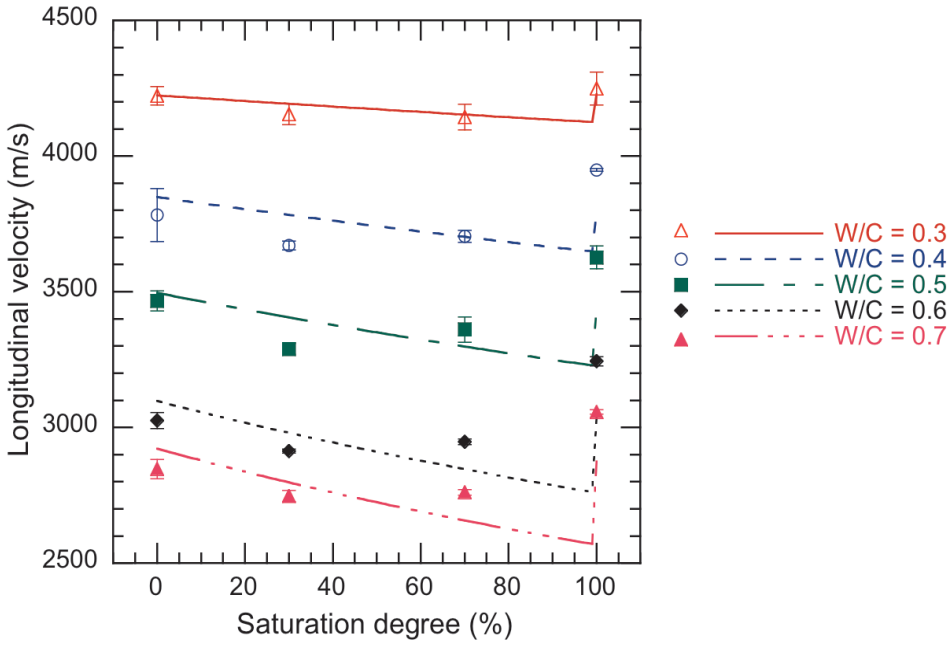

Figure 13.8: Comparison between measured ultrasonic longitudinal velocities (dots) and Mori-Tanaka model (lines) estimates vs. saturation degree

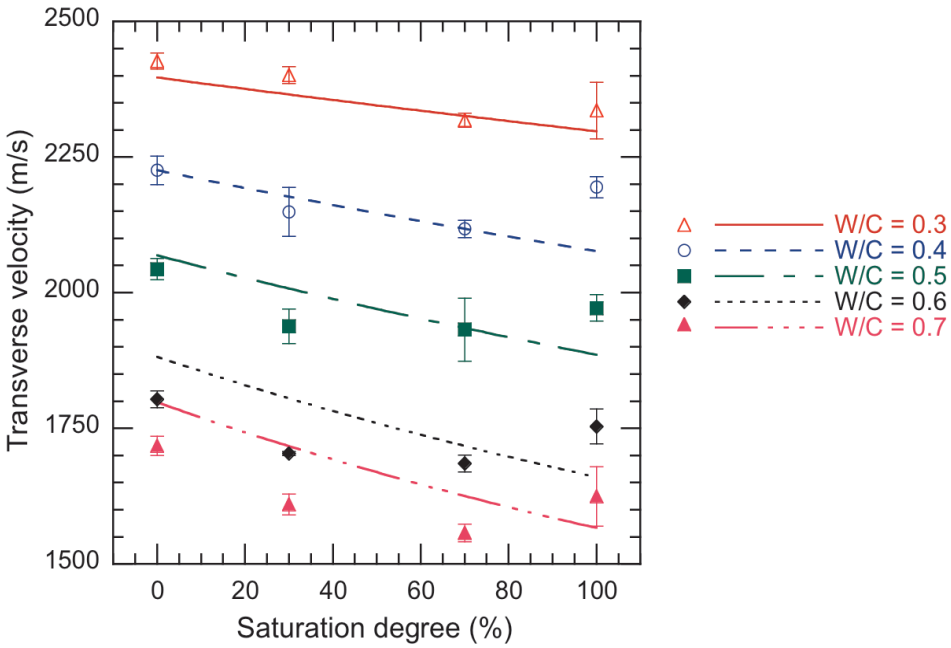

Figure 13.9: Comparison between the measured ultrasonic transverse velocities (dots) and the Mori-Tanaka model (lines) estimates when varying the saturation degree

It is noted from Fig.13.8 that the computed longitudinal velocity trend follows the

Table 13.1: Varied aspect ratio for different W/C ratio compositions

W/C	aspect ratio α
0.3	0.5
0.4	0.4
0.5	0.3
0.6	0.26
0.7	0.2

recorded data. For each W/C ratio, the longitudinal velocity decreases to reach a minimum in the neighborhood of $S_r = 98\%$, then increases to reach a maximum at fully saturation. The maximum reached by the theoretical velocity (at $S_r = 100\%$) is notably less than the corresponding measured velocity.
It is remarked that the increase in the estimated velocities is abrupt compared to a smooth increase in the experimental ones. The abrupt increase in the theoretical velocity can be explained by the abrupt increase in the pore bulk modulus as modeled earlier (Fig.10.11). A smoother increase in the longitudinal velocity would be achieved if the gap between the pores and the matrix bulk moduli was not so large. This stands to the possibly strong assumption of air-filled pores when the material is dry. Pores may contain air-vapor and / or have different bulk modulus than those of air.
In general, the fit between the longitudinal velocity measurements and the theory is largely satisfactory, especially for 0.3, 0.4 and 0.5 W/C ratio. The latter are characterized by a relatively low porosity. The 0.6 and 0.7 W/C samples present a high porosity that may cause interaction between the inclusions. Such effect may not be considered enough within the model.
Measured and estimated transverse velocities are plotted versus saturation degree, in Fig.13.9. The micromechanical determined transverse velocities appear to decrease uniformly at moderate rate from dry state to complete water saturation. This behavior was expected since the pore fluid has null shear modulus for all the saturation states and, consequently, the only effect of increasing the saturation degree on transverse velocity is the increase in density.
As for computed longitudinal velocities, computed transverse ones depart increasingly from measured transverse velocities with increasing water saturation and porosity. Indeed, the measured transverse velocities show an increase when approaching fully saturation state that is not detected in the theoretically estimated transverse velocities: no minimum of transverse estimated velocity was observed. It should be noted that the measured velocity increase at fully saturated state is much smaller in the transverse velocity than in the longitudinal velocity.
Figure 13.10 shows the relative error between the estimated and the measured longitudinal and transverse velocities for the different considered W/C ratios and when

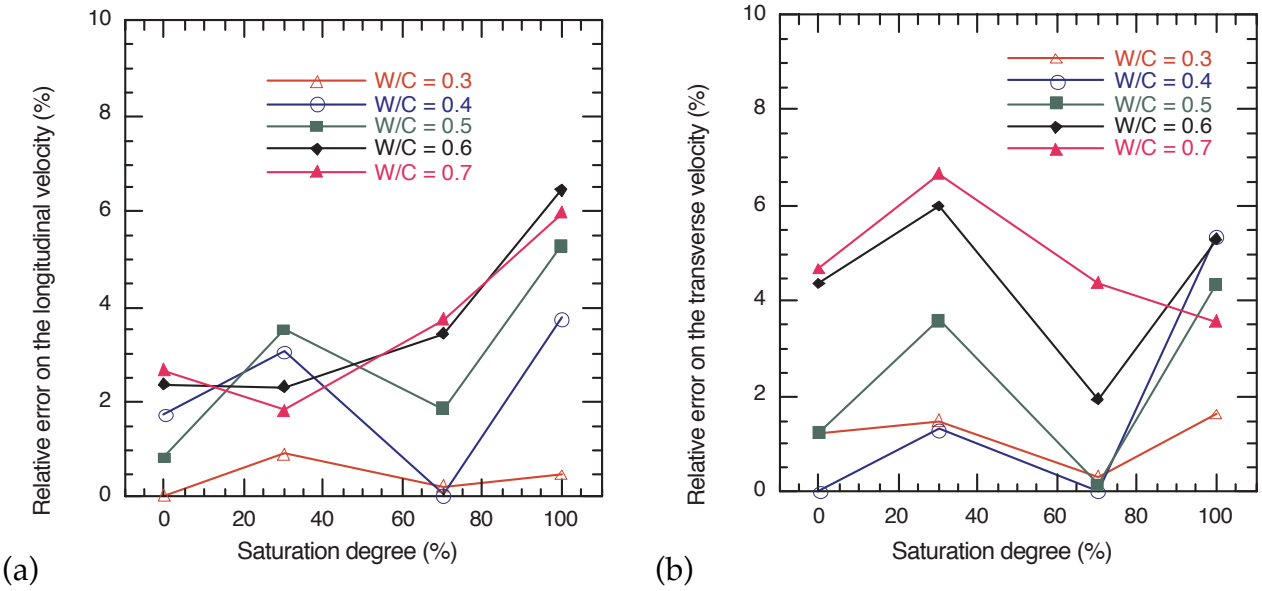

Figure 13.10: Relative error between (a) longitudinal and (b) transverse Mori-Tanaka estimated velocity and measured velocity

varying the saturation degree. The relative error on both longitudinal and transverse velocities is found to be increasing with the W/C ratio of the considered cement paste. This is due to the effect of increasing porosity in the estimated velocities. Moreover, it is noted that the computed curve departs appreciably from the measured values at the higher saturation degrees (almost 100%), especially for the transverse velocities. This discrepancy could be due to the variation of the pore shape when drying the material and that was not included in the above simulation. Indeed, if the pores' aspect ratio was varied not only with respect to the W/C ratio but also to the saturation degree, a better fit between the measured and the modeled velocities would be obtained. However, such simulations are not presented in the present report in order to minimize the number of input parameter within the model and to allow an inverse problem to be developed. But in general, both measured and computed velocities show a pronounced similar trends with increasing saturation with a relative error not exceeding 6.5%. Then the agreement between the computed and the measured velocities can be considered as very satisfactory. Accordingly, the Mori-Tanaka model is proved to be a representative model of the cement paste composite structure. It can provide a reliable relationship between the cement paste porosity and the macroscopic ultrasonic velocity.

Chapter 14

Air-entrained cement paste

14.1 Ultrasonic measured results

The ultrasonic measurements were carried out on the air-entrained cement paste cylindrical cores using the previously presented device (chapter 8). In order to justify the choice of the measured ultrasonic parameters (i.e. pulse velocities), the wavelength to macropores diameter D was determined for each measurement. Figure 14.1 shows the range of the wavelength λ to macropores's diameter for all measured velocities. It is

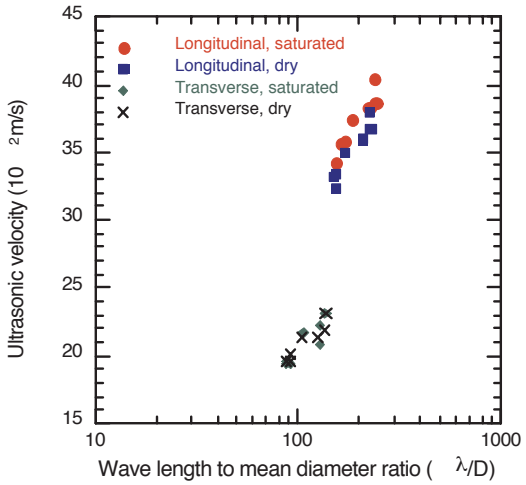

Figure 14.1: ultrasonic wave velocities versus wavelength (λ) to macropore diameter ratio for the air-entrained cement paste.

noted that this ratio is about two times larger for the longitudinal wave than for the transverse one. But for both velocities, it is clear that $\frac{\lambda}{D} >> 1$. Thus, in this work, the effect of high order multiple scattering in the air entrained cement paste was neglected and the measured data was the phase velocity.
The effect of macroporosity on the ultrasonic longitudinal and transverse phase velocities propagating into the dry and saturated samples was investigated. Figure 14.2 shows both the longitudinal and transverse ultrasonic pulse velocities versus porosity for the two considered saturation states of the air-entrained cement paste. The ultrasonic velocities were directly measured on the samples as detailed previous chapter.

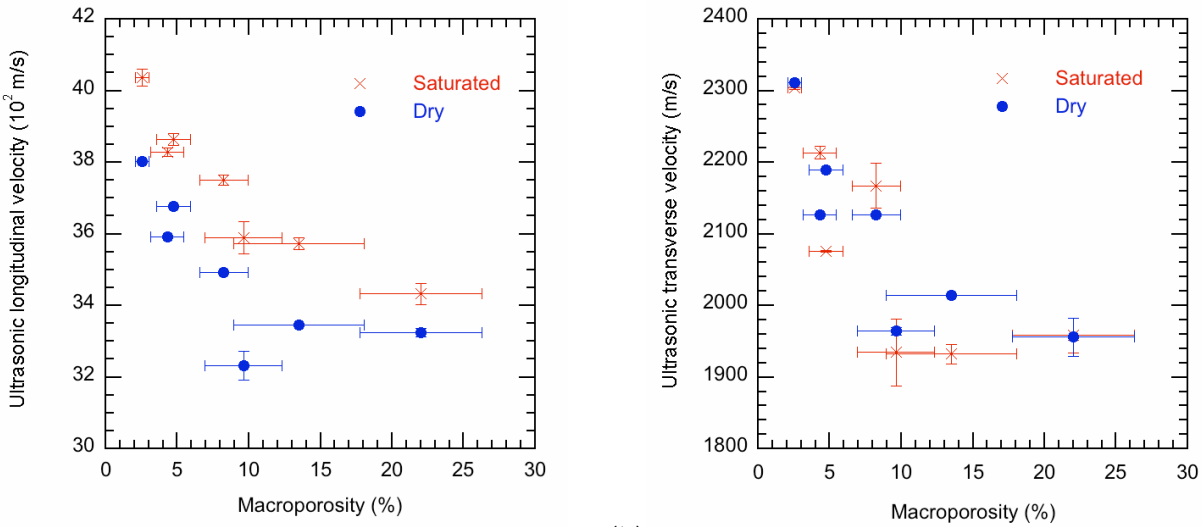

(a) (b)

Figure 14.2: Variation of (a) longitudinal and (b) transverse ultrasonic velocity vs. porosity for saturated and dry air-entrained cement paste.

Vertical error bars correspond to the standard deviation of velocity estimated from three measurements. Horizontal error bars refer to the standard deviation of macroporosity determined by image processing over the twelve different investigated sections.

It is noted that both transverse and longitudinal experimentally determined velocities decrease when macroporosity increases. Besides, it is remarked that the longitudinal velocities values are almost the double of the transverse values for both dry and saturated states.

Comparison between the longitudinal velocities measured at saturated and dry states (Fig.14.2(a)) indicates a decrease in the longitudinal velocity during the drying of the samples. This is principally due to two phenomena. First, the presence of water in the saturated sample induces an increase of the propagated wave velocity inside the material (the ultrasonic longitudinal velocity is higher in water than in air). Secondly, drying a cementitious sample creates cracks even at relatively low temperature (60 °C), which decreases the velocity in a dried sample.

However for the transverse velocities (Fig.14.2(b)), the dry and saturated measured velocities trends are overlapped. This means that the saturation state doesn't affect the transverse velocity. Indeed, air and water that represent the filled material of the micropores in the dry and saturated states respectively have both similar transverse properties, namely transverse ultrasonic velocity.

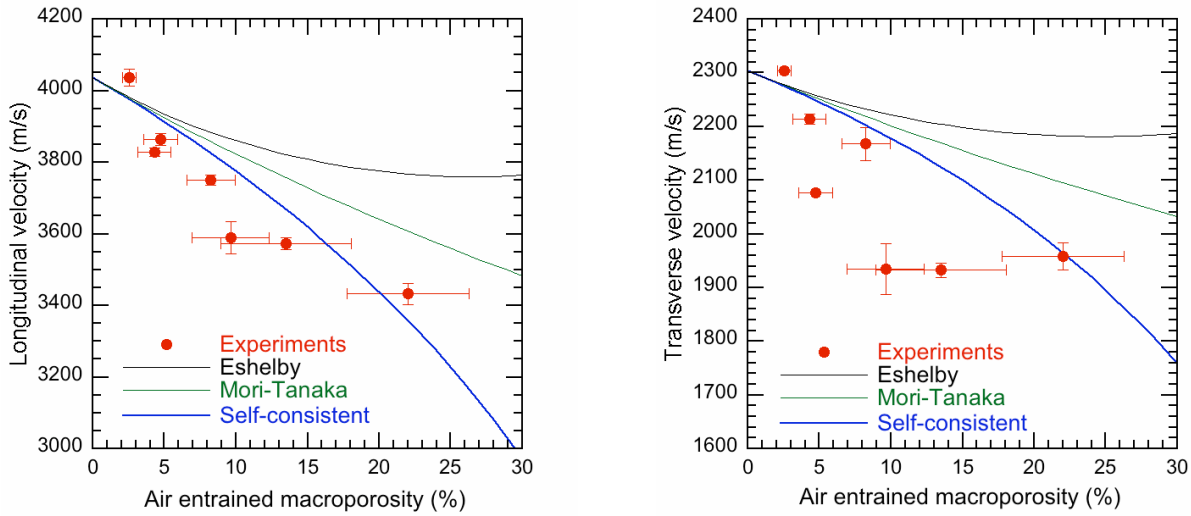

(a) (b)

Figure 14.3: Experimental and estimated velocities for saturated cement paste material vs porosity (a) Longitudinal (b) Transverse

14.2 Correlations

It has been shown in the previous part that the self-consistent model give a very good approximation of the homogenized elastic moduli of the air-entrained cement paste. Here, two other models, the dilute inclusion model and the Mori-Tanaka model for spherical pores, are plotted in addition to the self-consistent model in order to illustrate the acceptable match.

Figures 14.3 and 14.4 show both the micromechanical and experimental evolution of ultrasonic velocities with macroporosity for the two considered saturation states. The longitudinal and transverse velocities of dry and fully saturated air-entrained cement paste were evaluated using the models presented above, based on two-phase formulations and assuming spherical inclusions (dry macropores). The same ultrasonic properties were directly measured on the samples as detailed previously. Vertical error bars correspond to the standard deviation of velocity estimated from three measurements. Horizontal error bars refer to the standard deviation of macroporosity determined by image processing over 12 air-entrained cement paste sections.

The micromechanical and experimental velocities decrease when macroporosity increases. This trend is coherent with all the models described above, where bulk and shear moduli were assumed to be inversely proportional to the inclusion volume fraction (porosity). In addition, longitudinal and shear velocities were assumed to be proportional to the elastic moduli and inversely proportional to density as given by Eqs.(8.7)-(8.8).

Comparison between the micromechanically estimated velocities in the saturated (Fig.14.3)

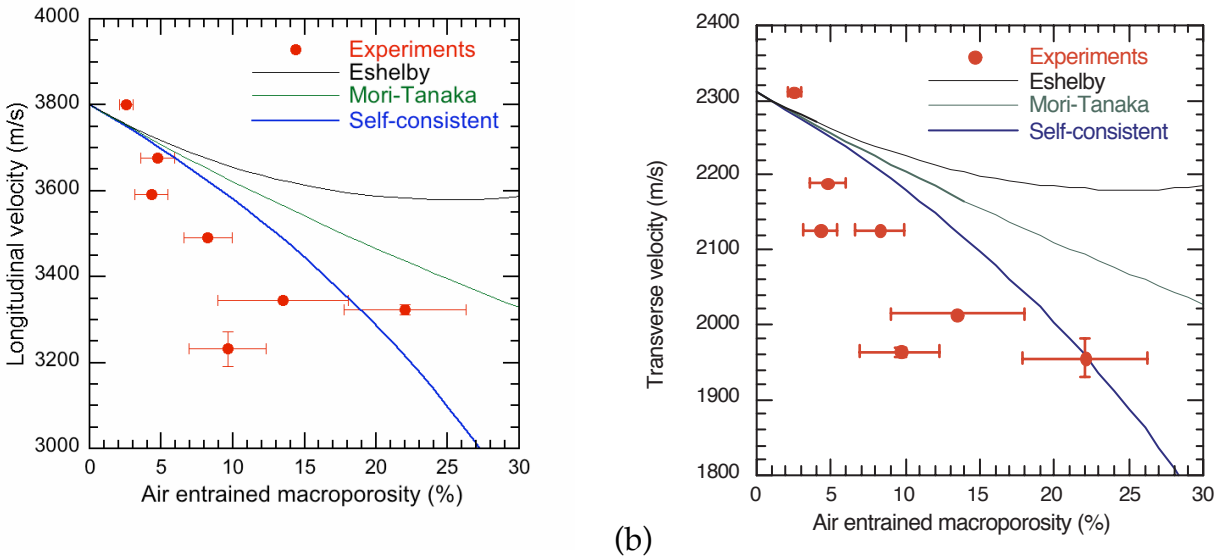

(a) (b)

Figure 14.4: Experimental and estimated velocities for dry cement paste material vs porosity (a) Longitudinal (b) Transverse

and dry (Fig.14.4) states, shows a decrease in the longitudinal and transverse velocities during the drying of samples. This is in accordance with the measured velocities.
According to Figs.14.3-14.4, the dilute inclusion model overestimates both transverse and longitudinal velocities, in dry and saturated states. This result was obtained for all macroporosities (all AE%) except for very low ones (less than 5%). This was expected as this model assumes low inclusions fractions and no interaction between the inclusions. This explains the enlarging gap between the dilute inclusion estimates and the ultrasonic measurements as macroporosity increases.
In both dry and saturated states, Mori-Tanaka predictions (Table 11.1) plotted in Figs.14.3-14.4 appear to fit better (than the dilute inclusion model) the experimental results but for macroporosity not exceeding 10%. Although the Mori-Tanaka model is considered to take into account the interactions between inclusions, its formulation is carried out while assuming that the matrix medium is a collection of non-interacting inhomogeneities. Thus, for volume fraction greater than 10%, the Mori-Tanaka model is not reliable for modeling the air-entrained cement paste composite. In addition, the estimated results were not in accordance with the measured results. The aforementioned disadvantage of the Mori-Tanaka model is particularly emphasized in the case of dynamic excitation because of the scattering phenomena caused by inhomogeneities present in the matrix and because of the interactions between them [161]. This problem was not highlighted when studying the cement paste material because of inclusions size. Indeed, the micropores, which are considered as inclusions in the cement paste material, are small enough so that the scattering phenomena are almost vanishing. However, the macropores assumed to be the inclusions phase of the air-entrained ce-

ment paste are of bigger size and can cause a scattering phenomena.
In the self-consistent formulation (Table 11.1), each particle considers the matrix medium as the still unknown effective medium. In such a scheme, the interactions between the inclusions are considered in the matrix modeling. The latter argue the good agreement that is shown in Figs.14.3-14.4 between the estimated self-consistent velocities and the ultrasonic measured ones. In fact, for the case of saturated air-entrained cement paste shown in Fig.14.3(a), it is noted that the longitudinal velocities estimated by the self-consistent models fit the measured data for all the porosities with a maximal relative error of 5.2 %. While, in Fig.14.3(b), three of the air-entrained cement paste compositions present a relatively low transverse velocity. This is due to the difficulties to measure transverse velocity, like the coupling between the sample and the transducer as well as the diffusion phenomenon.
For the dry state illustrated in Fig.14.4, the self-consistent model shows similarities with the experimental results as those observed for the saturated state. A small discrepancy was noted between the estimated self-consistent longitudinal and transverse velocities and the measured ones for the dry state. This was caused by the creation of micro-cracks during the drying of the samples. Such cracks influence the measured velocity by decreasing it but it was not taken into consideration in the micromechanical modeling here developed.

Conclusion

In this part, the frequency of 500kHz was considered to be within the low frequency range. Thus, the ultrasonic propagation was described by the theory of homogenization. The Mori-Tanaka and the self-consistent micromechanical models were applied to the cement paste and the air-entrained cement paste material, respectively, to estimate the longitudinal and transverse velocities. Different saturation states were simulated. The obtained results were compared to the measured ultrasonic velocities.

Hence, experimental measurements showed that longitudinal and transverse velocities decrease as the degree of saturation increases until reaching a minimum at a partially saturated state and then increases at fully saturation. Similar trends were observed when applying micromechanical modeling to estimate the ultrasonic velocities propagating into the cement paste and the air-entrained cement paste.

Indeed, for the cement paste material, the Mori Tanaka model was applied when assuming that the matrix elastic properties depend on the W/C ratio and the saturation state. It was also assumed that pores are penny shaped spheroids with aspect ratio decreasing when the W/C ratio increases.
The air-entrained cement paste material longitudinal and transverse velocities were estimated based on the self-consistent model. The material was assumed to be a two-phase composite with spherical inclusions; macropores, and a cement paste matrix. The latter was assumed to be saturation dependent as it includes the microporous material structure.

Assuming these considerations for both materials, the micromechanical predictions show a fair agreement with the experimental data.

Conclusions

The cement-based materials are used for waste's storage, historical monuments or more generally in structures. Thus, the monitoring and the follow-up of these structures are of great interest for many engineering fields. In civil engineering, the degradation of the cement-based materials is generally caused by the penetration of aggressive agents through connected pores. Consequently, porosity has a practical importance in controlling such materials. It is recognized as significant durability indicator.

Current on-site tests aim to determine the material's hydraulic properties when involving cost effective methods that would not disturb or damage it. Thus, many nondestructive technologies have been developed, namely ultrasound. Hence, prediction of hydraulic parameters by means of nondestructive ultrasound method was among the major incentives for this thesis.
Indeed, the present work aimed to propose a correlation between the ultrasonic velocity and the porosity of cementitious materials. It was based on the micromechanical modeling of cementitious material with different W/C ratios and saturation degrees. The challenge was on the application of micromechanical models to civil engineering materials. It should be emphasized that micromechanical modeling was developed in close interaction with experimental work that has been undertaken in Ecole Centrale de Lille since many years. The latter was concerned with classical and commonly used testing methods in civil engineering, like the water imbibition or mercury intrusion porosimetry, but also with more sophisticated methods that were carried out to investigate the microstructure of the material, such as microtomography and SEM.

In this thesis the investigated material was the cement paste. This material is a critical binding material in mortar and concrete. The study of the air-entrained cement paste aimed to uncouple the effects of porosity and water content on the velocity variation. This study included laboratory tests on both cement paste and air-entrained cement paste. Five water/cement ratio were considered for this investigation: 0.3, 0.4, 0.4, 0.5, 0.6 and 0.7. For each composition, dry, fully and partially (30 and 70 %) saturation states were studied. The work focused also on the effects of these parameters on measured longitudinal (V_L) and transverse (V_T) ultrasonic velocities.

A study was performed on the microstructure of cement paste involving different techniques. The water imbibition was considered as reliable measurement of the connected porosity in the cement paste material. The obtained results showed an increase of porosity from 21.13% to 47.34% when the W/C ratio increased from 0.3 to 0.7. Mercury intrusion porosimetry was used for the characterization of the pore structure and distribution in cement paste. For that test, sample preparation and data interpretation needed great care, especially with regard to the ink-bottle effect. The investigation

on the macroporous structure of the air-entrained cement paste was performed based on X-ray microtomgraphy. The application of the SEM image technique enhanced the characterization of the developed phases within a hydrating cement paste. Accurate specimen preparation was important to ensure high quality images. All these techniques provided information on the different phases forming the cement paste material and concluded that it is a composite material with a matrix and embedded inclusions: pores. Hence, these observations helped in deciding about the micromechanical modelling assumptions. They have been very useful for making the micromechanical modelling finer and closer to the actual physics.

Accordingly, detailed literature review and synthesis of existing work on multiphase composite homogenization methods were essential. The necessary tools to model a porous structure was also studied.
The followed approach has been gradual and consisted first in applying different homogenization models to estimate the behavior of the cement paste material. This required the identification of elastic parameters of the different constituents of the cement paste, namely, the matrix and pores. The behavior of cement paste matrix moduli was suggested to vary with the W/C ratio and the saturation state. Pores were assumed to be air-filled in the case of dry cement paste and water-filled in the case of fully saturation. However, air voids were supposed to be air-filled for both saturation states when modeling the air-entrained cement paste. In the case of partial saturation, an attempt to understand the behavior of air and water present in pores was proposed. Both fluids were supposed to form a suspension into the porous volume and a first step homogenization was carried out based on Reuss model.
The study showed clearly the impact of the change in the phases properties and saturation on the macroscopic elastic properties. Following a comparative study on different micromechanical models, two models were selected in the thesis: the Mori-Tanaka and the self-consistent schemes. Both are considered to take into account the interaction between inclusions. A sensitivity analysis was performed on the shape and volume fraction of pores. The matrix was considered to be continuous. However, the porous volume was modeled as spheroidal inclusions with an aspect ratio dependent on the cement paste W/C ratio. Penny shaped pores were found to give good representation of the porous volume. The aspect ratio was supposed to be the same of all pores for a fixed W/C. Beside, it was considered to decrease gradually between 0.5 and 0.2 when the W/C ratio increased from 0.3 to 0.7
The saturation degree of cementitious material strongly influences their dynamic properties. Indeed, the saturated cement paste material is mechanically more rigid than the dry one. However, the partially saturated cement paste dynamic properties, mainly longitudinal velocity, were found to be lower than both dry and fully saturated states. The porosity, the pore geometry and the saturation degree were identified as key parameters that affect the longitudinal and transverse velocities. The proposed micromechanical modeling allowed considerable understanding of such effects and provided

physical interpretations of several relations between velocity, porosity and saturation.

The main results show that the selected models give satisfactory results for both cement paste and air-entrained cement paste. For instance, the relative error in estimating the cement paste elastic moduli was lower than 8%. Thus, these results construct a base for upcoming development of nondestructive ultrasonic methods that may be a viable approach for the monitoring of cementitious materials durability. The accuracy and reliability of the on site measurement set-up is on progress.
Considering the promising correlations obtained for cement paste, further studies are necessary to establish whether the non-destructive ultrasonic measurements may be useful to infer durability of mortar and concrete in situ structures.
Besides, correlations that should be targeted for further studies are between the ultrasonic velocities when including the surface wave and permeability, since the latter is as significant indicator of durability as the porosity.

Appendices

Appendix A

Elastic constants relations

Table A.1: Elastic constants relations

	λ	$G = \mu$	K	E	ν	V_L	V_T
λ, G			$\frac{3\lambda + 2G}{3}$	$\frac{G(3\lambda + 2G)}{\lambda + G}$	$\frac{\lambda}{2(\lambda + G)}$	$\sqrt{\frac{\lambda + 2G}{\rho}}$	
λ, E		$(E - 3\lambda) + \frac{\sqrt{(E - 3\lambda)^2 + 8\lambda E}}{4}$	$(3\lambda + E) + \frac{\sqrt{(3\lambda + E)^2 - 4\lambda E}}{6}$		$-(E + \lambda) + \frac{\sqrt{(E + \lambda)^2 + 8\lambda^2}}{4\lambda}$		
λ, ν		$\frac{\lambda(1 - 2\nu)}{2\nu}$	$\frac{\lambda(1 + \nu)}{3\nu}$	$\frac{\lambda(1 + \nu)(1 - 2\nu)}{\nu}$			
λ, K		$\frac{3(K - \lambda)}{2}$		$\frac{9K(K - \lambda)}{3K - \lambda}$	$\frac{\lambda}{3K - \lambda}$		
G, E	$\frac{\mu(2G - E)}{E - 3G}$		$\frac{GE}{3(3G - E)}$		$\frac{E - 2G}{2G}$		
G, ν	$\frac{2G\nu}{1 - 2\nu}$		$\frac{2G(1 + \nu)}{3(1 - 2\nu)}$	$2G(1 + \nu)$			
G, K	$\frac{3K - 2G}{3}$			$\frac{9KG}{3K + G}$	$\frac{3K - 2G}{2(3K + G)}$	$\sqrt{\frac{K + 4/3G}{\rho}}$	$\sqrt{\frac{G}{\rho}}$
E, ν	$\frac{\nu E}{(1 + \nu)(1 - 2\nu)}$	$\frac{E}{2(1 + \nu)}$	$\frac{E}{3(1 - 2\nu)}$			$\sqrt{\frac{E}{\rho(1 - \frac{2\nu^2}{(1 - \nu)})}}$	
E, K	$\frac{3K(3K - E)}{9K - E}$	$\frac{3EK}{9K - E}$			$\frac{3K - E}{6K}$		
ν, K	$\frac{3K\nu}{1 + \nu}$	$\frac{3K(1 - 2\nu)}{2(1 + \nu)}$		$3K(1 - 2\nu)$			
V_L, V_T	$\rho(V_L^2 - 2V_T^2)$	ρV_T^2	$\rho(V_L^2 - (4/3)V_T^2)$	$\rho V_T^2 \frac{3V_L^2 - 4V_T^2}{V_L^2 - V_T^2}$	$\frac{1 - 2(V_T/V_L)^2}{2 - 2(V_T/V_L)^2}$		

Appendix B

Elastic constant tensor

Consider a body subjected to a uniform strain U_{ij}, the elastic constants tensor is given by the following equation [120]:

$$C_{ijkl} = \frac{d^2W}{dU_{ij}dU_{kl}} \tag{B.1}$$

Where: W is the energy density.
The symmetry relation given in Eq.(B.1) means that the elastic constant tensor **C** will have only 45 independent components.
If the initial stress tensor σ_{ij} is symmetric, then the body torque is zero and it becomes rotationally invariant. Thus, the following relations are obtained:

$$\begin{aligned}
\sigma_{11} &= C_{2121} - C_{1221} = C_{3131} - C_{1313} \\
\sigma_{22} &= C_{1212} - C_{1221} = C_{3232} - C_{2332} \\
\sigma_{33} &= C_{1313} - C_{1331} = C_{2323} - C_{2332}
\end{aligned}$$

$$\begin{aligned}
\sigma_{12} &= C_{1112} - C_{1121} = C_{2122} - C_{1222} = C_{3132} - C_{1323} \\
\sigma_{13} &= C_{1113} - C_{1131} = C_{2123} - C_{1223} = C_{3133} - C_{1333} \\
\sigma_{23} &= C_{1213} - C_{1231} = C_{2223} - C_{2232} = C_{3233} - C_{2333}
\end{aligned}$$

$$C_{1123} = C_{1132} \quad ; \quad C_{1233} = C_{2133} \quad ; \quad C_{1322} = C_{2231}$$

$$C_{1223} = C_{1232} = C_{2132}$$

$$C_{1231} = C_{1321} = C_{2131}$$

$$C_{1323} = C_{1332} = C_{2331}$$

This reduces the number of independent components to 27.
For orthotropic materials [223] , there would be nine independent, non-zero elastic constants with the relations:

$$\begin{aligned}
c_{11} &\neq c_{22} \neq c_{33} \\
c_{12} &\neq c_{23} \neq c_{13} \\
c_{44} &\neq c_{55} \neq c_{66}
\end{aligned}$$

Or in a matrix form, such that:

$$c_{ij} = \begin{pmatrix}
c_{11} & c_{12} & c_{13} & 0 & 0 & 0 \\
c_{12} & c_{22} & c_{23} & 0 & 0 & 0 \\
c_{13} & c_{23} & c_{33} & 0 & 0 & 0 \\
0 & 0 & 0 & c_{44} & 0 & 0 \\
0 & 0 & 0 & 0 & c_{55} & 0 \\
0 & 0 & 0 & 0 & 0 & c_{66}
\end{pmatrix} \tag{B.2}$$

For an isotropic material, the elastic constants are given by the relation [203]:

$$C_{ijkl} = K\delta_{ij}\delta_{kl} + \mu(\delta_{ik}\delta_{jl} + \delta_{il}\delta_{jk} - \frac{2}{3}\delta_{ij}\delta_{kl})$$

Thus,there are only two non-zero independent elastic constants according to the relations:

$$\begin{array}{ccccccc} c_{11} & = & c_{22} & = & c_{33} & = & \lambda + 2\mu \\ c_{12} & = & c_{13} & = & c_{23} & = & \lambda \\ c_{44} & = & c_{55} & = & c_{66} & = & \mu \end{array}$$

Where:
$c_{11} = C_{1111}$
$c_{22} = C_{2222}$
$c_{33} = C_{3333}$
$c_{12} = C_{1122}$
$c_{13} = C_{1133}$
$c_{23} = C_{2233}$
$c_{44} = C_{1212}$
$c_{55} = C_{1313}$
$c_{66} = C_{2323}$

Appendix C

Proof of the Hashin-Shtrikman statements

The functional Π is given by:

$$\Pi(p_{ij}, \varepsilon'_{ij}) = \Pi_0 - \frac{1}{2}\int_V \Delta C^{-1}_{ijkl} p_{ij} p_{kl} - p_{ij}\varepsilon'_{ij} - 2p_{ij}\varepsilon_{ij} dV \tag{C.1}$$

Π will reach a minimum (maximum) if $\delta\Pi = 0$ and $\delta^2\Pi > 0$ ($\delta^2\Pi < 0$). In order to determine the minimum and the maximum of this function, the first and second variation of the function Π are computed in the sense of Gateau.
Recall of the Gateau variation
The n-th order Gateau variation is [188]:

$$\delta^n G\Pi(p_{ij}, \varepsilon'_{ij}) = \frac{d^n}{d\alpha^n}\Pi(p_{ij}, \varepsilon'_{ij}), \qquad \forall n \geq 1 \tag{C.2}$$

such that:

$$\Delta\Pi = \Pi(p_{ij} + \delta p_{ij}, \varepsilon'_{ij} + \delta\varepsilon'_{ij}) - \Pi(p_{ij}, \varepsilon'_{ij}) \tag{C.3}$$

$$= \delta\Pi + \frac{1}{2!}\delta^2\Pi + \frac{1}{3!}\delta^3\Pi + \frac{1}{4!}\delta^4\Pi + \cdots \tag{C.4}$$

The Gateau variation operation defined previously follows the same rule as the differentiation operation in elementary calculus.

First, differentiate Π and show that $\delta\Pi$ is null.

$$\delta\Pi = -\frac{1}{2}\int_V \Delta C^{-1}_{ijkl}(\delta p_{ij}p_{kl} + p_{ij}\delta p_{kl}) - \delta p_{ij}\varepsilon'_{ij} - p_{ij}\delta\varepsilon'_{ij} - 2\delta p_{ij}\varepsilon_{ij}dV \tag{C.5}$$

$$= -\frac{1}{2}\int_V \Delta C^{-1}_{ijkl}\delta p_{ij}p_{kl} + \underbrace{\Delta C^{-1}_{klij}}_{=\Delta C^{-1}_{ijkl}\text{, because C has minor symmetry}} p_{ij}\delta p_{kl}$$

$$-\delta p_{ij}\varepsilon'_{ij} - p_{ij}\delta\varepsilon'_{ij} - 2\delta p_{ij}\underbrace{(\varepsilon_{ij} - \varepsilon'_{ij})}_{=\varepsilon_{ij}}dV \tag{C.6}$$

$$= -\frac{1}{2}\int_V 2\Delta C^{-1}_{ijkl}\delta p_{ij}p_{kl} + \delta p_{ij}\varepsilon'_{ij} - p_{ij}\delta\varepsilon'_{ij} - 2\delta p_{ij}\varepsilon_{ij}dV \tag{C.7}$$

$$= -\frac{1}{2}\int_V 2\underbrace{(\Delta C^{-1}_{ijkl}p_{kl} - \varepsilon_{ij})}_{=0}\delta p_{ij} + \delta p_{ij}\varepsilon'_{ij} - p_{ij}\delta\varepsilon'_{ij}dV \tag{C.8}$$

$$= -\frac{1}{2}\int_V \delta p_{ij}\varepsilon'_{ij} - p_{ij}\delta\varepsilon'_{ij}dV \tag{C.9}$$

If the subsidiary condition (Eq.2.42) is verified, i.e

$$t_{ij,j} = p_{ij,j} + (C_{ijkl}\varepsilon'_{ij})_{,j} = 0 \tag{C.10}$$

then, one can write:

$$\delta t_{ij} = \delta p_{ij} + C_{ijkl}\delta\varepsilon'_{kl} = 0 \qquad \text{and} \qquad t_{ij,j} = 0 \tag{C.11}$$

Substituting Eq.(C.11) in Eq.(C.9) leads to:

$$\delta\Pi = -\frac{1}{2}\int_V \varepsilon'_{ij}(\delta t_{ij} - C_{ijkl}\delta\varepsilon'_{kl}) - \delta\varepsilon'_{ij}(t_{ij} - C_{ijkl}\varepsilon'_{ij})dV \tag{C.12}$$

$$= -\frac{1}{2}\int_V (\varepsilon'_{ij}\delta t_{ij} - t_{ij}\delta\varepsilon'_{ij}) \underbrace{-\varepsilon'_{ij}C_{ijkl}\delta\varepsilon'_{kl}) + \delta\varepsilon'_{ij}C_{ijkl}\varepsilon'_{ij}}_{=0\text{, because } C \text{ has the minor symmetry}} dV \tag{C.13}$$

$$= -\frac{1}{2}\int_V (\underbrace{\varepsilon'_{ij}}_{=\frac{1}{2}(u'_{i,j}+u'_{j,i})}\delta t_{ij} - t_{ij}\delta\underbrace{\varepsilon'_{ij}}_{=\frac{1}{2}(u'_{i,j}+u'_{j,i})})dV \tag{C.14}$$

$$= -\frac{1}{2}[(\int_{\partial V}\delta t_{ij}n_j u'_i dS - \int_V \delta t_{ij,j}u'_i dV) -$$

$$(\int_{\partial V} t_{ij}n_j\delta u'_i dS - \int_V t_{ij,j}\delta u'_i dV)] \tag{C.15}$$

If the boundary condition on the displacement is verified (Eq.2.34) $u'_i = 0$ and the subsidiary condition (Eq.C.10) is satisfied $t_{ij,j} = 0$, then the first statement is proved:

$$\delta\Pi = 0 \tag{C.16}$$

As for the second statement of Hashin-Shtrikman variational principle, $\delta^2\Pi$ is computed.
From Eq.(C.3) one can write:

$$\begin{aligned}
\Delta\Pi &= \Pi(p_{ij}+\delta p_{ij}, \varepsilon'_{ij}+\delta\varepsilon'_{ij}) - \Pi(p_{ij}, \varepsilon'_{ij}) && \text{(C.17)}\\
&= \frac{1}{2}\int_V (\underbrace{-\Delta C^{-1}_{ijkl} p_{ij}\delta p_{kl} - \Delta C^{-1}_{ijkl}\delta p_{ij} p_{kl}}_{=-2\Delta C^{-1}_{ijkl} p_{kl}\delta p_{ij}, \text{because } \Delta C^{-1}_{ijkl} \text{ has the minor symmetry}} \\
&\quad + p_{ij}\delta\varepsilon'_{ij} + \delta p_{ij}\varepsilon'_{ij} + 2\delta p_{ij}\varepsilon_{ij})dV \\
&\quad + \frac{1}{2}\int_V (-\Delta C^{-1}_{ijkl}\delta p_{ij}\delta p_{kl} + \delta p_{ij}\delta\varepsilon'_{kl})dV && \text{(C.18)}\\
&\overset{Eq.C.4}{=} \delta\Pi + \frac{1}{2!}\delta^2\Pi && \text{(C.19)}
\end{aligned}$$

Using the expression of $\delta\Pi$ found in Eq.(C.5) and substituting $\delta p_{ij} = \delta t_{ij} - C_{ijkl}\delta\varepsilon'_{kl}$ (Eq.C.11); $\delta^2\Pi$ is given by:

$$\begin{aligned}
\delta^2\Pi &= \int_V (-\Delta C^{-1}_{ijkl}\delta p_{ij}\delta p_{kl} + \delta p_{ij}\delta\varepsilon'_{kl})dV && \text{(C.20)}\\
&= \int_V (-\Delta C^{-1}_{ijkl}\delta p_{ij}\delta p_{kl} + \underbrace{\delta t_{ij}\delta\varepsilon'_{kl}}_{=0}) - C_{ijkl}\delta\varepsilon'_{kl})dV && \text{(C.21)}\\
&= -\int_V (\Delta C^{-1}_{ijkl}\delta p_{ij}\delta p_{kl} + C_{ijkl}\delta\varepsilon'_{kl})dV && \text{(C.22)}
\end{aligned}$$

As $\Delta\mathbf{C}$ is symmetric matrix, then

$$\text{if} \quad \Delta\mathbf{C}^{-1} \quad \text{is definite positive} \Longrightarrow \Delta\mathbf{C} \quad \text{is definite positive} \qquad \text{(C.23)}$$

So, if $\Delta\mathbf{C} > 0$, $\delta^2\Pi < 0$, therefor, Π achieves a maximum value. For the other case, $\Delta\mathbf{C} < 0$, the judgement on the signe of $\delta^2\Pi$ is not obvious.
Consider the following positive integral:

$$I = \int_V (C_{ijkl})^{-1}\delta p_{ij}\delta p_{kl}dV > 0 \qquad \text{(C.24)}$$

Substitute $\delta p_{ij} = \delta t_{ij} - C_{ijkl}\delta\varepsilon'_{kl}$ into Eq.(C.24):

$$\begin{aligned}
I &= \int_V ((C_{ijkl})^{-1}\delta t_{ij}\delta t_{kl} - \underbrace{2\delta t_{ij}\delta\varepsilon'_{kl}}_{=0} + C_{ijkl}\delta\varepsilon'_{ij}\delta\varepsilon'_{kl})dV && \text{(C.25)}\\
&= \int_V ((C_{ijkl})^{-1}\delta t_{ij}\delta t_{kl} + C_{ijkl}\delta\varepsilon'_{ij}\delta\varepsilon'_{kl})dV && \text{(C.26)}
\end{aligned}$$

Eqs.(C.24)-(C.26) imply the inequality:

$$\int_V (C_{ijkl})^{-1}\delta p_{ij}\delta p_{kl}dV > \int_V C_{ijkl}\delta\varepsilon'_{ij}\delta\varepsilon'_{kl}\delta\varepsilon'_{kl})dV \tag{C.27}$$

which leads to

$$\begin{aligned}\delta^2\Pi &= -\int_V (\Delta C^{-1}_{ijkl}\delta p_{ij}\delta p_{kl} + C_{ijkl}\delta\varepsilon'_{kl}\delta\varepsilon'_{kl})dV &\text{(C.28)}\\ &\geq -\int_V (\Delta C^{-1}_{ijkl} + (C_{ijkl})^{-1})\delta p_{ij}\delta p_{kl}dV &\text{(C.29)}\end{aligned}$$

Consider the following formulation:

$$\begin{aligned}\Delta\mathbf{C}^{-1} + \mathbf{C}^{-1} &= \Delta\mathbf{C}^{-1} + \mathbf{C}^{-1} : (\mathbf{C} - \mathbf{C}) : (\mathbf{C} - \mathbf{C})^{-1} &\text{(C.30)}\\ &= \Delta\mathbf{C}^{-1} + (\mathbf{C}^{-1} : \mathbf{C} - \mathbf{I}) : \Delta\mathbf{C}^{-1} &\text{(C.31)}\\ &= \Delta\mathbf{C}^{-1} + \mathbf{C}^{-1} : \mathbf{C} : \Delta\mathbf{C}^{-1} - \Delta\mathbf{C}^{-1} &\text{(C.32)}\\ &= \mathbf{C}^{-1} : \mathbf{C} : \Delta\mathbf{C}^{-1} &\text{(C.33)}\end{aligned}$$

Thus, Eq.(C.29) writes:

$$\delta^2\Pi \geq -\int_V \mathbf{p} : \mathbf{C}^{-1} : \mathbf{C} : \Delta\mathbf{C}^{-1} : \mathbf{p}dV \tag{C.34}$$

So, if $\Delta\mathbf{C}^{-1} < 0$, $\delta^2\Pi > 0$ and then Π achieves a global minimum.

Appendix D

Expressions of the Eshelby's tensor

The Eshelby tensor is a fourth rank tensor that can be expressed by a 6-by-6 matrix. It has the minor symmetries ($\mathbb{S}_{ijkl} = \mathbb{S}_{jikl} = \mathbb{S}_{ijlk} = \mathbb{S}_{jilk}$) but not the major ones ($\mathbb{S}_{ijkl} = \mathbb{S}_{klij}$) and is given by [32]

$$\mathbb{S}_{ij} = \begin{bmatrix} \mathbb{S}_{1111} & \mathbb{S}_{1122} & \mathbb{S}_{1133} & \sqrt{2}\mathbb{S}_{1123} & \sqrt{2}\mathbb{S}_{1131} & \sqrt{2}\mathbb{S}_{1112} \\ \mathbb{S}_{2211} & \mathbb{S}_{2222} & \mathbb{S}_{2233} & \sqrt{2}\mathbb{S}_{2223} & \sqrt{2}\mathbb{S}_{2231} & \sqrt{2}\mathbb{S}_{2212} \\ \mathbb{S}_{3311} & \mathbb{S}_{3322} & \mathbb{S}_{3333} & \sqrt{2}\mathbb{S}_{3323} & \sqrt{2}\mathbb{S}_{3331} & \sqrt{2}\mathbb{S}_{3312} \\ \sqrt{2}\mathbb{S}_{2311} & \sqrt{2}\mathbb{S}_{2322} & \sqrt{2}\mathbb{S}_{2333} & 2\mathbb{S}_{2323} & 2\mathbb{S}_{2331} & 2\mathbb{S}_{2312} \\ \sqrt{2}\mathbb{S}_{3111} & \sqrt{2}\mathbb{S}_{3122} & \sqrt{2}\mathbb{S}_{3133} & 2\mathbb{S}_{3123} & 2\mathbb{S}_{3131} & 2\mathbb{S}_{3112} \\ \sqrt{2}\mathbb{S}_{1211} & \sqrt{2}\mathbb{S}_{1222} & \sqrt{2}\mathbb{S}_{1233} & 2\mathbb{S}_{1233} & 2\mathbb{S}_{1231} & 2\mathbb{S}_{1212} \end{bmatrix} \tag{D.1}$$

Note that for an isotropic, symmetric fourth rank tensor $\mathbf{A}$, can be expressed as:

$$\mathbf{A} = A^{sy}\mathbf{J} + A^{dev}\mathbf{K} \tag{D.2}$$

where $A^{sy} = \mathbf{J} :: \mathbf{A} = \frac{1}{3}A_{iijj}$ and $A^{dev} = \frac{1}{5}\mathbf{K} :: \mathbf{A} = \frac{1}{15}(3A_{ijij} - A_{iijj})$ Knowing that $\mathbf{J} = \frac{1}{3}\mathbf{i}\otimes\mathbf{i}$; $\mathbf{K} = \mathbf{I} - \mathbf{J}$ and $\mathbf{i}$ and $\mathbf{I}$ are the second and fourth rank unity tensors.

Let α be the aspect ratio of a spheroidal inclusion with x_3 its revolution axis; $\alpha = \frac{a_3}{a_1}$ and $a_1 = a_2$.
The expression of the Eshelby's tensor can then be expressed analyticaly as given in the following.

D.1 Ellipsoidal inclusion

The non-null components of the Eshelbys' tensor are [203]:

$$\mathbb{S}_{3333} = \frac{1}{2(1-\nu)}\left[2(1-\nu)(1-g)+g-\alpha^2\frac{3g-2}{\alpha^2-1}\right] \tag{D.3}$$

$$\mathbb{S}_{1111} = \mathbb{S}_{2222} = \frac{1}{4(1-\nu)}\left[2(1-\nu)g-\frac{1}{2}-(\alpha^2-\frac{1}{4})\frac{3g-2}{\alpha^2-1}\right] \tag{D.4}$$

$$\mathbb{S}_{3311} = \mathbb{S}_{3322} = \frac{1}{4(1-\nu)}\left[4\nu(1-g)-g+\alpha^2\frac{3g-2}{\alpha^2-1}\right] \tag{D.5}$$

$$\mathbb{S}_{1122} = \mathbb{S}_{2211} = \frac{1}{4(1-\nu)}\left[-(1-2\nu)g+\frac{1}{2}-\frac{1}{4}\frac{3g-2}{\alpha^2-1}\right] \tag{D.6}$$

$$\mathbb{S}_{1133} = \mathbb{S}_{2233} = \frac{1}{4(1-\nu)}\left[-(1-2\nu)g+\alpha^2\frac{3g-2}{\alpha^2-1}\right] \tag{D.7}$$

$$\mathbb{S}_{2323} = \frac{1}{4(1-\nu)}\left[(1-\nu)(2-g)-g+\alpha^2\frac{3g-2}{\alpha^2-1}\right] \tag{D.8}$$

$$\mathbb{S}_{2332} = \mathbb{S}_{3223} = \mathbb{S}_{3232} = \mathbb{S}_{3131} = \mathbb{S}_{3113} = \mathbb{S}_{1331} = \mathbb{S}_{1313} = \mathbb{S}_{2323} \tag{D.9}$$

$$\mathbb{S}_{1212} = \frac{\mathbb{S}_{1111}-\mathbb{S}_{1122}}{2} \tag{D.10}$$

$$\mathbb{S}_{1221} = \mathbb{S}_{2112} = \mathbb{S}_{2121} = \mathbb{S}_{1212} \tag{D.11}$$

Where:

$$g = \frac{\alpha}{(1-\alpha^2)^{3/2}}\left[\cos^{-1}\alpha-\alpha(1-\alpha^2)^{1/2}\right] \quad \text{for} \quad 0<\alpha<1 \quad \text{"Oblate spheroid"}, \tag{D.12}$$

$$g = \frac{\alpha}{(\alpha^2-1)^{3/2}}\left[\alpha(\alpha^2-1)^{1/2}-\cosh^{-1}\alpha\right] \quad \text{for} \quad 1<\alpha<\infty \quad \text{"Prolate spheroid"}. \tag{D.13}$$

D.2 Spherical inclusion

For the particular case of spherical inclusions ($\alpha = 1$), previous equations become not applicable and require a study of these functions around $\alpha = 1$. This gives [232]:

$$\mathbb{S}_{1111} = \mathbb{S}_{2222} = \mathbb{S}_{3333} = \frac{7-5\nu}{15(1-\nu)} \tag{D.14}$$

$$\mathbb{S}_{1122} = \mathbb{S}_{1133} = \mathbb{S}_{2211} = \mathbb{S}_{2233} = \mathbb{S}_{3311} = \mathbb{S}_{3322} = \frac{5\nu-1}{15(1-\nu)} \tag{D.15}$$

$$\mathbb{S}_{1212} = \frac{4-5\nu}{15(1-\nu)} \tag{D.16}$$

$$\mathbb{S}_{1221} = \mathbb{S}_{2112} = \mathbb{S}_{2121} = \mathbb{S}_{2323} = \mathbb{S}_{2332} = \mathbb{S}_{3223} = \mathbb{S}_{3232} = \mathbb{S}_{3131} = \mathbb{S}_{3113} = \mathbb{S}_{1331} = \mathbb{S}_{1313} = \mathbb{S}_{1212} \tag{D.17}$$

D.3 Flat disk

The flat disk are used to model cracks and are carachterized by $\alpha = 0$.

$$\mathbb{S}_{3333} = 1 \tag{D.18}$$

$$\mathbb{S}_{3311} = \mathbb{S}_{3322} = \frac{\nu}{1-\nu} \tag{D.19}$$

$$\mathbb{S}_{2323} = \frac{1}{2} \tag{D.20}$$

$$\mathbb{S}_{2332} = \mathbb{S}_{3223} = \mathbb{S}_{3232} = \mathbb{S}_{3131} = \mathbb{S}_{3113} = \mathbb{S}_{1331} = \mathbb{S}_{1313} = \mathbb{S}_{2323}. \tag{D.21}$$

D.4 Cylinder

Inclusion are modeled as cylinder with a cicular cross-section generally in the case of composite containing fibers. The aspect ratio is then assumed to $\alpha = \infty$. The Eshelby non-null components are as follows.

$$\mathbb{S}_{1111} = \mathbb{S}_{2222} = \frac{5-4\nu}{8(1-\nu)} \tag{D.22}$$

$$\mathbb{S}_{1122} = \mathbb{S}_{2211} = \frac{4\nu-1}{8(1-\nu)} \tag{D.23}$$

$$\mathbb{S}_{1133} = \mathbb{S}_{2233} = \frac{\nu}{2(1-\nu)} \tag{D.24}$$

$$\mathbb{S}_{1212} = \mathbb{S}_{1221} = \mathbb{S}_{2112} = \mathbb{S}_{2121} = \frac{3-4\nu}{8(1-\nu)} \tag{D.25}$$

$$\mathbb{S}_{2323} = \mathbb{S}_{2332} = \mathbb{S}_{3223} = \mathbb{S}_{3232} = \mathbb{S}_{3131} = \mathbb{S}_{3113} = \mathbb{S}_{1331} = \mathbb{S}_{1313} = \frac{1}{4} \tag{D.26}$$

Appendix E

WU-Eshelby Tensor

The isotropic and deviatoric parts of the Wu-Eshelby tensor for an inclusion with a given aspect ratio α are as expressed in function of the matrix and inclusion bulk and shear moduli (K_i, G_i) and (K_j, G_j) in the following form:

$$P_{ij} = \frac{1}{\left(1 + (1 - \frac{1}{P0})\right)\left(\frac{K_j}{K_i} - 1\right)} \tag{E.1}$$

$$Q_{ij} = \frac{1}{\left(1 + (1 - \frac{1}{Q0})\right)\left(\frac{G_j}{G_i} - 1\right)} \tag{E.2}$$

where $P0$ and $Q0$ are given by [55]:

$$P0 = \frac{F_1}{F_2} \tag{E.3}$$

$$Q0 = \frac{1}{5}\left[\frac{2}{F_3} + \frac{1}{F_4} + \frac{F_5}{F_2} + \frac{F_6F_7 - F_8F_9}{F_2F_4}\right] \tag{E.4}$$

Functions F_1 to F_9 are expressed such that:

$$F_1 = 1 - \frac{3}{2}(f + g) + R\left(\frac{3}{2}f + \frac{5}{2}g - \frac{4}{3}\right) \tag{E.5}$$

$$F_2 = R\left[2g - 3f - 3g^2 + 2R(f - g + 2g^2)\right] \tag{E.6}$$

$$F_3 = f + \frac{3}{2}g - R(f + g) \tag{E.7}$$

$$F_4 = 1 - \frac{1}{4}\left[f + 3g - R(f - g)\right] \tag{E.8}$$

$$F_5 = f - R\left(f + g - \frac{4}{3}\right) \tag{E.9}$$

$$F_6 = -f + R(f + g) \tag{E.10}$$

$$F_7 = 2 - \frac{1}{4}\left[3f + 9g - R(3f + 5g)\right] \tag{E.11}$$

$$F_8 = -1 + \frac{1}{2}f + \frac{3}{2}g + R\left(2 - \frac{1}{2}f - \frac{5}{2}g\right) \tag{E.12}$$

$$F_9 = f - R(f - g) \tag{E.13}$$

R is defined in function of the matrix bulk and shear moduli:

$$R = \frac{3G_i}{3K_i + 4G_i} \tag{E.14}$$

While

$$g = \frac{\alpha}{(1-\alpha^2)^{3/2}}\left[\cos^{-1}\alpha - \alpha(1-\alpha^2)^{1/2}\right] \qquad \text{for} \quad 0 < \alpha < 1 \quad \text{"Oblate spheroid"}, \tag{E.15}$$

$$g = \frac{\alpha}{(\alpha^2-1)^{3/2}}\left[\alpha(\alpha^2-1)^{1/2} - \cosh^{-1}\alpha\right] \qquad \text{for} \quad 1 < \alpha < \infty \quad \text{"Prolate spheroid"}. \tag{E.16}$$

And

$$f = \alpha^2\frac{3g-2}{1-\alpha^2} \tag{E.17}$$

Simplified expressions of the previous Wu-Eshelby tensor dilatatin and deviatoric parts were proposed in some researchs and are resumed in the Table E for three spheroidal inclusion aspect ratios α.

Figures E.1-E.2 show a comparison between the exact and the approximated ex-

Table E.1: The coefficients P_{ij} and Q_{ij} for spheoidal inclusions

inclusion shape	P_{ij}	Q_{ij}
Spheres $\alpha = 1$	$\frac{K_i+\frac{4}{3}G_i}{K_j+\frac{4}{3}G_i}$	$\frac{G_i+\zeta_i}{G_j+\zeta_i}$
Needles [218, 228]	$\frac{K_i+G_i+\frac{1}{3}G_j}{K_j+G_i+\frac{1}{3}G_j}$	$\frac{1}{5}\left[\frac{4G_i}{G_i+G_j} + 2\frac{G_i+\gamma_i}{G_j+\gamma_i} + \frac{K_j+\frac{4}{3}G_i}{K_j+G_i+\frac{1}{3}G_j}\right]$
Penny cracks [219]	$\frac{K_i+\frac{4}{3}G_j}{K_j+\frac{4}{3}G_j+\pi\alpha\beta_i}$	$\frac{1}{5}\left[1 + \frac{8G_i}{4G_j+\pi\alpha(G_i+2\beta_i)} + 2\frac{K_j+\frac{2}{3}(G_j+G_i)}{K_j+\frac{4}{3}G_j+\Pi\alpha\beta_i}\right]$
$K_j/K_i << 1$ & $G_j/G_i << 1$		
$\beta_i = G_i\frac{3K_i+G_i}{3K_i+4G_i}$; $\gamma_i = G_i\frac{3K_i+G_i}{3K_i+7G_i}$; $\zeta_i = \frac{G_i}{6}\frac{9K_i+8G_i}{K_i+2G_i}$		

pressions of the isotropic and deviatoric parts of the Wu-Eshelby tensor. Concerning the isotropic part, the exact and the approximated expressions are almost exact when varying the inclusion aspect ratio. However, the approximated deviatoric part slightly underestimate the exact solution. Thus, using one or the other solutions would not affect much the Wu-Eshelby tensor. Nevertheless, in this work the exac solution will be used.

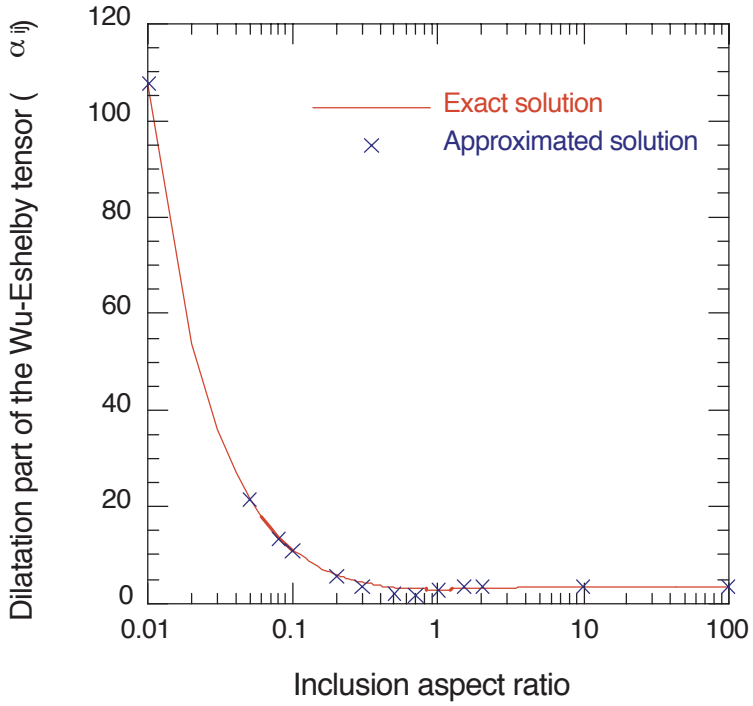

Figure E.1: Exact and approximated isotropic part of the Wu-Eshelby tensor for a porous two-phase composite with $K_i = 45000\ GPa$, $G_i = 18000\ GPa$, $K_j = 0.145\ GPa$ and $G_j = 0\ GPa$

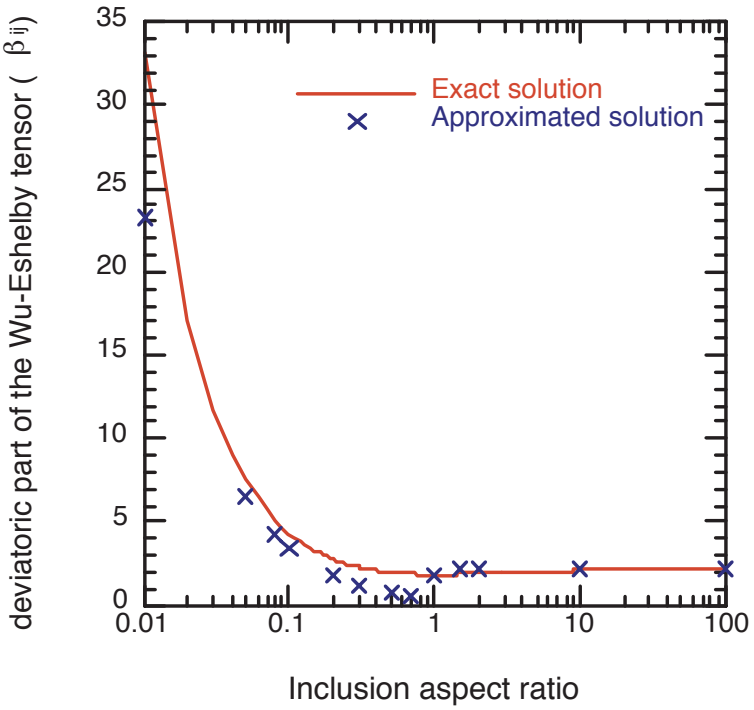

Figure E.2: Exact and approximated deviatoric part of the Wu-Eshelby tensor for a porous two-phase composite with $K_i = 45000\ GPa$, $G_i = 18000\ GPa$, $K_j = 0.145\ GPa$ and $G_j = 0\ GPa$

Appendix F

Double inclusion sub-problems

1. In the first sub-problem, V_1 and V_0 are considered as a single inclusion V_0 with the same stiffness $\mathbf{C}_0$, by subjecting both inclusions to the same eigenstrain $\boldsymbol{\varepsilon}_0^*$. The strain and stress inside and outside V_0 are then:
   Inside V_0 :

$$\boldsymbol{\varepsilon}_{V_0}^{in} = \boldsymbol{\varepsilon}^{\infty} + \mathbb{S}_{V_0,\mathbf{C}_V} : \boldsymbol{\varepsilon}_0^* \tag{F.1}$$
$$\boldsymbol{\sigma}_{V_0}^{in} = \mathbf{C}_0 : (\boldsymbol{\varepsilon}^{\infty} + \mathbb{S}_{V_0,\mathbf{C}_V} : \boldsymbol{\varepsilon}_0^*) \tag{F.2}$$

   Inside V_0 in the homogenized medium:

$$\boldsymbol{\varepsilon}_{V_0}^{hom} = \boldsymbol{\varepsilon}^{\infty} + \mathbb{S}_{V_0,\mathbf{C}_V} : \boldsymbol{\varepsilon}_0^* - \boldsymbol{\varepsilon}_0^* \tag{F.3}$$
$$\boldsymbol{\sigma}_{V_0}^{hom} = \mathbf{C}_V : (\boldsymbol{\varepsilon}^{\infty} + \mathbb{S}_{V_0,\mathbf{C}_V} : \boldsymbol{\varepsilon}_0^* - \boldsymbol{\varepsilon}_0^*) \tag{F.4}$$

   Outside V_0

$$\boldsymbol{\varepsilon}_{V_0}^{out} = \boldsymbol{\varepsilon}^{\infty} + \boldsymbol{\varepsilon}_0^{'} \tag{F.5}$$
$$\boldsymbol{\sigma}_{V_0}^{out} = \mathbf{C}_V(\boldsymbol{\varepsilon}^{\infty} + \boldsymbol{\varepsilon}_0^{'}) \tag{F.6}$$

   where $\boldsymbol{\varepsilon}_0^{'}$ is the perturbation strain.

2. In the second sub-problem, V_0 and V are considered as a single phase V that is free of strain. Only V_1 is subjected to the eigenstrain $\boldsymbol{\varepsilon}_2^* = \boldsymbol{\varepsilon}_1^* - \boldsymbol{\varepsilon}_0^*$. The strain and stress inside and outside V_1 are:

   Inside V_1:

$$\boldsymbol{\varepsilon}_{V_1}^{in} = \mathbb{S}_{V_1,\mathbf{C}_V} : \boldsymbol{\varepsilon}_2^* \tag{F.7}$$
$$\boldsymbol{\sigma}_{V_1}^{in} = \mathbf{C}_1 : (\mathbb{S}_{V_1,\mathbf{C}_V} : \boldsymbol{\varepsilon}_2^*) \tag{F.8}$$

   Inside V_1 in the homogenized medium:

$$\boldsymbol{\varepsilon}_{V_1}^{hom} = \mathbb{S}_{V_1,\mathbf{C}_V} : \boldsymbol{\varepsilon}_2^* - \boldsymbol{\varepsilon}_2^* \tag{F.9}$$
$$\boldsymbol{\sigma}_{V_1}^{hom} = \mathbf{C}_V : (\mathbb{S}_{V_1,\mathbf{C}_V} : \boldsymbol{\varepsilon}_2^* - \boldsymbol{\varepsilon}_2^*) \tag{F.10}$$

   Outside V_1 :

$$\boldsymbol{\varepsilon}_{V_1}^{out} = \boldsymbol{\varepsilon}_2^{'} \tag{F.11}$$
$$\boldsymbol{\sigma}_{V_1}^{out} = \mathbf{C}_V : \boldsymbol{\varepsilon}_2^{'} \tag{F.12}$$

   where $\boldsymbol{\varepsilon}_2^{'}$ is the perturbation strain.

Since we deal with linear elasticity, the two previous problems can be superposed and the obtained strains and stresses in the three zones are:

Inside V_1:

$$\begin{aligned} \boldsymbol{\varepsilon}_{V_1} &= \boldsymbol{\varepsilon}^{in}_{V_0} + \boldsymbol{\varepsilon}^{in}_{V_1} \\ &= \boldsymbol{\varepsilon}^{\infty} + \mathbb{S}_{V_0,\mathbf{C}_V} : \boldsymbol{\varepsilon}^{*}_0 + \mathbb{S}_{V_1,\mathbf{C}_V} : \boldsymbol{\varepsilon}^{*}_2 \qquad \text{(F.13)} \\ \boldsymbol{\sigma}_{V_1} &= \boldsymbol{\sigma}^{in}_{V_0} + \boldsymbol{\sigma}^{in}_{V_1} \\ &= \mathbf{C}_1 : (\boldsymbol{\varepsilon}^{\infty} + \mathbb{S}_{V_0,\mathbf{C}_V} : \boldsymbol{\varepsilon}^{*}_0 + \mathbb{S}_{V_1,\mathbf{C}_V} : \boldsymbol{\varepsilon}^{*}_2) \qquad \text{(F.14)} \end{aligned}$$

Inside V_1 in the homogenized medium:

$$\begin{aligned} \boldsymbol{\varepsilon}^{hom} &= \boldsymbol{\varepsilon}^{\infty} + \mathbb{S}_{V_0,\mathbf{C}_V} : \boldsymbol{\varepsilon}^{*}_0 - \boldsymbol{\varepsilon}^{*}_0 + \mathbb{S}_{V_1,\mathbf{C}_V} : \boldsymbol{\varepsilon}^{*}_2 - \boldsymbol{\varepsilon}^{*}_2 \qquad \text{(F.15)} \\ \boldsymbol{\sigma}^{hom} &= \mathbf{C}_V : (\boldsymbol{\varepsilon}^{\infty} + \mathbb{S}_{V_0,\mathbf{C}_V} : \boldsymbol{\varepsilon}^{*}_0 - \boldsymbol{\varepsilon}^{*}_0 + \mathbb{S}_{V_1,\mathbf{C}_V} : \boldsymbol{\varepsilon}^{*}_2 - \boldsymbol{\varepsilon}^{*}_2) \qquad \text{(F.16)} \end{aligned}$$

Inside $V_0 - V_1$:

$$\begin{aligned} \boldsymbol{\varepsilon}_{V_0-V_1} &= \boldsymbol{\varepsilon}^{out}_{V_1} + \boldsymbol{\varepsilon}^{in}_{V_0} \\ &= \boldsymbol{\varepsilon}^{'}_2 + \boldsymbol{\varepsilon}^{\infty} + \mathbb{S}_{V_0,\mathbf{C}_V} : \boldsymbol{\varepsilon}^{*}_0 \qquad \text{(F.17)} \\ \boldsymbol{\sigma}_{V_0-V_1} &= \boldsymbol{\sigma}^{out}_{V_1} + \boldsymbol{\sigma} V_0{}^{in} \\ &= \mathbf{C}_0 : (\boldsymbol{\varepsilon}^{'}_2 + \boldsymbol{\varepsilon}^{\infty} + \mathbb{S}_{V_0,\mathbf{C}_V} : \boldsymbol{\varepsilon}^{*}_0) \qquad \text{(F.18)} \end{aligned}$$

Inside $V_0 - V_1$ in the homogenized medium:

$$\begin{aligned} \boldsymbol{\varepsilon}^{hom}_{V_0-V_1} &= \boldsymbol{\varepsilon}^{'}_2 + \boldsymbol{\varepsilon}^{\infty} + \mathbb{S}_{V_0,\mathbf{C}_V} : \boldsymbol{\varepsilon}^{*}_0 - \boldsymbol{\varepsilon}^{*}_0 \qquad \text{(F.19)} \\ \boldsymbol{\sigma}^{hom}_{V_0-V_1} &= \mathbf{C}_V : (\boldsymbol{\varepsilon}^{'}_2 + \boldsymbol{\varepsilon}^{\infty} + \mathbb{S}_{V_0,\mathbf{C}_V} : \boldsymbol{\varepsilon}^{*}_0 - \boldsymbol{\varepsilon}^{*}_0) \qquad \text{(F.20)} \end{aligned}$$

Outside V_1 :

$$\begin{aligned} \boldsymbol{\varepsilon}_V &= \boldsymbol{\varepsilon}^{out}_{V_0} + \boldsymbol{\varepsilon}^{out}_{V_1} \\ &= \boldsymbol{\varepsilon}^{\infty} + \boldsymbol{\varepsilon}^{'}_0 + \boldsymbol{\varepsilon}^{'}_2 \qquad \text{(F.21)} \\ \boldsymbol{\sigma}_V &= \boldsymbol{\sigma}^{out}_{V_0} + \boldsymbol{\sigma}^{out}_{V_1} \\ &= \mathbf{C}_V : (\boldsymbol{\varepsilon}^{\infty} + \boldsymbol{\varepsilon}^{'}_0 + \boldsymbol{\varepsilon}^{'}_2) \qquad \text{(F.22)} \end{aligned}$$

Since it was assumed that V_0 and V_1 are of the same shape, then $\mathbb{S}_{V_0,\mathbf{C}_v} = \mathbb{S}_{V_1,\mathbf{C}_v}$. Taking into consideration this assumption and that of $\boldsymbol{\varepsilon}^{*}_2 = \boldsymbol{\varepsilon}^{*}_1 - \boldsymbol{\varepsilon}^{*}_0$, simplifies the stress and strain inside the inclusion V_1 (Eq.F.13) to:

$$\begin{aligned} \boldsymbol{\varepsilon}_{V_1} &= \boldsymbol{\varepsilon}^{\infty} + \mathbb{S}_{V_1,\mathbf{C}_V} : \boldsymbol{\varepsilon}^{*}_1 \qquad \text{(F.23)} \\ \boldsymbol{\sigma}_{V_1} &= \mathbf{C}_1 : (\boldsymbol{\varepsilon}^{\infty} + \mathbb{S}_{V_1,\mathbf{C}_V} : \boldsymbol{\varepsilon}^{*}_1) \qquad \text{(F.24)} \end{aligned}$$

Similarly, the stress and strain inside zone V_1 in the homogenized medium are expressed as:

$$\begin{aligned} \boldsymbol{\varepsilon}^{hom} &= \boldsymbol{\varepsilon}^{\infty} + \mathbb{S}_{V_1,\mathbf{C}_V} : \boldsymbol{\varepsilon}^{*}_1 - \boldsymbol{\varepsilon}^{*}_1 \qquad \text{(F.25)} \\ \boldsymbol{\sigma}^{hom} &= \mathbf{C}_V : (\boldsymbol{\varepsilon}^{\infty} + \mathbb{S}_{V_1,\mathbf{C}_V} : \boldsymbol{\varepsilon}^{*}_1 - \boldsymbol{\varepsilon}^{*}_1) \qquad \text{(F.26)} \end{aligned}$$

Considering now the mechanical equivalence between the heterogeneous (Eqs.F.24-F.18) and homogenous (Eqs.F.26-F.20) problems inside V_1 and $V_0 - V_1$ ends to the following relations:
Inside V_1 :

$$\mathbf{C}_1 : (\boldsymbol{\varepsilon}^{\infty} + \mathbb{S}_{V_1,\mathbf{C}_V} : \boldsymbol{\varepsilon}_1^*) = \mathbf{C}_V : (\boldsymbol{\varepsilon}^{\infty} + \mathbb{S}_{V_1,\mathbf{C}_V} : \boldsymbol{\varepsilon}_1^* - \boldsymbol{\varepsilon}_1^*) \tag{F.27}$$

Inside $V_0 - V_1$:

$$\mathbf{C}_0 : (\boldsymbol{\varepsilon}_2^{'} + \boldsymbol{\varepsilon}^{\infty} + \mathbb{S}_{V_0,\mathbf{C}_V} : \boldsymbol{\varepsilon}_0^*) = \mathbf{C}_V : (\boldsymbol{\varepsilon}_2^{'} + \boldsymbol{\varepsilon}^{\infty} + \mathbb{S}_{V_0,\mathbf{C}_V} : \boldsymbol{\varepsilon}_0^* - \boldsymbol{\varepsilon}_0^*) \tag{F.28}$$

Expressing $\boldsymbol{\varepsilon}_1^*$ in terms of $\boldsymbol{\varepsilon}^{\infty}$ from Eq.(F.27) and averaging Eq.(F.23) over V_1 writes:

$$\begin{aligned} \langle \boldsymbol{\varepsilon} \rangle_{V_1} &= \left[I + \mathbb{S}_{V_0,\mathbf{C}_V} : ((\mathbf{I} - \mathbf{C}_V^{-1}\mathbf{C}_1)^{-1} - \mathbb{S}_{V_0,\mathbf{C}_V})^{-1} \right] \boldsymbol{\varepsilon}^{\infty} && \text{(F.29)} \\ &= \left[\mathbf{I} - \mathbb{S}_{V_0,\mathbf{C}_V} : (I - \mathbf{C}_V^{-1}\mathbf{C}_1) \right]^{-1} \boldsymbol{\varepsilon}^{\infty} && \text{(F.30)} \\ &= \mathbf{T}^{V1} \boldsymbol{\varepsilon}^{\infty} && \text{(F.31)} \end{aligned}$$

When expressing, know, $\boldsymbol{\varepsilon}_0^*$ in terms of $\boldsymbol{\varepsilon}^{\infty}$ from Eq.(F.28), one remark that $\boldsymbol{\varepsilon}_2^{'}$ remains in the expression. To come over this, an average on $V_0 - V_1$ can be considered and the following statement of Mori-Tanaka applied.
Tanaka and Mori have shown [202] that "when a single inclusion V with uniform transformation strain is within an infinite homogeneous body, the volume integrals of total strain and stress vanish if the integration is carried out in the region $V^{'} - V$, where $V^{'}$ is a domain surrounding V and is of shape similar to that of V" [1]. See Fig.F.1 for illustration.
Such consideration implies that:

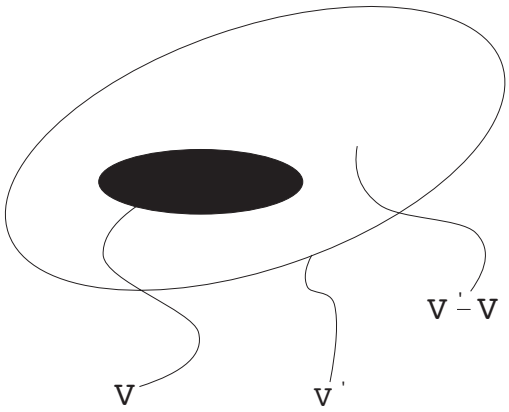

Figure F.1: The average on $V^{'} - V$ vanishes when $V^{'}$ and V are ellipsoids of the same shape

$$\langle \boldsymbol{\varepsilon}_2^{'} \rangle_{V_0 - V_1} = 0$$

[1] cited in [157]

Accordingly, formulation of $\langle \boldsymbol{\varepsilon}_0^* \rangle_{V_0-V_1}$ can be determined in terms of $\boldsymbol{\varepsilon}^\infty$. Besides, average of Eq.(F.17) writes:

$$\begin{aligned} \langle \boldsymbol{\varepsilon} \rangle_{V_0-V_1} &= \left[I + \mathbb{S}_{V_0,\mathbf{C}_V} : ((\mathbf{I} - \mathbf{C}_V^{-1}\mathbf{C}_0)^{-1} - \mathbb{S}_{V_0,\mathbf{C}_V})^{-1} \right] \boldsymbol{\varepsilon}^\infty && \text{(F.32)} \\ &= \left[\mathbf{I} - \mathbb{S}_{V_0,\mathbf{C}_V} : (\mathbf{I} - \mathbf{C}_V^{-1}\mathbf{C}_0) \right]^{-1} \boldsymbol{\varepsilon}^\infty && \text{(F.33)} \\ &= \mathbf{T}^{V0} \boldsymbol{\varepsilon}^\infty && \text{(F.34)} \end{aligned}$$

Combining Eq.(F.31) and Eq.(F.34) yields to:

$$\langle \boldsymbol{\varepsilon} \rangle_{V_1} = \mathbf{T}^{V1} : (\mathbf{T}^{V0})^{-1} \langle \boldsymbol{\varepsilon} \rangle_{V_0-V_1} \tag{F.35}$$

The previous equation (Eq.F.35) identifies the strain concentration tensor for a two-phase composite formulated by the double inclusion model as:

$$\bar{\mathbf{A}}^{DI} = \left[f_1 \mathbf{I} + f_0 (\mathbf{T}^{V1})^{-1} \mathbf{T}^{V0} \right]^{-1} \tag{F.36}$$

Bibliography

[1] J. Aboudi. Micromechanical analysis of composites by the method of cells - Update. *Appl. Mech. Rev.*, 49 (10) :S83-S91, 1996. 9

[2] ACI committee 201. Proposed revision of: Guide to durable concrete. *ACI materials journal*, 544-582, 1991. 1

[3] AFPC-AFREM, *Concrete durability: determination of apparent density and water accessible porosity* (in French), 121-125, 1997. 74

[4] D.G. Aggelis, T. Shiotani, Surface wave dispersion in cement-based media: Inclusion size effect. *NDT & E International*, 41:319-325, 2008. 163

[5] D.G. Aggelis. Numerical simulation of surface wave propagation in material with inhomogeneity: Inclusion size effect. *NDT & E International*, 42: 558-563, 2009. 163

[6] A. A. Almusallam. Effect of degree of corrosion on the properties of reinforcing steel bars. *Construction and Building Materials*, 15: 361-368, 2001. 1

[7] P. Anugonda, J.S. Wiehn and J.A. Turner. Diffusion of ultrasound in concrete. *Ultrasonics*, 39:429-435, 2001. 151

[8] H. N. Atahan, O. N. Oktar and M. A. Taşdemir. Effects of water-cement ratio and curing time on the critical pore width of hardened cement paste. *Construction and Building Materials*, 23: 1196-1200, 2009. 103

[9] B.A. Auld. *Acoustic Fields and Waves in Solids*, volume 1. Jhon Wiley & sons, 1973. 101

[10] S.S. Barboura. *Modélisation micromécanique du comportement de milieux poreux non linéaires : Applications aux argiles compactées*. PhD thesis, Université de Pierre et Marie Curie, Paris, France, 2007. 133

[11] P.A.M. Basheer, S.E. Chidiac and A.E. Long. Predictive models for deterioration of concrete structures. *Construction and Building Materials*, 10(1): 27-37, 1996. 1

[12] D. Benavente, M.A. García del Cura, R. Fort, S. Ordóñez. Durability estimation of porous building stones from pore structure and strength. *Engineering Geology*, 74:113-127, 2004. 1

[13] D.P. Bentz. Three-dimensional computer simulation of Portland cement hydration and microstructure development. *J. Am. Ceram. Soc.*, 80(1):3-21, 1997. 2

[14] Y. Benveniste. A new approach to the application of Mori-Tanaka's theory in composite materials. *Mechanics of Materials*, 6:147-157, 1987. 2, 41

[15] P.A. Berge, B.P. Bonner and J.G. Berryman. Ultrasonic velocity-porosity relationships for sandstone analogs made from fused glass beads. *Geophysics*, 60(1):108-119, 1995. 53

[16] R. Berliner, M. Popovici, K.W. Herwig, M. Berliner, H.M. Jennings and J.J. Thomas. Quasielastic neutrons scattering study of the effect of water-to-cement ratio on the hydration kinetics of tricalcium silicate. *Cement and Concrete Research*, 28(2):231-243, 1998. 71

[17] O. Bernard, F.-J. Ulm, E. Lemarchand. A multiscale micromechanics-hydration model for the early-age elastic properties of cement-based materials. *Cement and Concrete Research*, 33:1293-1309, 2003. 67, 117

[18] J.G. Berryman. Long-wavelength propagation in composite elastic media I. Spherical inclusions. *J. Acoust. Soc. Am.*, 68(6):1809-1819, 1980. 2, 3, 46

[19] J.G. Berryman. Long-wavelength propagation in composite elastic media II. Ellipsoidal inclusions. *J. Acoust. Soc. Am.*, 68(6):1820-1831, 1980. 2, 3, 46

[20] J.G. Berryman. Elastic waves in fluid-saturated porous media. *Lecture Notes in Physics*, 154:38-50, 1981. 123

[21] J.G. Berryman. Waves in partially saturated porous media. *Wave propagation and inversion*, 1-25, 1992. 3, 131, 153

[22] J.G. Berryman. *Origin of Gassmann's equations*. Stanford Exploration Project, Report 102:187-192, 1999. 132, 151

[23] J.G. Berryman and P.A. Berge . Critique of two explicit schemes for estimating elastic properties of multiphase composites. *Mechanics of Materials*, 22:149-164, 1996. 2, 49

[24] J.G. Berryman and G.W. Milton. Exact results for generalized Gassmann's equations in composite porous media with two constituents. *Geophysics*, 56:1950-1960, 1991. 117, 151

[25] M.A. Biot. General theory of three-dimensional consolidation. *Journal of Applied Physics*, 12(2):155-164, 1941. 130

[26] M.A. Biot. Theory of propagation of elastic waves in a fluid-saturated porous solid. I. Low-frequency range. *The Journal of the acoustical Society of america*, 28(2):168-178, 1956. 16, 151, 153

[27] M.A. Biot. Theory of propagation of elastic waves in a fluid-saturated porous solid. II. Higher Frequency Range. *The Journal of the acoustical Society of america*, 28(2):179-191, 1956. 131, 151, 153

[28] M.A. Biot. Mechanics of deformation and acoustic propagation in porous media. *J. appl. Phys.*, 33(4):1482-1498, 1962. 130, 131

[29] T. Böhlke and A. Bertram. The evolution of Hooke's law due to texture development in FCC polycrystals. *International Journal of Solids and Structures*, 38:9437-9459, 2001. 28

[30] M. Bornert. *Morphologie microstructurale et comportement mécanique; caractrisations expérimentales, approches par bornes et estimations autocohérentes généralisées*. PhD thesis, Ecole Nationale des Ponts et Chausses, Paris, France, 1996. 9, 27

[31] M. Bornert, T. Bretheau and P. Gilomini. *Homogénéisation en mécanique des matériaux 1. Matériaux aléatoires élastiques et milieu périodiques*. Hermes Science Publications, 2001. 12

[32] M. Bornert, T. Bretheau and P. Gilomini. *Homogénéisation en mécanique des matériaux 2. Comportements non linéaires et problèmes ouverts*. Hermes Science Publications, 2001. 189

[33] H.J.H. Brouwers. The work of Powers and Brownyard revisited: Part 1. *Cement and Concrete Research*, 34:1697-1716, 2004. 71

[34] H.J.H. Brouwers. The work of Powers and Brownyard revisited: Part 2. *Cement and Concrete Research*, 35:1922-1936, 2005. 71

[35] R.J.S. Brown and J. Korringa. On the dependence of the elastic properties of a porous rock on the compressibility of the pore fluid. *Geophysics*, 40(4):608-616, 1975. 151

[36] B. Budiansky. On the elastic moduli of some heterogeneous materials. *J. Mech. Phys. Solids*, 13:223-227, 1965. 16, 45, 46

[37] R. Burridge and J.B. Keller. Poroelasticity equations derived from microstructure. *J. Acoust. Soc. Am.*, 70(4):1140-11406, 1981. 154

[38] V.A. Buryachenko. Micromechanics of Heterogeneous Materials. Springer, 2007. 27

[39] J.G. Cabrera. Deterioration of Concrete Due to Reinforcement Steel Corrosion. *Cement & Concrete Composites*, 18:47-59, 1996. 1

[40] J.M. Carcione. *Handbook of geophysical exploration seismic exploration, Volume 31: Wave fileds in real media: wave propagation in anisotropic, anelastic and porous media*. Pergamon, Tokyo, 2001. 101

[41] P.P. Castañeda. New variational principles in plasticity and their application to composite materials. *J. Mech. Phys. Solids*, 40(8):1757-1788, 1992. 34

[42] Ö.Z. Cebeci. Pore structure of air-entrained hardened cement paste. *Cement and concrete research*, 11:257-265, 1981. 141

[43] X. Chateau and L. Dormieux. Micromechanics of saturated and unsaturated porous media. *Int. J. Numer. Anal. Meth. Geomech.*, 26:831-844, 2002. 134

[44] S. Chatterji. An explanation for the unsaturated state of water stored concrete. *Cement & Concrete Composites*, 26:75-79, 2004. 133

[45] J.D.N. Cheeke. *Fundamentals and applications of ultrasonic waves*. CRC Press, 2002. 99, 100

[46] R.M. Christensen, K.N. Lo. Solutions for effective shear properties in three phase sphere and cylinder models. *J. Mech. Phys. Sotid*, 27:315-330, 1979. 46, 111

[47] D.W. Christensen Jr, T. Pellien , and R.F. Bonaquist. Hirsh model for estimating the modulus of asphalt concrete. *Journal of the Association of Asphalt Paving Technologists*, 72:97-121, 2003. 28

[48] R. Ciz and B. Gurevich. Amplitude of Biot's slow wave scattered by a spherical inclusion in a fluid-saturated poroelastic medium. *Geophys. J. Int.*, 160:991-1005, 2005. 131

[49] R. Ciz and S.A. Shapiro. Generalization of Gassmann equations for porous media saturated with a solid material. *Geophysics*, 72(6):A75-A79, 2007. 132

[50] G. Consolati, F. Quasso. Evolution of porosity in a Portland cement paste studied through positron annihilation lifetime spectroscopy. *Radiation Physics and Chemistry*, 68:519-521, 2003. 69

[51] G. Constantinides. *Invariant mechanical mropeties of Calcium-Silicate-Hydrates (C-S-H) in cement-based materials: Instrumented nanoindentation and microporomechanical modeling*. PhD thesis, Massachusetts Institute of Technology, USA, 2006. 67

[52] G. Constantinides, F.-J. Ulm. The effect of two types of C-S-H on the elasticity of cement-based materials: Results from nanoindentation and micromechanical modeling. *Cement and Concrete Research*, 34:67-80, 2004. 66, 117, 118

[53] R.A. Cook and K.C. Hover. Mercury porosimetry of hardened cement pastes. *Cement and Concrete Research*, 29:933-943, 1999. 81, 118

[54] R.L. Day and B.K. Marsh. Measurement of porosity in blended cement pastes, *Cement and Concrete Research*, 18:63-73, 1988. 82

[55] E.A. Dean. Elastic moduli of porous sintered materials as modeled by a variable-aspect-ratio self-consistent oblate-spheroidal-inclusion theory. *Journal of the American Ceramic Society*, 66(12):847-854, 1983. 193

[56] S. Diamond. Mercury porosimetry: An inappropriate method for the measurement of pore size distributions in cement-based materials. *Cement and Concrete Research*, 30:1517-1525, 2000. 79, 81

[57] S. Diamond and E.E. Lachowski. Investigation of the composition and morphology of individual particles of Portland cement paste: 2. Calcium sulfoaluminates. *Cement and Concrete Research*, 13:335-340, 1983. 66

[58] S.N. Domenico. Effect of brine-gas mixture on velocity in an unconsolidated sand reservoir. *Geophysics*, 41(5):882-894, 1976. 162

[59] L. Du and K.J. Folliard. Mechanisms of air entrainment in concrete. *Cement and Concrete Research*; 35:1463-1471, 2005. 63, 68

[60] N.C. Dutta and H. Odé . Seismic reflections from a gas-water contact. *Geophysics*, 48(2):148-162, 1983. 131

[61] P. Duysinx. *Optimisation topologique: du milieu continu à la structure élastique*. PhD thesis, Université de Liège; faculté des sciences appliquées, France, 1996. 34

[62] G. J. Dvorak. Transformation field analysis of inelastic composite materials. *Proceedings: Mathematical and Physical Sciences*, 437:311-327, 1992. 9

[63] F. Eggers and U. Kaatze. Broad-band ultrasound measurement techniques for liquids. *Meas. Sci. Technol.*, 7:1-19, 1996. 102, 103

[64] S.E. Elliot and B.F. Wiley. Compressional velocities of partially saturated, unconsolidated sands. *Geophysics*, 40(6):949-954, 1975. 162

[65] J.D. Eshelby. The determination of the elastic field of an ellipsoidal inclusion, and related problems. *Proceedings of the Royal Society of London. Series A, Mathematical and Physical Sciences*, 241(1226):376-396, 1957. 16, 21, 35, 37

[66] J.D. Eshelby. The elastic field outside an ellipsoidal inclusion. *Proceedings of the Royal Society of London. Series A, Mathematical and Physical Sciences*, 252(1271):561-569, 1959. 37

[67] G. Faivre. Hétérogénéités ellipsoïdales dans un milieu élastique anisotrope. *Le Journal de physique*, 32:325-331, 1971. 37

[68] Fascicule de recommandations : Centre des études et de recherche industriel de béton (CERIB). 77

[69] R.F. Feldman. The porosity and pore structure of hydrated portland cement paste. *Materials Research Society Symposium Proceedings*, 137:59-73, 1989. 82

[70] R.F. Feldman and P.J. Sereda. A model for hydrated Portland cement paste as deduced from sorption - length change and mechanical properties. *Materials and Structures*, 1(6):509-520, 1968. xv, 68, 69

[71] C. Friebel. *Mechanics and acoustics of viscoelastic inclusion reinforced composites: micro-macro modeling of effective properties*. PhD thesis, Université catholique de Louvain, Belgium, 2007. 42

[72] R. Fox. Probing the body with Doppler ultrasound. *Physics Education*, 31(2):85-90, 1996. 100

[73] H. Fujimura, K. Sakata, H. Kiyama, S. Nishibayashi. *Experimental studies on the behavior of the porosity in cement paste* (in Chinese). Report of the Faculty of Engineering, Tottori University study, 2(1):59-70, 1971. 75

[74] C. Gallé. Effect of drying on cement-based materials pore structure as identified by mercury intrusion porosimetry: A comparative study between oven-, vacuum-, and freeze-drying. *Cement and Concrete Research*, 31:1467-1477, 2001. 75, 82

[75] F. Gassmann. Elastic waves through a packing of spheres. *Geophysics* 16(4):673-685, 1951. 130, 132

[76] R.E. Gebhardt. Survey of North American Portland Cements: 1994. *Cement, Concrete, and Aggregates, CCAGDP*, 17(2):145-189, 1995. 65

[77] J. Geertsma and D.C. Smit. Some aspects of elastic wave propagation in fluid-saturated porous solids. *Geophysics*, 26(2):169-181, 1961. 151

[78] H. Gercek. Poisson's ratio values for rocks. *International Journal of Rock Mechanics & Mining Sciences*, 44:1-13, 2007. 96

[79] S. Ghabezloo. *Comportement thermo-poro-mécanique d'un ciment pétrolier*. PhD thesis, Ecole Nationale des Ponts et Chaussées, Paris, France, 2008. 75

[80] S. Ghabezloo. Association of macroscopic laboratory testing and micromechanics modelling for the evaluation of the poroelastic parameters of a hardened cement paste. *Cement and Concrete Research*, 40(8):1197-1210, 2010. 117

[81] M. Goueygou, Z. Lafhaj and F. Soltani. Assessment of porosity of mortar using ultrasonic Rayleigh waves. *NDT & E International*, 42:353-360, 2009. 2

[82] M. Goueygou, B. Piwakowski, S. Ould Naffa and F. Buyle-Bodin. Assessment of broadband ultrasonic attenuation measurements in inhomogeneous media. *Ultrasonics*, 40:77-82, 2002. 100

[83] Z.C. Grasley, G.W. Scherer, D.A. Lange, J.J. Valenza. Dynamic pressurization method for measuring permeability and modulus: II. Cementitious materials. *Materials and Structures*, 40(7):711-721, 2006. 163

[84] A. Grimaldi and R. Luciano. Tensile stiffness and strength of fiber-reinforced concrete, *Journal of the Mechanics and Physics of Solids*, 48:1987-2008, 2000. 111

[85] E. Guillon, F. Benboudjema and M. Moranville. Modelling the mechanical evolution of a chemically degraded cement paste at the microstructure scale. *Proceedings of FramCos 5 - 5th International Conference on Fracture Mechanics of Concrete and Concrete Structures*, 1:555-562, 2004. 2

[86] P. Halamickova and R.J. Detwiler. Water permeability and chloride ion diffusion in portland cement mortars: relationship to sand content and critical pore diameter. *Cement and Concrete Research*, 25(4):790-802, 1995. 154

[87] T.C. Hansen. Physical structure of hardened cement paste. A classical approach. *Materials and Structures*, 19(6):423-436, 1986. 71

[88] Z. Hashin. *The elastic moduli of heterogeneous materials*. Technical Report No. 9, office of naval research, 1960. 16, 29

[89] Z. Hashin. On elastic behaviour of fibre reinforced materials of arbitrary transverse phase geometry. *J. Mech. Phys. Solids*, 13:119-134, 1965. 34

[90] Z. Hashin. The differential scheme and its application to cracked materials. *J. Mech. Phys. Solids*, 36(6):719-733, 1988. 52

[91] Z. Hashin and S. Shtrikman. Note on a variational approach to the theory of composite elastic materaials. *The Franklin Institute Laboratories*, 271:336-341, 1961. 30

[92] Z. Hashin and S. Shtrikman. On some variational principles in anisotropic and nonhemogeneous elasticity. *J. Mech. Phys. Solids*, 10:335-342, 1962. 34

[93] Z. Hashin and S. Shtrikman. A variational approach to the theory of the elastic behaviour of multiphase materials. *J. Mech. and Phys. of Solids*, 11:127-140, 1963. 16, 29, 31

[94] N. Hearn and R.D. Hooton. Sample mass and dimension effects on mercury intrusion porosimetry results. *Cement and Concrete Research*, 22:970-980, 1992. 82

[95] C. Hellmich and H. Mang. Shotcrete elasticity revisited in the framework of continuum micromechanics: from submicron to meter level. *Journal of Materials in Civil Engineering*, 17(3):246-256, 2005. 117

[96] M.G. Hernández, J.J. Anaya, M.A.G. Izquierdo and L.G. Ullate. Application of micromechanics to the characterization of mortar by ultrasound. *Ultrasonics*, 40:217-221, 2002. 3

[97] M.G. Hernández, J.J. Anaya, L.G. Ullate, M. Cegarra, T. Sanchez. Application of a micromechanical model of three phases to estimating the porosity of mortar by ultrasound. *Cement and Concrete Research*, 36:617-624, 2006. 3

[98] M.G. Hernández, J.J. Anaya, L.G. Ullate, A. Ibañez. Effect of the fluid in the inclusions of cement paste on the ultrasonic velocity. *Ultrasonics*, 42:865-869, 2004. 3

[99] M.G. Hernández, J.J. Anaya, L.G. Ullate, A. Ibañez. Formulation of a new micromechanic model of three phases for ultrasonic characterization of cement based materials. *Cement and Concrete Research*, 36(4):609-616, 2006. 3, 51, 111

[100] M.G. Hernández, M.A.G. Izquierdo, A. Ibáñez, J.J. Anaya and L.G. Ullate. Porosity estimation of concrete by ultrasonic NDE. *Ultrasonics*, 38:531-533, 2000. 2

[101] A.V. Hershey. The elasticity of an isotropic aggregate of anisotropic cubic crystals. *J. Appl. Mech.* 21:236-240, 1954. 44

[102] R. Hill. The elastic behaviour of a crystalline aggregate. *Proc. Phys. Soc. A*, 65:349-354, 1952. 27

[103] R. Hill. Elastic properties of reinforced solids: Some theoretical principles. *J. Mech. Phys. Solids*, 11: 357-372, 1963. 12, 21, 23, 27

[104] R. Hill. Theory of mechanical properties of fiber-strengthened materials: I. Elastic behaviour. *Mech. Phys. Solids*, 12:199-212, 1964. 34

[105] R. Hill. Continuum micro-mechanics of elastoplastic polycrystals.*J. Mech. Phys. Solids*, 13:89-101, 1965. 46

[106] R. Hill. A self-consistent mechanics of composite materials. *J. Mech. Phys. Solids*, 13:213-222, 1965. 44

[107] R. Hill. The essential structure of constitutive laws for metal composites and polycrystals. *Mech. Phys. Solids*, 15:79-95, 1967. 12

[108] M. Hori and S. Nemat-Nasser. Double-inclusion model and overall moduli of multi-phase composites. *Mechanics of Materials*, 14:189-206, 1993. 50

[109] B. Hosten. Reflection and transmission of acoustic plane waves on an immersed orthotropic and viscoelastic solid layer. *J. Acoust. Soc. Am.*, 89(6):2745-2752, 1991. 101

[110] K.C. Hover. *Significance of Tests and Properties of Concrete and Concrete-Making Materials, Chapter 26: Air Content and Density of Hardened Concrete*. ASTM International, 2006. 63

[111] C.L. Hsieh, W.H. Tuan. Poisson's ratio of two-phase composites. *Materials Science and Engineering*, A 396:202-205, 2005. 34

[112] H. Ito, J. DeVilbiss, and A. Nur. Compressional and shear waves in saturated rock during water-steam transition. *Proceedings of the fourth workshop geothermal reservoir engineering*, Standford University, Standford, California, 84-95, 1978. 97

[113] L.J. Jacobs and J.O. Owino. Effect of aggregate size on attenuation of Rayleigh surface waves in cement-based materials. *Journal of Engineering Mechanics*, 126:1124-1130, 2000. 151

[114] S. Jansson. Homogenized nonlinear constitutive properties and local stress concentrations for composites with periodic internal structure. *Int. J. Solids Structures*, 29(17):2181-2200, 1992. 9

[115] H.M. Jennings. A model for the microstructure of calcium silicate hydrate in cement paste. *Cement and Concrete Research*, 30:101-116, 2000. 67

[116] H. Jeong, D.K. Hsu, R.E. Shannon and P.K. Liaw. Characterization of anisotropic elastic constants of Silicon-Carbide particulate reinforced aluminum metal matrix composites: Part II. Theory. *Metallurgical and materials transactions A*, 25A:811-819, 1994. 17, 21

[117] B. Johannesson and O.B. Pedersen. Analytical determination of the average Eshelby tensor for transversely isotropic fiber orientation distributions. *Acta Materialia*, 46(9):3165-3173, 1998. 18

[118] D.L. Johnson. Equivalence between fourth sound in liquid He II at low temperatures and the Biot slow wave in consolidated porous media. *Appl. Phys. Lett.*, 37(12):1065-1067, 1980. 153

[119] D.L. Johnson and T.J. Plona. Acoustic slow waves and the consolidation transition. *J. Acoust. Soc. Am.*, 72:556-565, 1982. 153

[120] F.A. Johnson. Elastic Constants. I. *Proceedings of the Royal Society of London. Series A, Mathematical and Physical Sciences*, 357(1690):289-295, 1977. 183

[121] M. Kaczmarek, M. Goueygou. Dependence of elastic properties of materials on their porosity: Review of models. *Journal of Porous Media*, 9(4):335-355, 2006. 3

[122] K.O. Kjellsen, A. Monsøy, K. Isachsen and R.J. Detwiler. Preparation of flat-polished specimens for SEM-backscattered electron imaging and X-ray microanalysis importance of epoxy impregnation. *Cement and Concrete Research*, 33(4):611-616, 2003. 90

[123] H. Klöcker, É. Berger and G. Damamme. Explicit expression of the polarisation tensor of a transversely isotropic matrix. *Comptes Rendus de l'Académie des Sciences - Series IIB - Mechanics-Physics-Astronomy*, 326:799-804, 1998. 30

[124] R.V. Kohn and R. Lipton. Optimal bounds for the effective energy of a mixture of isotropic, incompressible, elastic materials. *Archive for Rational Mechanics ans Analysis*, 102(4):331-350, 1988. 34

[125] K. Komloš, S. Popovics, T. Nürnbergerová, B. Babál and J.S. Popovics. Ultrasonic pulse velocity test of concrete properties as specified in various standards. *Cement and Concrete Composites*, 18:357-364, 1996. 1

[126] S.H. Kosmatka, B. Kerkhoff and W.C. Panarese. *Design and Control of Concrete Mixtures*; Chapter 6. Cement Association of Canada, fifth Canadian edition, 1991. 63, 68

[127] M. Krus, K.K. Hansen, H.M. Künzel, Porosity and liquid absorption of cement paste. *Materials and Structures*, 30:394-398, 1997. 75

[128] R. Kumar and B. Bhattacharjee. Study on some factors affecting the results in the use of MIP method in concrete research. *Cement and Concrete Research*, 33:417-424, 2003. 81

[129] T. Kundu. *Nondestructive Evaluation*. Kirk-Othmer Encyclopedia of Chemical Technology, John Wiley & Sons, Inc. 2004. 1

[130] G.T. Kuster and M.N. Toksöz. Velocity and attenuation of seismc waves in two-phase media: Part I. Theoretical formulations. *Geophysics*, 39:587-606, 1974. 2, 47, 48, 49

[131] G.T. Kuster and M.N. Toksöz. Velocity and attenuation of seismic waves in two-phase media: Part II. Experimental results. *Geophysics*, 39:607-618, 1974. 2

[132] Y.W. Kwon and J.M. Berner. Micromechanics model for damage and failure analyses of laminated fibrous composites. *Engineering Fracture Mechanics*, 52(2):231-242, 1995. 9

[133] Z. Lafhaj, M. Goueygou, A. Djerbi, M. Kaczmarek. Correlation between porosity, permeability and ultrasonic parameters of mortar with variable water/cement ratio and water content. *Cement and Concrete Research*, 36:625-633, 2006. 105

[134] Z. Lafhaj and M. Goueygou. Experimental study on sound and damaged mortar: Variation of ultrasonic parameters with porosity. *Construction and Building Materials*, 23:953-958, 2009. 100

[135] L. Lam, Y.L. Wong and C.S. Poon. Degree of hydration and gel/space ratio of high-volume fly ash/cement systems. *Cement and Concrete Research*, 30:747-756, 2000. xvi, 114

[136] E.N. Landis, and S.P. Shah. Frequency-dependent stress wave attenuation in cement-based materials. *Journal of Engineering Mechanics*, 121(6):737-743, 1995. 100, 151

[137] E.N. Landis, E.N. Nagy and D.T. Keane. Microstructure and fracture in three dimensions. *Eng. Fract. Mech.*, 70:911-925, 2003. 83

[138] E.N. Landis, E.N. Nagy, D.T. Keane. Microtomographic measurements of internal damage in Portland-cement-based composites. *J. Aerosp. Eng.*, 10:2-6, 1997. 83

[139] N. Laws. On the thermostatics of composite materials. *J. Mech. Phys. Solids*, 21:9-17, 1973. 21

[140] G. Li, Y. Zaho and S.-S. Pang. Four-phase sphere modeling of effective bulk modulus of concrete. *Cement and Concrete Research*, 29:839-845, 1999. 111

[141] S. Li. *Introduction to micromechanics and nanomechanics*. Lecture notes (CE236/C214), departement of Civil and nvironmenatal Engineering, University of California, Berkeley, USA. 9, 29

[142] G. Lielens. *Micro-macro modeling of structured materials*. PhD thesis, UCL/FSA, Louvain-la-Neuve, Belgium, 1999. 44

[143] P. Lipinski and M. Berveiller. Elastoplasticity of micro-inhomogeneous metals at large strains. *Int. J. Plast.*, 5:149-172, 1989. 46

[144] J. Llorca, A. Needleman and S. Suresh. An analysis of the effects of matrix void growth on deformation and ductility in metal ceramic composites. *Acta Metall. Mater.*, 39(10):2317-2335, 1991. 9

[145] B. Loret, N. Khalili. A three phase model for unsaturated soils. *Int. J. Numer. Anal. Meth. Geomech.*, 24:893-927, 2000. 137

[146] S. Maalej, Z. Lafhaj, M. Bouassida. Mechanical properties of cement-based material: comparison between micromechanical models and experimental results. *Proceedings of the first International Conference of Geotechnical Engineering (ICGE-08)*, Hammamet, Tunisia, , 2008. 9

[147] S. Maalej, Z. Lafhaj, M. Bouassida. Comparison between ultrasonic and micromechanical cement paste elastic moduli: influence of pores aspect ratio. *Proceedings of the third International Congress. Design and Modelling of Mechanical Systems*, Hammamet, Tunisia, , 2009. 163

[148] S. Maalej, Z. Lafhaj, M. Bouassida. Determination of cement paste mechanical properties: comparison between micromechanical and ultrasound results. *Computational modelling of concrete structures (Proceedings of EURO-C 2010)*, Rohrmoos/Schladming, Austria, 173-177, 2010. 116

[149] S. Maalej, Z. Lafhaj, M. Bouassida. Micromechanical assessment of ultrasound velocity in entrained air cement paste. *Proceedings of the tenth European Conference on NDT*, Moscow, Russia, , 2010. 141

[150] V.M. Malhotra and N.J. Carino. *Handbook on Nondestructive testing of concrete*. Second edition, CRC press london, Washington, D.C., 2004. 1

[151] K. Z. Markov. Justification of an effective field method in elasto-statics of heterogeneous solids. *Journal of the Mechanics and Physics of Solids*, 49(11):2621-2634, 2001. 2

[152] J.C. Maxwell. *A treatise on electricity and magnetism*. Clarendon Press, Oxford, 1873. 2

[153] P.K. Mehta, P.J.M. Monteiro. *Concrete: Structure, Properties, and Materials*. Prentice-Hall International Series in Civil Engineering and Engineering Mechanics; second edition, 1993. 68, 111

[154] A. Mizrach and U. Flitsanov. Nondestructive ultrasonic measurement method for evaluation avocado ripening. *Proc. Second IS on Sensors in Horticulture*, Acta Hort., 421:111-119, 1998. 100

[155] J. Mobley, K.R. Waters, C.S. Hall, J.N. Marsh, M.S. Hughes, G.H. Brandenburger and J.G. Miller. Measurements and predictions of the phase velocity and attenuation coefficient in suspensions of elastic microspheres. *J. Acoust. Soc. Am.*, 106(2):652-659, 1999. 103

[156] P.J.M. Monteiro and C.T. Chang. The elastic-moduli of calcium hydroxide,*Cement and Concrete Research*, 25(8):1605-1609, 1995. 163

[157] T. Mori and K. Tanaka. Average stress in matrix and average elastic energy of materials with misfitting inclusions. *Acta Metallurgica*, 21:571-574, 1973. 2, 21, 41, 199

[158] M. Moukwa and P.-C. Aïtcin. The effect of drying on cement pastes pore structure as determined by mercury prosimetry. *Cement and Concrete Research*, 18:745-752, 1988. 64

[159] T. Mura. Micromechanics of defects in solids. Martinus Nijhoff, The Hague, 1982. 9

[160] P. Navi, C. Pignat. Three-dimensional characterization of the pore structure of a simulated cement paste. *Cement and Concrete Research*, 29:507-514, 1999. 157

[161] C.-W. Nan, K.-F. Cai and R.-Z. Yuan. A relation between multiple-scattering theory and micromechanical models of effective thermoelastic properties. *Ceramics International*, 22:457-461, 1996. 170

[162] S. Nemat-Nasser and M. Hori. *Micromechanics: Overall properties of heterogeneous materials*. Amesterdam; New York: Elsevier, 1999. 44, 50

[163] A.M. Neville. *Properties of concrete*. Fourth and Final Edition, Pearson Education Limited, 2OO2. 67, 71

[164] A.N. Norris. A differential scheme for the effective moduli of composites. *Mechanics of materials*, 4:1-16, 1985. 2, 52

[165] A.N. Norris, A.J. Callegari and P. Sheng. A generalized differential effective medium theory. *J Mech Phys Solids*, 33(6):525-543,1985. 52

[166] E. Ohdaira, N. Masuzawa. Water content and its effect on ultrasound propagation in concrete – the possibility of NDE. *Ultrasonics*, 38:546-552, 2000. 159

[167] A.V. Oppenheim, R.W. Schafer with J.R. Buck. *Discrete-time signal processing*. second edition, Prentice-Hall, NJ, 1999. 105

[168] J.V. Perfettini, E. Revertegat and N. Langomazino. Evaluation of cement degradation induced by the metabolic products of two fungal strains. *Experientia*, 47:527-533,1991. 1

[169] B. Persson. Moisture in concrete subjected to different kinds of curing. *Matererials & Structures*, 30:533-44, 1997. 133

[170] B. Pichler, C. Hellmich and J. Eberhardsteiner. Spherical and acicular representation of hydrates in a micromechanical model for cement paste: prediction of early-age elasticity and strength. *Acta Mechanica*, 203:137-162, 2008. 118

[171] O. Pierard, C. Friebel and I. Doghri. Mean-field homogenization of multi-phase thermo-elastic composites: a general framework and its validation. *Composites Science and Technology*, 64:1587-1603, 2004. 44

[172] O. Pierard, C. González, J. Segurado, J. LLorca and I. Doghri. Micromechanics of elasto-plastic materials reinforced with ellipsoidal inclusions. *International Journal of Solids and Structures*, 44:6945-6962, 2007. 2

[173] J.S. Popovics and J.L. Rose. A survey of developments in ultrasonic NDE of concrete. *IEEE Transactions on ultrasonics, ferroelectrics, and frequency control*, 41(1):140-143, 1994. 100

[174] L. Pourcelot and F. Patat. Progress and perspectives in ultrasound imaging (in frensh). *IRBM*, 30:47-52, 2009. 100

[175] M.J.W. Povey. *Ultrasonic techniques for fluids characterization*. Academic Press, San Diego, California, 1997. 99

[176] T.C. Powers. Void spacing as a basic for producing air-entrained concrete. *J. Am. Concr. Inst.*, 25(9):741-760, 1954. 63, 88

[177] D.R. Raichel. *The science and applications of acoustics*. Second Edition, Springer Science, 2006. 100

[178] V.S. Ramachandran. *Concrete admixutes handbook: Properties, Science, and Technology*. Second Edition, Noyes publications, New Jersey, U.S.A., 1995. 61

[179] K.L. Rens, C.L. Nogueira and D.J. Transue. Bridge Management and Nondestructive Evaluation. *Journal of Performance of Constructed Facilities*, 19(1):3-16, 2005. 1

[180] M.H. Repacholi and D.A. Benwell. *Essentials of medical ultrasound: a practical introduction to the principles, techniques and biomedical applications*. The HUMANA press Inc. Clifton, 1982. 100

[181] S. Roels, J. Elsen, J. Carmeliet and H. Hens. Characterisation of pore structure by combining mercury porosimetry and micrography. *Materials and Structures*, 34:76-82, 2001. 82

[182] M.G. Richardson. *Fundamentals of durable reinforced concrete*. Spon Press, London, New York, 2002. 63

[183] F. Rollet, M. Mansell and S. Cochran. Determining moisture content in concrete under simulated precipitation using ultrasonic propagation time measurements. *Nondestructive Testing and Evaluation*, 23(4):241-255, 2008. 159

[184] D.M. Roy, P.W. Brown, D. Shi, B.E. Scheetz and W. May. *Concrete microstructure porosity and permeability*. Report SHRP-C-628, Nat. Res. Counc., Washington DC, 1993. 73

[185] W. Sachse and Y.-H. Pao. On the determination of phase and group velocities of dispersivewaves in solids. *J. Acoust. Soc. Am.*, 49(8):4320-4327, 1978. 103

[186] E. Sakai,T. Kasuga, T. Sugiyama, K. Asaga and M. Daimon. Influence of superplasticizers on the hydration of cement and the pore structure of hardened cement. *Cement and Concrete Research*, 36:2049-2053, 2006. 61

[187] H.S. Salem. Determination of the acoustic coupling factor of Biot's theory of elasticity, using in situ seismic measurements. *Energy Sources*, 23:917-936, 2001. 153

[188] J. Salençon. *Handbook of Continuum Mechanics: General Concepts-thermoelasticity*. First edition, Springer, 2001. 185

[189] M.M. Salta and E.V. Pereira. *Factors influencing the corrosion in reinforced concrete. State of the art*. Report, Laboratório Nacional de Engenharia Civil, LNEC, Lisboa. 1

[190] J. Sanahuja, L. Dormieux and G. Chanvillard. Modelling elasticity of a hydrating cement paste. *Cement and Concrete Research*, 37:1427-1439, 2007. 71, 117

[191] L.M. Schwartz and D.L. Johnson. Long-wavelength acoustic propagation in ordered and disordered suspensions. *Phys. Rev. B*, 30:4302-4313, 1984. 135

[192] I. Sevostianov, N. Yilmaz, V. Kushch and V. Levin. Effective elastic properties of matrix composites with transversely-isotropic phases. *International Journal of Solids and Structures*, 42:455-476, 2005. 37

[193] S.P. Shah, S. Choi. Nondestructive techniques for studying fracture processes in concrete. *Int. J. Fract.* , 98:351-359, 1999. 83

[194] T.J. Sheppard. Solid state gas metering - the future. *Flow Meas. Instrum.*, 5(2):103-106, 1994. 100

[195] D. Shi and D.N. Winslow. Contact angle and damage during mercury intrusion into cement paste, *Cement and Concrete Research*, 15:645-654, 1985. 82

[196] M. Shink. *Compatibilité élastique, comportement mécanique et optimisation des bétons de granulats légers*. PhD thesis, Université Laval, Qéubec, 2003. 24

[197] M.M. Shukla and N.T. Padial. A calculation of the Debye characteristic temperature of cubic crystals. *Revista Brasileira de Física*, 3(1):39-45, 1973. 28

[198] F. Soltani. *Caractérisation de la pâte de ciment par des méthodes ultrasonores*. PhD thesis, Ecole Centrale de Lille, France, 2010. 97

[199] S.R. Stock, N.K. Naik, A.P. Wilkinson and K.E. Kurtis. X-ray microtomography (microCT) of the progression of sulfate attack of cement paste. *Cement and Concrete Research*, 32:1673-1675, 2002. 83

[200] P.E. Stutzman and J.R. Clifton. Specimen preparation for scanning electron microscopy. *Proceedings of the Twenty-First International Conference on Cement Microscopy*, Las Vegas, Nevada, USA, 10-22, 1999. 90

[201] P.E. Stutzman. (2001) Scanning electron microscopy in concrete petrography. *The American Ceramic Society*, 59-72, 2000. xv, 68, 92

[202] K. Tanaka and T. Mori. Note on volume integrals of the elastic field around an ellipsoidal inclusion. *Journal of Elasticity*, 2(3):199-200, 1972. 199

[203] G. P. Tandon and G.J. Weng . Average stress in the matrix and effective moduli of randomly oriented composites. *Composites Science and Technology*, 27:111-132, 1986. 184, 190

[204] H.F.W. Taylor. *Cement chemistry*. 2nd edition, Thomas Telford edition, London, 1997. 61, 65, 71

[205] Technical file (Fiche technique) FOSROC, Norme EN 934-2 cf. règlement NF 085. 62

[206] P.D. Tennis and H.M. Jennings. A model for two types of calcium silicate hydrate in the microstructure of portland cement paste, *Cement and Concrete Research* 30:855-863, 2000. 66, 117

[207] K. Tharmaratnam and B.S. Tan. Attenuation of ultrasonic pulse in cement concrete. *Cement and Concrete Research*, 20:335-345, 1990. 100

[208] J.J. Thomas, and H.M. Jennings. Effect of heat treatment on the pore structure and drying shrinkage behavior of hydrated cement paste. *J. Am. Ceram. Soc.*, 85(9)2293-2298, 2002. 157

[209] J.J. Thomas, H.M. Jennings and A.J. Allen. The surface area of cement paste as measured by neutron scattering: evidence for two C-S-H morphologies. *Cement and Concrete Research*, 28(6):897-905, 1998. 66

[210] T. Uomoto. *Non- Destructive Testing in Civil Enngineering 2000*. Elsevier Tokyo, Oxford, 2000. 1

[211] V.V. Vasiliev and E. V. Morozov. *Advanced mechanics of composite materials*. First edition, Elsevier, Oxford, 2007. 96

[212] K. Velez, S. Maximilien, D. Damidot, G. Fantozzi, F. Sorrentino. Determination by nanoindentation of elastic modulus and hardness of pure constituents of Portland cement clinker. *Cement and Concrete Research*, 31:555-561, 2001. 2, 118

[213] I. Vlahinić, H.M. Jennings, J.J. Thomas. A constitutive model for drying of a partially saturated porous material. *Mechanics of Materials* 41:319-328, 2009. 163

[214] H.Q. Vu. *Estimation des propriétés poromécaniques effectives des argiles : apport des méthodes d'homogénéisation*. PhD thesis, Ecole Nationale Suprieure de Gologie de Nancy, Nancy, France,2006. 18

[215] J. P. Watt, G.F. Davies and R.J. O'Connell. The elastic properties of composite materials. *Reviews of geophysics and space physics*, 14(4)541-563, 1976. 23

[216] L. J. Walpole. On bounds for the overall elastic moduli of inhomogeneous systems-I. *J. Mech. Phys. Solids*, 14:151-162, 1966. 16

[217] L. J. Walpole. On bounds for the overall elastic moduli of inhomogeneous systems-II. *J. Mech. Phys. Solids*, 14:289-301, 1966. 16

[218] L.J. Walpole. On the overall elastic moduli of composite materials. *J. Mech. Phys. Solids*, 17:235-251, 1969. 194

[219] J. B. Walsh. New analysis of attenuation in partially melted rock. *Journal of geophysical research*, 74(17):4333-4337, 1969. 194

[220] J. B. Walsh, W.F. Brace and A.W. England. Effect of porosity on compressibility of glass. *Journal of The American Ceramic Society*, 48(12):605-608, 1965. 16

[221] H. Wang and Q. Li. Prediction of elastic modulus and Poisson's ratio for unsaturated concrete. *International Journal of Solids and Structures*, 44:1370-1379, 2007. 134

[222] E.W. Washburn. Note on a method of determining the distribution of pore sizes in a porous material. *Proc. Natl. Acad. Sci.*, 7:115-116, 1921. 79

[223] G. Washer, P. Fuchs and B. Graybeal. Elastic properties of reactive powder concrete. *Non-Destructive Testing in Civil Engineering (NDT-CE) Berlin*, 2003. 183

[224] G.J. Weng . A micromechanical theory of grain-size dependence in metal plasticity. *J. Mech. Phys. Solids*, 31(3):193-203, 1983. 46

[225] K.W. Winkler and A. Nur. Seismic attenuation: Effects of pore fluids and frictional sliding. *Geophysics*, 47(1):1-15, 1982. 162

[226] P.J. Withers, W.M. Stobbs and O.B. Pederson. The application of the Eshelby method of internal stress determination to short fiber metal matrix composites. *Acta metall.*, 37(11):3061-3084, 1989. 39

[227] H.S. Wong, M.K. Head and N.R. Buenfeld. Characterizing the pore structure of cement-based materials using backscattered electron and confocal microscopy. *Measuring, Monitoring and Modeling Concrete Properties*, 495-502, 2006. 86

[228] T.T. Wu. The effect of inclusion shape on the elastic moduli of a two-phase material. *Int. J. Solids Struct.*, 2:1-8, 1966. 39, 46, 194

[229] Y. Xi and H.M. Jennings. Shrinkage of cement paste and concrete modelled by a multiscale effective homogeneous theory. *Materials and Structures*, 30:329-339, 1997. 69, 119

[230] I.O. Yaman, N. Hearn and H.M. Aktan. Active and non-active porosity in concrete: Part I: Experimental evidence. *Materials and Structures*, 35:102-109, 2002. 3, 114

[231] I.O. Yaman, H.M. Aktan and N. Hearn. Active and non-active porosity in concrete Part II: Evaluation of existing models. *Materials and Structures*, 35:110-116, 2002. 3, 77, 157, 159

[232] C.C. Yang. Approximate elastic moduli of lightweight aggregate. *Cement and Concrete Research*, 27(7):1021-1030, 1997. 51, 190

[233] C.C. Yang and R. Huang. Double inclusion model for approximate elastic moduli of concrete material. *Cement and Concrete Research*, 26(1):83-91, 1996. 51

[234] N. Yang, J.H. Kim, J.J. Thomas, O. Balogun and S. Krishnaswamy. Characterization of water-saturated porous cement paste by a lazer based ultrasonic NDE technique. *American Institute of Physics*, 1211:1541-1548,2010. 159

[235] G. Ye. *Experimental study and numerical simulation of the development of the microstructure and permeability of cementitious Materials*. PhD thesis, Delft University of Technology, The Netherlands, 2003. xv, 66

[236] M.W. Zemansky and R.H. Dittman. *Heat and thermadynamics: An intermediate textbook*. The McGraw-HILL Companies, seventh edition, 1997. 100

[237] J.-j. Zheng and X.-z. Zhou. Analytical method for prediction of water permeability of cement paste. *ACI Materials Journal*, 105(2):200-206, 2008. 154

[238] R.W. Zimmerman. Elastic moduli of a solid containing spherical inclusions. *Mechanics of Materials*, 12:17-24, 1991. 52

[239] R.W. Zimmerman, M.S. King and P.J.M. Monteiro. The elastic moduli of mortar as a porous-granular material. *Cement and Concrete Research*, 16:239-245, 1986. 3, 49

[240] A. Zofka, M.O. Marasteanu, T.R. Clyne, X. Li and O. Hoffmann. *Developement of simple asphalt test for determination of RAP blending charts*. Final Report, University of Minnesota, Minnesota Department of Transportation Office of Research Services, 2004. 28

[241] T.I. Zohdi and P. Wriggers. Computational Micro-macro Material Testing. *Archives of Computational Methods in Engineering-State of the art reviews*, 8(2):3-106, 2001. 15, 16, 46